

Milan Padilla

Spatially Resolved Characterization and Simulation of Interdigitated Back Contact Silicon Solar Cells

Spatially Resolved Characterization and Simulation of Interdigitated Back Contact Silicon Solar Cells

Dissertation

zur Erlangung des akademischen Grades
des Doktors der Naturwissenschaften (Dr. rer. nat.)
der Technischen Fakultät
der Albert-Ludwigs-Universität Freiburg im Breisgau

vorgelegt von
Milan Padilla

angefertigt am Fraunhofer-Institut für Solare
Energiesysteme ISE, Freiburg im Breisgau

September 2015

Erstgutachter: Prof. Dr. Eicke R. Weber
Zweitgutachter: Prof. Dr. Leonhard M. Reindl
Dekan: Prof. Dr. Georg Lausen
Tag der mündlichen Prüfung: 16.12.2015

Schriftenreihe der Reiner Lemoine-Stiftung

Milan Padilla

**Spatially Resolved Characterization and Simulation
of Interdigitated Back Contact Silicon Solar Cells**

Shaker Verlag
Aachen 2016

Bibliographic information published by the Deutsche Nationalbibliothek

The Deutsche Nationalbibliothek lists this publication in the Deutsche Nationalbibliografie; detailed bibliographic data are available in the Internet at <http://dnb.d-nb.de>.

Zugl.: Freiburg, Univ., Diss., 2015

Copyright Shaker Verlag 2016

All rights reserved. No part of this publication may be reproduced, stored in a retrieval system, or transmitted, in any form or by any means, electronic, mechanical, photocopying, recording or otherwise, without the prior permission of the publishers.

Printed in Germany.

ISBN 978-3-8440-4242-9

ISSN 2193-7575

Shaker Verlag GmbH • P.O. BOX 101818 • D-52018 Aachen

Phone: 0049/2407/9596-0 • Telefax: 0049/2407/9596-9

Internet: www.shaker.de • e-mail: info@shaker.de

Für meine Eltern

Abstract

Interdigitated back contact (IBC) solar cells currently have the highest efficiency of all silicon solar cells on the laboratory and industrial scale. Great research efforts have been made to reduce the production costs and enable more widespread commercial application of this cell architecture. Despite the great interest of companies and the research community in IBC cells and the recent success of spatially resolved characterization techniques, there is little knowledge about applying these characterization techniques on IBC cells. The complex device structure of IBC cells requires consideration of the three-dimensional current flow and carrier density distributions that these imaging techniques are based on. This dissertation aims to close that knowledge gap by analyzing IBC cells with luminescence imaging, lock-in thermography and spectrally resolved light beam induced current mapping (SR-LBIC) at all important solar cell operating conditions.

The acquired knowledge through this work enables the study of IBC cells with powerful imaging methods that were thus far applied only to simple cell structures like Al-BSF cells. The IBC cell analysis is carried out on a fundamental level and a practical level. On the fundamental level, it was done by studying the inherently inhomogeneous image contrast patterns caused by the interdigitated doping structure. On the practical level, it was done by studying the detection of local processing faults, that are grouped into resistive, shunting and surface recombination / optical faults. Local cell characteristics are investigated at short-circuit, maximum power point, open-circuit and in the dark under forward- and reverse-bias. For a deeper understanding of the device physics, in particular numerical modeling of luminescence imaging was developed. This modeling serves as a powerful complementary approach to the conventional experimental work. Besides providing progress in understanding device physics, new characterization methods are developed in this work. This includes short-circuit current density mapping by SR-LBIC for arbitrary silicon solar cells and the adaptation of series resistance imaging to IBC cells.

All acquired knowledge on the interpretation of regular patterns as well as the signature of the investigated local processing faults in the images from several measurement techniques is summarized in user-friendly flowcharts and tabular guidelines for future reference.

Zusammenfassung

Rückseiten kontaktierte (IBC) Solarzellen haben derzeit die höchste Effizienz aller Silizium Solarzellen im Labor und im industriellen Maßstab. Große Anstrengungen werden getätigt um die Produktionskosten dieser Solarzellen zu senken und so eine kommerzielle Anwendung dieser Zellarchitektur weiter ermöglichen. Trotz des großen Interesses von Firmen und Forschungsinstituten an IBC Zellen und trotz des Erfolgs ortsaufgelöster Charakterisierungsmethoden, gibt es für die Anwendung dieser Charakterisierungsmethoden an IBC Zellen wenig fundierte Kenntnisse. Die komplexe Struktur von IBC Zellen erfordert die Berücksichtigung des dreidimensionalen Stromflusses und der dreidimensional Ladungsträgerdichtenverteilung, auf denen diese Methoden beruhen. Diese Dissertation hat zum Ziel diese Wissenslücke durch die Analyse von IBC Zellen mittels Lumineszenz Imaging, Lock-in Thermographie und Kartierung spektral aufgelöster lichtinduzierte Ströme (SR-LBIC) an allen wichtige Arbeitspunkten der Solarzelle zu schließen.

Das durch diese Arbeit erlangte Wissen ermöglicht die Analyse von IBC Zellen mit mächtigen bildgebenden Methoden die zuvor nur an einfacheren Zellstrukturen wie Al-BSF verwendet wurden. Die IBC Zellanalyse wird auf einer fundamentalen und einer praktischen Ebene ausgeübt. Auf der fundamentalen Ebene wird eine Studie der inhärent inhomogenen Bildkontrastmuster, die durch die interdigitale Dotterstruktur erzeugt werden, durchgeführt. Auf der praktischen Ebene wird eine Studie zur Erkennung von lokaler Prozessfehlern durchgeführt, die gruppiert sind in Widerstands-, Shunt- und Oberflächenrekombinationsfehler. Lokale Zellcharakteristika werden untersucht unter Kurzschlussbedingungen, am Punkt maximaler Leistung, im Leerlaufzustand und im Dunkeln unter Vorwärts- und Rückwärtsspannung. Für ein tieferes Verständnis über die Zellphysik wurde vor allem die numerische Modellierung von Lumineszenz Imaging entwickelt. Diese Modellierung ist ein äußerst hilfreicher komplementärer Ansatz zur konventionellen experimentellen Arbeit. Neben Fortschritten im physikalischen Verständnis wurden auch neue Charakterisierungsmethoden im Rahmen dieser Arbeit entwickelt. Dies beinhaltet

die orts aufgelöste Kartierung von Kurzschlussstromdichten über SR-LBIC für beliebige Solarzellen sowie die Anpassung von Serienwiderstands Imaging für IBC Zellen.

Das gesamte erlangte Wissen über die Interpretation der regelmäßigen Muster, sowie die Signatur der untersuchten lokalen Prozessfehler bei bildgebenden Messtechniken ist in benutzerfreundlichen Flussdiagrammen und tabellarischen Leitfäden für eine einfache spätere Nutzung zusammengefasst.

Contents

1	Introduction	1
2	Theoretical Background	5
2.1	Solar cell physics	5
2.1.1	Semiconductor physics and operation principle	6
2.1.2	Recombination mechanisms and injection conditions	12
2.1.3	Diode models and I-V curve analysis	22
2.1.4	Peltier effect	26
2.2	IBC solar cell design and current flow	29
2.3	Physical principles of applied imaging techniques	37
2.3.1	Luminescence imaging	37
2.3.2	Lock-in thermography	42
3	SR-LBIC for short-circuit current density mapping	51
3.1	Literature overview	52
3.2	Experimental setup and spatial resolution	54
3.3	J_{sc}^{loc} -mapping principle	56
3.4	Pseudo- J_{sc}^{loc} and optical loss mapping	61
3.5	Quantified local J_{sc} losses in IBC cells	64
4	Luminescence imaging of local cell characteristics	71
4.1	Literature overview	72

4.2	Experimental setup and spatial resolution	75
4.3	Interpretation of luminescence patterns and contrasts	80
4.3.1	PL: Luminescence imaging under illumination	80
4.3.2	EL: Luminescence imaging in the dark	85
4.4	Numerical modeling of luminescence images	90
4.4.1	Luminescence intensity and optical blurring . .	92
4.4.2	Example simulation results	97
4.5	Surface recombination parameters from modeled luminescence images	101
4.5.1	Sensitivity analysis	101
4.5.2	Matching experiments with simulation data . .	105
4.6	Local series resistance imaging	109
4.6.1	Definition, voltage calibration and image interpretation	109
4.6.2	Lateral transport effects	116
5	Lock-in thermography of local cell characteristics	121
5.1	Literature overview	122
5.2	Experimental setup, emissivity and spatial resolution .	125
5.3	Local power dissipation and Peltier effect modeling . .	130
5.3.1	Simulation model	131
5.3.2	Modeling results and consequences for LIT . .	138
5.4	Heat sources, power calibration and contrast patterns	148
6	Detection of local processing faults	161
6.1	Literature overview	162
6.2	Local series resistance faults	166
6.2.1	Simulated I-V and luminescence characteristics	166
6.2.2	Experimental verification	178
6.3	Local shunting faults	187
6.3.1	Pinholes	187
6.3.2	Spikes	194
6.4	Optical and passivation faults	204

6.5	Breakdown patterns	208
7	Discussion and guidelines for IBC cell characteriza- tion	215
7.1	Guidelines for pattern and contrast interpretation . . .	216
7.2	Guidelines for identification of local processing faults .	223
7.3	Review and limitations of the proposed methods . . .	236
8	Summary and outlook	243
	Ausführliche Zusammenfassung in deutscher Sprache	251
A	Details on all investigated solar cells	259
	Bibliography	262
	List of symbols, abbreviations and physical constants	295
	List of publications	305
	Acknowledgements	309

Chapter 1

Introduction

After turbulent years of overcapacity, dumping pricing, bankruptcies and policy changes, the global photovoltaics market is growing strongly and more sustainably again with major solar cell and solar module manufacturers reporting production capacity expansions, predominantly by Chinese, Taiwanese and US companies. In 2014, photovoltaic energy constituted over 1 % of the global energy production and 5.8 % of the electric energy in Germany [1]. The most recent World Energy Outlook by the International Energy Agency predicts solar energy to be the cheapest and most sustainable source of energy by 2050 [2]. Silicon wafer based solar cell technology continues to be the predominant material system on the market with over 90 % market share. After many years of research and development, advanced high efficiency silicon solar cell technologies are being produced on an industrial scale, further lowering the energy production costs. As both markets and products diversify, the market segment of highest efficiency solar panels is predicted to grow strongly over the next years [3].

One silicon solar cell technology that vastly outperforms the conversion efficiency of mainstream industrial technology (efficiency 17–20 %) is the so-called interdigitated back contact (IBC) cell. This complex cell design has all metal contacts on the rear, which allows

allowing higher current generation and also shows excellent reliability and performance under standard testing conditions and increased temperatures. The company SunPower industrially manufactures IBC cells with median conversion efficiency beyond 24 % [4] and the company Panasonic holds the current world record for conversion efficiency at 25.6 % [5, 6]. The higher relative efficiency of best in class IBC cells reduces the amount of area to generate the same output power as average conventional cells by about 30 %. IBC cells by SunPower are also used in the SolarImpulse 2 airplane, that is entirely fueled by a battery system storing solar energy and is currently on a flight around the world [7]. Several major manufacturers such as Trina Solar, Yingli, Panasonic, Sharp and Hareon Solar have declared that IBC structures are the goal of their technological roadmap [8] and great efforts are made to simplify the IBC cell production process to be more economically competitive to the mainstream design, without compromising on efficiency.

On the other hand spatially resolved characterization of silicon solar cells, that is the detailed local analysis of solar cells, has seen enormous advances over the past 15 years with the application of luminescence imaging and lock-in thermography. Thanks to these imaging techniques and recently developed data analysis methods, it is now possible to accurately locate and quantify efficiency losses from processing faults in solar cell manufacturing that were inaccessible in standard global cell and module measurements. Using spatially resolved characterization, cell manufacturers are more quickly able optimize production lines and eliminate problems that lower the overall cell efficiency.

Aim of this dissertation

Despite the enormous interest of companies and the research community in IBC cells and the vast success of spatially resolved characterization, there is little knowledge about applying these characterization techniques on IBC cells. The established imaging methods were developed and verified using the standard, more simple cell designs that do not bear the complexity of IBC cells. The complex device struc-

ture of IBC cells requires three-dimensional treatment of current flow and carrier density distributions that the imaging techniques in this work are based on [9].

This dissertation aims to close that knowledge gap by analyzing IBC cells with luminescence imaging, lock-in thermography and spectrally resolved light beam induced current mapping (SR-LBIC) at all important solar cell operating conditions. The analyses in this dissertation work on a fundamental level, discussing patterns and contrasts in imaging but also on a more applied level with processing fault characterization. The investigations are carried out both by experiments and numerical simulations of characterization experiments that enable very detailed understanding of the subject.

Outline

This work is divided into one chapter summarizing the necessary theoretical background (chapter 2), three result chapters each dealing with the application of an imaging/mapping technique on IBC cells (chapters 3-5), a result chapter applying the acquired knowledge to study local processing faults (chapter 6), a discussion chapter with resulting guidelines (chapter 7) and a chapter with a summary and outlook (chapter 8). Each result chapter begins with a literature overview about the history and state-of-the-art on the topic with regard to silicon solar cell characterization. In more detail:

Chapter 2 covers the fundamental semiconductor physics for the microscopic description of solar cell operation, the diode-models and the Peltier effect. The IBC cell design concepts studied in this work are introduced including illustrations on current flow. Finally, the physical principles behind luminescence imaging and lock-in thermography are presented.

Chapter 3 deals with spatially resolved short-circuit current density mapping using SR-LBIC. For this, a novel data analysis evaluation method is presented that allows studying the net effect of local electrical and optical short-circuit current losses at standard testing conditions for diverse solar cell designs.

Chapter 4 presents an in-depth analysis of luminescence imag-

ing on IBC cells at all important operating conditions including general interpretations of patterns and contrasts. A numerical model for simulating luminescence experiments is introduced and a method is proposed for obtaining local surface recombination parameters by modeled luminescence images. Also, series resistance imaging is studied in detail, resulting in an adapted interpretation of a conventional analysis technique to the IBC cell concept.

Chapter 5 discusses lock-in thermography on IBC cells, similarly to chapter 4. A focus is set on the Peltier effect and how it influences the measurement signals. Through numerical simulations and experimental data, interpretations of the observed patterns and contrasts as well as a power calibration method are presented.

Chapter 6 uses the knowledge from the previous three chapters and a combination of the imaging techniques to characterize some of the common problems encountered in IBC cell production. Special attention is put on series resistance losses by contacting faults, shunting by pinholes and spikes as well as breakdown behavior.

Chapter 7 reviews and discussed the obtained results through flowcharts and tabular guidelines for future reference in research and development. Critical remarks on the limitations of the presented methods is included at the end.

Chapter 8 contains a summary of the main achievements of this work, short summaries of each chapter an outlook for future endeavors.

All solar cells presented in this work were fabricated by researchers at Fraunhofer ISE. Technical details on all cells are found in appendix A. Many of the presented results were published in scientific journals or presented at conferences. In these cases, only material used from publications where the author of this work was the first author. A list of co-authored publications can be found at the end of this dissertation. The introduction to each chapter further states collaborations and where else the particular content was published.

Chapter 2

Theoretical Background

This chapter summarizes the most important theoretical background required for the results and discussions in this work. Basic knowledge of quantum mechanics, semiconductor physics, material science and optoelectronics by the reader is preconditioned. The presented theory in this chapter is based on either text book knowledge or other established literature. Only silicon photovoltaics with single junctions are treated in this work (i.e. no tandem concepts). All schematics were created by the author but similar can also be found in literature.

Section 2.1 treats solar cell physics through semiconductor equations, recombination mechanisms, diode modeling and the Peltier effect. Section 2.2 introduces the interdigitated back contact solar cell design (IBC) studied in this work and explains differences to conventional cells. Finally, section 2.3 explains the physical principles behind the luminescence imaging and lock-in thermography techniques used in this work.

2.1 Solar cell physics

This section begins with a review of the physics describing charge carrier density distributions and current flows in a solar cell because this plays an important role for the physical interpretation of lumi-

nescence imaging and lock-in thermography in this work. It then discusses in 2.1.2 the recombination mechanisms and injection conditions of IBC cells. The equations presented in section 2.1.1 and 2.1.2 are also the foundation for the numerical device simulation software used in this work. This is followed in 2.1.3 by an introduction to current-voltage curves and how they can be described using diode models, which is much used throughout this work. The equations described in these sections can be found in standard textbook literature such as [10, 11]. Finally, the section ends in 2.1.4 with an introduction to the Peltier effect in solar cells based on [12], as this becomes important in chapter 5.

2.1.1 Semiconductor physics and operation principle

A crystalline silicon photovoltaic solar cell is a semiconductor device with a pn junction that can convert photon energy into electrical energy for consumption. In a first approximation, photons with energy E_γ and wavelength λ higher than the bandgap E_g (1.12 eV in undoped silicon at 300 K [13]) are absorbed and create excess electron-hole pairs. These electron-hole pairs are dissociated at room temperature and diffuse within the cell. Without electrical biasing (open-circuit), illumination results in a voltage within the cell and if short-circuited, an electrical current flows out of the cell. In n-type base material, holes are the minority carriers which are extracted if bias voltages below open-circuit are applied. Most of the presented expressions are a function of temperature. All experiments and simulations in this thesis were conducted close to 25 °C. Most expressions are a function of location \vec{r} within the three-dimensional solar cell but for brevity, \vec{r} or other spatial indexes are omitted in this chapter.

Charge carrier distribution

As a function of energy E , figure 2.1 schematically depicts for the conduction (C) and valence band (V), the density of states (D_n, D_p), Fermi-Dirac distributions (f_n, f_p) and resulting charge carrier densi-

ties of electrons n and holes p . The figure also shows the conduction and valence band energies E_C and E_V as well as the quasi-Fermi levels Φ_{F_n} and Φ_{F_p} to describe electron and hole distribution respectively. The bandgap is defined as $E_g = E_C - E_V$. The integrated charge carrier densities are calculated via

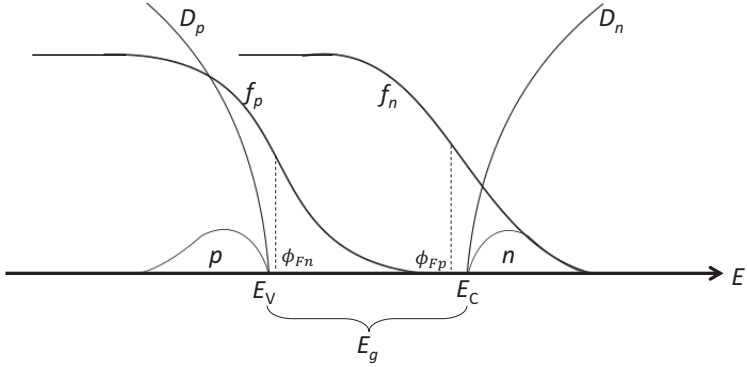


Figure 2.1: Carrier density distributions under excitation. Electron and hole densities are described by two separate quasi-Fermi levels. Adapted from [10].

$$n = \int_{E_C}^{\infty} D_n(E) f_n dE \quad p = \int_{-\infty}^{E_V} D_p(E) f_p dE, \quad (2.1)$$

where the density of states can be expressed as

$$D_n(E) = 4\pi \left(\frac{2m_n^*}{h^2} \right)^{3/2} \sqrt{E - E_C}, \quad (2.2)$$

$$D_p(E) = 4\pi \left(\frac{2m_p^*}{h^2} \right)^{3/2} \sqrt{E_V - E}. \quad (2.3)$$

where m_n^* and m_p^* are the effective electron and hole masses and h the Planck constant. The Fermi distribution for electrons and holes is described by

$$f_n(E) = \frac{1}{\exp\left(\frac{E - \Phi_{Fn}}{kT}\right) + 1}; \quad f_p(E) = \frac{1}{\exp\left(\frac{\Phi_{Fp} - E}{kT}\right) + 1}, \quad (2.4)$$

where k is the Boltzmann constant and T the temperature. The Fermi distribution can be approximated by the Boltzmann distribution at room temperature for energies significantly higher than the Fermi level. This simplifies the integrals and makes them analytically solvable, provided that at least $E - \Phi_{Fn} > 3kT$ according to [10]. Using the approximation one obtains

$$f_n(E) = \frac{1}{\exp\left(\frac{E - \Phi_{Fn}}{kT}\right) + 1} \approx \exp\left(-\frac{E - \Phi_{Fn}}{kT}\right), \quad (2.5)$$

and the respective relation for p . Solving the integrals 2.1 by inserting equations 2.3 and 2.5, one obtains

$$n = N_C \exp\left(-\frac{E_C - \Phi_{Fn}}{kT}\right); \quad p = N_V \exp\left(-\frac{\Phi_{Fp} - E_V}{kT}\right), \quad (2.6)$$

with the respective effective densities of states

$$N_C = 2 \left(\frac{2\pi m_n^* kT}{h^2}\right)^{3/2}; \quad N_V = 2 \left(\frac{2\pi m_p^* kT}{h^2}\right)^{3/2}. \quad (2.7)$$

Without illumination and doping, electrons and holes are in equilibrium and an intrinsic charge carrier concentration n_i as a function of temperature establishes. Analytically, n_i is expressed as

$$n_i^2 = N_C N_V \exp\left(-\frac{E_g}{kT}\right). \quad (2.8)$$

The value for n_i in intrinsic silicon at 300 K has been reevaluated several times in literature. The currently most used value in the silicon photovoltaic community is $9.65 \cdot 10^9 / \text{cm}^3$ by Altermatt et al. [14]. While this value is small compared to typical doping densities, the parameter n_i^2 appears as a sensitive term in many analytical expressions and can significantly influence calculation results. The bandgap of silicon is also a function of doping density. At high doping densities e.g. at diffused surfaces, bandgap narrowing (BGN) [15] may decrease E_g and increase n_i to an effective intrinsic carrier density $n_{i,\text{eff}}$ and effective bandgap $E_{g,\text{eff}}$. According to the law of mass action in equilibrium, $np = n_i^2$. Consequently, equilibrium carrier concentrations p_0 and n_0 for p-type and n-type material are

$$p_0 = N_A ; n_0 = \frac{n_i^2}{N_A} \text{ for p-type and,} \quad (2.9)$$

$$n_0 = N_D ; p_0 = \frac{n_i^2}{N_D} \text{ for n-type,} \quad (2.10)$$

where N_D is the donor density (typically phosphorous) and N_A the acceptor density (typically boron) and assuming complete ionization of all doping atoms. Under external electrical or optical excitation however, excess charge carriers alter this relation. Combining equations 2.6 and 2.8 leads to the fundamental relation

$$np = N_C N_V \exp\left(\frac{E_C - E_V}{kT}\right) = n_i^2 \exp\left(\frac{\Phi_{F_n} - \Phi_{F_p}}{kT}\right). \quad (2.11)$$

The term $\Phi_{F_n} - \Phi_{F_p}$ is often named quasi-Fermi level splitting $\Delta\eta$ in units of eV. Divided by the elementary charge q , $(\Phi_{F_n} - \Phi_{F_p})/q$ can be interpreted as an implied voltage within the cell, which will be used in section 4.6 of this work. Excess carriers (Δn and Δp) are charge carriers in addition to the equilibrium conditions, generated by excitation. In a good approximation, quasi neutrality of excess carriers can be assumed in silicon solar cells, meaning that the excess electron and hole densities are in balance ($\Delta n = \Delta p$) outside of the

space charge region in the solar cell [16–18].

Charge carrier flow

The electrical potential ψ is linked to the charge carrier concentrations via Gauss's law, which relates the net charge carrier density ρ_Q to an electrical field $\vec{\nabla}\psi$ via

$$\epsilon\epsilon_0\Delta\psi = -\rho_Q = -q(p - n + N_D - N_A). \quad (2.12)$$

where q is the elementary charge, ϵ_0 the vacuum permittivity, ϵ the relative permittivity and Δ the Laplace operator. Now that the equations for charge carrier density distributions in solar cells under excitation are established, charge carrier flow i.e. current flow is described. According to the drift-diffusion approximation, the flow of electrons and holes is composed of a drift part driven by electric fields and a diffusive part driven by concentration gradients. The total current \vec{J} is the sum of electron and hole currents \vec{J}_n and \vec{J}_p

$$\vec{J} = \vec{J}_n + \vec{J}_p. \quad (2.13)$$

These currents are proportional and pointed towards the gradients in quasi-Fermi levels as in

$$\vec{J}_n = -q\mu_n n \vec{\nabla}\Phi_{Fn} \quad \vec{J}_p = q\mu_p p \vec{\nabla}\Phi_{Fp} \quad (2.14)$$

where μ_n and μ_p are the respective electron and hole mobility. Several parametrizations for mobility in silicon have been published in literature and implemented in numerical simulations. For a recent publication, refer to [19]. The term $q\mu_n n$ is often called conductivity σ as

$$\sigma_n = qn\mu_n \quad \sigma_p = qp\mu_p. \quad (2.15)$$

Furthermore, via the Einstein relation [20], the mobility of minority electrons and holes is related to the diffusion coefficient D via

$$D_{n/p} = \frac{kT}{q} \mu_{n/p} . \quad (2.16)$$

Another useful expression to classify bulk doping density in this work is the base resistivity ρ^{base} which is related to the net doping density $N_{\text{dop}} = N_D - N_A$ via

$$\frac{1}{\rho^{\text{base}}} = q N_{\text{dop}} \mu_{\text{maj}} , \quad (2.17)$$

where μ_{maj} is the mobility of the majority carriers in the base. The continuity equation fundamentally links changes in the charge carrier density and current flow with generation G and recombination R within the solar cell as in

$$\frac{\partial n}{\partial t} = G_n - R_n - \nabla \cdot \vec{J}_n ; \quad \frac{\partial p}{\partial t} = G_p - R_p - \nabla \cdot \vec{J}_p . \quad (2.18)$$

This work only deals with solar cells working in a steady state or a quasi steady state, such that $\partial n / \partial t \approx 0$. Combining equation 2.18 with 2.14 leads to

$$-\vec{\nabla} \cdot (q \mu_n n \vec{\nabla} \Phi_{Fn}) = q(G_n - R_n) \quad \vec{\nabla} \cdot (q \mu_p p \vec{\nabla} \Phi_{Fp}) = q(G_p - R_p) . \quad (2.19)$$

Equations 2.19 and 2.12 is what is essentially solved by numerical simulation programs such as PC1D [21] and Quokka [17] where the variables Φ_{Fn} , Φ_{Fp} and ψ at given generation and boundary conditions describe the solar cell.

Figure 2.2 schematically illustrates the band bending of an illuminated pn junction (with surface recombination). Under open-circuit

(a), no current is extracted out of the cell and all recombination occurs in the volume and at the surfaces. Under short-circuit (b), band-bending is highest and the maximum amount of current flows out of the cell. Under open-circuit conditions, $\Delta\eta$ between the contacts equals the measured open-circuit voltage V_{oc} . Under short-circuit however, there is zero voltage between the contacts. However, there is quasi-Fermi level splitting and thus excess carrier distributions in both p and n regions. For simulated energy band diagrams of a typical solar cell at all important operating conditions refer to [22].

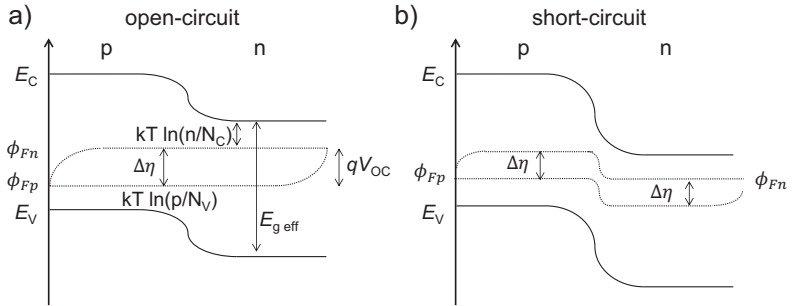


Figure 2.2: Schematic of the energy levels in an illuminated pn junction solar cell under open-circuit (a) and short-circuit (b). Adapted from [23]

2.1.2 Recombination mechanisms and injection conditions

Only a part of all photon energy reaching a single junction silicon solar cell from the sun's spectrum can theoretically be converted into electrical energy. Losses can be grouped into electrical, optical and thermalization losses. Optical losses are all photons that are not contributing to excess carrier generation. This can be caused by optical reflection on the front surface, the escape of photons out of the cell after reflection on the rear side but also parasitic absorption such as free carrier absorption (FCA) [24]. Once a photon flux Φ_λ penetrated the cell at $z = 0$, the photon flux decreases exponentially as a function of the absorption coefficient α which is a function of

photon wavelength λ , resulting in a specific generation profile $G(\lambda, z)$ via

$$G_\lambda(\lambda, z) = \alpha(\lambda)\Phi(\lambda, z = 0)e^{(-\alpha(\lambda)z)} . \quad (2.20)$$

The total photogenerated current J_{gen} is obtained by integration over cell thickness d and all wavelengths of the spectrum Φ_λ via

$$J_{\text{gen}} = q \int_0^d \int_{\lambda_1}^{\lambda_2} G_\lambda(\lambda, z) d\lambda dz . \quad (2.21)$$

Following photon absorption, excess charge carriers (e.g. electrons) are energetically lifted from the valence band over the bandgap into the conduction band. The excess photon energy is dissipated in the cell by 'thermalization' due to inelastic electron-phonon scattering on a picosecond timescale. This 'hot-carrier' excess energy is irretrievable as of today's solar cell technology. Once excess charge carriers are generated, there are radiative recombination and Auger recombination as the two intrinsic recombination mechanisms, as well as recombination via defect energy levels in the bandgap named Shockley-Read-Hall (SRH) recombination. The fundamental efficiency limitation of a single pn junction photovoltaic device under AM1.5G irradiation is the so-called Shockley-Queisser limit [25] which is 30% for the silicon bandgap. Since silicon is an indirect bandgap semiconductor, the intrinsic Auger recombination further reduces the theoretically feasible limit to 29.43%, as recently reevaluated by Richter et al. [26].

Increasing the efficiency of a silicon solar cell equates to increasing current generation and minimizing recombination. Recombination R can be expressed as a function of excess carrier density by a minority carrier lifetime τ as

$$R = \frac{\Delta n}{\tau} . \quad (2.22)$$

Equation 2.22 is valid for all types of volume recombination. If recombination takes place at a surface, the recombination rate bears the units of $1/\text{cm}^2\text{s}$. This yields the definition of surface recombination velocity (SRV)

$$R_{\text{surf}} = S\Delta n . \quad (2.23)$$

Surface recombination can occur via Auger recombination as well as via defects described by Shockley-Read-Hall recombination. Since solar cells have surfaces with doping profiles and/or band bending from field effect passivation, recombination on a surface region is typically described from the recombination on the physical surface until the doping profile drops to the base doping level N_{dop} . The total recombination activity of a surface region X is described by a saturation current density J_0^{X} ¹, typically in units of fA/cm^2 and can be calculated analytically or numerically [27]. The surface recombination velocity at the physical surface is labelled S_0 . Alternatively to J_0 , an effective surface recombination velocity S_{eff} is defined via

$$S_{\text{eff}} = \frac{J_0 N_{\text{dop}}}{q n_i^2} . \quad (2.24)$$

In solar cells, the base and the various surfaces each have a different recombination activity which can be summarized by an effective lifetime τ_{eff} . In this context, the surface recombination velocity is also described by a surface lifetime which in the simplest approximation in a symmetric sample of thickness d is $\tau_{\text{surf}} = d/2S_{\text{eff}}$ [28]. τ_{eff} is a reciprocal sum over the lifetimes of all recombination channels n as in

¹Often named dark saturation current density or recombination current density prefactor. Each surface region has its own J_0 though. Not to be confounded with J_0 in the diode model, that summarizes the whole cell's J_0 values weighted with their respective surface area. A J_0 value may also be attributed to the base.

$$\frac{1}{\tau_{\text{eff}}} = \sum_n \frac{1}{\tau_n}, \quad (2.25)$$

where the lowest lifetime limits τ_{eff} the most. As IBC cells are commonly produced on high quality n-type wafers, surface recombination limits cell performance usually more strongly than bulk lifetime. For a given mobility and lifetime, a diffusion length L is defined as

$$L = \sqrt{D\tau}. \quad (2.26)$$

This value, which when using τ_{eff} becomes L_{eff} . This value is an indicator for how far charge carriers may travel on average from the point of generation until they recombine.

Conductive boundary approach

In this work the simulation program Quokka [17] is used in sections 4.3.1, 4.6, 5.3 and 6.2 to simulate device physics of IBC solar cells. In Quokka, diffusion profiles on surfaces are described by conductive boundaries [29], where each boundary on the cell front and rear side requires a J_0 or S_{eff} parameter for recombination and a sheet resistance R_{sh} to describe lateral current flow in the diffused surface. The following equations are stated for a p-type solar cell with an n-type emitter [17]. Electron recombination current into a boundary plane is described as

$$\sigma_n \vec{n} \vec{\nabla} \Phi_{Fn} = J_{\text{rec},J_0} = J_0 \left(\frac{np}{n_{i,\text{eff}}^2} - 1 \right) \quad \text{or} \quad (2.27)$$

$$J_{\text{rec},S} = qS_{\text{eff}}(n - n_0), \quad (2.28)$$

where \vec{n} is the normal vector to the plane of the conductive boundary and vice versa for holes. The conduction of carriers in diffused

layers (e.g. emitter or back-surface field) is accounted by a two-dimensional continuity equation via the transversal gradient ∇_t of the quasi-Fermi level of the majority carrier $\Phi_{F\text{maj}}$ in the plane of the particular surface via

$$\nabla_t \left(\frac{1}{R_{\text{sh}}} \nabla_t \Phi_{F\text{maj}} \right) = -J_{\text{diff}} . \quad (2.29)$$

where J_{diff} is the total current density from the base into the emitter minus the collected current density at the contact. Current flow into a metal contact with the terminal voltage V_{term} through a contact resistance R_c .

$$J_{\text{diff}} = \sigma_n \vec{n} \vec{\nabla} \Phi_{Fn} + \sigma_p \vec{p} \vec{\nabla} \Phi_{Fp} - \frac{V_{\text{term}} - \Phi_{F\text{maj}}}{R_c} . \quad (2.30)$$

Refer to [29] or [17] for more details on all boundary conditions for numerical device simulations. In the following, details on the three recombination mechanisms are presented.

Radiative recombination

Radiative recombination is the inverse process to excess carrier generation through photon absorption. An electron in the conduction band recombines with a hole in the valence band and a photon is emitted. Since one electron and one hole are involved in this two particle interaction, the radiative recombination rate R_{rad} is proportional to the total charge carrier density and a proportionality factor B as

$$R_{\text{rad}} = Bnp . \quad (2.31)$$

B describes the probability for spontaneous emission of a photon with energy E_γ , wavelength λ or angular frequency ω with $E_\gamma = hc/\lambda = \hbar\omega$. Radiative recombination is a quantum mechanical pro-

cess between two energy states. Under equilibrium conditions ($np = n_i^2$), the radiative recombination is in balance with the generation of excess carriers from thermal energy. This intrinsic process emits photons isotropically and can be described by Planck's law similar to a black body via

$$R_{\text{rad}}^0 = \frac{1}{4\pi^2 h^3 c^2} \int_0^\infty \frac{\alpha(E_\gamma) E_\gamma^2}{\exp\left(\frac{E_\gamma}{kT}\right) - 1} dE_\gamma. \quad (2.32)$$

Under illumination however, the emission spectrum needs to be described by the generalized Planck's law that reflects non-equilibrium carrier density resulting in spontaneous photon emission. Würfel treated radiative recombination in a detailed balance approach under the assumption of negligible stimulated emission [10]. This also accounts for the case of non-equilibrium carrier density where spontaneous emission is mathematically expressed as

$$R_{\text{rad}} = \frac{1}{4\pi^2 h^3 c^2} \int_0^\infty \frac{\alpha(E_\gamma) E_\gamma^2}{\exp\left(\frac{E_\gamma - (\Phi_{Fn} - \Phi_{Fp})}{kT}\right) - 1} dE_\gamma. \quad (2.33)$$

At 300 K and typical injection conditions $E_\gamma - (\Phi_{Fn} - \Phi_{Fp}) \gg kT$ and by using equation 2.11, equation 2.33 can be simplified to

$$R_{\text{rad}} \approx \exp\left(\frac{\Phi_{Fn} - \Phi_{Fp}}{kT}\right) \left(\frac{1}{4\pi^2 h^3 c^2} \int_0^\infty \alpha(E_\gamma) E_\gamma^2 \exp\left(-\frac{E_\gamma}{kT}\right) dE_\gamma \right). \quad (2.34)$$

Using equation 2.11 leads to

$$R_{\text{rad}} = \frac{np}{n_i^2} R_{\text{rad}}^0, \quad (2.35)$$

thereby, the spontaneous emission probability is $B = R_{\text{rad}}^0 n_i^2$ after integration over E_γ . In real solar cells, B is strongly dependent on temperature and also a function of injection level due to Coulomb interaction, which has been addressed experimentally e.g. by Trupke et al. [30] and parametrized using numerical simulations by Altermatt et al. [31]. More details on the use of radiative recombination for luminescence imaging is presented in section 2.3.

Auger recombination

Band to band Auger recombination is a mechanism where an electron (vice versa for holes) falls from the conduction band level to recombine into the valence band but instead of emitting a photon the excess energy is transferred to another free electron in the conduction band or to a free hole in the valence band which then thermalizes. Auger recombination is a three particle process requiring either two electrons and one hole (nnp) or two holes and one electron (ppn). This intrinsic recombination mechanism is a performance limiting effect in highest efficiency silicon solar cells and generally regions of the solar cell with high doping concentration such as emitters or back-surface fields. The recombination rate of each channel can be expressed by

$$R_{\text{Aug},n} = C_n (n^2 p - n_{i,\text{eff}}^2 n_0) \quad (2.36)$$

$$R_{\text{Aug},p} = C_p (np^2 - n_{i,\text{eff}}^2 p_0) \quad (2.37)$$

where C_n and C_p are the respective Auger coefficients for electrons and holes. Experimental data on silicon with doping concentrations below $1 \cdot 10^{18} / \text{cm}^3$ deviates from the model in equation 2.37 though, which is why Hangleiter and Häcker [32] proposed enhancement factors g_{nnp} and g_{ppn} to account for Coulomb interaction at low injection levels. The net Auger recombination rate is the sum of electron and hole channels

$$R_{\text{Aug}} = R_{\text{Aug},n} + R_{\text{Aug},p} = C_n g_{nnp}(n^2 p - n_{i,\text{eff}}^2 n_0) + C_p g_{ppn}(np^2 - n_{i,\text{eff}}^2 p_0). \quad (2.38)$$

Often cited values are those from Dziwior and Schmid [33] with $C_n = 2.8 \cdot 10^{-31} \text{cm}^6/\text{s}$ and $C_p = 9.9 \cdot 10^{-32} \text{cm}^6/\text{s}$. Since silicon is an indirect semiconductor, Auger recombination is the dominant intrinsic recombination channel. The most recent parametrization that is being established in the community is the one by Richter et al. [34], which is also used for the numerical simulations in this work.

Shockley-Read-Hall recombination

Finally, recombination may also occur via intermediate energy levels in the bandgap. Such energy levels may stem from imperfections in the crystal lattice, dangling bonds at the surfaces and also impurity contamination, in particular by metals. The rate for Shockley-Read-Hall recombination for a particular defect energy level E_t (also called trap level) and defect density N_t is expressed as

$$R_{\text{SRH}} = \frac{np - n_{i,\text{eff}}^2}{\tau_{p0}(n_1 + n) + \tau_{n0}(p_1 + p)}, \quad (2.39)$$

where τ_{p0} and τ_{n0} are the hole/electron capture time constants. τ_{p0} and τ_{n0} are assumed to be identical when no particular defect is investigated. These factors are parametrized by

$$\tau_{n0,p0} = \frac{1}{v_{\text{th}} \sigma_{\text{SRH},n/p} N_t}, \quad (2.40)$$

where v_{th} is the thermal velocity and $\sigma_{\text{SRH},n/p}$ the capture cross sections to the particular defect. The absence of the boron-oxygen complex in n-type Czochralski grown (Cz) silicon makes n-type silicon less sensitive to impurities allowing higher τ_{eff} [35]. Therefore, despite of the lower mobility of holes, L_{eff} of n-type Cz material is higher,

yielding much higher efficiency potential than p-type cell if volume recombination is dominating¹ Float zone (Fz) silicon has even higher purity than Cz but currently too expensive for mass production in photovoltaics. Further, n_1 and p_1 are defined as

$$n_1 = n_{i,\text{eff}} \exp\left(\frac{E_t - E_i}{kT}\right), \quad (2.41)$$

$$p_1 = n_{i,\text{eff}} \exp\left(-\frac{E_t - E_i}{kT}\right), \quad (2.42)$$

where E_i is the intrinsic energy, which is defined as the energy level in the middle of the effective bandgap. Thereby, defects with high capture cross sections that are located at an energy level in the middle of the bandgap have a severe impact on carrier lifetime. SRH recombination is most severe in the bulk of multicrystalline silicon. In this work however, only high quality Cz and Fz type silicon wafer are considered. There, SRH and Auger recombination at the surfaces are the primary efficiency limiting recombination mechanisms.

Injection conditions

The importance of each recombination channel for solar cell operation is a function of all parameters in equations 2.31, 2.38 and 2.39 and the local excess carrier density level Δn . Figure 2.3 shows calculated lifetime versus excess carrier density data created with an online calculator [36]. The graph shows effective lifetime (black, equation 2.25), which is a result of radiative (blue), Auger (red) and SRH (green) recombination for two n-type 1 Ωcm silicon wafers. For the simulation, τ_{p0} in the base was varied between two very different levels in order to emulate an IBC cell with very different τ_{eff} ². The average injection levels of the main operating conditions (see section 2.1.3) of an IBC cell are indicated by colored surfaces and the doping

¹The world record n-type Cz silicon solar cell by Panasonic has 25.6% efficiency while the record is at 21.4% for p-type Cz by Trina Solar [6].

²Furthermore it was assumed that $\tau_{n0} = \tau_{p0}$ and $E_t = E_i$; hence a symmetric defect.

level N_{dop} is highlighted as well. Figure 2.3 (a) is representative for a 20% efficient cell with low level injection lifetime $\tau_{p0} = 200 \mu\text{s}$ and (b) a state of the art 24% efficient cell with τ_{p0} of 2000 μs . Lifetime calculations are based on the parametrization by Trupke et al. [30] for radiative recombination and Richter et al. [34] for Auger recombination. The J_{sc} , MPP and V_{oc} injection levels were determined from numerical device simulations using Quokka (see section 4.4) for two IBC cells similar to the assumed τ_{p0} and efficiency data.

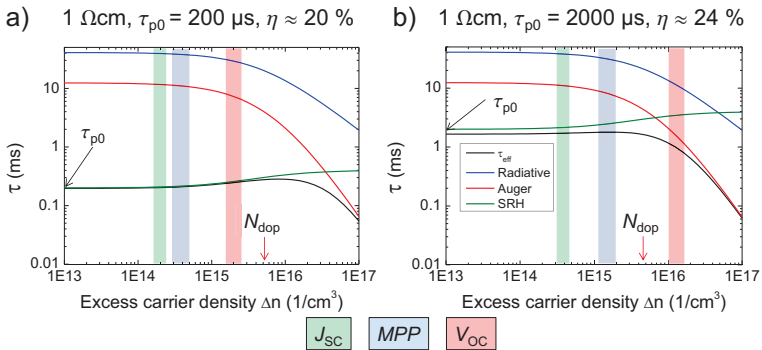


Figure 2.3: Numerical calculations of radiative (blue), Auger (red), SRH (green) recombination and resulting τ_{eff} (black) versus excess carrier density of two $1 \Omega\text{cm}$ n-type wafers at 300 K obtained from analytical models. The injection levels for two IBC cells at crucial operating conditions are highlighted by the colored surfaces. $\sim 20\%$ efficient cells (a) operate at low or medium injection levels ($\Delta n < N_{\text{dop}}$) while $> 24\%$ efficient cells operate at medium to high injection levels ($\Delta n \geq N_{\text{dop}}$).

Since IBC cells collect minority carriers on the rear side of the cell (see section 2.2), they operate under higher injection levels than most conventional front side emitter solar cells by default. It can be seen how the lifetime of the state of the art solar cell (b) is limited by SRH recombination at MPP and Auger recombination at V_{oc} . This graph allows for an important remark in the context of this work. Silicon solar cell characterization often assumes low injection conditions, meaning that $\Delta n \ll N_{\text{dop}}$. Under such conditions in the silicon base, a clear distinction between minority and majority carrier effects can be made. The graphs show however, that for highest

efficiency IBC cells (b), Δn in the bulk can be of the order of or even greater than N_{dop} , depending on the operating condition. For lower efficiency cells, the injection level is rather below the doping level but already within a range where the minority/majority carrier distinction is less well justified. This is labeled as 'medium injection' in this work. Implications of this for an n-type cell are e.g. that holes may yield series resistance effects in the bulk and electron collection may limit current collection at J_{sc} (see sections 4.6 and 6.2). The solar cells presented in this work have conversion efficiencies in the range of 19% to 22% and ρ^{base} between 1 Ωcm and 10 Ωcm .

2.1.3 Diode models and I-V curve analysis

A solar cell can be modeled as an equivalent circuit. Figure 2.4 shows schematics of the two most common models, the one-diode (a) and two-diode model (b) for solar cells. In the diode model, the cell is essentially a giant diode with a saturation current density J_0 and a current source $J_{\text{gen}} \geq 0$ when under illumination. For a more realistic model, a series resistance R_s is introduced which causes voltage drops at high current densities and a parallel resistance R_p to represent ohmic contributions, often called shunting. In the two diode model, the diode is split into two diodes where diode 1 (J_{01}) reflects the recombination channels in the base and the surfaces while diode 2 (J_{02}) reflects the recombination in the space charge region of the pn junction. Furthermore, each diode in these models bears an 'ideality factor' n that may reflect non-ideal diode-like behavior. The ideal theoretical values are $m = 1$, $n_1 = 1$ and $n_2 = 2$ [10]. Mathematically, the one diode model follows the equation

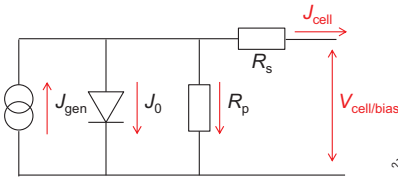
$$J(V) = J_0 \exp\left(\frac{q(V - JR_s)}{mkT} - 1\right) + \frac{V - JR_s}{R_p} - J_{\text{gen}} , \quad (2.43)$$

and, using $V \gg kT$, the two-diode model the equation

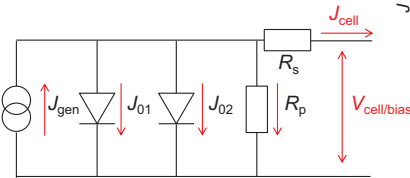
$$J(V) = J_{01} \exp\left(\frac{q(V - JR_s)}{n_1 kT}\right) + J_{02} \exp\left(\frac{q(V - JR_s)}{n_2 kT}\right) + \frac{V - JR_s}{R_p} - J_{\text{gen}}. \quad (2.44)$$

An example of a current-density vs. voltage curve (light I-V, black) and power curve ($V \cdot J$, red) is depicted in figure 2.4 (c). The graph also shows the behavior in the dark, by setting $J_{\text{gen}} = 0$. All curves were created with an online calculator [36].

a) One diode model



b) Two diode model



c) Sample light I-V, dark I-V, pseudo I-V and power curve

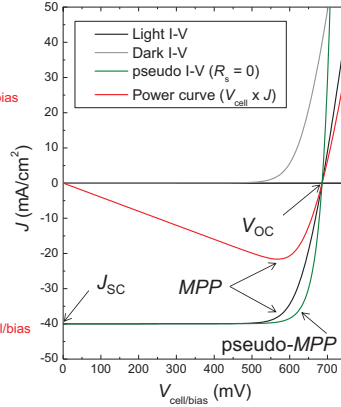


Figure 2.4: Schematic of a one-diode model (a), two-diode model (b) and example characteristic curve of a silicon solar cell (c) under illumination (black), in the dark (gray), current free pseudo I-V from a Suns- V_{oc} measurement (green) and power curve (red).

The arrows point at the most important operating conditions of the light I-V curve, namely short-circuit (SC with current density J_{sc}), open circuit (OC with voltage V_{oc}) and maximum power point MPP , where the product of $|V \cdot J|$ is largest and $V_{\text{bias}} < V_{\text{oc}}$. Between $0 < V_{\text{bias}} < V_{\text{oc}}$, photo generated current is extracted and an opposite recombination current flows across the diode or the parallel resistance. Under open-circuit voltage, no current is extracted from the cell. The green curve presents a schematic Suns- V_{oc} mea-

surement, where the cell voltage is measured at varying illumination intensity, which can be calibrated to a known J_{sc} value, hence the name pseudo I-V. No current is extracted from the cell ($J = 0$) and therefore the pseudo I-V curve is indicative of recombination and can be assumed free of series resistance [37]. An analogous pseudo power with a pseudo *MPP* curve can be calculated. The fill factor *FF* and pseudo fill factor *pFF* of a cell are defined as

$$FF = \frac{V_{MPP} J_{MPP}}{V_{oc} J_{sc}} \text{ and} \quad (2.45)$$

$$pFF = \frac{V_{pMPP} J_{pMPP}}{V_{oc} J_{sc}}, \quad (2.46)$$

and the conversion efficiency η as

$$\eta = \frac{V_{mpp} J_{MPP}}{P_{in}} = \frac{V_{oc} J_{sc} FF}{P_{in}}, \quad (2.47)$$

where P_{in} is the total incident illumination power density. For an AM1.5G spectrum, $P_{in} = 1000 \text{ W/cm}^2 = 100 \text{ mW/cm}^2$ and $T = 25 \text{ }^\circ\text{C}$ ¹. The comparison between I-V and pseudo I-V curve indicates the impact of series resistance on the *FF*. In this work, current extraction from the cell in I-V curve is always defined with a negative sign. For convenience, J_{sc} by itself is stated as a positive number.

Because this work contains several discussions that involve arguments about R_s and R_p , figure 2.5 shows examples of numerically calculated light I-V curves for increasing R_s (a) and R_p values. As can be seen, at first, increasing R_s leads a linear current voltage behavior at high voltage bias, which lowers the cells *FF* while keeping V_{oc} , J_{sc} the same. At extreme values of $R_s > 15 \text{ } \Omega\text{cm}^2$ however, the cell's absolute J_{sc} decreases as well. The *pFF* is unaffected by R_s . For varying R_p , low parallel resistance values lead to ohmic currents flowing in parallel to the diodes and thus a linear a current voltage behavior emerges, especially at low bias voltages. Unlike R_s , a low

¹Standard testing conditions (STC) according to IEC 60904-2, Ed. 2,2008

R_p value immediately affects the cell's pFF (data not shown). A low R_p value also decreases a cell's V_{oc} and under extreme circumstances also J_{sc} .

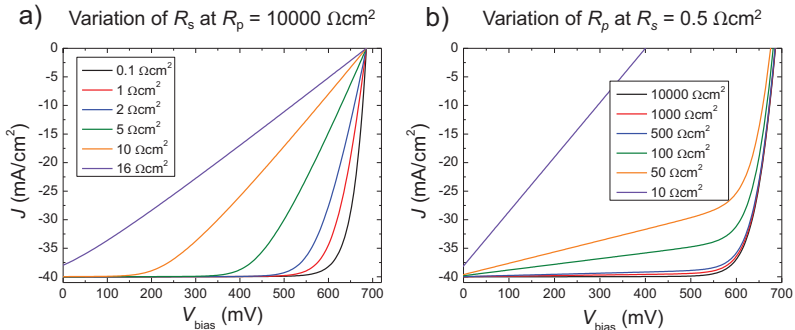


Figure 2.5: Examples of numerically calculated illuminated I-V curves based on a two-diode model for a sweep over global R_s (a) and global R_p (b). Increasing R_s lowers the cells FF and R_p the cell's pFF and V_{oc} .

Diode models always present a simplification to the physics of large area solar cell devices but they may be very helpful in explaining conventional loss mechanisms at the global and local level. Primarily, the diode model assumes that the input parameter J_0 , R_s and R_p are injection independent input parameters. The complex physical reality of a solar cell always bears injection dependent lifetime effects that can be modeled by the ideality factors m , n_1 and n_2 which themselves can also be a function of injection [38]. There are many experimental methods for determining each of the diode model parameters experimentally but no diode model perfectly represents the behavior of all possible solar cells. Excellent agreement between alternative determination techniques (e.g. determination of R_s [39]) is rarely achieved. There are alternative diode models in literature, such as the inclusion of a third diode to represent edge recombination [38] or introducing variable resistances in the base [40]. For the discussions in this work, the one-diode model is mostly sufficient.

2.1.4 Peltier effect

The Peltier effect in semiconductors is an effect where energy is transferred from one area of the device to another without affecting the net power balance of the system [41]. It is therefore not a loss mechanism impacting solar cell efficiency, which is why there is little research on the Peltier effect in photovoltaics. In chapter 5 of this work, spatially resolved power densities during solar cell operation are investigated using lock-in thermography. There, Peltier heating and cooling will be demonstrated to impact the results in IBC cells. The following presents a brief introduction to the Peltier effect in semiconductors. The primary reference for this subsection is the dissertation by H. Straube [12].

Basically, Peltier heating and cooling occurs when charge carriers cross over energy barriers while flowing through the different regions of a semiconductor. The schematic in figure 2.6 illustrates this principle for the case of an n-doped semiconductor with two metal contacts without current flow (a) and with current flow caused by a voltage bias (b). Electrons in the conduction band carry a free energy F which is equal to the Fermi energy E_F . The inner energy U however is larger because of the charge carrier's kinetic energy (in form of entropy S_E) which is proportional to the temperature T of the device. The difference between Fermi energy and inner energy is called Peltier coefficient Π and is defined in units of eV in this work. When a bias voltage is applied (b) electrons flow from the metal contact at higher potential to the lower potential. The injected carriers need to first overcome the barrier Π and thereby locally take energy from the crystal, which consequently cools the crystal. When exiting the semiconductor, the electrons fall back to the lower barrier and release that energy and thus heat the crystal. This leads to a transfer of latent heat that is tied to a current flow. In a first approximation for a semiconductor, Π is simply $E_C - E_F + \frac{3}{2}kT$ but in reality, the coefficient may be a function of the scattering processes in the material. The Peltier coefficient in a metal is < 1 meV and negligible in this work [42].

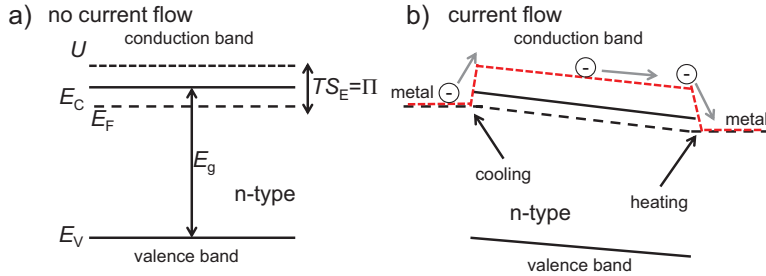


Figure 2.6: Schematic band diagram of an n-doped semiconductor without current flow (a) and with current flow (b) via an applied voltage. Charge carriers in the conduction band have an additional energy described by a Peltier coefficient Π that acts as an energy barrier when current flows from the metal in and out of the semiconductor. Electrons take energy from the crystal when entering the semiconductor and hence locally cool the device but this energy is released upon exiting again resulting in a latent heat transfer.

Analytical models exist for calculating the Peltier coefficient for electrons and holes as a function of conduction/valence band energies, Fermi levels, temperature and a parameters that depends on which scattering process are dominant in the material [43]. The Peltier coefficient therefore also depends on the dopant type. Figure 2.7 shows theoretically calculated majority carrier Peltier coefficients (lines) and experimental results from [44–46] at 300 K for various dopant types including phosphorous and boron. It can be seen, that especially for low dopant concentrations, the calculated results vary significantly from the experimental values. This can be explained by an additional, less well-known contribution for the Peltier effect called phonon drag effect, which can be described as a second Peltier coefficient. When a current flows through an isothermal material, the charge carriers interact with phonons in the crystal lattice. Through scattering, phonons gain momentum. This material effect is typically only relevant at low temperatures < 200 K but is non negligible at room temperature for silicon. This momentum can be re-transferred to the charge carriers and thus contribute to a latent heat flow in the material. A total Peltier coefficient is defined by the sum of diffusive and phonon drag Peltier coefficient. A full discussion and consideration of the phonon drag Peltier coefficient is beyond the scope of this

work. More information can be found in [12]. For simplicity, only the absolute theoretically determined value (lines) from figure 2.7 will be used as input parameters for the simulations in section 5.3.

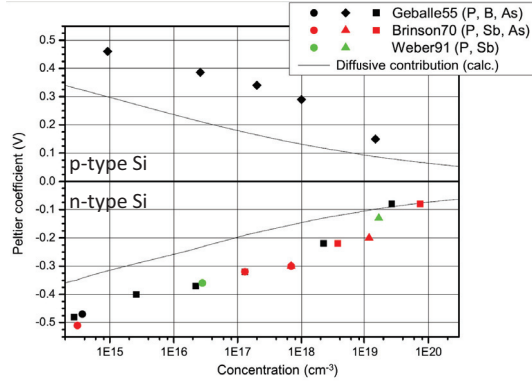


Figure 2.7: Majority carrier Peltier coefficients (here in units of V) from theoretical calculations (lines, [43]) and experimental results (points) at 300 K as a function of doping concentration for several dopants. The graph is adapted from [12] where data was gathered from [44–46]. Donator dopants have a positive Peltier coefficient and acceptor dopants a negative one.

In an operating solar cell, there are minority and majority charge carrier flows. Minority carriers also have a Peltier coefficient $\Pi_{\min,n/p}$. Since the majority carrier Peltier coefficients $\Pi_{\text{maj},n/p}$ can be assumed to be constant and independent of additional carrier concentration, $\Pi_{\min,n/p}$ are given via [12]

$$\Pi_{\min,n} = E_{g,\text{eff}} - (\Phi_{Fn} - \Phi_{Fp}) - \Pi_{\text{maj},p} , \quad (2.48)$$

for a p-doped region, where holes are majority carriers and

$$\Pi_{\min,p} = E_{g,\text{eff}} - (\Phi_{Fn} - \Phi_{Fp}) - \Pi_{\text{maj},n} . \quad (2.49)$$

for an n-doped region, where electrons are majority carriers. This makes $\Pi_{\min,n/p}$ a function of operating conditions as it is a function

of $\Phi_{Fn} - \Phi_{Fp}$. Section 5.3.1 will discuss in more detail all the current flows and Peltier effects taking place in a typical n-type IBC cell with a back-surface field (see figure 5.3), as this will be used for the simulation of local power densities.

2.2 IBC solar cell design and current flow

Interdigitated back contact silicon solar cells are the focus of this dissertation. This section motivates the basic design strategies of IBC cells and illustrates how the design affects the current flow within the device. Today, IBC cells are produced with the highest median cell efficiency of all worldwide wafer-based silicon solar cells in industrial production. The company SunPower achieves $> 24\%$ efficiency in industrial IBC cell manufacturing [47] and Panasonic also holds the world record efficiency on the laboratory scale at 25.6% efficiency on an IBC structure [5]. The IBC concept is the cell design with the highest potential of all single junction silicon solar cells and is stated by several cell manufacturers to be the goal of their technological road map [3].

IBC principle and designs

The interdigitated back contact (IBC) solar cell was introduced by Schwartz and Lammert in 1975 [48], originally for applications under concentrated light. All IBC cell designs have in common, that both n-contact and p-contact metallization as well as all electron and hole charge carrier collection via an emitter and back surface field (BSF) surface doping occur on the rear side of the cell. Very high photogenerated currents are therefore achievable, because no optical shading occurs and also the front side can be fully optimized towards passivation as it needs no contacting functionality. The metallization being only on the rear side also allows for more freedom in using wider fingers without the usual compromise between losses from series resistance in the fingers and optical shading. The IBC design principle of having all metal on the back of the cell can also be realized with

a metal grid that is not 'interdigitated'. Strictly speaking, IBC cells are part of a more general cell design category named 'back-contact back-junction' (BC-BJ) solar cells. However, only the term IBC is used in this work as it is currently the one most widely used in the community for this principle and in this work only BC-BJ cells with interdigitated metal grids are presented.

Figure 2.8 depicts a cross section schematic of a standard n-type IBC cell design (a) as well as a front side and a rear side photograph (b,c) of a typical 'laboratory size' IBC cell investigated in this work. The dashed rectangles in figure 2.8 (b) and (c) outline the 2 cm x 2 cm active cell area. The bus bars lie outside of the active cell area. Crosses mark the location where the pins of the standard chuck contact the cell for four point probe measurements. Excess carriers are generated by light absorption passing through an anti-reflective coating (ARC). The rear side doping is an alternation between p^+ boron doped emitter doping regions (green) to collect holes and n^+ phosphorous doped back-surface field regions to collect electrons and reduce hole recombination. In many designs, there is an unpassivated area between emitter and BSF doping which is called 'gap'. The front side of the cell is typically textured with random pyramids from alkaline texturing on the monocrystalline wafer. All cells investigated in this work have a random pyramid front side texture. The front side can be either undoped, a n^+ doped front surface field (FSF) or a p^+ doped front floating emitter (FE). The motivation behind an FSF is to reduce series resistance losses from lateral electron transport in the bulk [49]. A FE may increase J_{sc} by offering an alternative path for holes [50, 51]. An undoped front side may yield the best passivation quality for higher V_{oc} [52]. Typically, emitter area coverage fractions over 80% are used to increase current collection at short-circuit. All presented designs in figure 2.9 have local contact openings in the emitter and BSF regions where typical contact openings are between 5 μm and 25 μm wide. A design where the emitter is fully contacted via an aluminum emitter is also briefly investigated in this work (see section 3.5). The fabrication of an IBC cell often involves many steps of patterning, cleaning, deposition and removal

of materials. The processing complexity is the main reason for the higher cost of IBC cells compared to conventional industrial cells. Much effort has been made to reduce the number of processing steps and use alternative doping and passivation technologies. For details on various IBC fabrication sequences refer to [53–56].

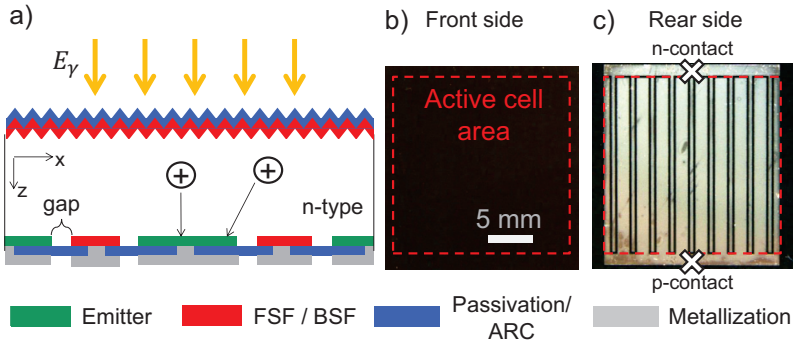


Figure 2.8: Schematic cross section (a) and photographs of the front side (b) and rear side (c) of a typical 4 cm^2 IBC cell investigated in this work. The active area is outlined by the dashed red square and location where the chuck’s pins contact the bus bars are marked by crosses.

Figure 2.9 depicts the other important IBC design variations besides the ‘standard’ design that are investigated in this work. Those are IBC cells without a gap between emitter and BSF (b) and cells where BSF metal fingers overlap emitter regions (c). Cells without gap allow an increased emitter coverage fraction and thus higher J_{sc} , but the contact between the highly doped regions has consequences on J_{02} recombination in the space charge region [57] and on breakdown behavior (see section 6.5). For designs (a) and (b) and in the photograph of figure 2.8 (c), the BSF fingers are much slimmer than the emitter fingers. This design is chosen to avoid overlap between BSF fingers and emitter regions because pinholes in the passivation layer may induce shunting (see section 6.3.1). Slimmer BSF fingers however come at the expense of series resistance losses from the BSF fingers, especially for industrial size cells which thus would require rather thick fingers [58]. In principle though, a decoupling of charge

carrier collection and metallization geometry for IBC cells is feasible [54]. Cells of type C exist with and without gap.

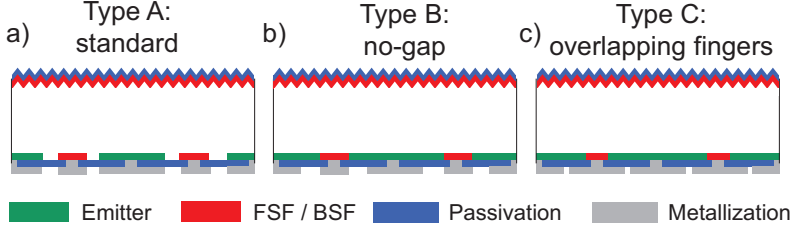


Figure 2.9: Schematic cross sections of the most important IBC design variations investigated in this work. (a) shows the standard design, in (b), there is no undoped gap between emitter and BSF region and in (c), the BSF finger metallization overlaps the emitter doping, allowing extremely high emitter coverage fractions using 'point' BSF structures (figure 2.10 (c)) at the risk of shunting via pinholes in the passivation layer.

Thus far, the cross sections have not detailed how the cell is structured in the y -direction. Figure 2.10 (a) depicts a top view schematic of the 'line-structure' type, which is typically chosen for the standard and no-gap designs. Figure 2.10 (b) shows a top view schematic of 'point-structure' that is possible when accepting overlapping BSF fingers (note that the dashed rectangles in (b) have same width for emitter and BSF). Such 'point' BSF structures can have circular or rectangular shape, with and without gap between BSF and emitter regions. Most cells investigated in this work are line-structure type with a two-dimensional current flow in the cross section of the respective unit cells. All findings are however assumed to be transferable to point-structure type cells as this yields no fundamental change to the lateral carrier transport.

Current flow

An important premise of this work is that the higher structural complexity of an IBC cell compared to a conventional industrial cell design yields intrinsic inhomogeneities when analyzed with imaging

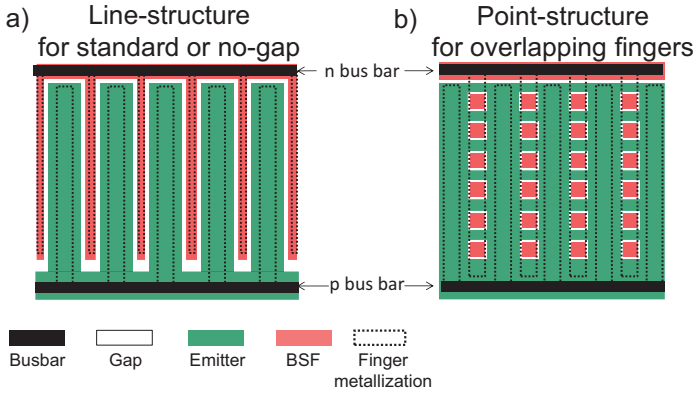


Figure 2.10: Top view schematics of the line-structure doping used for the standard and no-gap design (a) and a point-structure schematic for cells where emitter and BSF fingers are equally wide and BSF fingers overlap emitter regions (b).

techniques caused by more complex charge carrier distributions and current flows with strong lateral components.

The most common silicon solar cell on the market consists of a p-type wafer with an phosphorous doped emitter on the front and a back surface that is fully metallized with aluminum which creates a p-doped back-surface field as well as the back contact, hence the name Al-BSF. To facilitate the comparison to an n-type IBC cell, in the following example, the n-type equivalent of the Al-BSF cell is shown to represent the standard industrial design: the PERT cell (passivated emitter, rear totally diffused cell). An n-type PERT cell has a boron doped emitter on the front and a fully phosphorous doped rear side.

Figure 2.11 presents a qualitative demonstration of the different electron and hole current paths between the industrial standard design (PERT, left column) and the standard IBC design (right column). Both cells have the same thickness of $180\ \mu\text{m}$ and half-pitch distance of $1100\ \mu\text{m}$. Figure 2.11 (a) shows schematics of the cell structures for the depicted hole (p, red) and electron (n, blue) current flows under high forward bias in the dark (b), under illumination

and J_{sc} conditions (c), *MPP* conditions (d) and V_{oc} conditions (e). The arrows in the schematics point towards the direction where holes (minority carriers in n-type silicon) flow under J_{sc} conditions. The arrows in the current graphs (b-e) are normalized and represent the mean direction of the current at the arrow's base. The current plots were obtained from numerical simulations using the program Quokka [17], used for many aspects of this work.¹

Inside a solar cell, electrons and holes that are generated through photon absorption or injected/extracted by an external circuit each flow towards a drain according to the continuity equation 2.19 and along the path of lowest resistance. Nevertheless, the electron and hole charge carrier flow is not independent because the net current flowing through the cell circuit must equalize. Additionally, at all positions in the base, quasi-neutrality ($\Delta n = \Delta p$) can be assumed which also creates an interdependence between the flow of both carrier types, especially under high injection conditions. The PERT structure, is the simplest structure and bears essentially one dimensional current flow in the base between front and rear side of the cell with electrons and holes flowing nearly either parallel or anti parallel to each other. The current direction depends on the carrier type and whether it is on average a local recombination current towards a surface or towards carrier extraction. Some lateral current flow in the PERT cell of the holes is notable at *MPP* conditions (c, left) because of the emitter sheet resistance. For the IBC cells, the current flow within the bulk has major lateral components under all operating conditions. At J_{sc} conditions, holes flow vertically towards the emitter along most of the cell but the holes generated over the BSF region need to flow a further distance diagonally within the bulk which leads to current losses, an effect discussed in sections 3.5 and 4.3.1. At *MPP* conditions (d), the hole current flows essentially towards the emitter for extraction while the electrons flow essentially laterally through the base. These complex current paths play a decisive

¹Details on the doping and recombination parameters of these cells are not relevant for this qualitative demonstration.

role in the interpretation of local series resistance in IBC cells discussed in sections 4.6 and 6.2. Note that at all operating conditions, the mean current densities do not always point towards extraction at the contacts but also towards recombination at some of the surfaces. Under V_{oc} conditions, all the excess carriers diffuse towards the surfaces of high recombination or recombine within the bulk, which will be addressed in sections 4.3.1 and 4.5.

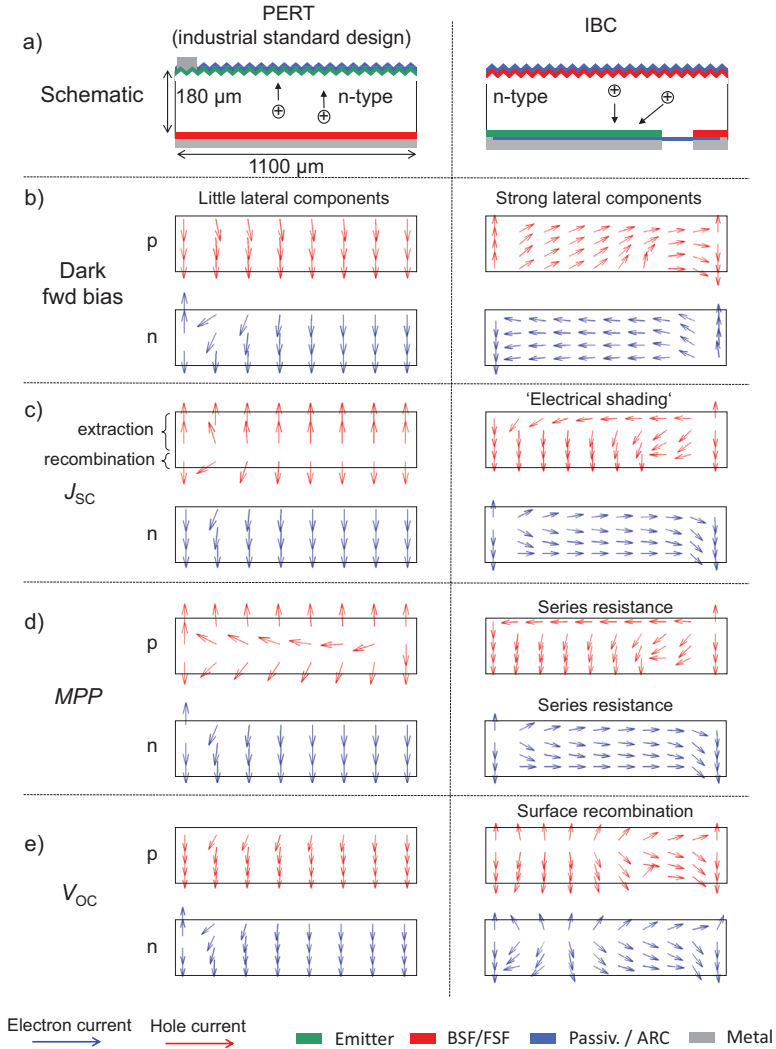


Figure 2.11: Schematics (a) and normalized arrows showing mean local current density flow direction for holes (p, red) and electrons (n, blue) for an n-type PERT (left column) and IBC unit cell (right column) in the dark (b), at J_{sc} (c), MPP (d) and V_{oc} (e) conditions. The more advanced IBC cell structure yields a higher complexity in lateral current flow and also carrier density which result in intrinsic inhomogeneities in imaging analysis of the cells. Current flows were obtained by numerical simulation using the program Quokka.

2.3 Physical principles of applied imaging techniques

In this section, the physical principles of signal generation for the two main imaging techniques of this work are introduced. The principle of spectrally resolved light beam induced current mapping (SR-LBIC) for chapter 3 is only explained briefly in section 3.2, because in-depth considerations of the technique were not necessary for this work. For a theoretical discussion on SR-LBIC physics refer to [59]. The word 'imaging' is used when data from an entire cell is acquired at once while 'mapping' is used when data is acquired in pixel by pixel scanning procedure.

2.3.1 Luminescence imaging

Luminescence imaging is the technique used in chapter 4 and in several sections of chapter 6 for the characterization of homogeneous IBC cells and IBC cells with processing faults. The physical principles behind the luminescence data acquisition and application for voltage calibration are presented in the following. A literature overview of the use of luminescence imaging for silicon solar cell characterization is presented in section 4.1. Technical details in the measurement setup used in this work can be found in section 4.2. The principle of photo- (PL) and electroluminescence (EL) imaging is to capture photons emitted by radiative recombination in silicon (see section 2.1.2). Because silicon is an indirect bandgap semiconductor, requiring the momentum of a phonon to allow an electron in the valence band to be raised over the bandgap after photon absorption, radiative recombination is a negligible recombination channel in silicon compared to Auger and SRH recombination. For comparison, a typical emission coefficient B for silicon at 300 K is $3 \cdot 10^{-15} \text{cm}^3\text{s}$ while it is $3 \cdot 10^{-10} \text{cm}^3\text{s}$ for GaAs, which is a direct bandgap semiconductor [60]. The highest theoretically achievable silicon solar cells efficien-

cies are limited by Auger- and not radiative recombination (see figure 2.3).

In the presence of recombination via defects (SRH), the injection level Δn is decreased. A low injection level is therefore related to low τ_{eff} but also reduced radiative recombination and hence luminescence signal. Note that all luminescence experiments in this work are conducted at steady state conditions. For dynamic luminescence measurements on silicon solar cells refer to [61].

The spontaneous emission spectrum of silicon has been investigated experimentally by various authors over the past decades as it can be used to determine the absorption coefficient $\alpha(\lambda)$ [62–65]. Excess carriers responsible for luminescence signal can be generated through optical excitation via lasers or LEDs (PL) or injected into the cell by an external circuit (EL). Optical and electrical excitation can be conducted in parallel, which is also named PL in this work. In luminescence imaging, the signal is captured through a camera lens in a pixel matrix, where it is spectrally integrated with the camera’s EQE. Many of today’s luminescence imaging tools in PV research are based on silicon detector chips, which’s EQE is sufficient to detect silicon emission. Figure 2.12 depicts a normalized experimental silicon emission spectrum at 300 K by Nguyen et al. [65] and the EQE of the silicon CCD camera used in this work cooled to $-50\text{ }^{\circ}\text{C}$. The emission spectrum and camera EQE limits the range of available optical excitation from lasers or LEDs to peak wavelengths below 900 nm, as reflection from the light source needs to be strongly suppressed in order not to interfere with the PL signal. This problem does not occur in EL imaging.

The camera delivers a two-dimensional image of the three-dimensional charge carrier density distribution in the cell. Signal contribution stems from the entire base of the cell and very little from the highly doped surfaces because of the low volume fraction and low excess carrier levels in them. The camera PL signal is integrated over the cell thickness d in a first approximation by

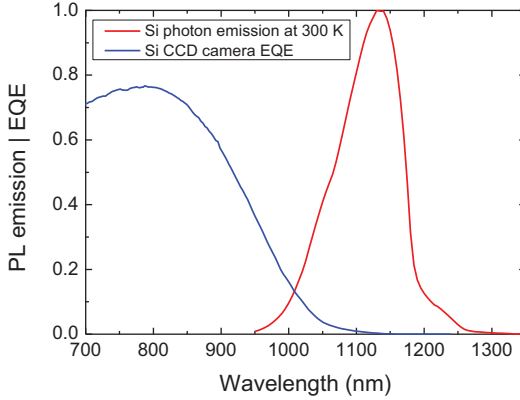


Figure 2.12: Normalized silicon luminescence emission spectrum at 300 K and absolute EQE of the silicon CCD camera used in this work cooled to -50 °C. Only the part of the PL spectrum is detected which overlaps with the camera EQE.

$$\text{PL} = A \int_0^d \frac{n(z) p(z)}{n_{i,\text{eff}}^2} dz . \quad (2.50)$$

with a calibration factor A . The net camera signal is however influenced by photon reabsorption, optical reflection, optical refraction, isotropic photon emission in the cell, as well as the camera optics transmission. All of this will be considered in section 4.4 for numerical modeling of luminescence images.

Voltage calibration

The calibration of PL signals to local voltage is essential for the determination of local series resistance in sections 4.6 and 6.2. From the theoretical considerations in section 2.1.2, it can be said that

$$\text{PL} \sim \frac{np}{n_{i,\text{eff}}^2} = \exp\left(\frac{\Phi_{Fn} - \Phi_{Fp}}{kT}\right) \stackrel{!}{=} \exp\left(\frac{qV_{\text{imp}}}{kT}\right), \quad (2.51)$$

so radiative recombination is directly proportional to charge carrier densities as well as an exponential function of quasi-Fermi level splitting. These two ways of interpreting luminescence signals are equivalent. The quasi-Fermi level splitting is now named implied voltage V_{imp} which is defined in all parts of the three-dimensional solar cell.

For series resistance imaging, a local voltage at the pn junction V_j needs to be defined. The following presents the established voltage calibration method in the community, which is theoretically motivated e.g. by Glatthaar et al. [66]. An extended discussion on the calibration factor and its sensitivity to measurement conditions can be found in [67]. Glatthaar et al. found that by solving the homogeneous and inhomogeneous continuity equation (2.19) under low injection conditions, the excess carrier density $n(z)$ is exponentially proportional to the junction voltage on the cell surface V_j . The luminescence signal detected by the camera and the junction voltage are related via

$$\text{PL} = C^{\text{loc}} \left(e^{V_j/kT} \right) + E^{\text{loc}} I_{\text{in}}, \quad (2.52)$$

where C^{loc} is a calibration constant accounting for all local experimental detection optics [67] and $E^{\text{loc}} I_{\text{in}}$ is an additional background term that is linearly proportional to a normalized illumination intensity I_{in} . This term represents the observed PL signal under illumination at short-circuit, composed of undesired remaining laser reflection as well as carrier density. Kasemann denotes this luminescence signal from charge carriers as 'diffusion limited carriers', which are carriers that cannot be extracted through diffusion from the cell despite J_{sc} conditions [9]. These carriers present an offset to the PL image and do not influence the local junction voltage. At low illumination intensities $I_{\text{in,low}}$ of typically 0.2 or 0.1 sun equivalent and below, the junction voltages across the solar cell can be assumed to be homogeneous and equal to $V_{\text{oc,low}}$. Because $V_{\text{oc}} \gg kT$, subtracting the $\text{PL}_{J_{\text{sc,low}}}$ image from the $\text{PL}_{V_{\text{oc,low}}}$ image results in

$$\text{PL}_{V_{\text{oc},\text{low}}} - \text{PL}_{J_{\text{sc},\text{low}}} = C^{\text{loc}} e^{\frac{V_{\text{oc},\text{low}}}{kT}} + E^{\text{loc}} I_{\text{in},\text{low}} - \left(C^{\text{loc}} e^{\frac{0}{kT}} + E^{\text{loc}} I_{\text{in},\text{low}} \right) \approx C^{\text{loc}} e^{\frac{V_{\text{oc},\text{low}}}{kT}}. \quad (2.53)$$

The calibration factor C^{loc} can thus be obtained via

$$C^{\text{loc}} = (\text{PL}_{V_{\text{oc},\text{low}}} - \text{PL}_{J_{\text{sc},\text{low}}}) e^{-V_{\text{oc},\text{low}}/kT}. \quad (2.54)$$

Once C^{loc} was determined for a specific solar cell at defined experimental conditions (image frame, lens etc.), equation 2.52 can be rearranged to calibrate a PL image to $V_{j,X}$ at arbitrary operating condition X (e.g. *MPP*) via

$$V_{j,X} = kT \ln \left(\frac{\text{PL}_X - \text{PL}_{J_{\text{sc}}}}{C^{\text{loc}}} \right). \quad (2.55)$$

In IBC cells, the rear side of the cell is not actually entirely covered with a pn junction. This conventional voltage calibration however yields meaningful results, as is presented in section 4.6 and was found by the author to be more robust than alternative proposed methods [68, 69]. Therefore, V_j is named $V_{j,\text{imp}}$ or $V^{\text{loc},\text{imp}}$ in this work. In particular the subtraction of the diffusion limited carrier signal plays an important role in IBC cells (see section 4.3.1). Regarding injection conditions, as was shown in figure 2.3, IBC cells operate in between low, medium and sometimes high injection conditions, for which the presented voltage calibration was not developed. Nevertheless, good results in experiments and simulations were achieved (see section 6.2) for IBC cells that are clearly operating under high injection. It is possible that greater inconsistencies may arise for cell efficiencies beyond 24 % which could not be verified in the frame of this work.

2.3.2 Lock-in thermography

Lock-in thermography is the imaging technique used in chapter 5 and in section 6.3 for the characterization of homogeneous IBC cells and IBC cells with processing faults, particularly shunting. The physical principles behind this complex measurement technique are described in the following. A literature overview of the use of lock-in thermography for silicon solar cell characterization is presented in section 5.1. Technical details about the measurement setup used in this work can be found in section 5.2. The theory for lock-in thermography in the context of solar cells is best described in the book by Breitenstein et al. [70].

Thermography, the image based detection of infrared black body radiation¹, has had great success for applications of non-destructive testing of diverse materials and electronic components. Thermographic images may be acquired with microbolometers or focal plane arrays (FPA). Microbolometer based cameras contain arrays of resistors which heat up as they absorb radiation, which is a rather slow mechanism. Such cameras are commonly used for the qualitative detection of hot spots in solar modules in the field and to assess insulation and heat distribution inside buildings. For high resolution analysis of individual solar cells, fast dynamic techniques are required. Semiconductor based FPA detectors are commonly made of low bandgap materials, most prominently InSb and HgCdTe (named MCT). The noise level of such detectors are described by the 'noise equivalent temperature difference' (NETD)² which is nowadays of the order of 10 – 20 mK [70].

The lock-in principle

Under steady state conditions, a local heat source in a solar cell results in an increased temperature that may extend several cm away from the source, making exact localization of faults nearly impos-

¹Often called heat radiation.

²NETD meaning the smallest temperature differences that the sensor can detect in a single image above the noise level [71].

sible. By using the lock-in principle, the detection of temperature increases of the order of few μK at much higher spatial resolution is possible. The lock-in principle is a widely used technique to measured differences between small signals an large DC offset. In the case of thermography, the offset is the steady state heat radiation of the sample at a given temperature. Unlike luminescence light emission, every black body emits or absorbs thermal radiation of wavelength λ with a spectrum following the Planck black body emission spectrum [72]

$$M_\lambda(T) = \frac{2\pi hc^2}{\lambda^5} \frac{1}{\exp(\frac{hc}{\lambda kT}) - 1}. \quad (2.56)$$

The IR camera integrates the incident signal over its spectral detection range. The black body is an idealized absorber and real bodies ('grey bodies') are characterized by an emissivity factor $\varepsilon < 1$. Section 5.2 will discuss emissivity in context of lock-in thermography and IBC cells. The lock-in principle correlates a noisy periodic measurement signal $F(t)$ with a noise-free periodic reference signal $K(t)$, both at a set frequency $f_{\text{lock-in}}$ and integrates the product of both to a signal S as

$$S = \frac{1}{t_{\text{int}}} \int_0^{t_{\text{int}}} F(t)K(t) dt. \quad (2.57)$$

for a desired integration time t_{int} . Thereby, the DC components of $F(t)$ as well as the statistical noise from the detection are suppressed. In real life experiments, the acquired raw data $F(t)$ is a digital set of values F_k (usually camera units) and the reference function $K(t)$ becomes a set of weighing factors. The output then becomes the sum

$$S = \frac{1}{N} \sum_{j=1}^N F_j K_j \quad (2.58)$$

where N is the total number of lock-in periods. The total measurement time is determined by the chosen number of lock-in periods via $t_{\text{int}} = N/f_{\text{lock-in}}$. According to Breitenstein et al., advantageous correlation functions (or weighing factors) are the harmonic functions sine and cosine because they evaluate only the basic harmonic of the thermal signal which carries the dominant information and suppresses higher harmonics [70]. Figure 2.13 depicts a schematic of two lock-in periods for rectangular voltage based excitation (blue), temperature (red), the correlation functions and the camera integration discussed in the following. For solar cell analysis, the measured signal $F(t)$ is a thermal signal created by periodic excitation using voltage bias and/or illumination of the cell. When a rectangular excitation is used¹ the temperature can be assumed to increase linearly. According to Stefan-Boltzmann's law [73], the total heat radiation power of a body is proportional to T^4 . Since in LIT, only small difference between temperature levels are measured, the heat radiation can be assumed to be linearly proportional to temperature. The camera captures the solar cell in at least four images j_1 to j_4 at defined times during the lock-in period, multiplies each local signal with the respective correlation function (curves) via weighing factors and adds it to the preceding data.

The use of both sine and cosine correlation functions further allows determining the phase of the signal also after the completed measurement. The sine function measures the component of the excitation that is in phase with the excitation (hence named 0° function) while the cosine function (red) is -90° phase shifted and is thus in phase with the temperature increase and hence local heating power density. The total signal $F(t)$ is described by an amplitude A and a phase ϕ as

$$F(t) = A \sin(2\pi f_{\text{lock-in}}t) \cos(\phi) + A \cos(2\pi f_{\text{lock-in}}t) \sin(\phi) \quad (2.59)$$

¹Rectangular meaning that the time scale in which steady state on- or off-conditions are reached is much smaller than the lock-in period.

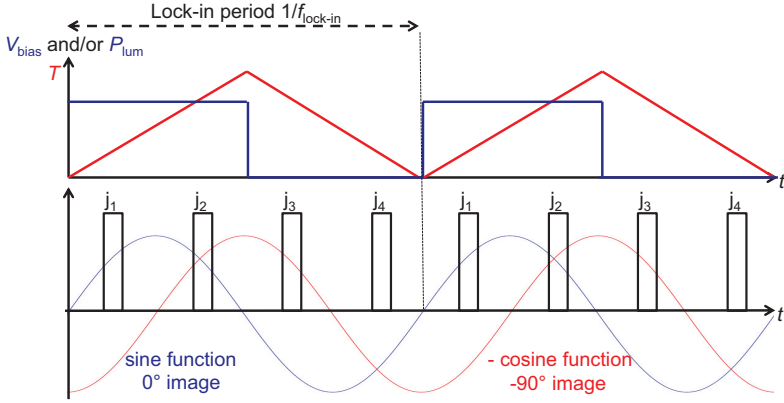


Figure 2.13: Schematic of the rectangular voltage bias and/or illumination of a solar cell (blue), linear temperature response of the cell (red), camera events j and correlation functions for the 0° and the power proportional -90° image during two lock-in periods.

The mathematical correlation between A , ϕ , S^{0° and S^{-90° , sketched in figure 2.14, are

$$A = \sqrt{(S^{0^\circ})^2 + (S^{-90^\circ})^2}, \quad (2.60)$$

$$\phi = \arctan\left(\frac{S^{-90^\circ}}{S^{0^\circ}}\right), \quad (2.61)$$

$$S^{0^\circ} = A \sin(\phi), \quad (2.62)$$

$$S^{-90^\circ} = -A \cos(\phi). \quad (2.63)$$

The images S^{0° and S^{-90° are referred to throughout this work as the '0°' and '-90°' images. From two images, the remaining two can be calculated.

Heat conduction within silicon

A local temperature increase in a silicon solar cell leads to the spread of a thermal wave $T(\vec{r}, t)$ within the sample, where \vec{r} is a three dimensional vector of location away from the origin of the heat source.

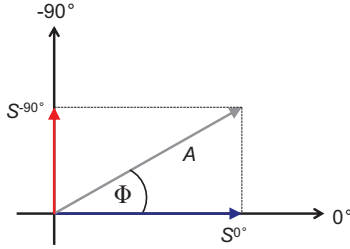


Figure 2.14: Relationship between A , ϕ , S^{0° and S^{-90° in a vector diagram.

To analytically or numerically calculate how a thermal wave spreads over time, the homogeneous differential heat equation

$$c_p \rho \frac{\partial T}{\partial t} - k_{th} \frac{\partial^2 T}{\partial r^2} = 0, \quad (2.64)$$

where c_p is the heat capacity, ρ is the material density and k_{th} the thermal conductivity has to be solved. For the simplest case of a one-dimensional plane wave, the solution in x direction is

$$T(x, t) = A \exp\left(\frac{-x}{\Lambda}\right) \exp\left(i\left(\omega t - \frac{x}{\Lambda}\right)\right) \quad (2.65)$$

where $\omega = 2\pi f_{\text{lock-in}}$. The factor

$$\Lambda = \sqrt{2k_{th}/\rho c_p \omega} \quad (2.66)$$

is a central parameter in LIT called thermal diffusion length and characterizes the spatial temperature spread during the lock-in period. In LIT, wafer based silicon solar cells can often be regarded as flat two-dimensional devices. Whether this is valid depends on the magnitude of Λ relative to the wafer thickness d . Cases of $\Lambda \gg d$ are named 'thermally thin'. Case of $\Lambda \ll d$ are named 'thermally thick'. Using textbook values for c_p and ρ in silicon at room temperature, equation 2.66 can be approximated to

$$\Lambda \approx \sqrt{29 \text{ mm}^2\text{Hz}/f_{\text{lock-in}}}. \quad (2.67)$$

Table 2.1 shows examples for $f_{\text{lock-in}}$, Λ and Λ/d for a 180 μm thick silicon solar cell. As $f_{\text{lock-in}}$ increases, Λ reduces and the spatial resolution becomes higher. This however comes at the cost of lower total thermal signal, since the cell has less time to heat up. Also, at $\Lambda > 60$ Hz, the sample becomes neither thermally thin nor thermally thick anymore, which may create difficulties for the data analysis as the theory is less well defined. The LIT measurement assumes that the electrical behavior of the cell reaches steady state conditions at much faster time scales than the lock-in period. This is well fulfilled at typical $f_{\text{lock-in}}$ values of 30 Hz but possibly not very well anymore under extreme conditions of e.g. 360 Hz for cells with large capacitance.

Table 2.1: Thermal diffusion lengths Λ and ratio between Λ and $d = 180 \mu\text{m}$ for several low to high lock-in frequencies for silicon. At frequencies beyond 60 Hz, the samples cannot be fully considered thermally thin anymore.

$f_{\text{lock-in}}$ (Hz)	1	10	30	60	120	180	360
Λ (mm)	5.39	1.71	0.98	0.70	0.49	0.40	0.28
$\Lambda / d_{\text{wafer}}$	29.96	9.47	5.47	3.87	2.73	2.23	1.58

Heat sources in LIT can be modeled as point sources (source smaller than a camera pixel), line sources and extended sources i.e. surfaces. In the simplest case of a point source in a thermally thin sample, the solution of equation 2.64 for the temperature distribution in a lock-in thermogram can be mathematically modeled with the non-analytical Kelvin function (modified Bessel functions) $\ker(x)$ and $\text{kei}(x)$ as

$$T(r, t) = A \left(\ker \left(\frac{r\sqrt{2}}{\Lambda} \right) + i \text{kei} \left(\frac{r\sqrt{2}}{\Lambda} \right) \right) \exp(i\omega t) \quad (2.68)$$

in cylindrical coordinates where r is the radius from the point source. The real part of $T(r, t)$ describes the 0° image and the imaginary part the -90° image. A graph of $\ker(x)$, $\kei(x)$ and $\sqrt{\ker(x)^2 + \kei(x)^2}$ in silicon is depicted in figure 2.15. Note that $\ker(x)$ has a significant negative component. The integral over $\ker(x)$ is zero and the integral over $\kei(x)$ is proportional to the power density of the source.

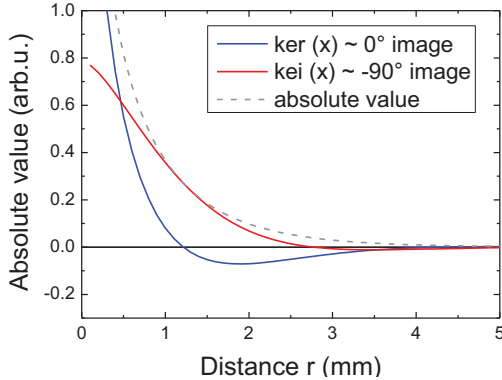


Figure 2.15: $\ker(x)$, $\kei(x)$ and $\sqrt{\ker(x)^2 + \kei(x)^2}$ with $x = (r\sqrt{2})/\Lambda$ for a diffusion length of $\Lambda = 1$ mm corresponding to $f_{\text{lock-in}} = 30$ Hz.

The amplitude A depends on the shape of the heat source at the camera resolution during data acquisition (e.g. point source vs large extended source) and the material specifics. For brevity, a tabular overview adapted from [70] of amplitudes of the 0° and -90° images for thermally thin and thermally thick samples for point, line and extended sources is presented in table 2.2, taken from [70]. P , p^l and p are the power densities of a point, line and extended source respectively and D the width of a camera pixel. In IBC cells, as will be shown in section 5.4, heat sources are a combination of point, line and extended heat sources.

Table 2.2: Amplitudes of 0° and -90° temperature signal at source position for different shapes of heat sources and thermally thin and thick samples. P , p' and p denote the amplitudes of the square shaped power bias. The ker- and kei-functions were approximated analytically and diverging sources were averaged across one camera pixel of width D . Taken from [70].

Sample type	Point source	Line source	Extended source
Th. thin S^{0°	$\frac{P}{\pi^2 dk} \ln \left(\frac{2}{D} \sqrt{\frac{\pi k_{\text{th}}}{\rho c_p \omega}} \right)$	$\frac{p'}{\pi d \sqrt{2k_{\text{th}} \omega c_p \rho}}$	0
Th. thin S^{-90°	$\frac{P}{4\pi k_{\text{th}} d}$	$\frac{p'}{\pi d \sqrt{2k\omega c_p \rho}}$	$\frac{2p}{\rho \pi c_p d \omega}$
Th. thick S^{0°	$\frac{2P}{\pi \sqrt{\pi D k_{\text{th}}}}$	$\frac{2p'}{\pi^2 k_{\text{th}}} \ln \left(\frac{4}{D} \sqrt{\frac{k_{\text{th}}}{\rho c_p \omega}} \right)$	$\frac{\sqrt{2p}}{\pi \sqrt{k_{\text{th}} \omega c_p \rho}}$
Th. thick S^{-90°	$\frac{P \sqrt{\rho c_p \omega}}{\pi^2 k_{\text{th}} \sqrt{2k_{\text{th}}}}$	$\frac{p'}{2\pi k_{\text{th}}}$	$\frac{\sqrt{2p}}{\pi \sqrt{k_{\text{th}} \omega c_p \rho}}$

Chapter 3

SR-LBIC for short-circuit current density mapping

This chapter presents a new data analysis method that uses spectrally resolved light beam induced current measurements (SR-LBIC) to obtain short-circuit current density (J_{sc}) maps with about 200 μm spatial resolution. Short-circuit current densities are often not homogenous across a solar cell, for example due to regions of lower excess carrier lifetimes, locally increased surface recombination, cell design as well as optical inhomogeneities in the production process. The method explained in the following is the first experimental quantification method of local J_{sc} losses for solar cells, representative for AM1.5G spectral distribution. It is applicable to IBC cells and other arbitrary cell designs. The method is based on a pixel by pixel interpolation of wavelength dependent EQE. The interpolated EQE is spectrally integrated with the AM1.5G spectrum to obtain J_{sc}^{loc} at each pixel, without the need for scaling. Additionally, since local reflection losses are also mapped, internal quantum efficiency based 'pseudo- J_{sc} ' maps are introduced which in combination with J_{sc}^{loc} -

maps allow obtaining maps of optical J_{sc}^{loc} losses caused by reflection.

After a literature overview in section 3.1 and details on the experimental setup in section 3.2, the new methods are introduced in section 3.3 and 3.4. In section 3.5 J_{sc}^{loc} -mapping is applied on IBC cells and yields the first accurate experimental determination of local 'electrical shading' type losses. A highly interesting application example of J_{sc} -mapping analysis on two aluminum emitter IBC cells is also presented.

The SR-LBIC based J_{sc}^{loc} -mapping method and advanced application examples were published by the author in [74]. The analysis of the aluminum emitter IBC cells in section 3.5 was obtained in collaboration with A. Kimmerle [56]. A comparison of this method to luminescence and lock-in thermography based J_{sc}^{loc} -imaging methods that emerged very recently was published in [75].

3.1 Literature overview

Material and solar cell characterization by beam induced currents

Measurements of spatially resolved photo generated currents for the study of photovoltaic devices were introduced in the 1980's. The main research efforts dealt with the assessment of crystal quality and the microscopic characterization of grain boundaries and diffusion lengths in silicon by Donolato [76], Luke et al. [77], Sawyer [78] and Zook [79]. Currents were induced by either a focused electron beam (EBIC) or light beam (LBIC). Using LBIC at several specific wavelengths was denoted spectrally resolved light beam induced current (SR-LBIC), which was also employed for the characterization of grain boundaries by Sawyer et al. [78]. SR-LBIC was later used also for large device areas to obtain EQE maps at individual wavelengths and for diffusion length mapping, first introduced by Stemmer et al. [80]. This technique was further refined and applied particularly to multicrystalline silicon solar cells by Rinio et al. [59], Isenberg et al. [81] and Schlosser et al. [82]. A major advancement to data acquisition

speed and versatility of SR-LBIC was introduced by Warta et al.'s system [83], which allowed parallel acquisition of multi-wavelength data including optical reflection losses (see section 3.2). Recently, Breitwieser et al. [84, 85] introduced LBIC with sub-micron resolution (μ LBIC) for investigations of solar cell cross sections and pn junctions.

While the terms LBIC and SR-LBIC are widespread in the silicon PV community, in other research fields, different names describing the same principle of semiconductor analysis exist. This includes ALBIC (area light-beam induced current) [86], OBIC (optical beam induced current) [87], SPRS (spatially resolved photocurrent spectroscopy) [88] and SPCM (scanning photocurrent microscopy) [89].

Other short-circuit current density mapping and imaging methods

Since the initial publication of the SR-LBIC based J_{sc}^{loc} -mapping method by the author, alternative methods have been proposed. These are based on illuminated lock-in thermography by Fertig et al. [90, 91], dark lock-in thermography by Breitenstein et al. [92] and photoluminescence by Höffler et al. [93]. In these publications, SR-LBIC is used as the reference method. Because these imaging methods are based on very different physical principles and experimental setups, each approach has advantages, drawbacks and limitations on accuracy and robustness. A comprehensive comparison of all techniques was recently presented by Fertig, the author of this work and others [75].

IBC cell characterization

SR-LBIC has been successfully used in recent years for IBC cell characterization. Local EQE maps were used to characterize losses at short-circuit conditions, particularly over the BSF doped regions. Such 'shadow like' current losses [94] are often referred to as 'electrical shading', a term which still sparks controversy, as the losses are not based on actual shading. The term is however used in this

work as it is the only widely known term for this effect. This loss mechanism is often the major current limiting factor in an IBC cell. EQE maps allowed assessing improvements with regard to 'electrical shading' in the finished solar cell during the design optimization process [95–97]. This includes the study of the effects of a p-doped front floating emitter as presented by Granek et al. [98] and recently Cesar et al. [51]. Reichel et al. [99] numerically simulated local EQE features using two-dimensional charge collection probability based on the reciprocity theorem by Donolato [100]. This approach is also used for simulating J_{sc} -maps in section 4.6 of this work. This work, unlike all previous studies, provides the net effect of 'electrical shading' on the local and global J_{sc} at excitation equivalent to the AM1.5G spectrum.

3.2 Experimental setup and spatial resolution

To obtain the SR-LBIC maps required for J_{sc}^{loc} mapping, a solar cell is held at short-circuit while a light spot with a diameter between few and several hundred microns scans the surface of the cell and measures the extracted photocurrent. The efficiency to collect excess carriers is wavelength dependent, as it is sensitive to the penetration depth of the light and thus the generation profile in the cell (equation 2.20). Nowadays, commercially available SR-LBIC systems for solar cell analysis are based on the experimental setup by Warta et al. [83]. In Warta's system, multiple modulated laser light sources at distinct wavelengths run simultaneously at different harmonics. Therefore, measurement time is independent of the number of used wavelengths, as long as the frequencies of laser intensity modulations are low enough for typical response times of a solar cell. The signal is demodulated by Fourier transform to obtain separate images for each wavelength. The measured current is scaled to local external quantum efficiency $\text{EQE}^{\text{loc}}(\lambda)$, which is the fraction of incident photons that resulted in the extraction of excess carriers from the

cell. Additionally, the local spectrally resolved reflectance $R^{\text{loc}}(\lambda)$ is measured via a photo-diode over the sample. Therefore, also internal quantum efficiency maps $\text{IQE}^{\text{loc}}(\lambda)$ are obtained, which present the ratio of non reflected photons to extracted carriers. Thus, IQE maps are free of optical reflection losses. Note that parasitic absorption of light is not removed in an IQE^{loc} map. The scaling for EQE^{loc} and R^{loc} maps for a given SR-LBIC setup is commonly performed via conventional global EQE and R of either the cell under investigation or a calibrated reference cell.

The experimental data for this work was acquired with the commercially available LOANA solar cell analysis system by to company pv-tools[101]. Modulated laser light was used from six diode lasers at 405 nm, 532 nm, 670 nm, 780 nm, 940 nm, and 1064 nm peak wavelength, all coupled onto the solar cell through the same optical fiber. The solar cell is kept at 25 °C by a temperature controlled chuck. At the working distance used in this work, the FWHM of the Gaussian laser beam profiles varied for each wavelength and ranged between 100 μm for 670 nm and 220 μm for 405 nm.

As it was unavailable, no bias-light during SR-LBIC measurement was used in this work. Consequently, the cells operate globally at very low injection conditions during measurements. For cells that show non-linear behavior of EQE with injection [102], it is important to obtain the global EQE and R measurements for scaling with a bias-light. EQE non-linearity in SR-LBIC then only becomes a problem in cases of severely inhomogeneous injection dependent lifetime (see [75]) or severe contacting faults (see section 6.2). Such non-linearities and injection dependencies are sometimes observed with dielectric passivation concepts [103], which is particularly relevant for cells with large area fractions of dielectric passivation such as PERL.

3.3 J_{sc}^{loc} -mapping principle

The locally measured short-circuit current I_{sc,λ_i}^{loc} at wavelength λ_i is scaled by a reference EQE $_{\lambda_i}^{ref}$ and I_{sc,λ_i}^{ref} via

$$EQE_{\lambda_i}^{loc} = \frac{EQE_{\lambda_i}^{ref}}{I_{sc,\lambda_i}^{ref}} I_{sc,\lambda_i}^{loc}. \quad (3.1)$$

The local short-circuit current density at a given incident spectral photon flux density $\Phi_{\lambda}(\lambda)$ is correlated with the EQE(λ) via

$$J_{sc}^{loc} = q \int_{\lambda_1}^{\lambda_2} EQE^{loc}(\lambda) \Phi_{\lambda}(\lambda) d\lambda, \quad (3.2)$$

where λ_1 and λ_2 should be chosen to sufficiently represent the range of non-negligible EQE of the desired spectrum. No additional weighting with the pixel and illumination area is necessary, because EQE $^{loc}(\lambda)$ is not area related. To reduce uncertainties in the local EQE, the step size of the mapping is chosen to be smaller than the laser spot sizes. This ensures that every part of the cell is illuminated over the course of the measurement. According to equation 3.2, calculating J_{sc}^{loc} requires the function EQE $^{loc}(\lambda)$ at each pixel. The experimental data from the setup yields EQE $_{\lambda_i}^{loc}$ at six wavelengths between 405 nm and 1064 nm. This already covers most of the spectral range where the AM1.5G spectrum has significant contributions in silicon. The function EQE $^{loc}(\lambda)$ is obtained by linear interpolation between the six points known from the SR-LBIC measurements. However, typical silicon solar cells exposed to AM1.5G spectrum receive contributions to J_{sc} from wavelengths between about 300 nm and 1170 nm, which are beyond the 405 nm to 1064 nm range of the employed SR-LBIC setup. To account for this, artificial SR-LBIC images at 300 nm and at 1170 nm are created by scaling the images at 405 nm and 1064 nm with the ratio between the global EQE at 405 nm and 300 nm, respectively 1064 nm and 1170 nm as in

$$EQE_{300nm}^{loc} = EQE_{405nm}^{loc} \frac{EQE_{300nm}}{EQE_{405nm}}, \quad (3.3)$$

$$EQE_{1170nm}^{loc} = EQE_{1064nm}^{loc} \frac{EQE_{1170nm}}{EQE_{1064nm}}. \quad (3.4)$$

Because of a penetration depth l_{Si}^{-1} of only 120 nm at 405 nm and 6 nm at 300 nm wavelength [63], this approximation will not influence the lateral spatial resolution for the short wavelengths. This also assumes that the relative lateral differences in local EQE are the same for 300 nm than for 405 nm. At the end of the cell's infrared response, a real SR-LBIC measured image at 1170 nm would be more blurred than the 1064 nm image due to a significantly higher l_{Si} in silicon and thus increased scattering of light at the rear side of the cell ($l_{Si\ 1064\ nm} = 1.15\ mm$, $l_{Si\ 1170\ nm} = 45.5\ mm$ [63]). The subsequent artificial sharpening of the J_{sc}^{loc} map is the used setup however not expected to have a great impact on the local level, provided that only quantitative data from structures $\gtrsim 150\ \mu m$ is investigated.

In principle, the interpolation could be refined with physical models and functions but simple linear interpolation has shown sufficiently good results for all silicon solar cells presented in [74] and is thus recommendable because of its robustness and little required user input. Equation 3.2 can of course alternatively be applied with spectral response $SR(\lambda)$ and illumination power density instead of EQE instead of photon flux.

Figure 3.1 shows an example for the average conventionally measured EQE by a monochromator (black line, also measured with LOANA), the average EQE from SR-LBIC measurements (red diamonds) as well as the two additionally inserted interpolation points (white diamonds) from the artificial SR-LBIC images at 300 nm and 1170 nm which result in the average linearly interpolated EQE (dashed red line). The data was obtained from a 243 cm² industrial multicrystalline silicon solar cell. The deviations between the linear interpolation and global measurement can be calculated from the EQE ratio

¹Defined as $1/\alpha$ in this work.

for each wavelength. The average in this example is below 1% and has a standard deviation of 8%, which represents the spread. For each case, basic statistical analysis indicates how well the SR-LBIC interpolation matches the global EQE measurement and thus helps estimating errors.

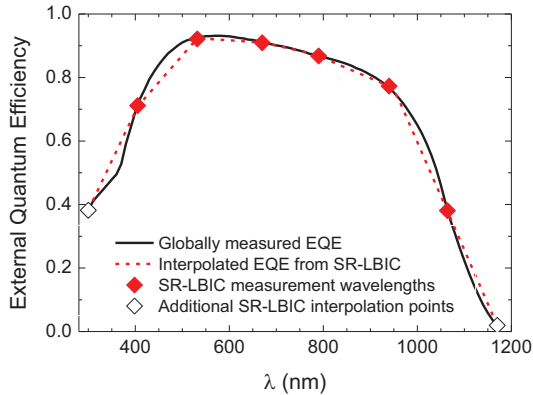


Figure 3.1: Averaged, linearly interpolated EQE of a whole 243 cm² industrial Al-BSF silicon solar cell compared to the conventionally measured global EQE. The red diamonds present the average SR-LBIC EQE measurements and the white diamonds the additional necessary interpolation points, calculated according to equations 3.3 and 3.4.

Figure 3.2 shows the resulting J_{sc}^{loc} map of the same cell used for figure 3.1. The arithmetic average J_{sc}^{loc} over this map is 33.9 mA/cm², while J_{sc} from a traditional sun simulator measurement with a xenon lamp spectrum is 33.3 mA/cm². The deviation of about 0.6 mA/cm² is of the order of the $\pm 2\%$ typically estimated errors even in calibrated I-V measurements using a sun simulator. Data acquisition time with the LOANA SR-LBIC system depends on the step size and integration time at each measurement point. At 100 μm step size a measurement time of about two minutes per cm² sample surface is required. The interpolation algorithm was implemented in MATLAB [104] and requires few minutes computation time on a modern office computer, depending on the image size.

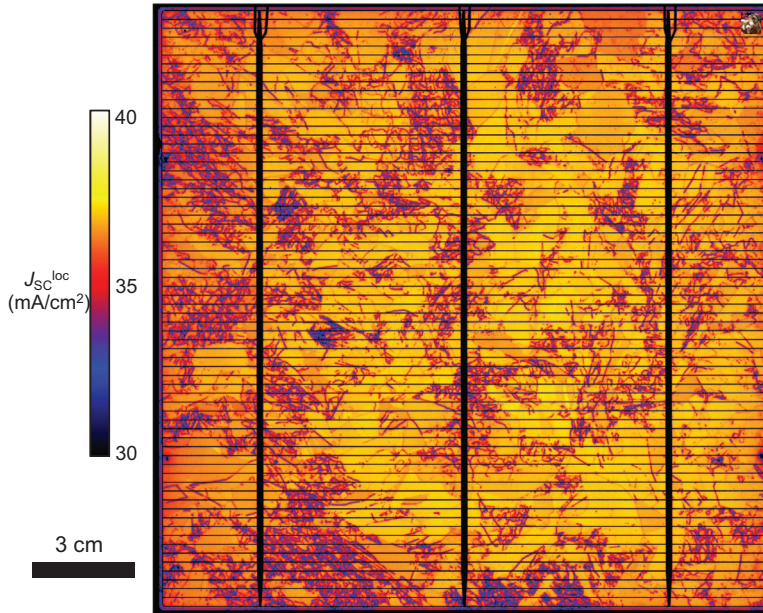


Figure 3.2: J_{sc}^{loc} map at 150 μm step size of an industrial Al-BSF multicrystalline silicon solar cell calculated using equation 3.2. The average J_{sc}^{loc} of 33.9 mA/cm^2 is in good agreement with the 33.3 mA/cm^2 obtained with a sun simulator.

Comparison to globally obtained values

Measurements on a range of investigated solar cells thus far have shown, that the resulting average J_{sc}^{loc} values match well those obtained from conventional sun simulator measurements and do not require additional scaling. Table 3.1 summarizes the absolute values and deviations between averaged J_{sc} from SR-LBIC with those obtained from IV measurements for all solar cells studied in [74] by the author of this work. The deviations of the average values range between +1.8% and -2.1%. There is no clear trend as to whether the linear interpolation over or underestimates J_{sc}^{loc} .

Table 3.1: Average J_{sc}^{loc} values obtained by the presented method (LBIC- J_{sc}) compared to values from sun simulator measurements (I-V J_{sc}). The agreement is near the typically estimated measurement errors of $\pm 2\%$ in global J_{sc} measurements. This confirms the good accuracy of the presented method. Data from publication [74]

by the author of this work.					
Material, design	Size, type	mean LBIC- J_{sc} (mA/cm ²)	I-V J_{sc} (mA/cm ²)	$\Delta (J_{sc}^{LBIC}, J_{sc}^{I-V})$ (mA/cm ²)	J_{sc} dev. (%)
mc-Si Al-BSF	243 cm ² p-type	33.9	33.3	0.6	1.8
mc-Si Al-BSF	156 cm ² p-type	35.1	34.7	0.4	1.1
Cast-mono Al-BSF	243 cm ² p-type	32.8	33.5	-0.7	-2.1
Cast-mono HIP-MWT	243 cm ² p-type, LFC	36.6	36.9	-0.3	-0.8
Cz-Si HIP-MWT	243 cm ² p-type	39.5	40	-0.5	-1.3
Fz-Si Al-BSF	243 cm ² p-type	35	34.9	0.1	0.3
Fz-Si IBC	4 cm ² n-type	39.2	39.6	-0.4	-1

3.4 Pseudo- J_{sc}^{loc} and optical loss mapping

Several commercially available SR-LBIC measurement setups like LOANA include parallel acquisition of local current and reflectance data which allows local IQE measurements. The interest of IQE is to discern between electrical and optical losses, since the IQE represents the quantum efficiency of the solar cell regarding only photons that were absorbed in the cell. Such information can be valuable, especially in the presence of lateral inhomogeneities of the generation caused by e.g. an inhomogeneous ARC or scratches (see section 6.4). IQE^{loc} maps can be calculated via

$$\text{IQE}^{loc}(\lambda) = \frac{\text{EQE}^{loc}(\lambda)}{1 - R^{loc}(\lambda)}. \quad (3.5)$$

Such IQE maps can now be used to interpolate a short-circuit current density in analogy to equation 3.2 via

$$\text{pseudo-}J_{sc}^{loc} = q \int_{\lambda_1}^{\lambda_2} \text{IQE}^{loc}(\lambda) \Phi_{\lambda}(\lambda) d\lambda. \quad (3.6)$$

This resulting new short-circuit current density maps are named 'pseudo- J_{sc}^{loc} ' maps. The following example shows an extreme case, where optical inhomogeneities strikingly impact the J_{sc}^{loc} performance. Figure 3.3 shows a regular J_{sc}^{loc} map (a), a photograph (b) and a pseudo- J_{sc}^{loc} map (c) of a monocrystalline silicon solar cell that received a non-perfect honeycomb texture via nanoimprint lithography [105], instead of a conventional pyramid texture. In this early attempt of process development, the honeycomb texturing failed to be imprinted at the sides of cell, leading to a locally planar surface and hence a strongly decreased J_{sc}^{loc} of $\simeq 31 \text{ mA/cm}^2$, as opposed to $\simeq 37 \text{ mA/cm}^2$ at the center of the cell. The pseudo- J_{sc}^{loc} map (c) confirms that the losses on the sides are primarily optical reflection losses, as the pseudo- J_{sc}^{loc} is homogeneous by comparison. Also, this analysis shows the electrically achievable J_{sc} of the device, if all optical reflection losses were eliminated, which is about $\simeq 39.5 \text{ mA/cm}^2$

in this example. In some cases J_{sc}^{loc} can be decreased by a combination of local optical and electrical properties, such as a poorer SiO₂ passivation at a (111) surface due to higher defect densities [106]. It should be possible to identify such effects with the presented pseudo- J_{sc} method.

Now, exclusively the optical reflection loss at short-circuit (ORL_{sc}^{loc}) can be analyzed by subtracting the J_{sc}^{loc} map from the pseudo- J_{sc}^{loc} map in units of mA/cm² via

$$ORL_{sc}^{loc} = \text{pseudo-}J_{sc}^{loc} - J_{sc}^{loc} . \quad (3.7)$$

Which by combining equations 3.2, 3.5 and 3.6 can also be written as

$$ORL_{sc}^{loc} = -q \int_{300\text{nm}}^{1170\text{nm}} R^{loc}(\lambda) IQE^{loc}(\lambda) \Phi_{\lambda}(\lambda) d\lambda . \quad (3.8)$$

The resulting ORL_{sc}^{loc} image is shown in figure 3.3 (d). Note the inverted colorbar for optical losses where a dark value means higher losses. This optical loss map only accounts for additional losses to J_{sc}^{loc} that were measured through optical reflection. Parasitic absorption e.g. by free carrier absorption [107] as an optical 'non-generation' loss will be observed as a lower pseudo- J_{sc}^{loc} value. An example for this phenomenon is shown in the next section.

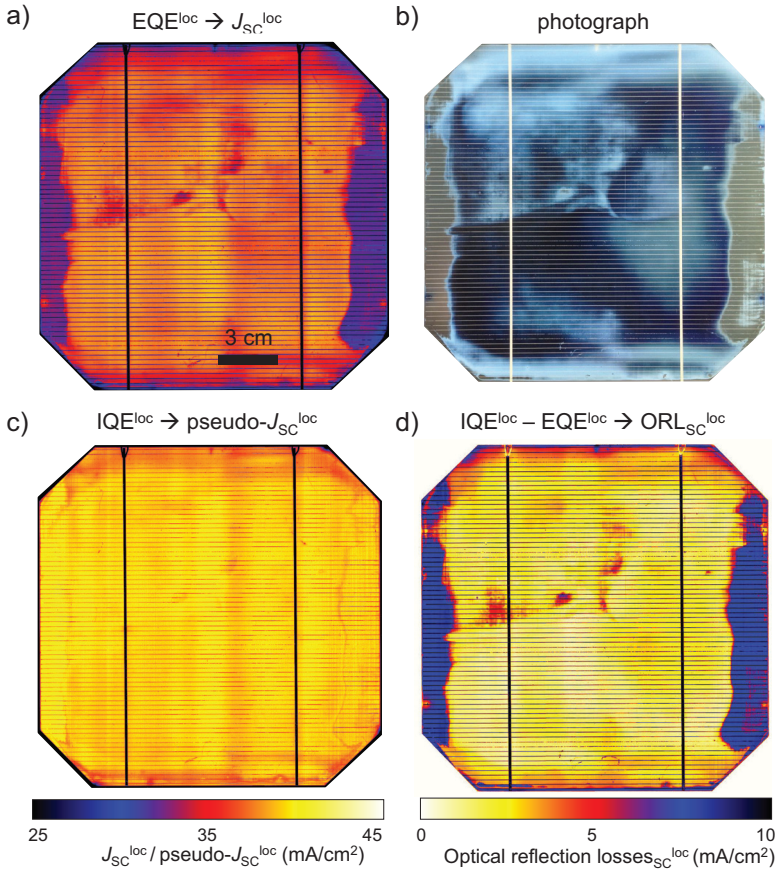


Figure 3.3: Example of a monocrystalline solar cell with an inhomogeneous honeycomb surface texture with a J_{sc}^{loc} map obtained from regular EQE maps of (a), photograph (b), pseudo- J_{sc}^{loc} map obtained from interpolated IQE maps (c), optical reflection loss map in units of mA/cm² obtained from difference between pseudo- J_{sc}^{loc} and J_{sc}^{loc} maps.

3.5 Quantified local J_{sc} losses in IBC cells

The primary motivation behind the IBC solar cell design is to eliminate optical shading losses due to front side metallization. However, this implies that the rear side cannot be entirely covered with a minority carrier collecting emitter doping. Collection efficiency of IBC cells is locally decreased by recombination of minority carriers that were generated over the BSF region. This recombination occurs at the n-doped BSF surface and/or within the bulk because the carriers need to travel further to reach the emitter. This well-known effect is often denounced 'electrical-shading' and has been studied via EQE maps from LBIC at individual wavelengths [96]. The presented method of J_{sc}^{loc} -mapping now allows direct access to the effective local short-circuit current density loss caused by 'electrical-shading'.

Figure 3.4 (a) shows the J_{sc}^{loc} map of IBC cell Fi2, as well as a schematic of the doping structure (bottom of (a)). The bright areas at the emitter yield current densities of up to 41.2 mA/cm^2 while the extracted current densities over the center of the BSF lines drop down to about 33 mA/cm^2 . Figure 3.4 (b) depicts the absolute value of an averaged line scan over the area in the dashed rectangle in (a), where a baseline of the average J_{sc}^{loc} at the center of the emitter (41.2 mA/cm^2) was subtracted. The line scan shows how much J_{sc}^{loc} is lost due to the 'electrical shading' effect at each position, because the center over the emitter is assumed to be unaffected by the BSF regions. The highest local loss is 8.0 mA/cm^2 , while the integral and hence total loss over the whole area is 1.7 mA/cm^2 .

In the examples shown thus far, the impact of the beam shape of the SR-LBIC lasers on the images has not been taken into consideration. However, the beam shape could play a significant role if the desired resolution of the structures is of the order or smaller than the FWHM of the laser beams. This is the case for this IBC cell, where the gap between emitter and BSF is $150 \text{ }\mu\text{m}$ wide. The laser beam width was determined by a knife-edge measurement, where the reflectance of each laser was measured across the edge of a razor blade [108]. The differentiated signal directly yields the laser profiles, which

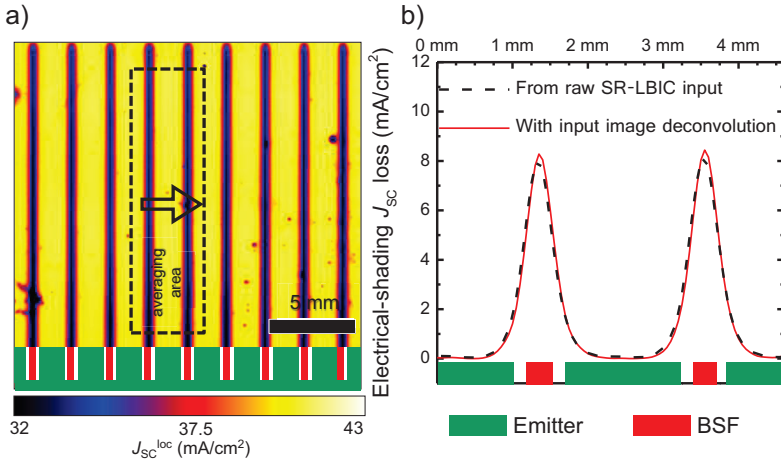


Figure 3.4: J_{sc}^{loc} map of IBC cell Fi2 (a), J_{sc}^{loc} loss line scan by across the highlighted area (b). A baseline of average measured J_{sc}^{loc} over the emitter was subtracted to quantify the loss due to 'electrical shading'. The red line shows the same result when the input SR-LBIC images were deconvoluted with their respective Gaussian laser beam shape functions. No significant impact of deconvolution was observed.

can be fit well by Gaussian functions (data not shown). These profiles were used to create point-spread functions to deconvolute the experimental SR-LBIC maps. The two-dimensional deconvolution was performed with the freely available plugin DeconvolutionLab for ImageJ [109]. The dashed line in figure 3.4 (b) shows the J_{sc}^{loc} loss according to the original SR-LBIC maps and the red line presents the 'electrical shading' loss after deconvolution of each input map. As expected, the deconvolution increased the peak loss by about 0.2 mA/cm^2 and the curve became slightly slimmer. However, the effect has no significant impact on the quantitative result and thus no deconvolution is required for this structure size in the particular setup used.

J_{sc}^{loc} in Al emitter IBC cells with local parasitic absorption

The following presents a study to exemplify the benefits of using SR-LBIC based EQE^{loc} , R^{loc} , J_{sc}^{loc} and pseudo- J_{sc}^{loc} analysis on IBC cells to unveil the J_{sc} limitations of a solar cell design. This analysis

was a result of a collaboration between the author and A. Kimmerle, who manufactured the solar cells and published an adapted version of this analysis in his dissertation [56]. The J_{sc}^{loc} maps were calculated and the figures were primarily created by the author of this work. The interpretations were made during immediate discussions with A. Kimmerle.

The following 5 cm x 5 cm large solar cells feature an emitter that was formed by screen printed aluminum metallization as in an Al-BSF cell using a metal paste containing boron [110]. This implies that the entire emitter has a silicon metal interface unlike the standard IBC design where only the center of the emitter has a contact opening (see figure 2.9). The peak acceptor concentration in the emitter is $1 \cdot 10^{19} / \text{cm}^3$ with a depth of about 6 μm [56]. While this method of forming the emitter requires fewer processing steps than conventional patterning and diffusions, the Al emitter features high recombination activity which limits the cell's V_{oc} . The Al emitter and phosphorous BSF doping of the cell were found in a QSSPC analysis to yield $J_0^{EM} = 200 \text{ fA/cm}^2$, $J_0^{BSF \text{ met}} = 146 \text{ fA/cm}^2$ for the contacted BSF and $J_0^{BSF \text{ uncontacted}} = 21 \text{ fA/cm}^2$ for the uncontacted BSF.

Figure 3.5 depicts a 1 cm x 1 cm large section of SR-LBIC EQE^{loc} maps at 780 nm (a), 1064 nm (b) and the J_{sc}^{loc} map (c) using the interpolation method described in section 3.3 for an IBC cell with conventional Al emitter design ('cell A', top graphs) and a cell where the Al emitter was structured with an additional 350 μm wide, uncontacted, phosphorous doped BSF line ('cell B', bottom graphs). The motivation for cell B was to reduce the area fraction of highly recombining Al emitter to allow higher V_{oc} without adding an additional processing step. From both EQE and the final J_{sc}^{loc} map, it can be observed that cell B suffers from processing inhomogeneities that significantly lower current extraction. This analysis focuses on a fault free area marked by the dashed rectangles.

When comparing the two cells, the EQE map at 780 nm and the final J_{sc}^{loc} map look qualitatively similar. However, the 1064 nm map

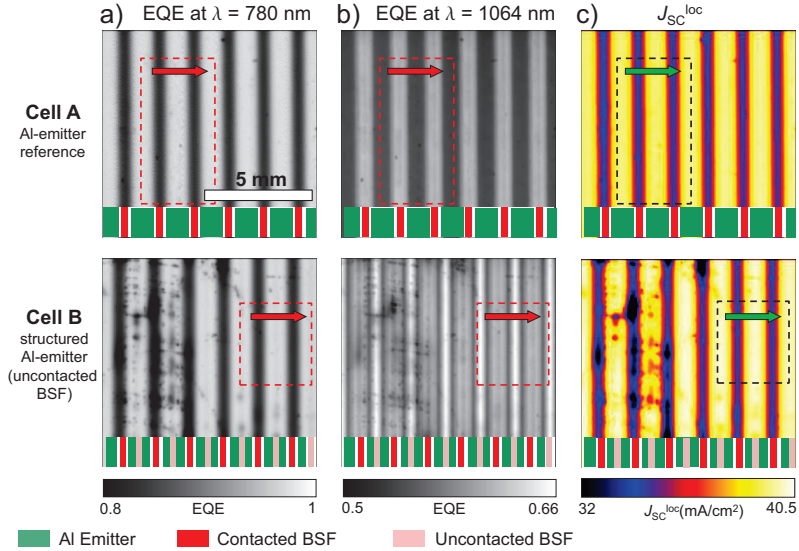


Figure 3.5: SR-LBIC EQE maps at 780 nm (a), 1064 nm (b) and J_{sc}^{loc} maps for an aluminum emitter IBC solar cell with a full aluminum emitter design (top) and an additional uncontacted BSF in the center of the emitter (bottom). The rectangles represent the ROIs used for line scan averages shown in figure 3.6.

where the absorption length in silicon is $950 \mu\text{m}$, shows atypical behavior compared to the 'electrical shading' effect (see figure 3.4). For cell A, the EQE at 1064 nm and hence current collection probability is lower over the whole emitter than the BSF, despite the shorter distance for holes to be collected. For cell B, an additional line pattern at 1064 nm excitation is apparent. For cell A and B, figure 3.6 shows line scan averages over the dashed rectangles from EQE (a,b) and respective optical reflection maps (e,f) that were acquired in parallel to the EQE maps. At 780 nm, the absorption depth into silicon is about $10 \mu\text{m}$ and no significant difference between cell A and cell B is observed. This means that differences in J_{sc}^{loc} must stem from losses on the rear side. In the 1064 nm map (b) there are significant deviations between cell A and B in the emitter region with a peak in EQE over the center of 66% for cell B as opposed to 54% for cell A, even though this area is further away from the hole collect-

ing Al emitter. The underlying emitter and BSF doping structure is geometrically much sharper defined than the EQE^{loc} observed peak. The blurring is caused by the fact that the 1064 nm photons are on average reflected multiple times before being absorbed.

EQE performance at photon energies close to the silicon bandgap is often related to optical reflection losses due to insufficient light trapping in the device. However, this does not explain the poor EQE of cell A since the local reflection at 1064 nm (f) shows only minor lateral differences in reflection of $< 1\%$. The optical reflection loss of cell B is actually higher over the emitter than in cell A (d, h). Therefore, the conclusion is that the loss over the emitter is caused by a parasitic absorption loss, namely free carrier absorption (FCA) in the highly doped Al emitter [107].

Finally, figure 3.6 (c) shows the quantitative effect of the structured emitter on $J_{\text{sc}}^{\text{loc}}$ and (f) the net $J_{\text{sc}}^{\text{loc}}$ gain due to the structuring by subtracting $J_{\text{sc}}^{\text{loc}}$ of cell A from cell B (g). The average gain in the fault free region is found to be 0.4 mA/cm^2 , proving that the additional uncontacted BSF line in the Al emitter yields not only a gain in V_{oc} but also in J_{sc} . On the other hand, the total J_{sc} from a sun simulator measurement was 39.4 mA/cm^2 for cell A and 39.2 mA/cm^2 for cell B. The spatially resolved investigations in figure 3.5 revealed that cell B has major local processing faults. Therefore, the lower performance of cell B stems from processing faults and not the design. This example demonstrates the capability of detailed SR-LBIC analysis for the quantitative characterization of subtle performance differences caused by design variations that are challenging to detect globally.

A brief summary of this chapter is presented in chapter 8.

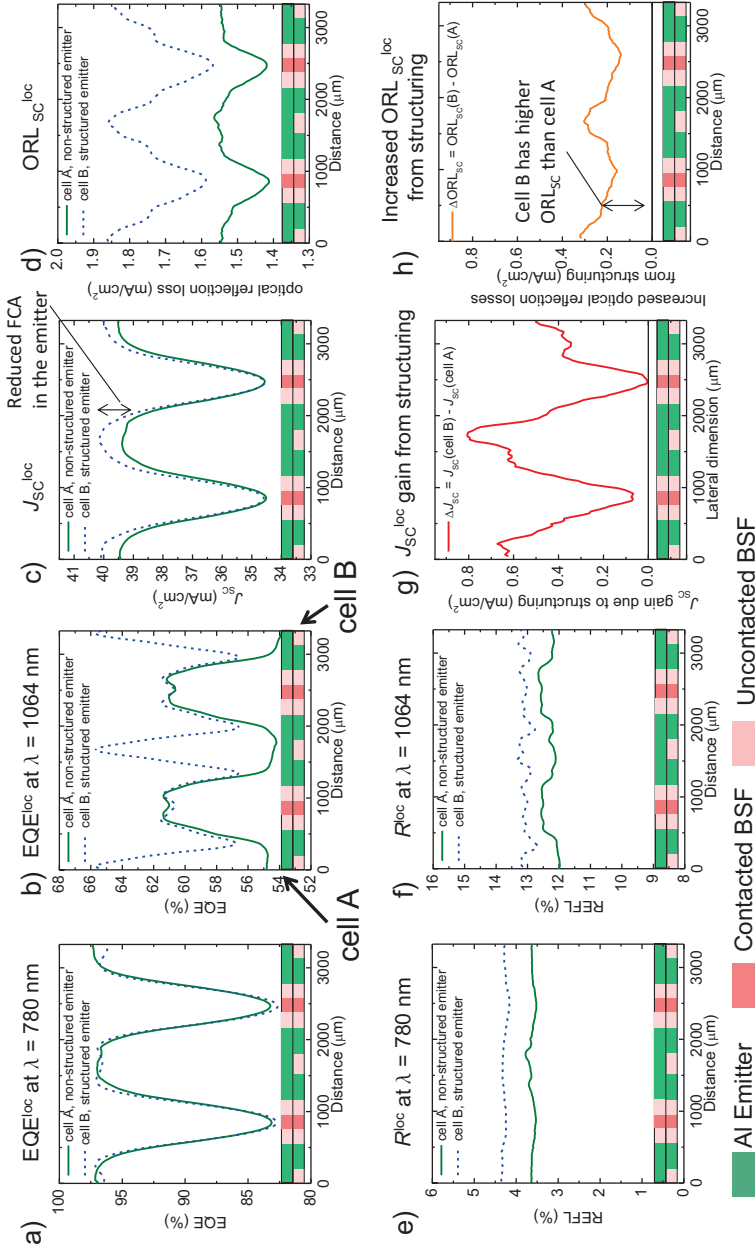


Figure 3.6: EQE^{loc} (a,b), R^{loc} (e,f), J_{sc}^{loc} (c) and ORL_{sc}^{loc} (d) line scan averages of the dashed rectangles in figure 3.5. (g) shows the net difference in J_{sc}^{loc} between cell A and B and thus J_{sc}^{loc} gain from the uncontacted BSF design. (h) shows the difference in ORL_{sc}^{loc}, where cell B shows higher optical reflection losses despite the J_{sc} gain. Parasitic absorption in the AI emitter is the likely cause for this atypical behavior.

Chapter 4

Luminescence imaging of local cell characteristics

This chapter discusses patterns and contrasts observed in luminescence imaging of IBC solar cells, how they can be interpreted and how they can be used for solar cell analysis. As introduced in section 2.2, the patterned doping structure of IBC cells makes lateral charge carrier density distribution and hence luminescence images of these cell inherently inhomogeneous, even on fault-free samples. This phenomenon had not previously been studied in detail. After a literature overview in section 4.1 and experimental considerations in section 4.2, exemplary images of photo- and electroluminescence are presented in section 4.3 to allow qualitative understanding of the device physics at all important operating conditions. The enhanced understanding of photoluminescence at V_{oc} , MPP and J_{sc} on IBC cells is then used to propose a method for obtaining surface recombination velocities (SRV) in section 4.5 and an adapted method and interpretation for local series resistance imaging in section 4.6. The numerical modeling of luminescence imaging that was developed for this work is

presented in section 4.4 and was much used for publications by the author [111–114]. The results in this chapter lay the foundation for the luminescence imaging based evaluation of local processing faults in chapter 6.

Experimental data from section 4.3 was obtained in collaboration with K. Hagedorn [115] and the development of the optical blurring model in section 4.4.1 was achieved in collaboration with H. Chu [116] in the scope of their respective Master’s thesis under supervision of the author. The numerical luminescence imaging model and method to obtain SRV was published in [111]. Section 4.6 on series resistance imaging was published in [112].

4.1 Literature overview

Over the past decade, great advancements in photo and electroluminescence imaging (PL/EL) applied to silicon solar cells have been made. The physical principles of this technique are explained in section 2.3.1. The publications by Fuyuki et al. dealing with electroluminescence imaging [117, 118] were the first to show that luminescence imaging on silicon solar cells yields a fast means of assessing minority carrier diffusion length and hence carrier lifetime. Following that, Trupke et al. [119] have demonstrated that using appropriate illumination, contactless quality assessment of silicon wafers and calibration to minority carrier lifetime using QSSPC [120] or QSSPL [121] is possible. The technological development of rather inexpensive silicon CCD cameras¹ for spatially resolved luminescence signal detection, has made PL imaging accessible and also preferred to lock-in thermography for many applications (see section 5.1) [122]. In 2008, Thorsten Trupke co-founded the company BT Imaging, specializing in measurement tools for luminescence imaging, which now competes with various enterprises that sell off-line and in-line tools to the PV industry, such as Greateyes, 3i and GPP Chemnitz. Today, luminescence imaging tools can be found at most PV companies, at the

¹As opposed to more expensive and more noise sensitive InGaAs cameras.

very least for the purpose of off-line control of process homogeneity. To characterize solar module degradation, particularly EL imaging is also used for studying degradation of solar modules under operation [123] as well as cell cracking by mechanical loads [124].

Notable contributions that followed Trupke et al.'s first work include PL studies on the cell precursor level, i.e. unfinished solar cells, by Abbott et al. [125] and Haunschild et al. [126] and on the silicon brick level by Mitchell et al. [127]. Important advances have been made in the accurate and reliable calibration of PL signal to minority carrier lifetime by Herlufsen et al. [128] using QSSPC and by Giesecke et al. using QSSPL [129] on wafer [130] and also cell level [131], summarized in [61]. Beyond carrier lifetime, PL imaging has also been developed to quantitatively determine bulk doping concentration [132], minority carrier mobility [133], local front and back-side surface recombination velocity before metallization [134], local diffusion lengths [135] and local saturation current densities [136].

Quantitative cell parameter imaging methods

Luminescence imaging was also developed to obtain spatially resolved information of diode model parameters (see section 2.1.3, equations 2.43 and 2.44), most famously the local series resistance R_s^{loc} . Methods to obtain R_s^{loc} based on PL imaging were developed by Trupke et al. [137], Kampwerth et al. [138], and Glatthaar et al. [139] and based on EL imaging by Hinken et al. [140], Haunschild et al. [141] and Breitenstein et al. [71]. All of these methods are based on calibrating local voltage drops caused by local series resistance in a terminal connected diode model, which was explained in detail by Glatthaar et al. [66] and introduced in section 2.3.1. Note that unlike Trupke's approach, Glatthaar et al.'s method, named C-DCR¹, does not assume uniform J_0 across the cell in a one-diode model and uses additional PL images to separate a J_0 image and an R_s^{loc} image. This concept was expanded by Shen et al. [142], who obtained

¹Coupled determination of dark saturation current density and series resistance

images of all two-diode model parameters by PL imaging using between 5 and 20 images at diverse operating conditions followed by fit algorithms. This approach has further sparked controversy over both accuracy of local values [92] and their agreement with global values [143, 144], sensitivity [67] and robustness of these quantitative methods in comparison with each other and with other spatially resolved techniques [145]. Increasing the number of free diode model parameters was found to yield larger inaccuracies, which lead Shen et al. to simplify their approach to a one diode model [146]. What complicates the discussion is that there is no well-defined standard for the determination of global diode model parameters such as R_s and global methods also bear significant uncertainties [39, 147].

Recently new concepts have been proposed even for the definition of local series resistance [148] and for adapting the concept of local voltages to local implied voltage distributions [40]. Also, more work was done on understanding the effects of lateral balancing currents with regards to spatial resolution [149]. Until now, no luminescence imaging method was found to be universally applicable, as they all use assumptions for the calibration and assume voltage and injection independent R_s^{loc} , J_0 and diode ideality factors, which is often inaccurate.

IBC cells and context in this work

All of the publications presented in this literature overview dealt only with conventional both-side contacted solar cells with uniformly doped structures (see figure 2.11). The implications of the complex IBC cell doping structure on luminescence imaging had not been studied. For IBC cells, prior to this work, only DeCeuster et al. showed qualitative PL images at open-circuit [150] and Schinke et al. showed a qualitative EL image [151]. Recently, Höffler et al. made an attempt to apply their new PL based $J_{\text{sc}}^{\text{loc}}$ imaging method on an IBC cell but without quantitative confirmation. Recently, Müller et al. (in collaboration with the author, see section 6.5) [152] and Chu et al. [153] presented qualitative images of breakdown patterns using EL.

4.2 Experimental setup and spatial resolution

The experimental setup built at Fraunhofer ISE used for photo- (PL) and electroluminescence (EL) imaging in this work is shown schematically in figure 4.1. The main components are an IBC specific contacting unit, a silicon CCD camera system with attached filters to detect luminescence signals from the cell, optical excitation of the cell by a laser, electrical excitation by a power supply, four-point current and voltage measurement of the cell¹ and a computer interface for data acquisition. Note that this setup allows for simultaneous optical and electrical excitation. All measurements take place at steady state conditions. The term PL is used in this work whenever illumination is involved².

In more detail: the IBC contacting unit incorporates a Pt100 sensor touching the rear side of the cell for temperature monitoring. The contacting unit is placed on a water cooled chuck with Peltier elements. The camera is a Princeton Instruments PIXIS:1024F 1 megapixel camera, cooled to about -50°C for reduced noise. The available lenses are a 50 mm Zeiss f1.4, optimized for infrared detection and a 80 mm Nikon f2.8 1:1 macro lens for higher magnification at the expense of lower signal to noise ratio (SNR). The laser is a Lisotschenko microoptics diode laser operating at a peak wavelength of 790 nm. The beam is expanded through custom made homogenization optics for industrial size 156 mm edge length wafers. The illumination inhomogeneity of the 2 cm x 2 cm solar cells in this work is $< 1\%$ across the cell area. A 950 nm and 976 nm longpass filter are placed in front of the lens to filter reflected laser light. The 4 quadrant power supply is a Kepco BOP10-10M and the current/voltage measurements are made with Hewlett-Packard 34401A multimeters.

¹Voltage is measured and controlled separately from the current conducting wires in order to exclude resistance losses through cables and contacts.

²There is no consensus in the community of whether to call e.g. luminescence imaging at *MPP* conditions PL or EL imaging. The term PL imaging is often associated to operation without electrical excitation i.e. V_{oc} conditions.

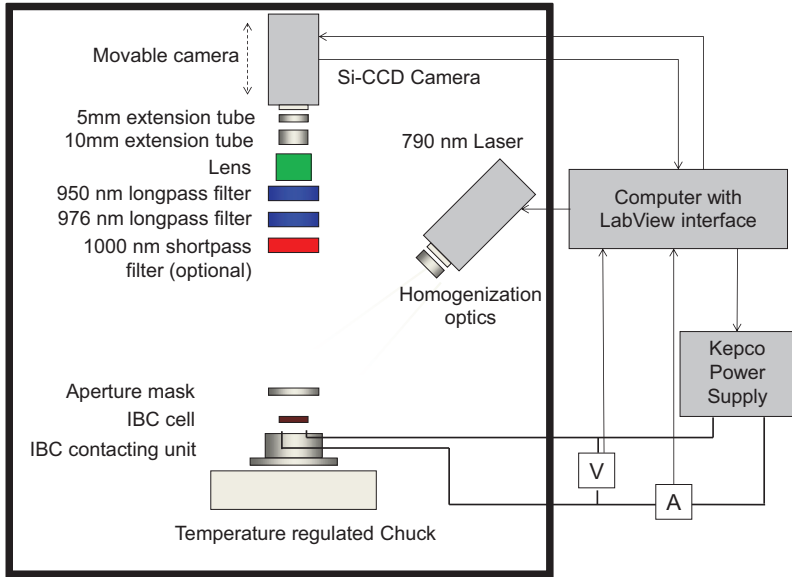


Figure 4.1: Schematic of the luminescence measurement setup. A contacted IBC cell on a temperature controlled chuck receives electrical and/or optical excitation. The luminescence signal is detected by a silicon CCD camera after filtering of reflected excitation laser light. A computer interface sets and records currents and voltages in a four point probe scheme.

More details on a typical luminescence setup can be found in [154].

To conduct the measurements near standard testing conditions (STC), all measurements in this work the solar cell is kept at 25 °C, unless specified otherwise. The deviations from 25 °C caused by switching laser illumination on and off is estimated to be ± 1 °C. Since the investigated 4 cm² silicon solar cells have a negligible heat capacitance, the temperature change by illumination occurs in less than one second. Since an AM1.5G spectrum is not achievable in this setup, the illumination intensity for all luminescence imaging is defined by the 1 sun equivalent, where 1 sun = $2.55 \cdot 10^{17} \frac{\text{photons}}{\text{cm}^2 \text{ s}}$ [61]. The luminescence intensity is calibrated to match the short-circuit current of a reference cell, which itself is calibrated by Fraunhofer ISE CalLab to match the global J_{sc} at 790 nm. The new LabView based computer interface was designed by the author in collaboration

with S. Haag and programmed by S. Haag. It allows fully software controlled setting of excitation conditions, defined measurement sequences and measurements of I-V and Suns- V_{oc} curves as in a sun simulator within the setup. This allows a direct comparison to global data from sun simulator measurements. After image acquisition, all luminescence images receive dark background subtraction and are normalized to counts per second (cts/s).

Spatial resolution and improvements by use of a shortpass filter

Additional extension tubes between camera and lens can be installed to reach frame sizes of down to 1 cm^2 which results in about $10 \text{ }\mu\text{m}$ per pixel. The spatial resolution in luminescence imaging of high efficiency silicon solar cells is typically not limited by the pixel size though. A factor that reduces the sharpness and contrast of luminescence images is a blurring effect named 'silicon CCD photon spread' [155, 156]. This is caused by the high absorption length of the $950 - 1200 \text{ nm}$ luminescence radiation that reaches the typically $< 100 \text{ }\mu\text{m}$ thick Si CCD chip. A significant fraction of photons are absorbed in neighboring pixels, creating a blurring effect. As shown by Walter et al. [155], this effect can be partially corrected by deconvolution using an adequate point spread function or, more easily, by employing a shortpass filter. The optional 1000 nm shortpass filter used in this work, in combination with the longpass filter stack effectively leaves only a window of photons between 976 nm and 1000 nm to enter the camera. This reduces the effect of isotropic luminescent photon emission (see section 4.4.1).

The impact of the shortpass filter for image contrast in IBC cell structures is depicted in figure 4.2. Figure 4.2 shows PL images of an IBC cell measured at 550 mV with (a) and without (b) a 1000 nm shortpass filter. The PL counts per second using the shortpass filter are reduced by an order of magnitude which implies ten fold longer integration times for SNR equivalent to the standard filter stack. Figure 4.2 (c) shows normalized average intensity profiles over the highlighted rectangles. The peaks are significantly narrower in (b) and

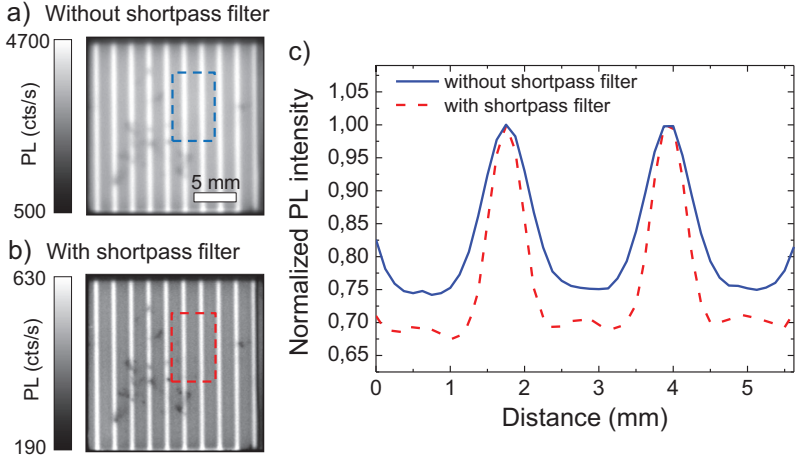


Figure 4.2: PL images of an IBC cell at 550 mV without (a) and with (b) an additional 1000 nm shortpass filter and normalized average PL intensity profiles over the highlighted rectangles (c). At the expense of SNR, the shortpass filter significantly increases image contrast primarily because of reduced photon spread in the silicon camera’s CCD.

the overall contrast (ratio between maximum and minimum value) is higher. The increased contrasts however are also a consequence of reduced blurring from isotropic photon emission in the sample. This will be discussed more in section 4.4. In conclusion, using a shortpass filter is recommended for achieving improved optical resolution if the expense integration time is acceptable. Luminescence images in this work are taken without a shortpass filter, except for all data in section 4.5.

Another aspect of spatial resolution is diffusion length. Luminescence images essentially display local charge carrier densities. Images of high efficiency Cz or Fz silicon solar cells tend to appear much more blurry than multicrystalline samples. The reason for this is the much higher τ_{eff} and thus L_{eff} . Especially under V_{oc} conditions, carriers flow from regions of high lifetime towards regions of low lifetime, an effect often denoted as lateral balancing currents [157]. This effect however is not considered a blurring effect in this work, because it is an intrinsic effect of the device that represents the physical reality

under operation.

All following PL images in this work include schematics of the rear side IBC doping structure to facilitate interpretation. The location of the different doping areas was often determined by overlaying the luminescence image with an image of the cell under illumination with a conventional incandescent light bulb. Since this image was taken including the longpass filters, it is effectively an infrared photograph. Due to the IR content of the light bulb emission, contrasts from reflected infrared light of the rear side metallization can be detected and used for guidance. An example for this is shown in figure 4.3, where (a) shows an IR photograph where the unmetallized gap regions are clearly visible, (b) a doping structure schematic and (c) an overlay of a PL image and the doping structure. Such a procedure only works if the contrasts in the IR photograph are sufficiently high. With some experience and the help of guidelines however (see section 7.1), an experimenter can easily identify the IBC doping regions in PL images without IR photographs, as the PL images often reflect the well known geometry of the cell structure.

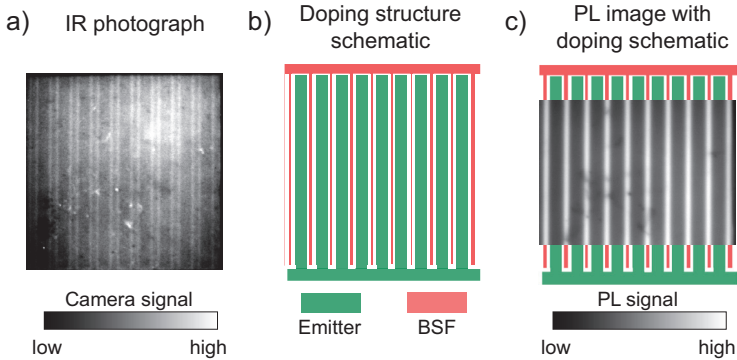


Figure 4.3: Infrared photograph of an IBC cell illuminated by a lightbulb (a), resulting doping schematic interpretation (b) and overlay of a PL image with the doping schematic (c). The unmetallized regions are clearly visible in the IR photograph, which facilitates interpreting contrasts in PL images.

4.3 Interpretation of luminescence patterns and contrasts

Electrical and optical excitation of a solar cell leads to injection and extraction of charge carriers. As was explained in section 2.3.1, the luminescence signal is proportional to the product of charge carrier densities which is inherently linked to the splitting of quasi-Fermi levels of electrons and holes and hence local implied voltages. The interpretations in the following are based on arguments about charge carrier density. A tabular summary with the interpretations for all luminescence patterns can be found in section 7.1. All images include schematics of the doping structure for easier understanding, where the emitter busbar is always located at the bottom and the BSF busbar at the top of the image.

4.3.1 PL: Luminescence imaging under illumination

When performing PL measurements, excess charge carriers are generated through photon absorption within the solar cell. At open circuit condition (V_{oc}) no current is extracted while at short-circuit (J_{sc}) the maximum amount of current and at maximum power point *MPP* a reduced fraction of photo generated carriers is extracted. A qualitative analysis of measurement examples at each of these key operating conditions is presented in the following.

V_{oc} : open-circuit conditions

At V_{oc} conditions charge carriers are generated homogeneously across the cell surface¹ and recombine in the base or on a surface. The V_{oc} PL image is virtually free of series resistance effects, as no current is transported out of the cell. Just like in conventional solar cells, signal intensity is indicative of excess charge carrier density and hence local

¹The absorption length at 790 nm is about 10 μm , which is much smaller than typical cell thickness. Therefore, inhomogeneities in the generation profile caused by rear side reflection are negligible.

effective lifetime τ_{eff} . The following examples serve as an introduction to the effects that lead to PL images at V_{oc} . Figure 4.4 shows three examples of cropped images at V_{oc} conditions at 1 sun illumination. Cells S2 (a), P1 (b) and cell A1 (c) are cells of the type B, C and B respectively (see figure 2.9). More details about all presented IBC cells can be found in the appendix A. The graphs at the bottom show the average line scan of PL counts per second (cts/s) across the area marked by the black rectangles. Note that all of these cells are line contacted at the center of the rear side diffusions. Note also, that most luminescence images in this work show the full 4 cm^2 cells.

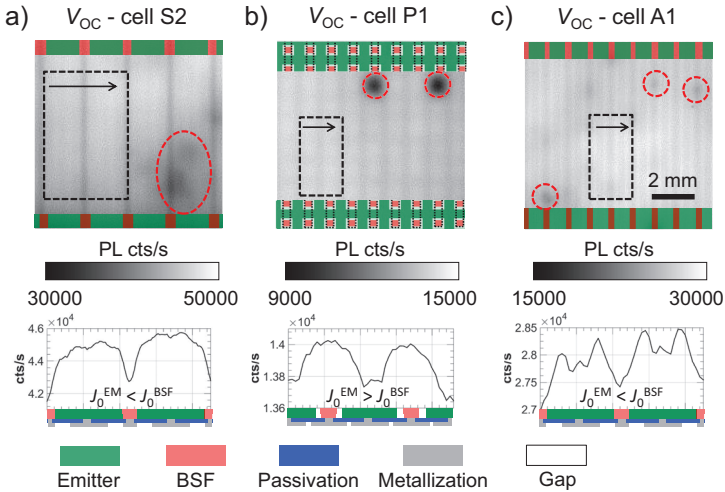


Figure 4.4: Cropped sample PL images of three IBC solar cell under V_{oc} conditions. The bottom graphs show the average intensity line scans across the dashed rectangles. Contrasts in the PL intensity can be attributed to varying recombination activity, both in the regular patterns ($J_0^{\text{EM}} < J_0^{\text{BSF}}$ or $J_0^{\text{EM}} > J_0^{\text{BSF}}$) as well as local production faults (red ellipses).

In all examples, a combination of regular patterns and dark spots are visible. The regular patterns correlate with the underlying doping structure. A relative lower PL intensity means lower charge carrier density, which is related to a lower local τ_{eff} and hence higher recombination [74]. The line patterns observed in figure 4.4 must be caused by the relative differences in the recombination rate of the

emitter, BSF and contact regions because the base and FSF can be assumed to be homogeneous. Whether the emitter or BSF signal is higher can directly be associated to whether J_0 of the emitter doping is lower or higher than J_0 of the BSF doping. From Kane-Swanson experiments on test structures [158] it was determined, for cell P1 $J_0^{\text{EM}} = 450 \text{ fA/cm}^2 > J_0^{\text{BSF}} = 74 \text{ fA/cm}^2$ and for cell A1 $J_0^{\text{EM}} = 92 \text{ fA/cm}^2 < J_0^{\text{BSF}} = 127 \text{ fA/cm}^2$.¹

Lateral balancing currents are flowing from areas with high τ_{eff} towards areas with higher recombination and thus lower τ_{eff} [157]. L_{eff} of these cells is of the order of several hundred μm . Therefore τ_{eff} of each region is naturally blurred and the actual difference in surface recombination activity (J_0 or S_{eff}) is underestimated. The luminescence patterns at V_{oc} conditions can be complex though as it depends on the surface recombination of other regions as well. Cell A1 has the most complex pattern, where the PL signal above the emitter contact opening is lower than on the sides but shows a bump. Presumably, in cell A1, a high J_0 value at the emitter's metal contact leads to a significant decrease in PL intensity. The bump could be caused by enhanced reflection of the luminescence photons at the metal contact. The surface recombination parameters of the gap regions, metal-semiconductor interfaces and front side also play a role, which will be presented in section 4.5.

Furthermore, dark areas in figure 4.4 (red ellipses) can be seen in all images. As lower PL intensity indicates higher recombination, these low signal areas are recombination centers and are caused by local shunting, material defects or poor surface passivation. Further investigations on cell P1 and S2 are presented in section 6.3.1 and 6.3.2 respectively.

J_{sc} : short-circuit conditions

At J_{sc} conditions, all photo generated excess minority charge carriers that do not recombine in the base or at the cell surfaces are extracted. As this is typically over 95% of the generated excess carriers, this

¹No J_0^{EM} value is available for cell S2.

results in a rather low PL signal. The residual luminescence signal stems from so called 'diffusion-limited' carriers [9, 66] (see section 2.3.1). Those are charge carriers that were neither extracted nor recombined via defects (SRH) or Auger recombination. All PL images of IBC cells at J_{sc} exhibit the same lateral pattern structure i.e. luminescence profiles with peaks of diffusion limited carrier densities above the BSF regions. Figure 4.5 shows examples of three different cells.

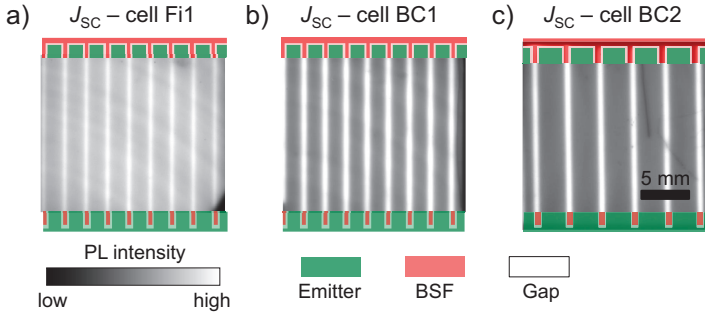


Figure 4.5: Experimental PL images at J_{sc} conditions of three different IBC solar cells. All images exhibit a periodic lateral pattern with peaks of diffusion-limited carriers above the BSF regions. These are excess carriers that were neither extracted, nor recombined via SRH or Auger recombination.

Charge carriers generated above the BSF regions have the furthest distance to reach the pn junction at a nearby emitter region. The resulting current loss was quantitatively determined by SR-LBIC using the J_{sc}^{loc} -mapping method described in section 3.3. To understand how the PL profiles at J_{sc} correlate with recombination and current extraction, numerical simulations of PL intensity calculated with the program Quokka [17] are used in the following. The simulation model is described in detail in section 4.4. Figure 4.6 depicts two sets of numerically simulated PL profiles at J_{sc} for a unit cell modeled after cell Fi1. Schematics of this unit cell are shown at the bottom of figure 4.6. Figure 4.6 (a) presents an increase of J_0^{BSF} from the reference of 140 fA/cm^2 (black) to 300 fA/cm^2 (red) and 500 fA/cm^2 (blue). As J_0^{BSF} increases, the global J_{sc} decreases since

more minority carriers recombine at the BSF surface. Consequently, the PL signal over the BSF region decreases. In (b), a variation of the gap width w^{gap} is shown from the 150 μm reference (black) to 75 μm (orange) and finally no gap (green). The increase in emitter coverage fraction significantly increases the global J_{sc} because the decreased distance to the pn junction means fewer carriers recombine before reaching it [49]. Now however, an increase in J_{sc} comes with reduction in PL intensity over the BSF region. This means that a low PL signal over the BSF region can be both a positive and a negative indicator for cell performance. This is different to local EQE measurements where a low EQE signal is always a negative performance indicator (see section 3.5).

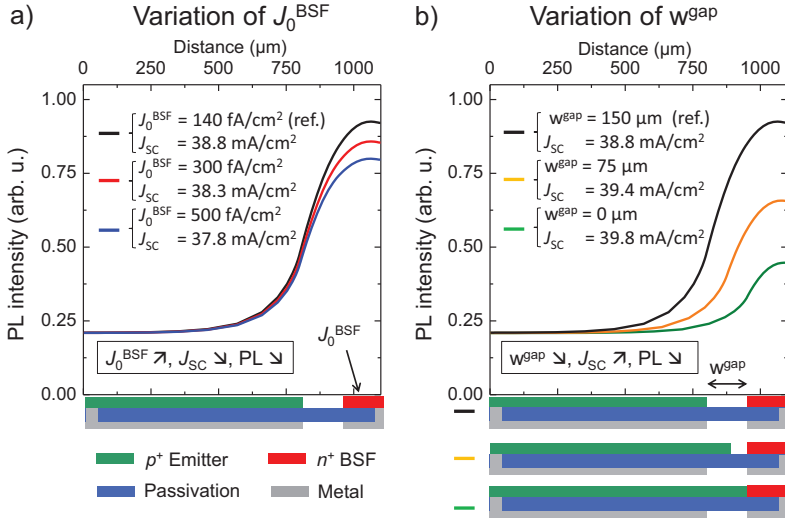


Figure 4.6: Numerical simulations of unit cell PL profiles at J_{sc} conditions for a variation of J_0^{BSF} (a) and w^{gap} (b). Increasing BSF surface recombination lowers the global J_{sc} and PL signal (a) but an increased J_{sc} caused by a w^{gap} design change also decreases the PL signal (b). Because of these opposing trends, PL images under J_{sc} conditions are rarely useful for assessments of current extraction.

Simulations such as in figure 4.6 (a) have shown that an increase in surface or base recombination results in reduced PL intensity at J_{sc} conditions. Higher recombination means lower τ_{eff} . In a direct

comparison between two cells of the exact same design, the peak PL intensity over the BSF regions is indicative of the underlying surface recombination. However, it will be shown in section 6.2 that this reasoning does not hold under all circumstances. PL imaging at J_{sc} was therefore found to be only suitable to a limited extent for qualitative assessment and not suitable for quantitative assessment of local J_{sc} .

***MPP* : maximum power point conditions**

The *MPP* presents similar conditions with respect to net current extraction as J_{sc} , since typically about 85 – 95% of J_{sc} is extracted at *MPP*. In the I-V curve as described in the diode model (see figure 2.5), series resistance leads to a reduction in current extraction. This also manifests in luminescence imaging where the PL signal at *MPP* is always higher than at J_{sc} because fewer photogenerated charge carriers are extracted. As a good example for this, figure 4.7 shows cell A1 at J_{sc} (a) and *MPP* (b) conditions scaled to the same counts per second. The *MPP* image looks qualitatively like a J_{sc} image. The regular line patterns are shaped almost the same but show an increased offset and reduced contrast in the *MPP* image. In the *MPP* image, some local inhomogeneities appear as increased signals that were invisible in the J_{sc} image (red ellipse). They can be attributed to locally increased series resistance, namely contact resistance. This will be discussed in great detail in section 6.2. It can already be noted, that the comparison of PL at J_{sc} and *MPP* allows for a qualitative identification of local series resistance faults. Quantitative determination of local series resistance on IBC cells is presented in section 4.6.

4.3.2 EL: Luminescence imaging in the dark

Without illumination and under forward bias, a silicon solar cell acts as a pn diode with exponentially increasing current limited by series resistance as a function of bias voltage. All injected charge carriers recombine within the cell and all power (product of voltage between the cell contacts and total current) is dissipated within the device.

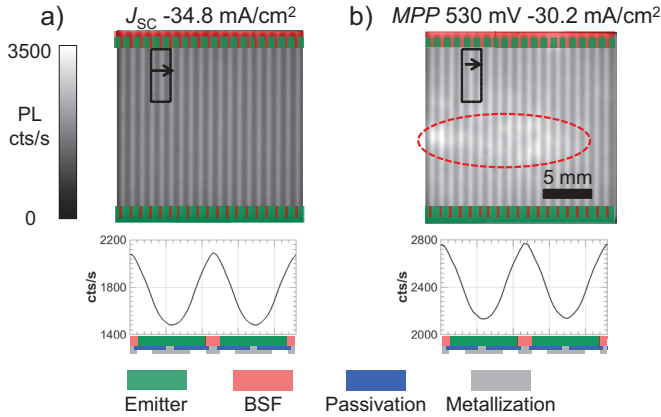


Figure 4.7: PL image at J_{sc} (a) and MPP (b) of cell A1 scaled to the same units. The MPP image also primarily shows diffusion limited carriers over the BSF region but also effects of reduced current extraction due to processing faults of locally high contact resistance (red ellipse).

Under reverse bias, the diodes conduct no current until sufficiently high voltage for breakdown processes is reached [41]. Luminescence imaging of such breakdowns are presented in section 6.5. This section briefly explains how the line patterns in EL imaging of IBC cells under forward bias are related to bias voltage, emitter sheet resistance R_{sh}^{EM} and base resistance ρ^{base} of the cell and also what use EL can be for practical application.

Line Patterns under forward bias

Figure 4.8 shows EL images of cell BC3 (a) and Fi2 (b) at low forward bias of 550 mV (left) and high forward bias of 690 mV (right). The graphs on the right depict the normalized EL intensity profiles for both bias voltages over the units cells marked in the dashed rectangles. R_{sh}^{base} is base resistivity calculated into a sheet resistance (ρ^{base}/d).

For both cells at low forward bias, the contrast between emitter and BSF regions is low and thus injection levels of excess carriers are rather homogeneous. Due to $J_0^{BSF} > J_0^{EM}$ in both cases, recombina-

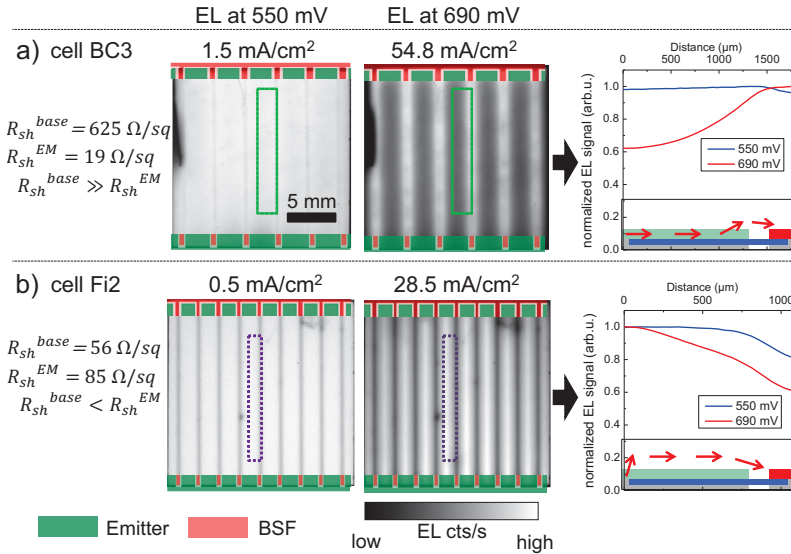


Figure 4.8: EL images of two cells with strongly different resistivity and emitter sheet resistance under low (550 mV) and high (690 mV) forward bias. The graphs show the normalized EL signal across a unit cell. At high bias voltage, the contrast indicates where minority carriers (holes) are primarily injected into the base, which is a function of ratio between base and emitter sheet resistance.

tion is increased at the BSF and the charge carrier density is lower at the BSF region. At high forward bias, a much more pronounced pattern emerges with peaks that represent the main locations of minority carrier injection into the base. The EL profile of cell BC3 peaks over the gap and BSF region while for cell Fi2, the peak is over the emitter contact. At high voltage, the pattern shows effects of series resistance because of the larger total current. As indicated by the unit cell cross section schematic (bottom of the graphs on the right), holes can predominantly flow from the p-contact to the edge of the emitter diffusion and only then get injected into the base (a), or they are injected directly over the p-contact and flow through the base towards the n-contact (b). Which current and thus primary injection path will be predominant depends mainly on the base and emitter sheet resistance. Cell BC3 (a) has a high R_{sh}^{base} (10 Ωcm) and low

R_{sh}^{EM} , so excess holes are mainly injected at the emitter edge. Cell Fi2 (b) on the other hand has a low R_{sh}^{base} ($1 \Omega\text{cm}$) and a higher R_{sh}^{EM} , hence excess holes are rather injected directly at the emitter contact.¹ The specific patterns that emerge represent intrinsic resistance effects of the cell under forward bias in the dark. As explained in section 2.2, this is however not representative for e.g. *MPP* conditions under illumination.

Local recombination, series and parallel resistance effects under forward bias

Besides regular patterns of fault free solar cells, EL imaging may also show dark spots caused by local processing faults. Just like conventional Al-BSF solar cells, dark spots in EL imaging may be caused by a high local surface or defect recombination [159], increased local contact resistance R_c [141] or shunting [160]. Shunting (ohmic or non-ohmic) implies that current from the surrounding area may flow into the fault and recombine, hence yielding lower EL signal. Figure

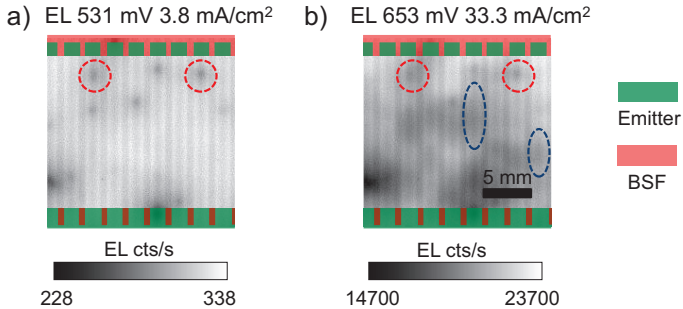


Figure 4.9: EL images of cell A1 at 531 mV (a) and 653 mV (b) forward bias. Dark spots indicate increased recombination, shunting or increased local contact resistance. Such images are useful for qualitative identification of processing faults but an unambiguous distinction of the fault type is not possible with EL imaging alone.

4.9 shows two EL images of cell A1 at 531 mV and 653 mV forward

¹Note again that luminescence signal from within the highly doped surface regions is negligible because of the low excess carrier densities there.

bias. A few dark spots are visible in (a, red circles) and larger dark areas emerge in (b, blue ellipses). It can be said, that dark spots in EL under forward bias always qualitatively indicate local processing faults. Shunting or J_{02} type faults are known to increase recombination already at low bias voltages while contact resistance effects emerge rather at high voltages (because of increased global current densities) [97]. It is however not possible to unambiguously distinguish between local shunting, R_c and J_0 effects using EL imaging. Results on local R_s and shunting fault detection are presented in sections 6.2 and 6.3 respectively.

Use of EL in practical application

It can be concluded that the fault free patterns in EL under forward bias are the result of base and sheet resistance effects as a function of current flowing through the cell. These parameters are typically well known in the fabrication process and no new information arises from the images. As operation in the dark is not representative for the illuminated case, quantitative studies of local series resistance in the dark are not further pursued in this work. EL imaging can be used to qualitatively identify the presence of local faults as dark spots but fails to unambiguously identify the type of fault. Generally, higher forward bias voltages result in higher contrasts and SNR.

4.4 Numerical modeling of luminescence images

This section provides details on the numerical simulation of luminescence imaging experiments used in this work. Two programs were used for the semiconductor simulations that the luminescence calculations are based on, namely COMSOL Multiphysics [161] and Quokka by A. Fell [17]. COMSOL Multiphysics is a finite element analysis (FEM) solver and simulation software for which C. Reichel has implemented all models from the PC1D software v.5.1 [21, 162] for a two-dimensional IBC unit cell. Quokka on the other hand, is a finite difference method (FDM) solver, specifically designed for the simulation of two or three dimensional silicon solar cells. The main difference between Reichel's COMSOL model and Fell's Quokka is the description of highly doped surfaces. In Reichel's COMSOL model, the highly doped surfaces are modeled by diffusion profiles, as it is common in state-of-the-art device simulation software such as Sentaurus Device [163] or Atlas [164]. Quokka on the other hand is based on the conductive boundary (CoBo) approach by R. Brendel [29]. In CoBo, uncontacted boundaries are described only by a J_0 and R_{sh} parameter (see section 2.1.2). While COMSOL is a more realistic representation of a solar cell, CoBo requires much fewer mesh elements and thus much less computational power. It also allows for a simpler manipulation of J_0 and R_{sh} , even independently from each other. Thus far, the simpler CoBo approach in Quokka has been increasingly successful and validations have been published, particularly for IBC cells [165, 166].

The luminescence imaging model was published by the author in [111] and used to obtain local surface recombination parameters (section 4.5, published in [111] using COMSOL), local series resistance imaging (section 4.6, published in [113], using Quokka) and local contacting fault characterization (section 6.2, published in [114], using Quokka). Modelling of luminescence experiments was also attempted and published in parallel by Fell et al. using Quokka [167]. A collaboration between A. Fell and the author resulted in the implementation

of the optical blurring model developed in this work as an option in Quokka [36].

Details on the solar cell simulation model

PC1D was used to simulate generation profiles by the 790 nm laser. The total photon-flux of the simulated source was calibrated to match J_{sc} for the AM1.5G spectrum. COMSOL and Quokka solve the two-dimensional Poisson and continuity equations 2.12 for the spatially resolved electrical potential and the quasi-Fermi levels for electrons and holes (equation 2.6). For COMSOL, the doping profiles were measured by electro-chemical-voltage profiling (ECV) and fitted with Gaussian and exponential functions. Sheet resistances can be calculated from the doping profile or directly measured with commercially available tools.

The half-pitch unit cell geometry of all simulated fault-free IBC cells is sketched in figure 4.10. The most important electrical models implemented into COMSOL include the mobility model by Klaasen [168], Auger recombination by Richter et al. [34], field-enhanced Shockley-Read-Hall recombination [169] and band-gap narrowing by del Alamo et al. [170] in COMSOL and by look-up table for Schenk's model [15] in Quokka. COMSOL simulations were performed using Maxwell-Boltzmann statistics, while Quokka uses Fermi-Dirac statistics. While the use of Boltzmann statistics may lead to imprecision, the author considers the use of Maxwell-Boltzmann statistics to be a good approximation for the doping densities described in this work [171]. The accuracy of electrical simulations in COMSOL and Quokka was verified by comparing I-V performance with results obtained by Sentaurus Device using the same geometry and physical models. Series resistance by the cell metallization was taken into account in the final I-V curve by an additive value, calculated using established analytic models [172].

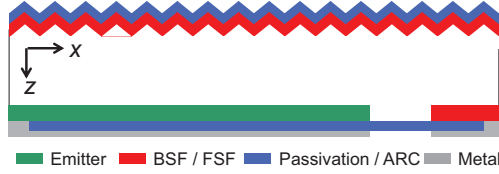


Figure 4.10: Cross section schematic of the line-contacted fault free IBC unit cell used for the luminescence imaging simulations.

4.4.1 Luminescence intensity and optical blurring

In the following, the analytical model to calculate the PL intensity and account for optical blurring is introduced. As explained in section 2.3.1, the radiative recombination rate r_{rad} of photons with the energy ($E_\gamma = hc/\lambda$) at a location \vec{r} in a semiconductor material is given by

$$r_{\text{rad}}(\vec{r}, E_\gamma) = \alpha(E_\gamma) \frac{E_\gamma^2}{4\pi^2 \hbar^3 c^2} \frac{1}{\exp\left(\frac{E_\gamma - (\Phi_{Fn}(\vec{r}) - \Phi_{Fp}(\vec{r}))}{kT}\right) - 1}. \quad (4.1)$$

Since for the spectrum of silicon at 300 K, $E_\gamma - (\Phi_{Fn} - \Phi_{Fp}) \gg kT$, equation. 4.1 can be simplified to

$$\begin{aligned} r_{\text{rad}}(\vec{r}, E_\gamma) &\approx \alpha(E_\gamma) \frac{E_\gamma^2}{4\pi^2 \hbar^3 c^2} \exp\left(-\frac{E_\gamma}{kT}\right) \left(\frac{n(\vec{r}) \cdot p(\vec{r})}{n_{i,\text{eff}}^2(\vec{r})}\right) \\ &= B(E_\gamma) \left(\frac{n(\vec{r}) \cdot p(\vec{r})}{n_{i,\text{eff}}^2(\vec{r})}\right). \end{aligned} \quad (4.2)$$

All terms that are a function of E_γ can also be expressed as a function of the photon wavelength λ . The energy dependent emission probability is summarized by the term $B(E_\gamma)$. Therefore, to simulate the luminescence intensity of a solar cell, essentially the electrical parameters needed are cross sectional maps of n , p and $n_{i,\text{eff}}$ of the unit cell in figure 4.10. In order to calculate the luminescence intensity emitted by the cell, in a first approximation a simple one-dimensional

analytical approach adapted from [135] is shown in equation 4.3 to calculate the PL intensity $PL(x)$ at a position x across a unit cell. The product $n \cdot p/n_{i, \text{eff}}^2$ is integrated over the cell thickness d and photon energy $\lambda = hc/E_\gamma$, taking into account the exponential reabsorption of photons in the base, the camera lens and filter transmissions T_{filters} and the camera's quantum efficiency η_{cam} . $K_{\text{cal, PL}}$ is a calibration constant that is set once for all simulated operating conditions. The spatial coordinates x and z refer to the cross section schematic in figure 4.10.

$$PL(x) = K_{\text{cal, PL}} \int_0^\infty \eta_{\text{cam}}(\lambda) T_{\text{Filters}}(\lambda) B(\lambda) \cdot \int_0^d \frac{n(x, z) p(x, z)}{n_{i, \text{eff}}^2(x, z)} \exp(-\alpha(\lambda)z) dz d\lambda . \quad (4.3)$$

Taking into account a wavelength dependent reflectance of emitted photons at the front surface R_f and the rear surface R_r and including the increased path $(2d - z)$ that rear side reflected photons have to travel to reach the cell surface results in

$$PL(x) = K_{\text{cal, PL}} \int_0^\infty \eta_{\text{Cam}}(\lambda) T_{\text{Filters}}(\lambda) B(\lambda) [1 - R_f(\lambda)] \cdot \int_0^d \frac{n(x, z) p(x, z)}{n_{i, \text{eff}}^2(x, z)} [\exp(-\alpha(\lambda)z) + R_r(\lambda) \exp(-\alpha(\lambda)(2d - z))] dz d\lambda . \quad (4.4)$$

Optical blurring

The $PL(x)$ calculation thus far was a one-dimensional line integration. In reality, photons are emitted isotropically and only a fraction of them reach the camera. As described by Schubert et al. [173, 174],

non perpendicular emission both from luminescence as well as thermal radiation can only be neglected when measuring a polished wafer with the camera at a long distance away from the sample. When imaging a random pyramid texture however, photons emitted at specific angles can be refracted at the surface and reach the camera after all. This results in a blurring effect for all experimental images, where high detected luminescence signals are under- and low intensity regions are overestimated.

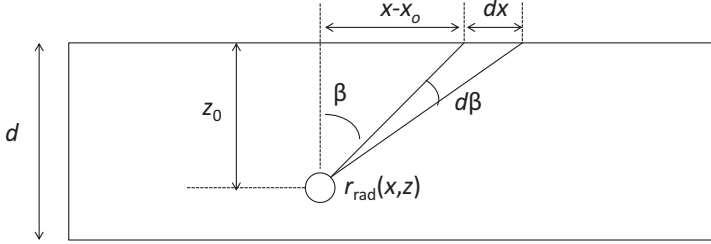


Figure 4.11: Schematic for the Lambertian optical blurring model.

Figure 4.11 shows the schematic for the following theoretical calculations. The signal $PL(x)$ along the unit cell receives contributions from all points sources of positions (x_0, z_0) over the pitch W . Thus, to include the point-spread into the simulation, equation 4.2 needs to be convoluted with a point-spread function J_{surf} such that

$$PL(x) = K_{\text{cal}} \int_0^{\infty} \eta_{\text{Cam}} T_{\text{Filters}} \cdot \int_0^W \int_0^d r_{\text{rad}}(x_0, z_0, \lambda) \exp(-\alpha r) J_{\text{surf}}(x, x_0, z_0) dx_0 dz_0 d\lambda . \quad (4.5)$$

with

$$r = \sqrt{(x - x_0)^2 + z_0^2} . \quad (4.6)$$

This point spread function yields the photon flux along the sur-

face. The most basic model for J_{surf} is the Lambertian model which was adapted from [174], where it was used for thermographic carrier density imaging of silicon. The Lambertian model assumes that the surface texture across hundreds of pyramids across a line element of a cell (y -direction) forms a completely random texture. Thereby all photons that reach the surface at $z = 0$ are assumed to have identical probability to reach the camera. Using trigonometric relationships results in

$$d\beta = \arctan \left(\frac{dx z_0}{dx (x - x_0) + (x - x_0)^2 + z_0^2} \right), \quad (4.7)$$

where β is the emission angle relative to the surface. From equation 4.7 one can calculate the luminescence photon flux density of a line at the surface via

$$J_{\text{surf}}(x, x_0, z_0) = \lim_{dx \rightarrow 0} \left(\frac{d\beta(dx)}{2\pi dx} \right) = \frac{z_0}{2\pi \left[(x - x_0)^2 + z_0^2 \right]} = \frac{z_0}{2\pi r^2}. \quad (4.8)$$

Mathematically this Lorentzian function diverges for point sources located exactly at the surface and is only physically sensible for $z_0 > 0$. Therefore all calculations were performed with the explicit calculation using differences in solid angles as in equation 4.7. Figure 4.12 shows an example of the luminescence signal $PL(x)$ reaching the camera for three different sources at $z_0 = 40 \mu\text{m}$, $80 \mu\text{m}$ and $140 \mu\text{m}$ away from the front surface. As a result, the signal intensity is shaped like a Lorentz distribution and depends on the distance of the point source to the front surface (z_0) and on the lateral offset ($x - x_0$) between the point source and the position where the photon exits the solar cell. This model can be adapted to represent more realistic conditions considering the angles of the surface texture. The use of a 1000 nm shortpass filter (see section 4.2) reduces the effect of blurring because isotropically emitted photons with short wavelengths experience rather strong reabsorption in the base and the long wavelength photons that would be detected far from the point source are filtered

out before reaching the camera.

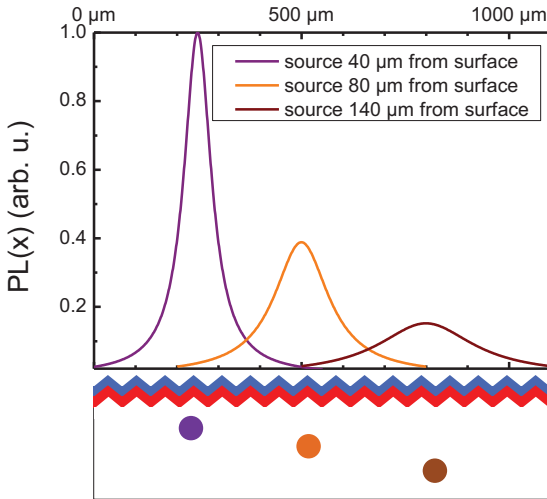


Figure 4.12: Luminescence intensity $PL(x)$ reaching the camera coming from point sources at different depths in the solar cell. Calculated using the Lambertian model and with consideration of photon reabsorption.

The blurring model was extended to consider back reflection as well, using the same geometric approach. The lengthy equations for this can be found in [116]. A good parameterization of the back reflectance can be difficult to obtain, as it is a mixture of diffuse and specular reflection and is not completely homogenous along an IBC cell [175]. By comparing PL simulations with and without inclusion of a homogenous back reflectance, changes of only up to 1 % in relative intensity across the unit cell were observed when using a 1000 nm shortpass filter [116]. A more realistic blurring model includes the 54.7° angles of the actual pyramid facets in $\langle 100 \rangle$ oriented monocrystalline silicon. In the scope of the Master's thesis by H. Chu [116] under supervision by the author, it was found, that the Lambertian model yields very similar results to a model considering these actually available angles for luminescence photons to escape the cell and reach the camera. Experimentally it can be difficult to have accurate data for all of the involved wavelength dependent factors of equation 4.4. If a shortpass filter is used, the range of relevant lumi-

nescence photon wavelengths is greatly reduced and the wavelength dependence in the integral may become negligible.

4.4.2 Example simulation results

The simulation results of this section as well as all of section 4.5 were obtained from a COMSOL model of cell Fi1, for which experimental input data is available. Figure 4.13 shows the product of charge carrier densities $(n \cdot p)/n_{i,\text{eff}}^2$ within the cross section of the unit cell (bottom graphs) and resulting PL(x) profiles (top graphs) after integration using equation 4.5 for 300 mV (a), 582 mV (b), 650 mV (c) and 683 mV (d). The x and z dimensions are on scale. Note that the 300 mV image is representative for J_{sc} conditions, because the net current extraction and thus charge carrier density distribution is virtually identical. Achieving convergence using COMSOL and Quokka's solvers at actual J_{sc} conditions (0 mV) is often not possible, because the quantities Φ_{Fn} and Φ_{Fp} for which the programs solve are nearly identical for e.g. 0 mV and 200 mV.

At 300 mV (a) the carrier densities are higher over the BSF region than over the emitter region, which results in an increased PL intensity over the BSF as observed in all investigated IBC cells (see section 4.3). At 582 mV (b), the cell's *MPP*, the voltage barrier that builds up at the junction between emitter and base begins to decrease the fraction of extracted current, which leads to increased carrier densities over the emitter region. This equates to a local increase of series resistance which will be treated in section 4.6. As much less current is being extracted at 650 mV (c), the PL intensities begin to balance out since surface recombination strongly influences the carrier density distribution rather than diffusion limited carriers or series resistance. At V_{oc} conditions of 683 mV (d), the emitter dominates the signal because of the higher surface recombination at the BSF. It is noticeable at 683 mV, that the total PL intensity above the emitter contact area is about 5% lower than that of the maximum over the remaining emitter area because of the recombination at the metal-semiconductor interface, which will be discussed later.

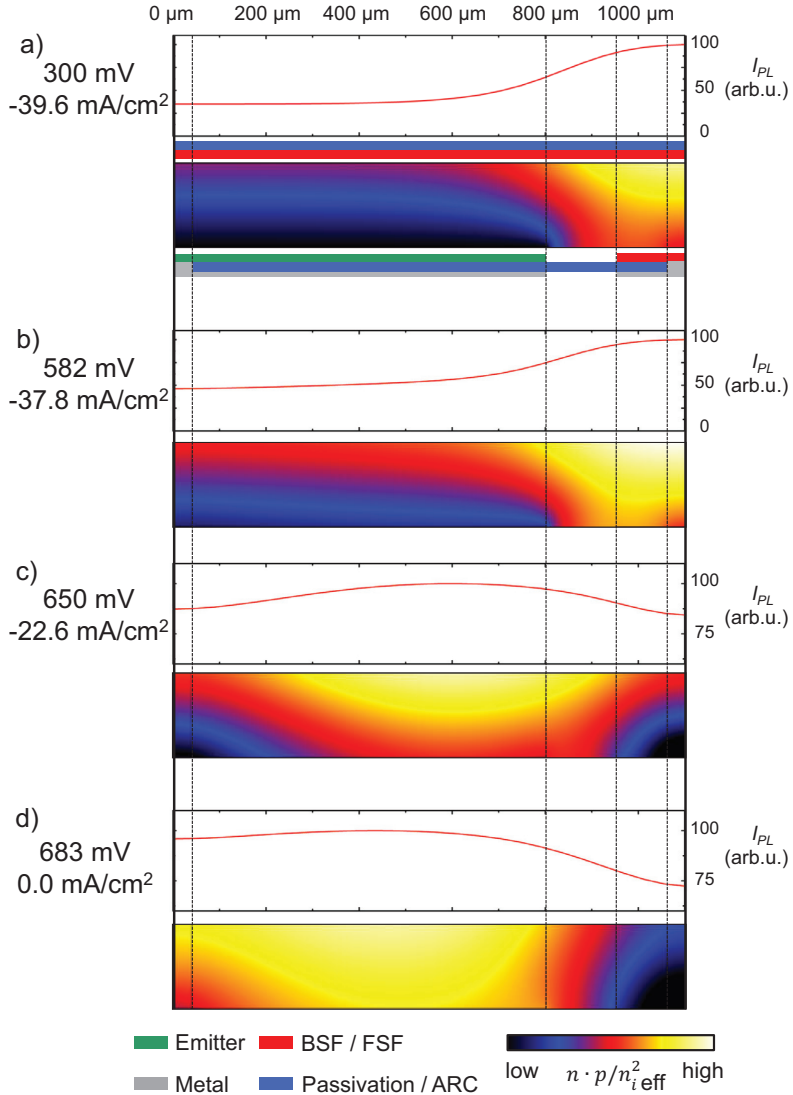


Figure 4.13: Simulated charge carrier densities product $(n \cdot p) / n_{i,\text{eff}}^2$ in a cross section of a cell (bottom graphs) and resulting PL(x) intensities (top graphs) using equation 4.5. The phenomenology observed in the experimental PL images in section 4.3 can now be studied on a cross sectional level.

Additionally, figure 4.14 shows the normalized PL profile of the unit cell at 600 mV with and without convolution with the Lambertian point spread function J_{surf} (equation 4.8). The impact of the blurring can be significant for quantitative evaluations and therefore should be considered for a proper simulation of luminescence experiments.

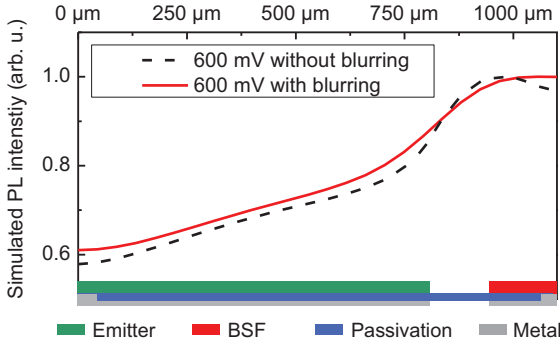


Figure 4.14: Simulated PL intensity across unit cell without (black) and with Lambertian blurring (red). Optical blurring from isotropic photon emission significantly impacts the luminescence profiles.

An alternative visualization of the PL profiles can be created by duplicating the results of a unit cell, stretching the signal to the actual cell length and adding a colorbar to the PL intensities. An example of this is depicted in figure 4.15 for the four PL profiles of figure 4.13. However, the depiction of PL data as profiles is more beneficial for detailed analysis, which is why all other luminescence simulations in this work are depicted as $PL(x)$ graphs.

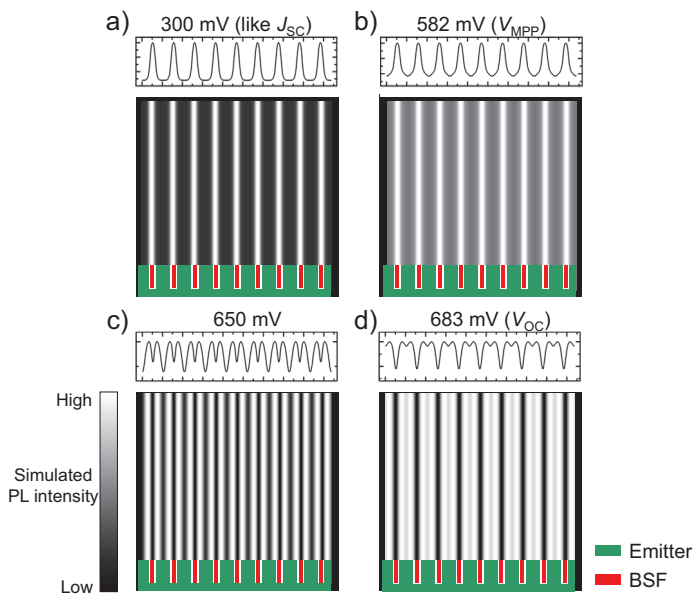


Figure 4.15: Simulated PL images at the four bias voltages 300 mV (a), 583 mV (b), 650 mV (c) and 683 mV (d), based on the PL(x) profiles of figure 4.13.

4.5 Surface recombination parameters from modeled luminescence images

This section proposes a method for extracting the surface recombination parameters of finished IBC solar cells by matching the intensity profiles of simulated and experimental PL images. Surface recombination parameters are typically determined by symmetric lifetime samples on solar cell test structures manufactured in parallel to the cells using the Kane-Swanson method with QSSPC measurements [158]. This method is however not applicable on the finished solar cell because the photoconductance based QSSPC method is not applicable for metallized samples because of the high density of free carriers in metals [131]. Therefore, the recombination parameters at silicon-metal interfaces of highly doped and passivated surfaces only are estimates obtained from analytical models [176, 177]. Also, these lifetime samples often do not experience all the temperature steps of a full solar cell process, so surface recombination on the finished cell may be significantly different than on the test structures.

In this section, again using the example of cell Fi1, first the sensitivity of the luminescence signal at V_{oc} to surface recombination parameters is presented, followed by a practical attempt of matching experiments with simulations. Note that since material parameters for silicon are known most accurately for 300 K (26.85 °C), for section 4.5, measurements and simulations were performed at 300 K.

4.5.1 Sensitivity analysis

As argued in section 4.3, luminescence images are most sensitive to surface recombination at V_{oc} . For cell Fi1 it is assumed that $\tau^{base} = 3.3$ ms and thus $L^{base} \approx 2$ mm, which is more than 11 times larger than the cell thickness of 180 μm . The local L_{eff} in the cell though is much smaller due to surface recombination. The six parameters for surface recombination in the COMSOL model are surface recombination velocities at the physical surface of the cell S_0 as illustrated in figure 4.16. Those are the SRV of the emitter contact

S^{EMcont} , the passivated emitter S^{EM} , the undiffused gap S^{gap} , the passivated BSF S^{BSF} , the BSF-contact S^{BSFcont} and the FSF S^{FSF} .

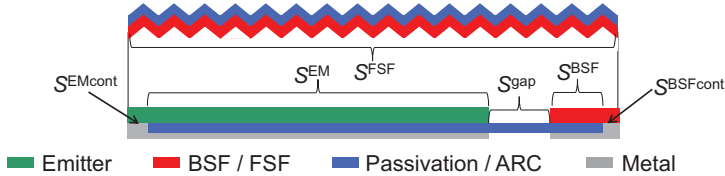


Figure 4.16: Schematic of the surface recombination velocities S_0 that were varied for the sensitivity analysis.

Figure 4.17 depicts examples showing the impact of varying SRV values to the PL profile relative to a reference simulation. The graphs were obtained by dividing one of three new simulations (yellow, red, blue) by the reference simulation (black dashed line). The reference J_0 values were obtained experimentally via lifetime samples. The S_0 SRVs corresponding to each J_0 at defined doping profiles (measured by SIMS or ECV) were obtained from calculations using the program EDNA [27]. Table 4.1 summarizes S_0 and corresponding J_0 values.

As expected, lowering any SRV leads to decreased recombination, increased carrier density and thus increased absolute luminescence signal and vice versa. A relative change in $\text{PL}(x)$ signal occurs not only directly over the diffused area but all across the unit cell. Each SRV has a specific signature impact on the luminescence signal. For example, increasing the FSF or BSF contact SRV can lead to the same inferior V_{oc} , but the resulting luminescence intensity profiles are very different. It was also found, that SRVs which are more limiting to the cell's final V_{oc} also impact the luminescence profile more strongly.

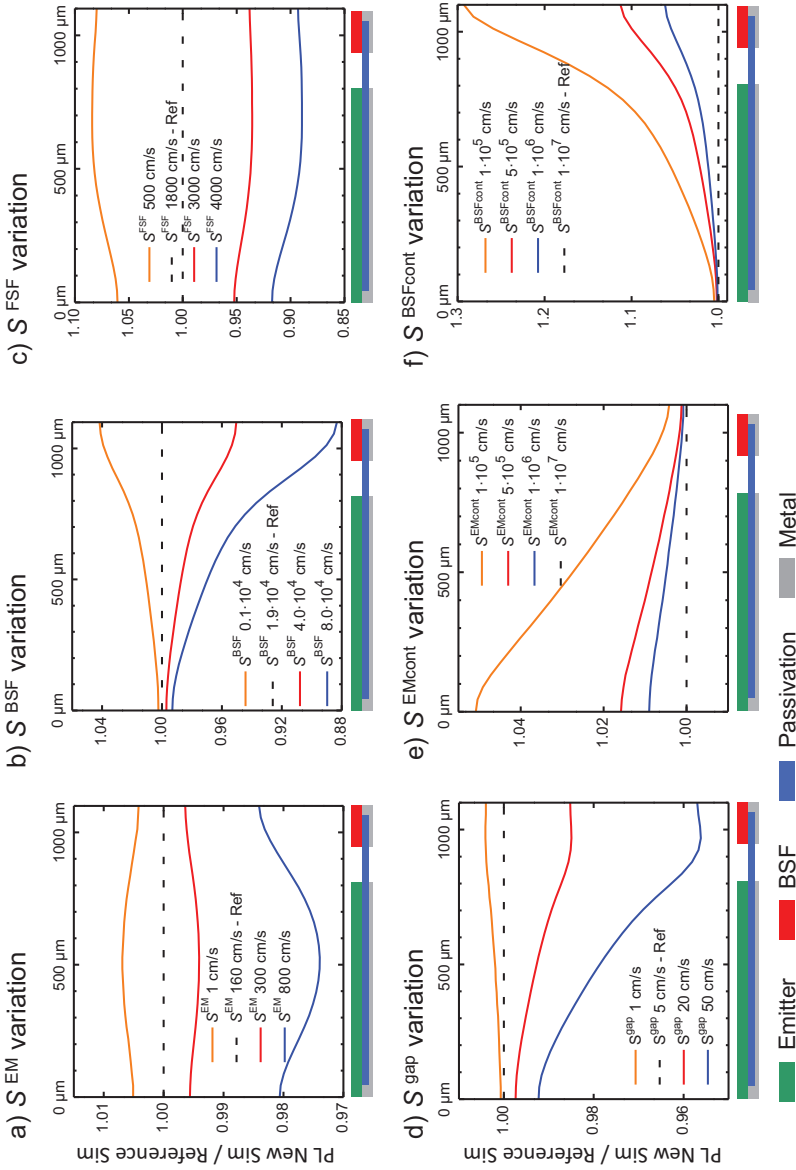


Figure 4.17: Ratio between $PL(x)$ simulations of a variation of surface recombination velocities (solid lines) relative to the reference PL simulation (black dashed line) for the six parameters illustrated in figure 4.16. Every surface recombination velocity, including that of the FSF, has a signature impact of the luminescence profile.

Table 4.1: Values of the surface recombination velocity S_0 and the corresponding J_0 according to EDNA used for the sensitivity analysis for PL(x) profiles in figure 4.17.

	EM	BSF	FSF	gap	EMcont	BSFcont	
Reference	S_0 (cm/s)	$1.9 \cdot 10^4$	$1.8 \cdot 10^3$	5	$1 \cdot 10^7$	$1 \cdot 10^7$	
	J_0 (fA/cm ²)	12	140	29	12	895	2040
Yellow	S_0 (cm/s)	1	$0.1 \cdot 10^4$	$0.5 \cdot 10^2$	1	$1 \cdot 10^5$	$1 \cdot 10^5$
	J_0 (fA/cm ²)	9	36	9	3	605	480
Red	S_0 (cm/s)	300	$4.0 \cdot 10^4$	$3.0 \cdot 10^3$	20	$5 \cdot 10^5$	$5 \cdot 10^5$
	J_0 (fA/cm ²)	15	237	43	46	800	1230
Blue	S_0 (cm/s)	800	$8.0 \cdot 10^4$	$4.0 \cdot 10^3$	50	$1 \cdot 10^6$	$1 \cdot 10^6$
	J_0 (fA/cm ²)	24	407	57	120	835	1550

4.5.2 Matching experiments with simulation data

In the following, experimental and simulated PL profiles across a fault free unit cell near V_{oc} conditions are compared and an attempt to improve their matching through variations of specific SRV values is presented. Improvements in matching can be studied qualitatively through direct comparison and quantitatively by calculating ratios and deviations between simulations and experiments. The smaller the spread of $PL(x)^{sim}/PL(x)^{exp}$, the better the matching.

Figure 4.18 shows pairs of direct comparisons (top graphs) of experimental $PL(x)$ (symbols) and simulated $PL(x)$ (lines) and the ratio between simulation and experiment (bottom graphs). The first pair of graphs (a) shows the result using the reference SRV values obtained from lifetime samples and EDNA. Table 4.2 summarizes the resulting simulated V_{oc} and SRV parameters for the four simulations in figure 4.18. Underlined numbers highlight which SRVs were changed relative to (a). The other graphs of figure 4.18 show the results for a decreased S^{FSF} (b), a decreased S^{EMcont} (c) and finally a set of several changes that was found to lead to an overall improved matching within a reasonable range of SRV values (d). Simulations (b) and (c) are shown to illustrate the effect on matching from a severe change of an SRV value. Since an increase/decrease in any SRV makes the whole simulated signal shift down/up, the axis of the simulated signal in the top graphs was shifted for ease of comparison. The calibration factor $K_{cal,PL}$ from equation 4.5 was kept constant so the ratio graphs are directly comparable.

In the reference comparison of figure 4.18 (a), the intensity over the emitter contact in the simulation is significantly lower than in the experiment. The simulated V_{oc} of 683 mV is slightly higher than the measured one of 680 mV. In (b), S^{FSF} was decreased from 1800 cm/s to 500 cm/s, which corresponds to a decrease in J_0^{FSF} from 29 fA/cm² to 5 fA/cm². The mismatch has increased notably, and there is an overall higher contrast between all regions. The FSF is homogenous across the front side, therefore a decreased recombination leads to a relative increase of the lateral effects from all other SRVs. With an improved FSF, the V_{oc} increases to 688 mV. This greatly exceeds the

Table 4.2: S_0 values used for the simulations in figure 4.18 V_{oc} in the solar cell simulation. The underlined values highlight which parameters have been changed compared the reference.

	V_{oc} (mV)	S^{EM} (cm/s)	S^{BSF} (cm/s)	S^{FSF} (cm/s)	S_{gap} (cm/s)	S^{EMcont} (cm/s)	$S^{BSFcont}$ (cm/s)
Reference 4.18 (a)	683	160	$1.9 \cdot 10^4$	1800	5	$1 \cdot 10^7$	$1 \cdot 10^7$
4.18 (b)	688	160	$1.9 \cdot 10^4$	<u>500</u>	5	$1 \cdot 10^7$	$1 \cdot 10^7$
4.18 (c)	687	160	$1.9 \cdot 10^4$	1800	5	<u>$1 \cdot 10^5$</u>	$1 \cdot 10^7$
4.18 (d)	678	<u>800</u>	<u>$3.0 \cdot 10^4$</u>	<u>3000</u>	5	<u>$1 \cdot 10^6$</u>	$1 \cdot 10^7$

experimentally measured value. It can be concluded that the finished cell does not have a lower FSF recombination activity than expected.

Figure 4.18 (c) shows the effect of improving the emitter-contact S^{EMcont} recombination from $1 \cdot 10^7$ cm/s to $1 \cdot 10^5$ cm/s. This is especially interesting, because of the lack of experimental data for metallized surfaces from test structures. $S_0 = 1 \cdot 10^7$ cm/s is the upper limit for S_0 as it corresponds to recombination of carriers at thermal velocity [13], which is the worst possible interface but which is often assumed since it is valid for e.g. an ohmic contact. Because in the reference simulation, the simulated signal above the emitter contact is also lower than the experimentally observed one, it may be concluded that S^{EMcont} is better than the conservative first assumption of $1 \cdot 10^7$ cm/s. Since V_{oc} also increases to 686 mV, $1 \cdot 10^5$ cm/s is however too low. An equivalent improved matching was not observed when lowering $S^{BSFcont}$ (data not shown).

Finally, (d) shows the result after a manual iterative approach. Here, S^{EM} was increased from 160 cm/s to 800 cm/s (J_0^{EM} from 12 fA/cm² to 24 fA/cm²). S^{BSF} was increased from $1.9 \cdot 10^4$ cm/s to $3.0 \cdot 10^4$ cm/s (J_0^{BSF} from 140 fA/cm² to 190 fA/cm²). S^{FSF} was increased from 1800 cm/s to 3000 cm/s, (J_0^{FSF} from 29 fA/cm² to 43 fA/cm²) and finally S^{EMcont} was decreased from $1 \cdot 10^7$ cm/s to $1 \cdot 10^6$ cm/s (J_0^{EMcont} from 895 fA/cm² to 835 fA/cm²). When normalizing the ratio graphs by their average value, one obtains relative deviations between simulation and experiment. The deviations were

of the order of $\pm 5\%$ in (a), $\pm 6\%$ in (b), $\pm 4\%$ in (c) and are reduced to $\pm 3\%$ in (d).

When discussing the results of this particular example, note that the initial SRVs that were drawn from EDNA and based on lifetime samples already delivered decent agreement between simulation and experiment in the first place. Over the large experimental region of interest that was studied, for cell Fi1 it was found that the emitter, BSF as well as the FSF of the finished cell are worse than predicted by the lifetime samples. Also, the SRV of the emitter metal contact is better than the pessimistic assumption of $1 \cdot 10^7$ cm/s, while further simulations indicate that the BSF metal contact has indeed an extremely high SRV of the order of the thermal velocity of charge carriers.

However, there remains a mismatch between experiment and simulation at V_{oc} that was not eliminated by all attempted SRV variations¹. It is unclear whether this was because the right combination of parameters has not been selected or whether the modeling of the solar cell (i.e. missing injection dependence of the SRV or semiconductor models) or modeling of the luminescence experiments (e.g. the optics) is insufficient. Missing input parameter aspects could include variations of the doping profiles, variations of the surface passivation quality as well as injection dependence of the surface recombination. Also, the doping profiles measured by ECV as well as the fit by analytical functions contain errors. The sensitivity analysis revealed that the PL profile is sensitive to all parameters, which leaves a six-dimensional parameter space for optimizer algorithms to operate on. Section 7.3 presents a brief discussion on challenges of the presented method and how it could be applicable in solar cell R&D and production.

¹A much greater number of simulations than those shown here have been performed.

4.6 Local series resistance imaging

The pursuit of increasingly efficient silicon solar cells has led to cell designs with selective doping areas, point contacts and other advanced structures such as IBC, PERC [178], PERL [179], MWT [180] and EWT [181] silicon solar cells. Optimizing such solar cell concepts towards cheaper, industrial processes, e.g. via larger structures and alternative metallization techniques is related to the challenge of increased series resistance R_s according to the diode model (see section 2.1.3) caused by prolonged current paths, poor local contact resistance and current crowding [182]. The IBC cell design studied in this work serves as an excellent example to study the physical principles of this characterization problem. The conventional PL based local series resistance imaging methods under illumination presented by Trupke et al. [137], Kampwerth et al. [138] and Glatthaar et al. [183] and in the dark by Hinken et al. [140] and Haunschild et al. [141] were developed on standard industrial silicon solar cells with homogeneous front and back side surface doping. There, each pixel in the camera image is modeled as one diode connected directly with the terminal via a local series resistance R_s^{loc} . This section investigates whether the basic methodology of these conventional R_s^{loc} approaches under illumination are applicable to cells with significant lateral carrier transport like IBC cells, where this assumption at first seems inadequate.

4.6.1 Definition, voltage calibration and image interpretation

In this work, series resistance R_s is defined as a power loss mechanism described by the one-diode model. R_s at *MPP* conditions is then measurable as a reduction of global *FF* in the illuminated I-V curve while not affecting the *pFF* of a current-free $\text{Suns-}V_{\text{oc}}$ measurement [184]. This power loss can be caused both by transport losses in the form of joule heat and by recombination. Both loss mechanisms can lead to an increase of $pFF - FF$, and therefore an increase in global R_s . In this context, the terminology of 'majority' and 'minor-

ity' carriers may be deceiving, because IBC cells typically operate at medium or even high injection at *MPP* (see section 2.1.2 and figure 2.3) and consequently, each carrier type may contribute to local and global R_s . R_s^{loc} here is defined in a terminal connected diode model as the effective resistance from an image pixel to the terminal, irrespective of the detailed current paths in the device. The basic equation is

$$V^{\text{loc-imp}} = V_{\text{bias}} - R_s^{\text{loc}} \cdot J^{\text{loc}} ; J^{\text{loc}} < 0 \text{ at } MPP, \quad (4.9)$$

where $V^{\text{loc-imp}}$ is the local implied voltage at the solar cell pn junction side (rear side for IBC cells). This presents a conceptual difference to standard cells with full emitter coverage where a pn junction is present at each pixel. V_{bias} is the bias voltage applied at the terminal and J^{loc} the local effectively extracted current density. The lumped R_s of a solar cell can be described as a superposition of multiple resistances such as sheet- (R_{sh}), contact- (R_c), base- and finger resistance. Kluska et al. [97] and Yang et al. [185] developed analytical models to assess each component's effect on the global R_s of an IBC cell. For PERL cells, which also exhibit significant lateral current flow, Altermatt et al. modeled internal resistance losses [186]. Each charge carrier type experiences a different set of resistance contributions as its current path follows the path of lowest resistance. A schematic of such current paths at *MPP* is shown in figure 4.19 for electrons (a) and holes (b) at *MPP* (see also figure 2.11 for other operating conditions).

Once again, numerical device modeling is employed but this time for qualitative understanding of series resistance imaging because matching between simulations and experiments is not necessary for this method. For this purpose, the solar cell simulator Quokka [17] is used because it allows convenient modification of the decisive parameters R_{sh} and ρ^{base} . Figures 4.19 (c) and (d) show the simulated current densities and current directions (arrows) for electrons and holes. The holes flow essentially vertically towards the collecting p^+ -emitter from where they flow laterally towards the contact openings, while the electrons essentially move laterally via the base or the

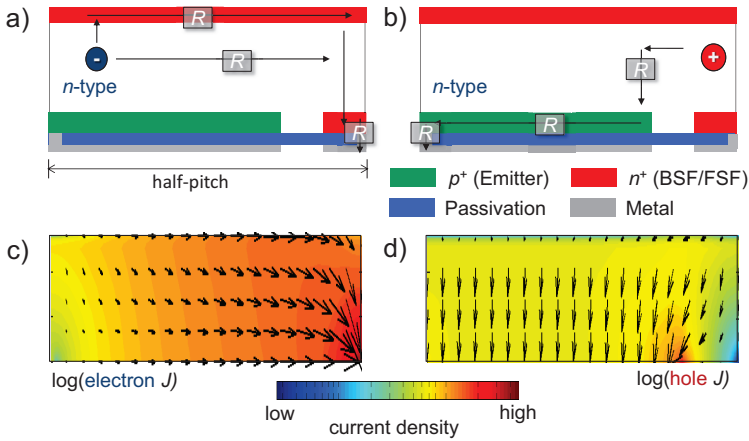


Figure 4.19: Cross section schematic (top) of doping, current paths and resistances of a typical n-type IBC cell at *MPP*. Simulated current densities and directions (bottom) for electrons (c) and holes (d).

n^+ -doped FSF until they reach the BSF. The current directions are different while, according to the quasi-neutrality assumption which is justified outside the space-charge region [17], the local excess carrier density of holes is always the same as of electrons. Finally, the net output currents of electrons and holes must equalize. This creates a complex interdependence between electron and hole current transport which must be kept in mind to understand the effective local series resistance phenomena observed in IBC cells.

Voltage calibration

For quantitative R_s^{loc} imaging, an appropriate calibration of the luminescence images is necessary to relate signals to local voltages. In this work, the voltage calibration used by all conventional methods that was theoretically motivated by Glatthaar et al. [183] and described in section 2.3.1 was applied. The PL image at J_{sc} is subtracted from the PL image at *MPP*. This subtracts the local diffusion-limited excess charge carrier density at J_{sc} since voltage differences from this fraction of excess carrier density relate to variations in J_{sc} but not to

voltage differences due to an increase of local or global R_s . The local voltage at *MPP* is calibrated via

$$V^{\text{loc-imp}} = V_T \left(\ln \text{PL}^{\text{MPP}} - \text{PL}^{J_{sc}} \right) - V_T \ln (C^{\text{loc}}), \quad (4.10)$$

where PL^{MPP} and $\text{PL}^{J_{sc}}$ are the measured PL image counts per second at *MPP* and J_{sc} . C^{loc} is the spatially-resolved calibration constant which relates PL signals to local voltages as presented by Glatthaar et al. [183] and described in section 2.3.1. Carrier profile variations along the depth of the cell are accounted for by the calibration constant as shown in [67]. The simulations of the studied cell designs show that at V_{oc} under 0.1 sun illumination, the lateral voltage variations are negligible (< 5 mV) and the globally measured V_{oc} differs < 2 mV from the mean $V^{\text{loc-imp}}$ at the rear of the cell. These are the assumptions of Glatthaar's voltage calibration. They are also fulfilled for IBC cells, provided that C^{loc} is extracted at sufficiently low irradiation. The final R_s^{loc} image is then obtained by

$$R_s^{\text{loc}} = \frac{V_{\text{bias}} - V^{\text{loc-imp}}}{J_{\text{sc}}^{\text{loc}} - J_0 \exp(V^{\text{loc-imp}}/V_T)}. \quad (4.11)$$

In the conventional methods [137, 138, 183] the local short-circuit current density, $J_{\text{sc}}^{\text{loc}}$ is assumed to be constant which is not necessarily true for IBC cells due to 'electrical shading' (see section 3.5). To include this aspect, an SR-LBIC measurement at 780 nm, directly scaled to match the global J_{sc} , was used for $J_{\text{sc}}^{\text{loc}}$.¹ Since the SR-LBIC maps have a much higher spatial resolution than the PL images, the $J_{\text{sc}}^{\text{loc}}$ images were blurred with 150 μm FWHM Gaussian blurring to resemble the point-spread function (optical blurring) of the PL emission in the cell (see figure 4.12). This modified method is based on Trupke et al.'s work as it evaluates R_s^{loc} directly at *MPP* conditions where R_s^{loc} values are most representative and most relevant. Also, the method by Glatthaar et al. requires two main input images to

¹The 780 nm SR-LBIC wavelength is closest to the 790 nm of the PL laser illumination.

obtain an R_s^{loc} and J_0^{loc} image and thus an additional experimental degree of freedom. R_s evaluations are in practice a function of the operating conditions, as shown e.g. by Fong et al. [147].

Exemplary results and discussion

Experimental results and the images that lead to the final R_s^{loc} image are discussed in the following because they help explain how R_s^{loc} correlates with doping structure, local voltages and extracted current density at *MPP* conditions. Figure 4.20 shows images and averaged line scans over the dashed rectangles when applying the modified Trupke R_s^{loc} method for cell BC4, a 19.6% efficient, 160 μm thick, 10 Ωcm n-type IBC cell with a 1750 μm half-pitch, 83% emitter (EM) coverage and a 150 μm passivated gap, ($R_c < 0.1 \Omega\text{cm}^2$, $R_{\text{sh}}^{\text{EM}} = 19 \Omega/\text{sq}$, $R_{\text{sh}}^{\text{BSF}} = 10 \Omega/\text{sq}$, $R_{\text{sh}}^{\text{FSF}} = 148 \Omega/\text{sq}$ [49]). Figure 4.20 (a) shows that the lateral voltage variation from the calibration image C^{loc} obtained at 0.1 sun is in the range of 2 mV, which can be attributed to differences in surface recombination between p^+ and n^+ doped regions. After voltage calibration of the PL *MPP* image, figure 4.20 (b) shows an offset of about 50 mV in voltage drop caused by R_s^{loc} , which implies that even close to the p^+ or n^+ contact, the local R_s is not negligible. This is in contrast to standard silicon solar cells, where R_s^{loc} is typically negligible next to a metal finger if the grid resistance is negligible. Furthermore, a lateral modulation in voltage drop with 25 mV amplitude is observed, which will be discussed later. The lateral voltage variations in (b) with 25 mV are large compared to the < 2 mV in (a), which further justifies the assumption of laterally constant voltage in the calibration image.

Figure 4.20 (c) shows the local $J_{\text{sc}}^{\text{loc}}$ profile obtained from SR-LBIC measurements, which is dominated by the 'electrical shading effect' from insufficient diffusion length. Figure 4.20 (d) depicts the effectively extracted local current density J^{loc} at *MPP*, which closely resembles the J_{sc} profile in this case. J^{loc} graphs show the magnitude of current density from the photo-generated current that is extracted from each pixel of cell after being subject to recombination

and series resistance losses. The 'electrical shading' loss influences R_s^{loc} via the denominator in equation 4.11. The finding underlines the relevance of a $J_{\text{sc}}^{\text{loc}}$ -map particularly when investigating IBC solar cells. The importance of a $J_{\text{sc}}^{\text{loc}}$ -map for practical purposes will be further discussed in section 6.2 and 7.3. Also, J^{loc} in the area above the p^+ contact is decreased due to the increased voltage caused by R_s^{loc} . This means that R_s^{loc} over the p^+ contact is high enough to reduce the extracted current density. This is surprising, since the region directly over the emitter contact is typically the point of highest $J_{\text{sc}}^{\text{loc}}$ (see section 3.5). The final R_s^{loc} image in (e) has an offset of approximately $1.6 \Omega\text{cm}^2$ and shows lateral R_s^{loc} variations with maxima over the p^+ and n^+ contact regions due to R_s losses in the electron and hole transport respectively. Locally, assuming a constant J_{sc} that is in reality lower leads to an underestimation of R_s^{loc} over the BSF. In cases of extremely high R_s^{loc} that even impacts J_{sc} (R_s^{loc} of the order of $15 \Omega\text{cm}^2$ and greater, see figure 2.5), R_s^{loc} imaging does not yield accurate results as was also noted by Trupke et al. [137].

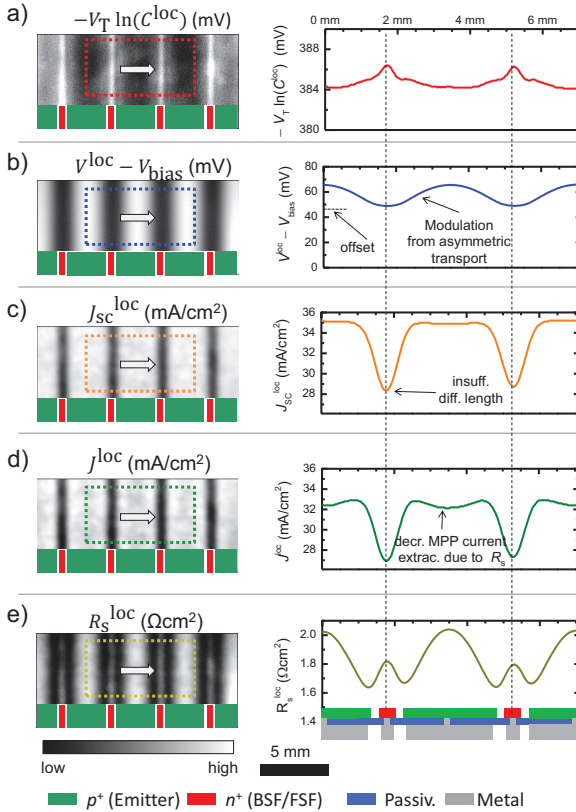


Figure 4.20: Resulting images of the modified Trupke R_s^{loc} method (equation 4.11) on IBC cell BC4 (left) and line scan averages over dotted areas (right): $-V_T \ln(C^{\text{loc}})$ from equation 4.10 (a), local voltage drops caused by series resistance (b), $J_{\text{sc}}^{\text{loc}}$ (c), locally extracted current density J^{loc} and (d) and resulting R_s^{loc} (e).

4.6.2 Lateral transport effects

Pitch variation

The following demonstrates that the lateral R_s^{loc} modulations reflect the lateral electron and hole current transport losses by comparing the measured R_s^{loc} of three cells of different pitch geometries. For this, simulated I-V curves, Suns- V_{oc} curves, luminescence images (calibration, J_{sc} , MPP) as well as the $J_{\text{sc}}^{\text{loc}}$ -map, are obtained using Quokka and subsequent calculations in the software MATLAB [104]. The luminescence imaging model presented in section 4.4 was implemented into Quokka by A. Fell for this purposes and is now publicly available [36]. From those results the R_s^{loc} images are calculated. As input parameters for the simulations, experimentally obtained base lifetime, R_{sh} and J_0 for all surfaces are necessary. The J_{sc} map was simulated from collection probability and generation profiles according to [99]. No additional free parameter fitting was performed to obtain the simulation results. The presented IBC cells are all line-contacted 2D designs but the result interpretation is fully transferable to point-contacted and thus to 3D designs.

Figure 4.21 shows R_s^{loc} images for 10 Ωcm IBC cells with different doping schematics. The half-pitch distances are 1750 μm (a, BC4), 1100 μm (b, BC5) and 650 μm (c, BC6), respectively. Figure 4.21 (d) shows the averaged line scan profiles over the marked areas from experiments (symbols) and simulations (solid lines). Note that simulations are only introduced here because they will assist explaining the electron and hole transport phenomena in the device. The simulated R_s^{loc} profiles are in good agreement with R_s^{loc} offsets and lateral variations. The 1750 μm sample has a higher R_s^{loc} offset and mean level than the 650 μm sample, which correlates with the decreasing difference between pFF and FF from measured Suns- V_{oc} and I-V data (see insets). The R_s^{loc} offset increases because the current path lengths and thus transport losses to the contacts increase for both carrier types with larger half-pitch distances. For the widest pitch, the highest R_s^{loc} is over the emitter contact, whereas for the smallest pitch, the highest R_s^{loc} is over the BSF contact. This means that the

R_s^{loc} contrast is related to lateral transport losses, which flips from being dominated by electron transport for the cell with the wide pitch to hole transport for the cell with small pitch. This effect can be attributed to reduced emitter coverage fraction of the short pitch samples, where holes suffer increased transport losses through the base (high injection). An analogous flip between electron- and hole-limited transport when increasing the half-pitch was also observed for 1 Ωcm material, but with lower offsets and lower lateral contrasts due to higher base conductivity (profiles not shown). However, the profiles do not distinguish which carrier type is responsible for the offset in R_s^{loc} . Section 6.2 show simulations demonstrating that the offset in R_s^{loc} images also relates to contact resistance. Increasing the contact resistance of either p- or n-contact by a given value will result in an identical response of the R_s^{loc} profile in form of an offset increase. This is because the net electron and hole output currents must equalize, so if one net carrier flow is hindered from exiting the cell at the contact, so is the other.

Influence of sheet resistance on transport limitations

The agreement between experimental and simulated R_s^{loc} curves motivates further simulations to better understand the role of electron and hole limited transport in the device. Figure 4.22 shows R_s^{loc} simulations of a 10 Ωcm IBC cell, where exclusively the sheet resistance of the emitter $R_{\text{sh}}^{\text{EM}}$ was varied in (a) and only the front-surface-field $R_{\text{sh}}^{\text{FSF}}$ was varied in (b). Therefore only hole transport is directly influenced in (a) and only electron transport is influenced in (b). The simulated R_{sh} variations only affected the FF , since unchanged surface recombination yielded a constant J_{sc} (39.9 mA/cm^2), V_{oc} (664 mV) and pFF (83.7%). The FF drops as the mean R_s^{loc} increases. Lowering $R_{\text{sh}}^{\text{EM}}$ in (a) decreases losses of the hole-transport through the p^+ -emitter. Between 200 Ω/sq and 20 Ω/sq , a transition from hole- towards electron-transport limited R_s^{loc} is observed. An analogous interpretation can be applied for (b), where the electron transport was influenced by $R_{\text{sh}}^{\text{FSF}}$. Decreasing $R_{\text{sh}}^{\text{FSF}}$ causes a shift from electron- to hole-limited transport.

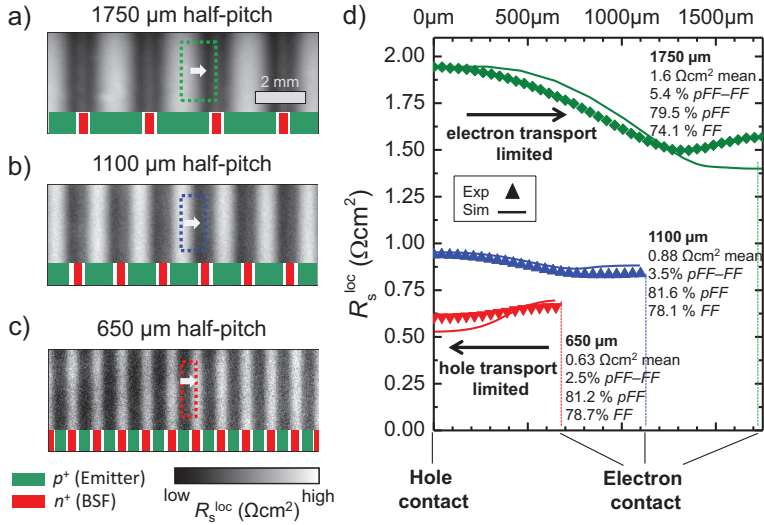


Figure 4.21: Experimental R_s^{loc} images and doping schematics of IBC cells for three half-pitch variations (a-c, BC4-BC6). Averaged line scan profiles from the experimental R_s^{loc} images and simulation results (d). The I-V values in (d) present experimental data.

It is noticeable, that both R_{sh} variations also lead to an increase of R_s^{loc} immediately above the p^+ -contact in (a) and n^+ -contact in (b) (see dotted ellipses), although transport of carriers generated there should not be directly affected by R_{sh} . Further simulations have shown that e.g. increasing $R_{\text{sh}}^{\text{EM}}$ leads to an increased excess carrier gradient through the base and thus change the mean current paths of the device. As a result, there is a higher carrier density at *MPP* above the contacts and thus higher R_s^{loc} according to the used definition of R_s^{loc} . This is yet another manifestation of the complex interdependence of electron and hole current transport. Each carrier flow may contribute to R_s^{loc} but is never fully independent of the other.

Agreement with global values

Finally, averaged R_s^{loc} values from the experimental and simulated images are compared with global values R_s^{global} from I-V curves using the Suns- V_{oc} vs. light-IV method [184]. Arithmetic image averaging

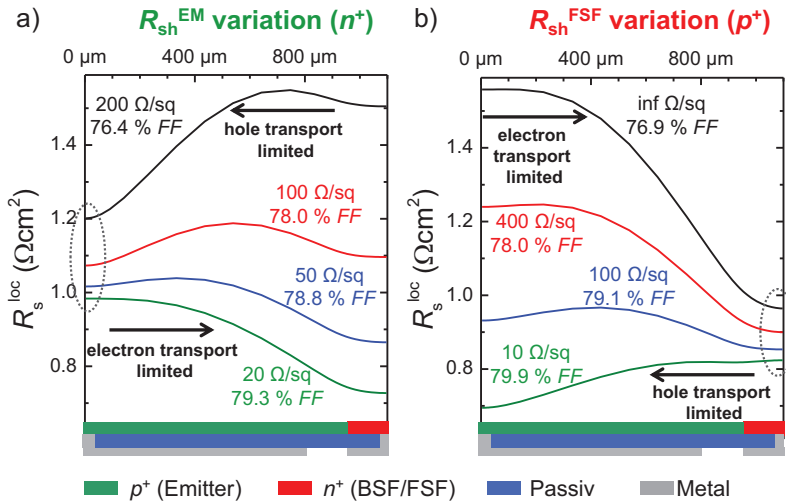


Figure 4.22: Simulated R_s^{loc} profiles for a variation of p^+ -emitter (a) and n^+ -front-surface-field (b) sheet resistances at constant surface recombination. Transitions between electron- and hole-transport limitations are observed.

was chosen in accordance with [144]. In practice, R_s^{global} is a function of the operating conditions of the measurement [147]. Note that as shown by Pysch et al. [39], different R_s^{global} methods can produce significantly different results. The Suns- V_{oc} vs. light-IV method [184] was chosen here, because of its low sensitivity to current measurement errors. All I-V measurements were performed using the same setup and 790 nm irradiation as for the PL imaging. Figure 4.23 summarizes the results for a set of 1 Ωcm and 10 Ωcm 4 cm^2 IBC cells with the 650 μm , 1100 μm and 1750 μm half-pitch [49] in experiments (triangles) and simulations (crosses). The solid lines serve as a guide to the eye for the simulations. The trends in the experiment are well reproduced by the simulations and the absolute simulated deviations between R_s^{global} and R_s^{loc} mean are $< 30\%$ for the smallest pitch and $< 5\%$ for the largest pitch. The simulations are free of current or voltage measurements errors but show similar discrepancies between R_s^{global} and R_s^{loc} mean as the experiments. This must be an effect intrinsic to the methods and subject for future investigations.

Here, R_s^{loc} mean is always higher than R_s^{global} . The inclusion of a simulated $J_{\text{sc}}^{\text{loc}}$ map had a negligible impact on the R_s^{loc} mean since the $J_{\text{sc}}^{\text{loc}}$ map predominantly impacts the image contrast.

All R_s^{loc} analysis thus far was performed to understand R_s^{loc} patterns of fault free IBC cells. Section 6.2 treats local series resistance effects caused by processing faults. A brief summary of this chapter is presented in chapter 8.

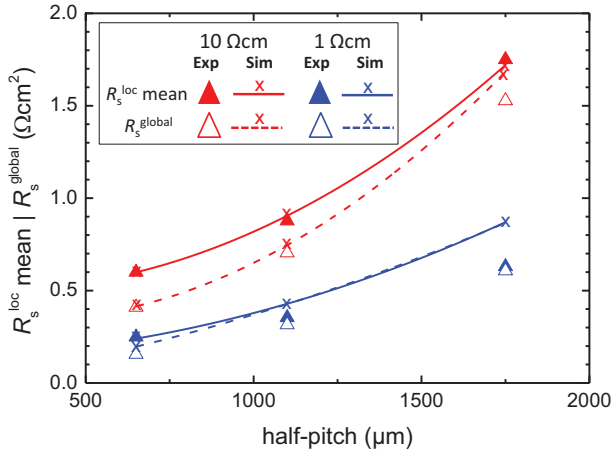


Figure 4.23: Experimental and simulated comparison of globally extracted and arithmetically image-averaged series resistances for IBC solar cells with varying pitch and base resistivity.

Chapter 5

Lock-in thermography of local cell characteristics

This chapter deals with the understanding and use of dark and illuminated lock-in thermography (LIT) for the spatially resolved characterization of IBC cells. LIT in the dark and under illumination detects local power density as opposed to PL imaging which detects local charge carrier density. This makes LIT yield complimentary information to luminescence imaging in solar cell analysis. For IBC cells however, the interpretation of contrast patterns using LIT is more complex than luminescence imaging and also more complex than for conventional cells due to the Peltier effect and the geometrical shape of the heat sources.

After a literature overview of LIT for silicon solar cell analysis in section 5.1, details on the experimental setup as well as considerations on emissivity and spatial resolution in the context of IBC cells are presented in section 5.2. To understand how power density in an IBC unit cell is distributed, section 5.3.1 introduces numerical modeling of spatially resolved power using equations for free-energy loss

analysis adapted to consider all Peltier components occurring within an IBC solar cell. By switching the Peltier effect on and off in the model, conclusions on the consequences of the Peltier effect in LIT are made in section 5.3.2. Based on this knowledge and theoretical considerations, section 5.4 presents experimental LIT results and attempts to interpret the patterns observed. Applications of LIT for shunt detection induced by processing faults, in particular pinholes and spikes, are presented in chapter 6.

The free-energy loss and Peltier model in this chapter was developed in collaboration with M. Selinger in the scope of her Master's thesis under supervision of the author [187]. Support with the implementation of the model using data from the program Quokka was provided by A. Fell.

5.1 Literature overview

This section provides an overview of lock-in thermography for silicon solar cell analysis and sets the context for the study of IBC cells in this chapter. The physical principles of lock-in thermography are detailed in section 2.3.2.

First attempts to applying lock-in thermographic on silicon solar cells were published by Breitenstein et al. [188] in 1994 who placed a temperature sensor over the cell on an xy-stage. Later, Rappich et al. presented temperature difference images of a crystalline silicon solar cell using a bolometric camera [189]. O. Breitenstein has since continuously published numerous works on applications of camera based lock-in thermography for silicon solar cell analysis and established this characterization approach in the photovoltaics community. Important discussions on the LIT theory, experimental implementation and specifics to solar cells were published in a textbook by Breitenstein et al. in 2003 [190] and in a revised edition in 2010 [70].

Lock-in thermography was the first relatively fast, contactless,

non-destructive imaging technique for solar cell analysis¹. Since 2005, the appearance of luminescence imaging (see section 4.1) has gradually rendered several LIT based characterization methods obsolete. Over the past decade, LIT and luminescence imaging have competed over being the 'best imaging technique' for solar cell characterization and the question was raised by Breitenstein et al.: 'Can luminescence imaging replace lock-in thermography' [122]. Several investigations by Breitenstein et al. determined that each technique has its strengths and weaknesses in quantitative analysis [145]. However, the mainstream photovoltaics community has adopted luminescence imaging as the primary technique due to its typically superior resolution and speed to analyze many common problems. For the detection of ohmic shunts as well as hot spots in module operation however, thermography remains the most widely used approach today [191].

Technical improvements of the technique were achieved over time. Kasemann et al. proposed a practical method to determine images of local emissivity factors to correct for e.g. the low emissivity of metal fingers in solar cells [192]. In order to increase the spatial resolution of LIT, which is blurred from thermal wave propagation, Straube et al. developed a theory for deconvolution of solar cell LIT images [193], which is commercially available as the software tool DECONV [194]. Straube et al. proposed a method for experimentally determining the Peltier coefficient in a solar cell pn junction using test structures [42].

Use of illuminated lock-in thermography

On the wafer level, measurements with a lock-in thermal camera system were first introduced to allow spatially resolved analysis of local effective minority carrier lifetime with competing methods named carrier density imaging (CDI) by Riepe et al. [195] and infrared lifetime mapping (ILM) by Bail et al. [174, 196]. Both methods have become obsolete because of the superior accuracy and spatial resolution of lifetime-calibrated photoluminescence imaging a few years later [61].

¹e.g. SR-LBIC or Corescan are considering mapping techniques and not imaging techniques.

Illuminated lock-in thermography (ILIT) for the analysis of local power losses in silicon solar cells was introduced by Isenberg et al. [107, 197]. Isenberg et al. [198] and Breitenstein et al. [199] further proposed using ILIT for series resistance imaging, which was also soon made obsolete by the more reliable luminescence based imaging methods [122, 137]. Kwapil et al. [200] demonstrated applications of ILIT for analysis of industrial silicon solar cells. Breitenstein published a comparison between DLIT and ILIT for conventional silicon solar cells in [201]. Other applications of ILIT was the excitation at different wavelengths to detect shunts in top and bottom layers of thin film tandem solar cells by Straube et al. [202].

Use of dark lock-in thermography

For solar cell analysis, a major motivation for the development of dark lock-in thermography (DLIT) was the desire to detect local shunts. DLIT was discovered to be highly sensitive to shunts [203–206] and individual parallel resistances of shunts could be determined [9]. Breitenstein et al. and Langenkamp et al. distinguished between various types of shunts, depending on the LIT signal as a function of bias voltage in the dark [207, 208]. To this day, DLIT analysis remains the most reliable imaging method for ohmic shunt detection in solar cells and shunt detection at timescales required for industrial in-line application has been achieved [209].

Breitenstein further extended the use of DLIT for quantitative imaging of local solar cell parameters in a two-diode model [210]. He developed a commercially available software named 'Local I-V' and 'Local I-V 2' for this purpose [211]. By acquiring four DLIT images at different bias voltages, fitting algorithms in the software determine J_{01} , J_{02} , R_p and the local ideality factor n_2 at each camera pixel. An additional image of R_s^{loc} and $J_{\text{sc}}^{\text{loc}}$ obtained by other imaging/mapping methods can be included. Assuming the superposition principle between dark and illuminated solar cell operation [212], the local I-V parameters of the cell under illumination can also be determined [213].

IBC cells and context of this work

This work presents the first study of lock-in thermography on IBC solar cells. The IBC cell structure makes the Peltier effect a non-negligible artifact, which has not been previously addressed in LIT literature. This chapter uses simulations to better understand the relation between local power densities and obtained lock-in thermography images in view of the Peltier effect. Current flow under illumination in IBC cells is very different from the dark (see figure 2.11). This renders analysis of regular IBC patterns in the dark ineffective, for which Local I-V was originally developed. The use of LIT for local shunt detection however proves to be well applicable also on IBC cells, which is presented in section 6.3.

5.2 Experimental setup, emissivity and spatial resolution

The physical principles of lock-in thermography for silicon solar cell analysis were presented in section 2.3.2. In analogy to the previous two chapters, details on the experimental setup and experimental considerations are presented in the following.

Experimental setup

The used LIT setup is a custom-made state-of-the-art product developed by the company IRCAM GmbH [214], in collaboration with members of Fraunhofer ISE including the author of this work. A schematic of the setup is shown in figure 5.1. The infrared camera has an InSb based MWIR FPA detector which is sensitive to IR radiation between $1.5 \mu\text{m}$ and $5 \mu\text{m}$ and is cooled by a stirling motor for enhanced SNR with an NETD $< 20 \text{ mK}$. All thermal radiation is a function of wavelength. Only spectrally integrated signals are used in LIT. Since in this work, all measurements are conducted near $25 \text{ }^\circ\text{C}$, no further consideration of spectral dependencies for LIT emission signals are made. At full resolution of 640×512 pixel the maximum

frame rate is 350 Hz. By reading out only a limited number of horizontal pixel lines from the detector, frame rates of several thousand Hz are possible. Typically, 512 x 512 pixel images are used since most silicon solar cells are square or pseudo-square shaped. The maximum frame rate of the IR camera limits the lock-in frequency $f_{\text{lock-in}}$ of the LIT measurement. Variable MWIR optimized lenses can be mounted depending on the desired frame size and resolution in μm per pixel. The camera acts as the master trigger for timing the periodic electrical and optical excitation of the cell via a trigger box.

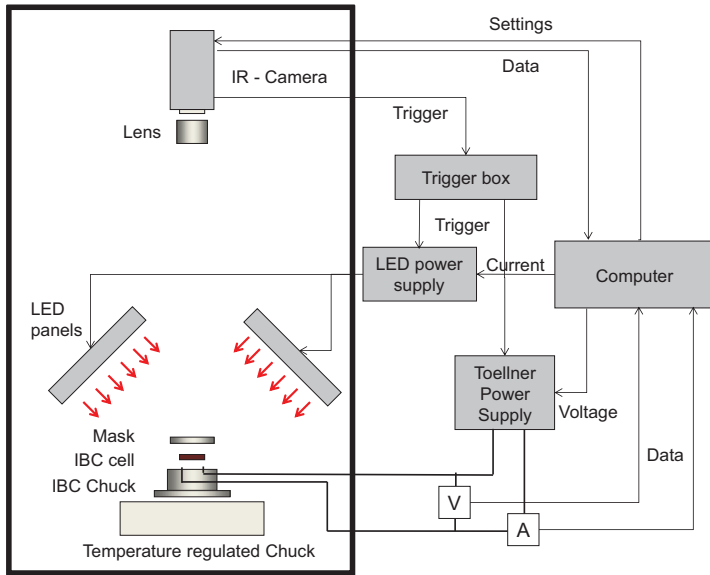


Figure 5.1: Schematic of the experimental lock-in thermography setup. The IR camera sends the trigger signals for periodic excitation of the solar cell by the electrical power supply and the LED panels. Two multimeters measure current and voltage at a given excitation in a steady state condition before and after the lock-in measurement.

The conventional LIT theory for solar cells requires that on/off switching of the applied excitation of the cell occurs on a much faster time scale than the lock-in period [70], such that the heating of the cell occurs under electrically quasi steady state conditions. The electrical voltage bias excitation is performed by a Toellner TOE7621

four-quadrant power supply. Typical settings yield rise-times¹ of $\sim 250 \mu\text{s}$. The optical excitation occurs via two panels which incorporate arrays of commercially available LEDs that emit at a peak wavelength of 470, 655 or 940 nm radiation. The wavelengths can be combined if desired and the maximum excitation power per wavelength is approximately 1 sun. The heat radiation of the LEDs is blocked by plexiglass in front of the panels. The inhomogeneity of the optical excitation is estimated to be $< 1\%$ for 4 cm^2 sized cells investigated in this work. The rise-times to full power of the LEDs is about $15 \mu\text{s}$. At a rather high $f_{\text{lock-in}}$ of 60 Hz the time during which excitation is active in a lock-in period is $8300 \mu\text{s}$ so electrical and optical excitation occurs sufficiently fast to assume quasi steady state conditions in the solar cell. The cell current at a given bias voltage is measured at the beginning and end of the measurement in the steady state by two Agilent 34450A multimeters.

The electrical contacting of the investigated 4 cm^2 IBC solar cells and the temperature regulated chuck is the same as the one used for luminescence imaging (see section 4.2). Good thermal contact between the IBC contacting unit and the temperature regulated chuck is required to allow stable conditions during the LIT measurements. Furthermore, the software allows recording of videos and has a scripting functionality to allow automated measurement sequences.

Emissivity

The emissivity ε is a factor between 0 and 1 that describes how closely a body or surface behaves to a black body (BB) in absorbing and emitting IR radiation [71]. Kasemann et al. published a method to obtain absolute and relative emissivity images of solar cells and thus correcting for this factor in the post processing of LIT results [192]. For conventional solar cells, this allows correcting for the low thermal signals of front side metal finger and busbar metallization and thus accurately detecting the thermal signal underneath the metal.

¹The time in which the output increases/decreases between an initial and 90 % of a desired value.

Although IBC cells lack front side metallization, emissivity contrasts are also present. This effective emissivity contrast is caused by the structured doping densities in the cell. Figure 5.2 shows individual thermographic images of four IBC cells placed sun-side up on the temperature regulated copper chuck that is set to 20 °C (a), 22.5 °C (b) and 30 °C (c). The contrasts increase the more the cell temperature T_{cell} varies from the ambient temperature T_{amb} . The contrasts are caused by free-carrier absorption and emission (FCA/FCE) in the heavily doped areas of the silicon [107, 174]. A higher density of free charge carriers yields a higher absorption coefficient $\alpha(\lambda)$ for thermal radiation if $T_{\text{cell}} < T_{\text{amb}}$. This implies that if $T_{\text{cell}} > T_{\text{amb}}$, the free carriers emit thermal radiation. The depth integrated doping density determines the concentration of free carriers so more heavily doped areas absorb/emit IR radiation more than lightly doped areas¹. The cell on the bottom right corner shows square shaped BSF regions although the metallization consists of lines. This proves that the contrast is not caused by the metallization on the rear side.

The emissivity correction procedure introduced by Kasemann et al. is applied IBC cells in the following. The method works by using images at two different cell temperatures $S^{\text{loc}}(T)$ and images of a black body $S_{\text{BB}}(T)$ at two temperatures T_1 and T_2 . The equation

$$\varepsilon^{\text{loc}} = \frac{S^{\text{loc}}(T_2) - S^{\text{loc}}(T_1)}{S_{\text{BB}}(T_2) - S_{\text{BB}}(T_1)}, \quad (5.1)$$

yields the local emissivity ε^{loc} of each pixel with $T_2 > T_1$ as shown in figure 5.2 (d) using images (a) and (c). This requires though that T_1 and T_2 are well-known and must be the same in the solar cell and black body images. If no black body is available or the accurate absolute temperature of the cells is unknown, also the relative emissivity [192]

¹The absolute absorption coefficient depends also depends on the doping type, hence whether electrons or holes are the free-carriers.

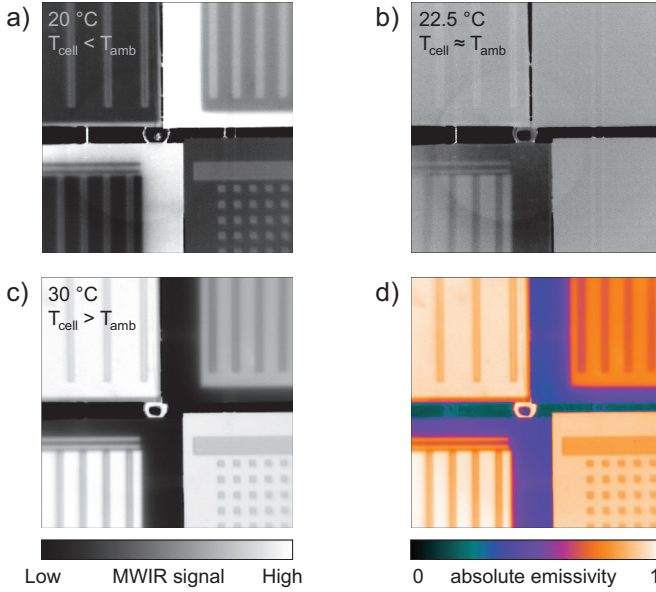


Figure 5.2: IR images of four different IBC solar cells placed sun-side up on a chuck at varying temperatures (a-c). The image contrasts are caused by emissivity differences between the doped regions in the silicon, as a function of the difference between cell and ambient temperature. The absolute emissivity image was calculated via equation 5.1 using images (a) and (c) and reflects the doping density of the different regions.

$$\epsilon_{\text{rel}}^{\text{loc}} = \frac{\epsilon^{\text{loc}}}{\langle \epsilon^{\text{loc}} \rangle} = \frac{S^{\text{loc}}(T_2) - S^{\text{loc}}(T_1)}{\langle S^{\text{loc}}(T_2) - S^{\text{loc}}(T_1) \rangle} \quad (5.2)$$

can be used which only requires calculating the mean value of $\langle S^{\text{loc}}(T_2) - S^{\text{loc}}(T_1) \rangle$. Lock-in thermography images can thus be corrected using [192]

$$S_{\text{corr}}^{\text{loc}} = \frac{S_{\text{raw}}^{\text{loc}}}{\epsilon_{\text{rel}}^{\text{loc}}}, \quad (5.3)$$

at each pixel. In this work all LIT images have been corrected using relative emissivity (equation 5.2). From the experience of the

author, the quantitative impact of doping related emissivity contrasts for IBC cells is much lower than from front side metallization of conventional cells but can still be significant in some cases.

Spatial resolution

The spatial resolution of LIT measurements is a more complex topic than for luminescence imaging, because it is not only influenced by the solar cell device physics and the emission/detection optics but also by the measurement parameters, mainly the lock-in frequency $f_{\text{lock-in}}$. As presented in section 2.3.2, the temperature spread of heat sources can be characterized by a thermal diffusion length Λ . Lower lock-in frequencies give the sample more time to heat up but also more time for that heat to spread. This presents a fundamental trade-off between SNR and spatial resolution in LIT. The optical resolution of the lenses in the used measurement setup ranges from 300 μm per pixel for 15.6 cm cell edge length to 39 μm per pixel for 2 cm wide cells down to 7.5 μm per pixel using a 1 : 2 micro optics lens.

5.3 Local power dissipation and Peltier effect modeling

This section introduces the equations used to calculate local power density from device simulations of an IBC cell, in particular under consideration of the Peltier effect (see section 2.1.4). The motivation behind this is to understand the heat sources and drains that are later interpreted in power calibrated -90° LIT images.

The free-energy loss analysis (FELA) developed by Brendel et al. [215] splits losses in solar cell operation into recombinative and resistive components and quantifies these as dissipated power densities in units of mW/cm^2 . This approach of calculating globally dissipated power density contributions seems suitable to be used to describe local effects observed from -90° LIT images, since the signal is in theory directly proportional to dissipated power [70]. However, it will be shown that the Peltier effect, which is not a concern for global

data [215] and for LIT on conventional solar cells with vertical current flow, presents a significant influence for the local power loss study of IBC cells.

Section 5.3.1 introduces the basic equations used in the numerical modeling, lists the ten different Peltier contributions inside a typical IBC cell and the practical implementation of Peltier coefficients in the model. Section 5.3.2 presents power balance data and details the magnitude of the Peltier effects at all relevant operating conditions. Finally, a spatially resolved analysis of calculated local power density line scans with and without consideration of the Peltier effect demonstrates how the effect may influence LIT data interpretation.

5.3.1 Simulation model

The following calculations use spatially resolved results from Quokka simulations as inputs. Table 5.1 lists the equations for the local power density calculations (in units of mW/cm^2) for the two models presented in this work. The column 'Model A: Free-energy loss' lists the FELA equations for thermalization, Joule heating and recombination before integration. Note that all values Φ_{Fn} , R_{SRH} , G etc. indicate spatially resolved values in a three-dimensional solar cell. Since mW/cm^2 is the typical unit of power density losses in solar cells and also lock-in thermography can only be calibrated power density per surface area, integrals or average values over the cell thickness d are displayed in table 5.1. The column on the right 'Model B: Including Peltier effect' shows the same equations but stating the released energy during a recombination event as the product of the recombination rate R with $E_{\text{g,eff}}$ instead of just $\Phi_{Fn} - \Phi_{Fp}$. Also the energy released during thermalization is proportional to $E_{\gamma} - E_{\text{g,eff}}$ instead of $E_{\gamma} - (\Phi_n - \Phi_p)$. The physical reality of a thermalization process in a semiconductor is that excess charge carrier energy dissipates via inelastic electron/hole-phonon scattering until the charge carrier reaches the conduction/valence band edge [41]. The carriers

do not relaxate until reaching the quasi-Fermi levels.¹ Both electrons and holes may recombine in different parts of the solar cell than they were generated in.

Table 5.1: Equations for power density sources (in units mW/cm²) in a solar cell. Model A describes heat sources according to FELA and Model B shows the locally actually released energy during recombination and thermalization.

Power density term (mW/cm ²)	Model A: Free-energy loss	Model B: Considering Peltier effect
Thermalisation : Q_{th}	$\int_0^d G(E_\gamma - (\Phi_n - \Phi_p)) dz$	$\int_0^d G(E_\gamma - E_{g,\text{eff}}) dz$
Joule : Q_{Joule}	$\frac{1}{d} \int_0^d \frac{ \vec{J}_n ^2}{qn\mu_n} + \frac{ \vec{J}_p ^2}{qp\mu_p} dz$	$\frac{1}{d} \int_0^d \frac{ \vec{J}_n ^2}{qn\mu_n} + \frac{ \vec{J}_p ^2}{qp\mu_p} dz$
Recombination in base : $Q_{\text{rec,base}}$	$\int_0^d R(\Phi_{Fn} - \Phi_{Fp}) dz$	$\int_0^d R \cdot E_{g,\text{eff}} dz$
Recombination at surfaces : $Q_{\text{rec,surf}}$	$R_{\text{SRH,surf}} (\Phi_{Fn} - \Phi_{Fp})$	$R_{\text{SRH,surf}} \cdot E_{g,\text{eff}}$
Peltier in base : $Q_{\text{Pel,base}}$	n/a	$\frac{1}{d} \int_0^d \vec{J}_{n/p} \vec{\nabla} \Pi dz$
Peltier at interfaces : $Q_{\text{Pel,int}}$	n/a	$\vec{J}_{n/p} (\Pi_2 - \Pi_1)$

As explained in section 2.1.4, when e.g. electrons flow from an n base to a p^+ emitter, energy is taken locally from the crystal and thus local cooling occurs. Upon later recombination, the full energy across the bandgap is released. The Peltier effect is a physical reality in a semiconductor device that does not affect the total power balance but does affect the locally released power densities i.e. heating and cooling in a solar cell. The Peltier effect across a material interface can be described by the difference in Peltier coefficients $\Pi_2 - \Pi_1$. Inside an extended area such as the base, a gradient in Peltier coefficient

¹Note that this model for recombination and thermalization is also an approximation though, since the Fermi-distribution and the particles kinetic energy prohibits that all carriers are exactly located at the band edge.

$\vec{\nabla}\Pi$ may also lead to Peltier heating/cooling.¹ Note that quasi-Fermi levels and Peltier coefficients are defined in units of eV in this work.

All Peltier contributions in an n-type IBC solar cell

Figure 5.3 illustrates the ten electron and hole currents where Peltier effects may be relevant in a typical n-type IBC cell with p^+ emitter, n^+ BSF, n-type FSF and line metal contacts (met). The electron and hole current flow directions in the band diagram are depicted for operation under forward bias in the dark as it is the simplest case to follow. Each current component bears an ID number from 1 to 10 for later reference. The Peltier heating or cooling at each interface of currents 1 through 8 is proportional to the difference between the Peltier coefficients between each side of the interfaces. All coefficients are indicated next to the band diagrams in figure 5.3. Currents 7 and 8 reflect base-FSF currents which can have a changing direction along the unit cell and thus cool in one area and heat in another. To be more in line with typical band-diagrams, the nomenclature p^+, n^+ was preferred here to 'emitter' or 'BSF' respectively. The nomenclature of the Peltier coefficient is

$$\Pi_{\text{min/maj,n/p}}^{\text{region}} \quad (5.4)$$

The majority Peltier coefficients Π_{maj} for various peak doping densities in silicon can be extracted from analytical models in literature [12] as a function of base doping density or peak doping density of diffused surfaces. The minority carrier Peltier coefficients are a function of $\Phi_{Fn} - \Phi_{Fp}$ at the interface and hence of the operating conditions as in equations 2.48 and 2.49.

¹Such a gradient could be caused by gradients of quasi-Fermi level in a solar cell (see equation 2.48) or gradients in doping across a thick piece of silicon.

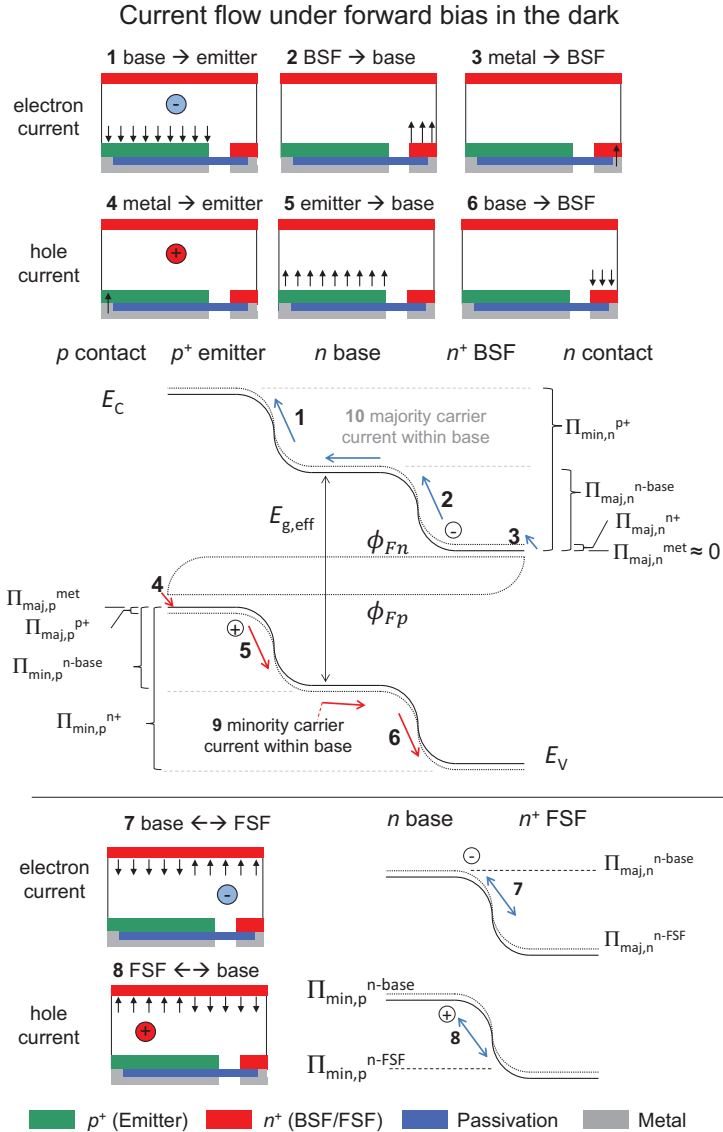


Figure 5.3: Schematic of all ten current flows in an n-type IBC solar cell that can induce local Peltier heating or cooling during operation. The arrows indicate the current direction under forward bias in the dark.

Currents 9 and 10 describe minority and majority carrier flow in the bulk. When calculating the Peltier power density for these contributions $Q_{\text{Pel,base}} = \vec{J}_{n/p} \vec{\nabla} \Pi$, one obtains for current 10

$$Q_{\text{Pel,n}}^{\text{n-base}} = \vec{J}_n \vec{\nabla} \Pi_{\text{maj,n}}^{\text{n-base}} \approx 0, \quad (5.5)$$

because there is no significant gradient $\vec{\nabla} \Pi_{\text{maj,n}}^{\text{n-base}}$ in a homogeneously doped base under the assumption of moderate injection conditions. Using equations 2.48, 2.49, 2.14 and $\vec{\nabla} E_{\text{gap,eff}} \approx 0$, it follows for the minority carrier current 9

$$Q_{\text{Pel,p}}^{\text{n-base}} = \vec{J}_p \vec{\nabla} \Pi_{\text{min,p}}^{\text{n-base}} \approx \vec{J}_p \vec{\nabla} (\Phi_{Fn} - \Phi_{Fp}) \approx -\vec{J}_p \vec{\nabla} \Phi_{Fp} = -\frac{|\vec{J}_p|^2}{qp\mu_p}, \quad (5.6)$$

which is negative and opposite to the Joule heat contribution of the minority carriers in the base. This means that Peltier cooling by holes flowing in the base in a first approximation cancels out the hole component of the Joule heat in the base.

All resulting Peltier coefficient differences for the ten currents are summarized in table 5.2. The majority Peltier coefficients of the metal contacts $\Pi_{\text{maj,n}}^{\text{met}}$ and $\Pi_{\text{maj,p}}^{\text{met}}$ are < 1 meV at 300 K and hence negligible [42]. As mentioned in section 2.1.4, all Peltier coefficients were defined to be positive and in units of eV in this work. The sign before $\Pi_2 - \Pi_1$ was set in order to fulfill the condition that all Peltier effects in the dark lead to cooling ($Q_{\text{Pel}} < 0$) [70]. If the current flows in the opposite direction, this is then correctly interpreted as Peltier heating ($Q_{\text{Pel}} > 0$). The necessary spatially resolved current densities through the interfaces and quasi-Fermi levels Φ_{Fn} and Φ_{Fp} before and after the interfaces are extracted from Quokka simulations at the desired operating conditions. Table 5.2 also lists under which operating conditions the Peltier effect will lead to local cooling, heating or whether both is possible (see results section 5.3.2 for confirmation). Whether a contribution is heating or cooling under il-

lumination depends on the net current flow direction. Under certain surface recombination parameters, small Peltier contributions could also switch from 'cool' to 'heat' in certain cell designs. A set of four Π_{maj} coefficients for the base, emitter, BSF and FSF is sufficient as input parameters to transfer the simulation of local power densities from model A to model B in table 5.1. Current 10 is omitted in the rest of this work, as it yields no relevant contribution for the investigated solar cells.

Table 5.2: List of the Peltier coefficients between all interface and base currents in an n-type IBC cell as depicted in figure 5.3 to numerically calculate the local Peltier heating or cooling. The right columns stating ‘cool’ or ‘heat’ at the key operating conditions are results from numerical simulations made in this work, presented in table 5.5.

ID	Type	Interface	$\Pi_2 - \Pi_1$ (interface) or $\vec{\nabla}\Pi$ (base)	dark	J_{sc}/MPP	V_{oc}
1	electron	base - emitter	$E_{g,eff} - (\Phi_{Fn} - \Phi_{Fp}) - \Pi_{maj,p}^{p+} - \Pi_{maj,n}^{n-base}$	cool	cool	cool
2	electron	BSF - base	$\Pi_{maj,n}^{n-base} - \Pi_{maj,n}^{n+}$	cool	heat	heat
3	electron	metal - BSF	$\Pi_{maj,n}^{n+} - \Pi_{maj,n}^{met} \approx \Pi_{maj,n}^{n+}$	cool	heat	heat
4	hole	metal - emitter	$\Pi_{maj,p}^{p+} - \Pi_{maj,p}^{met} \approx \Pi_{maj,p}^{p+}$	cool	heat	heat
5	hole	emitter- base	$E_{g,eff} - (\Phi_{Fn} - \Phi_{Fp}) - \Pi_{maj,n}^{n-base} - \Pi_{maj,p}^{p+}$	cool	heat	heat
6	hole	base - BSF	$\Pi_{min,p}^{n+} - \Pi_{min,p}^{n-base} = \Pi_{maj,n}^{n-base} - \Pi_{maj,n}^{n+}$	cool	cool	cool
7	electron	base - FSF	$\Pi_{maj,n}^{n-base} - \Pi_{maj,n}^{n-FSF}$	both	both	both
8	hole	FSF - base	$\Pi_{min,p}^{n-base} - \Pi_{min,p}^{n-FSF} = \Pi_{maj,n}^{n-base} - \Pi_{maj,n}^{n-FSF}$	both	both	both
9	hole (min)	within base	$\vec{\nabla}(\Phi_{Fn} - \Phi_{Fp}) \approx \vec{\nabla}\Phi_{Fp}$	cool	cool	cool
10	electron (maj)	within base	$\vec{\nabla}\Pi_{maj,n}^{n-base} \approx 0$	n/a	n/a	n/a

5.3.2 Modeling results and consequences for LIT

In this subsection, modeling results for sample IBC solar cell BC2 are presented. The cell with 1 Ωcm base resistivity is from the same batch as the one discussed and modeled using Quokka in section 4.6. All relevant input parameters can be found there or in appendix A. A 1 sun equivalent generation profile at 940 nm was used this time, as this is the standard excitation wavelength for ILIT in this work. E_γ is thus 1.32 eV. Arbitrary excitation spectra and generation profiles can be used but the local thermalization power in table 5.1 must be accordingly wavelength dependent. The majority carrier Peltier coefficients obtained from analytical models in literature as a function of doping density are listed in table 5.3. Doping of a surface is always a profile $N_{\text{dop}}(z)$ but only the peak doping density is relevant for the Peltier coefficient since the doping profile is typically less than 3 μm deep.

Table 5.3: Peltier coefficients for silicon taken from analytical models from literature [12, 43] as inputs for the local power density simulation of cell BC2. 'var' indicates minority carrier Peltier coefficients which are a local function of operating conditions (equations 2.48, 2.49).

	emitter	base	BSF	FSF
doping type	p^+	n	n^+	n^+
peak N_{dop} (cm^{-3})	$2 \cdot 10^{19}$	$5 \cdot 10^{15}$	$7.3 \cdot 10^{19}$	$4.7 \cdot 10^{18}$
Π_n (eV)	var	280	80	120
Π_p (eV)	95	var	var	var

Power balance and Peltier contributions

Before proceeding with spatially resolved analysis of all heat sources and drains, a power balance is made to verify that the sum of all powers equals the net power that dissipates inside the cell. Table 5.4 compares the main power contributions after all calculations for conditions of 680 mV forward bias in the dark and under 1 sun illumination at J_{sc} , MPP , and V_{oc} conditions. Figure 5.4 yields a graphical presentation of these values. All values are in units of mW/cm^2 .

$P_{\text{gen}} = qE_{\gamma} \int G(z)dz$ is the integrated power of the photon flux penetrating the cell. $Q_{\text{elec}} = V_{\text{bias}} \cdot J_{\text{ext}}$ is the total electrical power dissipated in or extracted from the cell. $Q_{\text{net}} = P_{\text{gen}} + Q_{\text{elec}}$ is the net power dissipation in the cell. The signs adapt automatically as a function of current extraction or injection (negative/positive J).

Next the integrated dissipative power densities are calculated using the equations of model A in table 5.1 for thermalization Q_{th} , Joule Q_{Joule} and recombination heat Q_{rec} .¹ The sum of these three components is $Q_{\text{tot}}^{\text{FELA}}$. Respectively for considering the Peltier effect in model B of table 5.1 with the sum of all Peltier heat sources/drains Q_{Pel} .² Q_{Joule} is identical in both models. The last two rows show the power balance via the absolute difference between $Q_{\text{tot}}^{\text{FELA}}$ and $Q_{\text{tot}}^{\text{FELA+Pel}}$ with respect to Q_{net} as well as the relative deviation (in %) between $Q_{\text{tot}}^{\text{FELA+Pel}}$ and Q_{net} .

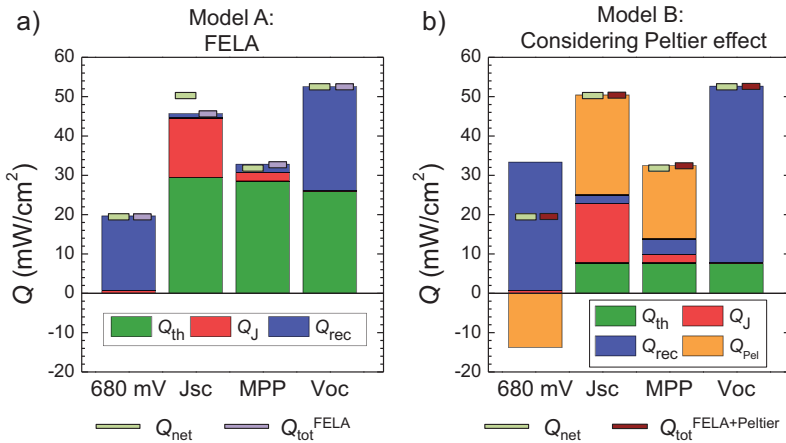


Figure 5.4: Graphical representation of the data shown in table 5.4. This aids visualizing the magnitude of the different contributions to total power and the agreement between global power Q_{net} and sum of all contributions in the models $Q_{\text{tot}}^{\text{FELA}}$, $Q_{\text{tot}}^{\text{FELA+Peltier}}$.

Deviations between the total power densities of the two models

¹Which is the sum of $Q_{\text{rec,base}}$ and $Q_{\text{rec,surf}}$

²Which is the sum of $Q_{\text{Pel,base}}$ and $Q_{\text{Pel,surf}}$

Table 5.4: Comparison of the main power contributions between model A and model B from table 5.1 for 680 mV forward bias in the dark, J_{sc} , MPP and V_{oc} conditions. The power balance between Q_{tot}^{FELA} and $Q_{tot}^{FELA+Peltier}$ shows excellent agreement at most conditions but only model B which considers the Peltier effect is physically sensible on a local level.

Power source/drain (mW/cm ²)	680 mV	J_{sc} (50 mV)	MPP	V_{oc}
P_{gen}	0.00	52.43	52.43	52.43
Q_{elec}	19.92	-1.85	-20.26	-0.01
Q_{net}	19.92	50.59	32.18	52.43
Model A: FELA only				
Q_{th} to $\Phi_{Fn} - \Phi_{Fp}$	0.00	29.37	28.51	26.00
Q_{Joule}	0.65	15.18	2.14	0.10
Q_{rec}^{FELA} over $\Phi_{Fn} - \Phi_{Fp}$	19.03	1.17	2.15	26.47
Q_{tot}^{FELA}	19.68	45.72	32.79	52.57
Model B: Considering Peltier effect				
Q_{th} to $E_{C/V}$	0.00	7.65	7.65	7.65
Q_{Joule}	0.65	15.18	2.14	0.10
Q_{rec} over $E_{gap,eff}$	32.69	2.13	3.99	44.91
Q_{Pel}	-13.82	25.47	18.72	-0.09
$Q_{tot}^{FELA + Pel}$	19.52	50.43	32.50	52.57
Power balance				
$Q_{tot}^{FELA} - Q_{net}$	-0.24	-4.87	0.62	0.15
$Q_{tot}^{FELA+Pel} - Q_{net}$	-0.40	-0.15	0.33	0.15
Dev. $Q_{tot}^{FELA+Pel}$ vs. Q_{net}	-2.05%	-0.30%	1.00%	0.28%

and the net power Q_{net} are $< 2.5\%$ for both models at most conditions.¹ These deviations can be considered remarkably small, when taking into account the large number of involved calculations and the fact that the results are also sensitive to the four fixed majority carrier Peltier coefficients parameters taken from literature. Note that J_{sc} was simulated at 50 mV because convergence at 0 mV was not achievable with the simulation program. Unlike for luminescence imaging, where charge carrier density distributions are virtually equal between 0 mV and 300 mV, the net power densities are different (see section 4.4.2).

This confirms that the implemented Peltier equations were successful and that this model can be used for subsequent analysis of spatially resolved data. Joule heat is equal for both models but the physically thermalization and recombination heat of model A is not sensible on the local level. The net Peltier heating and cooling balance out the differing heat sources in model B. In model A, the thermalization heat presents over 50 % of the total density. This is balanced by Q_{Pel} in model B. For both models, the total power is dominated by recombination in the dark at 680 mV, Joule heat at J_{sc} , recombination at V_{oc} and a mixture between Joule heat and recombination at *MPP*.

Next, table 5.5 shows in detail the individual power densities of heating (> 0) and cooling (< 0) of the nine relevant Peltier contributions from figure 5.3. Figure 5.5 yields a graphical presentation of the data in table 5.5. At 680 mV, a mixture of exclusively cooling contributions², mainly from electron flow is observed with BSF-base current (ID 2) cooling as the most prominent effect. Under illumination at J_{sc} conditions, all interface currents lead to Peltier heating except for hole base-BSF (ID 6) and the hole current within the base (ID 9), which is opposite to the hole Joule heating in the base. The

¹The only significant deviation is for J_{sc} in the FELA model, possibly due to numerical inaccuracies.

²The only exception is the electron FSF-base current with a small net heating contribution.

emitter-base hole current (ID 5) has a very large heating contribution. At *MPP*, the numbers are very similar except for reduced Peltier heating of ID 5 and cooling of ID 9, caused by the reduced quasi-Fermi level gradients in the base at *MPP* conditions. At V_{oc} conditions, only electron base-emitter current (ID 1) and hole emitter-base (ID 5) have significant but still small and opposite cooling/heating contribution respectively, which cancels out the net Peltier power. The Peltier effect is least relevant for V_{oc} conditions as was also argued by Breitenstein et al. for conventional cells [70].

Table 5.5: Overview of the all integrated Peltier heating and cooling contributions of the BC2 cell simulation from table 5.4 in mW/cm^2 for the nine relevant current components from figure 5.3. Depending on the operating conditions, very different currents dominate the net Peltier power.

ID	Type	Interface	680 mV	J_{sc} (50 mV)	<i>MPP</i>	V_{oc}
Q_{Pel} 1	electron	base - emitter	-2.04	0.00	-0.24	-2.52
Q_{Pel} 2	electron	BSF - base	-5.16	7.34	7.57	0.99
Q_{Pel} 3	electron	metal - BSF	-2.34	2.82	2.93	0.00
Q_{Pel} 4	hole	metal - emitter	-2.78	3.63	3.48	0.00
Q_{Pel} 5	hole	emitter- base	-0.73	25.61	6.33	2.52
Q_{Pel} 6	hole	base - BSF	-0.70	-0.24	-0.24	-0.99
Q_{Pel} 7	electron	base - FSF	0.40	0.39	-0.03	0.49
Q_{Pel} 8	hole	FSF - base	-0.40	0.05	0.03	-0.49
Q_{Pel} 9	hole	within base	-0.06	-14.15	-1.11	-0.09
Q_{Pel}	Sum	(mW/cm^2)	-13.82	25.47	18.72	-0.09

Another IBC cell modeled after cell Fi1 was simulated for this work, which showed the same net cooling and heating effects from the nine Peltier contributions (data not shown). These results demonstrate which Peltier contributions lead to heating and cooling effects as a function of operating conditions, which was summarized in table 5.2. The FSF currents can have both heating and cooling properties under the same operating condition as e.g. holes can flow in at one place and out at another place.

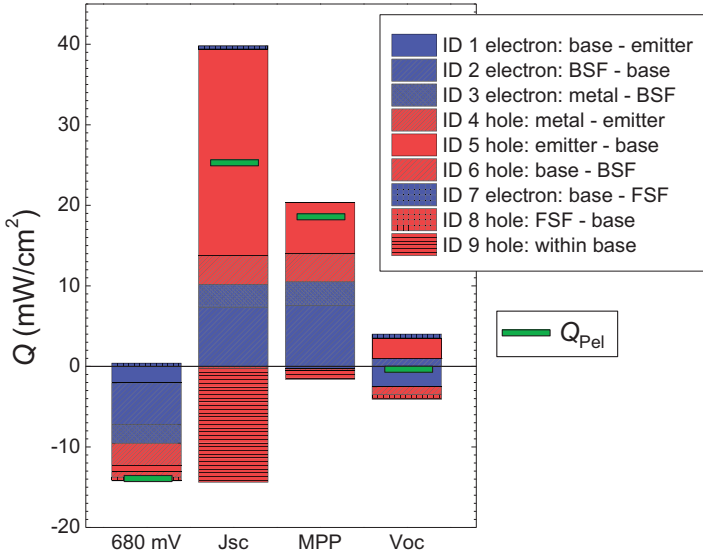


Figure 5.5: Graphical representation of the integrated Peltier power density data in table 5.5. Electron/hole interface current contributions are marked in blue/red respectively and the hole current within the base in orange (ID 9). Q_{Pel} marks the sum of all contributions.

Local heating and cooling

In the following, the depth integrated power density profiles of the heat sources for the calculations using model A and model B in table 5.4 are presented. Figure 5.6 depicts the power density profiles Q^{loc} along the unit cell for Q_{Joule} (red), Q_{th} (green), Q_{rec} (blue) and Q_{Pel} (yellow) using the conventional FELA (Model A, left graphs) and with Peltier effect (Model B, right graphs) for 680 mV (a), J_{sc} (b), MPP (c) and V_{oc} (d). Note that the y-axis limits are identical between the model comparisons but not between operating conditions.

Thermalization heat presents a much smaller offset in model B than model A because $E_{\gamma} - E_{\text{g,eff}} < E_{\gamma} - (\Phi_{Fn} - \Phi_{Fp})$. Subsequently, the power densities in model B are more inhomogeneous than in model A. Unlike model A, model B contains highly localized negative power density values and hence areas of net cooling.

Sharp peaks of high power density are noticeable at the 10 μm wide contacting openings of this half-pitch unit cell. These power densities reach up to several hundred mW/cm^2 and generate a significant mean Peltier contribution, as was shown in table 5.5 and figure 5.5.

Using model B yields higher recombination power densities than model A because of $E_{g,\text{eff}} > (\Phi_{Fn} - \Phi_{Fp})$. This effect seems partially compensated by Peltier cooling in the dark (a). At J_{sc} (b) and *MPP* (c) however, increased recombination at the contacts is paired with Peltier heating. Furthermore, the thermalization heat using model A exhibits a slight variation across the unit cell because of spatially varying $\Phi_{Fn} - \Phi_{Fp}$ which is physically not sensible for thermalization heat.

In figure 5.6 (a), the Q^{loc} is distributed fairly equally along the emitter and BSF diffusions with an expected lower recombination over the gap region and slightly higher recombination in the BSF region than the emitter region. Under J_{sc} conditions (b), the power density is dominated by Joule heat at the edge of the emitter diffusion, likely because this is where minority carriers generated over the gap and BSF region accumulate when entering the emitter. Furthermore in model B, very large Peltier heating occurs at the contacts because of the high local current densities there. At *MPP*, the situation is similar to J_{sc} but with smaller Joule heat contributions. Finally, the Q^{loc} profiles at V_{oc} (d) are clearly dominated by the surface recombination velocities i.e. J_0 values, which strongly vary between diffused surfaces and metal contact areas.

In a final step, figure 5.7 presents the sum of the power profiles $Q_{\text{tot}}^{\text{FELA}}$ for model A and $Q_{\text{tot}}^{\text{FELA+Pel}}$ for model B respectively for each operating condition. These graphs represent the net local power sources/drains that occur under operation using the two models.

The graphs of model A show the free-energy losses in the different regions, which is a correct method of describing losses of theoretically available electrical energy in a solar cell according to Brendel et al. [215]. On the other hand, the equations of model B reveal the actual released heating power, which is what the LIT signal is effectively

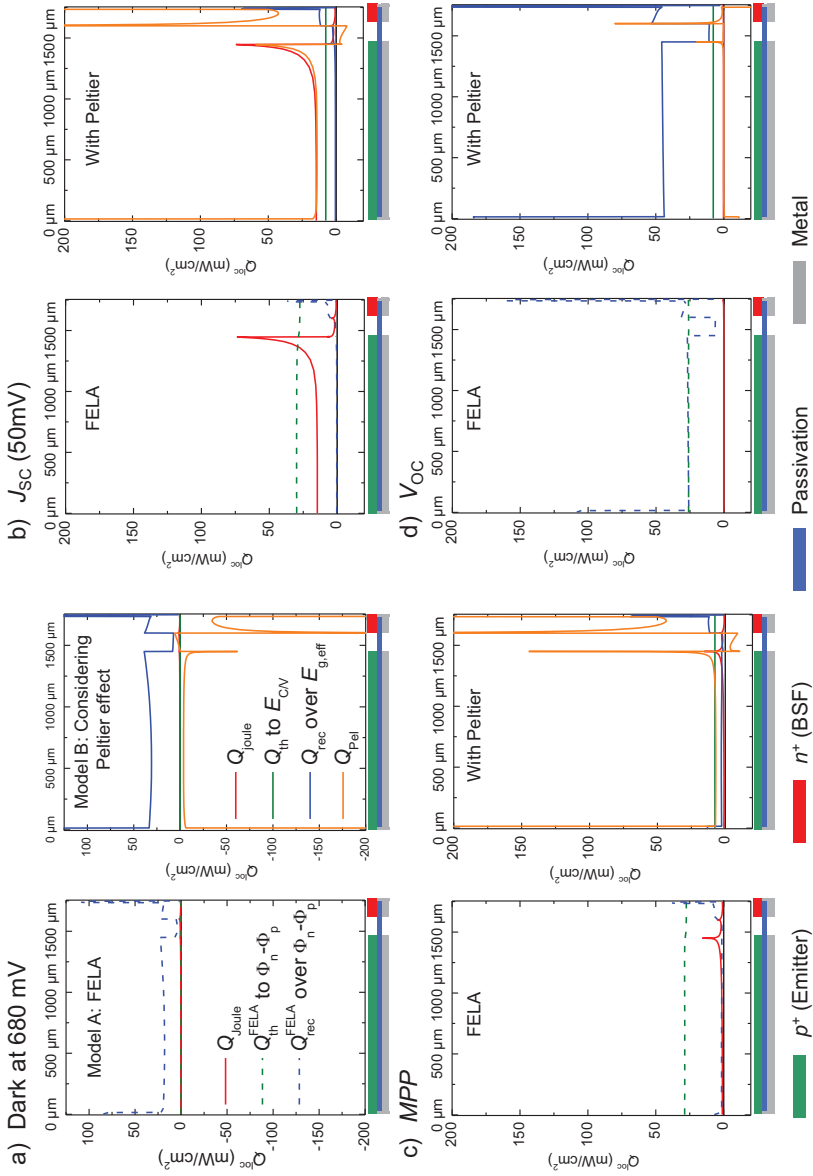


Figure 5.6: Power density profiles from Joule, recombination, thermalization and Peltier heat for the two models in comparison for operation in the dark (a), J_{sc} (b), *MPP* (c) and V_{oc} (d). Using the physically more sensible model B reveals much larger recombination heat, smaller thermalization heat and large local contributions of both Peltier heating and cooling.

based on. The consequence is, that conventional power calibration of LIT will show the released power density (red) but not the actually lost power (black). Consequences of this are addressed using experimental data in the following section.

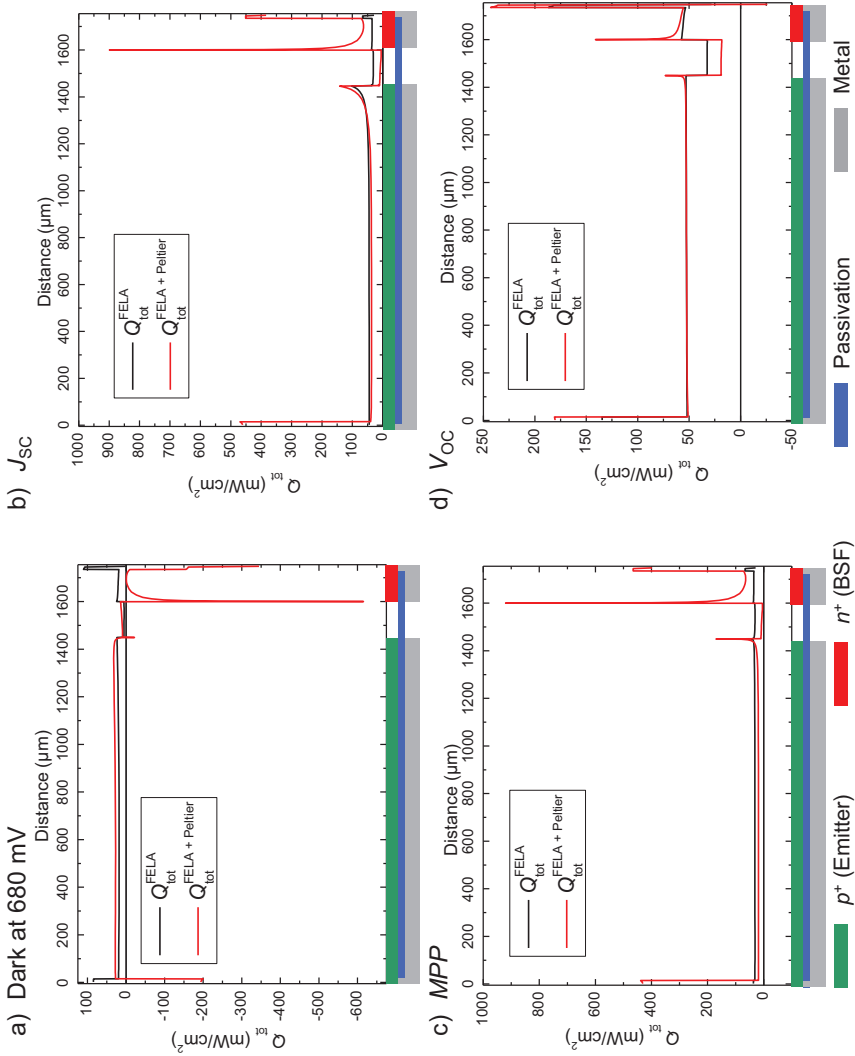


Figure 5.7: Total power density profiles Q_{tot} along an IBC unit cell calculated using FELA (Model A, black) and considering the Peltier effect (Model B, red) for operation in the dark (a), J_{sc} (b), MPP (c) and V_{oc} (d). In all cases, consideration of the Peltier effect yields significantly increased lateral contrasts, especially over the metal contact areas.

5.4 Heat sources, power calibration and contrast patterns

This section deals with experimental LIT on IBC cells. It highlights general observations and assesses the usefulness of LIT in the presence of the Peltier effect. First, an example of point-, line- and extended heat sources observable in all four LIT images is presented. This is followed by the description of the -90° image LIT power calibration method used in this work. Further, an example of experimental LIT in comparison to luminescence imaging is shown. Finally, graphs of the intensity profiles over fault free unit cells at high $f_{\text{lock-in}}$ are presented.

Point, line and extended heat sources

As explained in section 2.3.2, lock-in thermography images always come in a set of four images, namely amplitude, phase, 0° and -90° that are mathematically connected to each other via equations 2.60–2.63. Out of two images, all others can be calculated. The thermal signal of the 0° and -90° image depends on whether the heat source can be classified as a point source (0-dimensional), line source (1-dimensional) or extended source (2-dimensional surface) at a given optical resolution. The second criterion is whether the sample can be considered thermally thin ($\Lambda \gg d$) or thermally thick ($\Lambda \ll d$). Analytic expressions from [70] were shown in table 2.2. Figure 5.8 depicts amplitude (a), phase (b), 0° (c) and -90° (d) images of cell Fi2 at J_{sc} conditions under 1 sun equivalent 940 nm illumination measured at $f_{\text{lock-in}} = 30$ Hz.

For the qualitative interpretation of the following images, textbook knowledge from conventional LIT on silicon solar cells according to [70] is used and adapted to this cell structure. The amplitude and the -90° image look very similar to each other, as do the phase and the 0° image. The 0° image is in phase with the excitation of the sample, while the -90° image is in phase with the 90° delayed temperature changes following the excitation. The resulting thermal

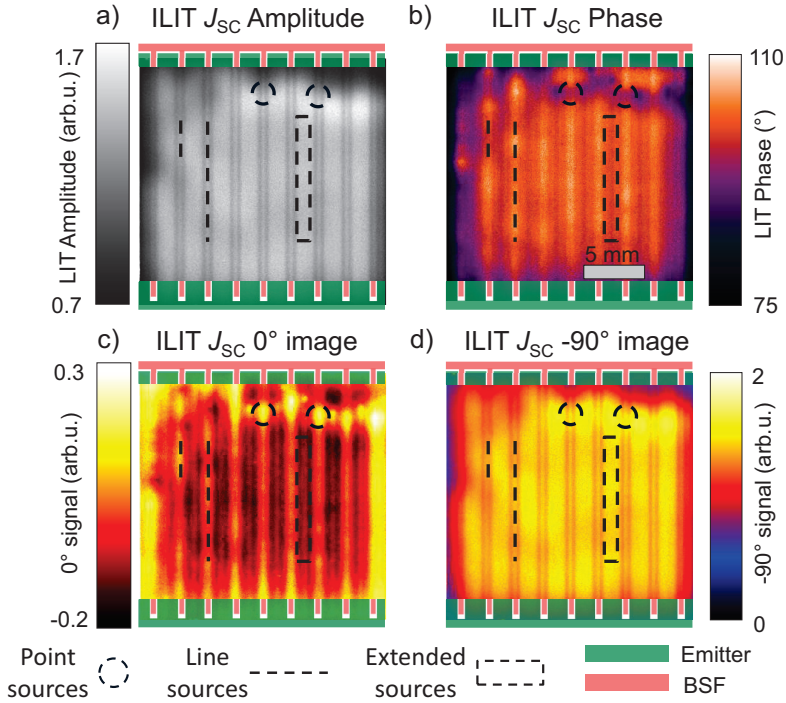


Figure 5.8: 30 Hz $f_{\text{lock-in}}$ amplitude (a), phase (b), 0° (c) and -90° (d) LIT images of cell Fi2 at 1 sun J_{sc} conditions (31.5 mA/cm^2) and 940 nm illumination. The 0° image best shows that one can observe point sources (circled spots), line sources (dashed line over BSF regions) but not extended sources (dashed rectangle over emitter). Extended sources do appear in the -90° image. Contrasts are strongly blurred in the -90° and amplitude images.

signal is complex, as various shapes of heat sources are involved and in close proximity to each other. $f_{\text{lock-in}}$ of 30 Hz is the minimal frequency to distinguish contrasts between $\sim 100 \mu\text{m}$ wide structures ($\Lambda = 1 \text{ mm}$) but already approaching the physical limitation of the measurement system at full frame of 60 Hz. The images were acquired by averaging over 60000 periods (33.5 minutes). At 30 Hz and $d = 180 \mu\text{m}$, $\Lambda/d \approx 5.47$ which may still be classified as thermally thin (see table 2.1).

While having no quantitative value for power calibration, it is well

known that the 0° image yields a high spatial resolution for point and line sources, which are indicated by the dashed shapes in figure 5.8. At this typical LIT camera resolution, some spots (dashed circles) can be considered point sources, the BSF diffusion (dashed lines) a line source and the emitter diffusion (dashed rectangle) an extended two-dimensional source. All of these heat sources have different thermal wave propagation functions and their proximity leads to a strong overlap at typical measurement conditions [216]. The 0° image's temperature waves have not only positive but also negative components so the overlapping may lead to misinterpretations (see figure 2.15).

The thermal diffusion can be observed in the -90° image (d), which is proportional to local heating power. The emitter diffusion that showed very little signal in the 0° image has a signal just as high as the BSF regions in the -90° image. This can be explained by the fact that an extended thermally thin source (here the emitter) bears no 0° signal (see equations in table 2.2). The contrast in the -90° image is greatly reduced and even the point sources are blurred from the 1 mm thermal diffusion length. Furthermore, the -90° image shows rather sharp signal decreases in the gap regions which is likely an optical artifact from poor reflectivity of infrared photons on the non metallized rear side. Such sharp lines were only observed in images with extremely low contrast. Finally, the phase image (b) yields information about the ratio of magnitudes between the 0° and -90° images ($\phi = \arctan(S^{-90^\circ}/S^{0^\circ})$). Since in fault free IBC cells a mixture of sources are present at this optical resolution, no quantitative information can be obtained from it. On a qualitative level though it serves as an excellent indicator for SNR because only if the 0° and -90° images contain signals above the noise level, patterns of distinct phase data are observed in the phase image instead of seemingly random data. No additional information can be drawn from the amplitude image.

Power calibration

It is desirable to calibrate -90° LIT images to local power density to gain quantitative information. Next, a procedure for such power cal-

ibration is introduced for the general case of DLIT and ILIT. While DLIT calibration is very simple and performed as in [190], an additional challenge lies in calibrating of power densities in ILIT. In the ILIT power calibration procedure proposed by Kasemann et al. [192] and Isenberg et al. [217], it was assumed that e.g. the thermalization heat at MPP and V_{oc} is identical. Subtracting two -90° ILIT images from each other yields a calibration image that accounts for thermalization heat. Here, an approach in accordance to model B from section 5.3 is used. Note that the term 'dissipated power' is avoided in the context of IBC cells in the presence of the Peltier effect. The main assumption is that in all -90° LIT images the signal $S_{\text{corr}}^{-90^\circ, \text{loc}}$ (emissivity corrected according to equation 5.3), is directly proportional to local power density. Note that for simplicity only monochromatic radiation excitation of wavelength λ and energy E_γ is assumed. Linear power calibration is made using a calibration factor $K_{\text{cal,LIT}}$ via

$$S_{\text{P,cal}}^{-90^\circ, \text{loc}} = K_{\text{cal,LIT}} S_{\text{corr}}^{-90^\circ, \text{loc}} . \quad (5.7)$$

$K_{\text{cal,LIT}}$ is obtained from the mean -90° signal and the total power density Q_{net} deposited¹ in the cell via [192]

$$K_{\text{cal,LIT}} = \frac{Q_{\text{net}}}{\langle S_{\text{corr}}^{-90^\circ, \text{loc}} \rangle} . \quad (5.8)$$

Q_{net} , which was also used for table 5.4 is the sum of the illumination power density that enters the cell and electrical power

$$Q_{\text{net}} = P_{\text{gen}} + Q_{\text{elec}} = P_{\text{gen}} + V_{\text{bias}} \cdot J . \quad (5.9)$$

The illumination power that enters the cell can be calculated

¹Note the choice of wording in 'deposited' as this word does not imply a power loss. Peltier heating can be considered a power deposition but not a power loss.

by the measured short-circuit current density $J_{sc,meas}$ and measured spectral response SR or EQE obtained from another setup via

$$P_{gen} = \frac{J_{sc,meas}}{SR(\lambda)} = \frac{J_{sc,meas} \cdot E_{\gamma}}{EQE(\lambda)q} . \quad (5.10)$$

The final equation for $S_{P,cal}^{-90^{\circ},loc}$ is

$$S_{P,cal}^{-90^{\circ},loc} = S_{corr}^{-90^{\circ},loc} \frac{J_{sc,meas}(E_{\gamma}/EQE) + V_{bias} \cdot J}{\langle S_{corr}^{-90^{\circ},loc} \rangle} . \quad (5.11)$$

By this procedure, a power density calibrated -90° image ($S_{P,cal}^{-90^{\circ},loc}$) in equation 5.7 is obtained that shows how much power density is locally deposited. Without illumination, $P_{gen} = 0$ and the calibration is simplified to the well known DLIT calibration [190]. It may be desirable for ILIT however, to subtract the homogeneous thermalization background signal Q_{th} (see figure 5.6) which is an offset to the images with no relevant information about actual losses of power that could have been retrieved. This power density is therefore an offset. Using $P_{gen} = \Phi \cdot E_{\gamma}$, a calibrated -90° image that is free of this thermalization power can be obtained by subtraction of an offset via

$$S_{P,cal,no\ th}^{-90^{\circ},loc} = S_{P,cal}^{-90^{\circ},loc} - Q_{th} = S_{P,cal}^{-90^{\circ},loc} - (P_{gen} - \Phi \cdot (E_{\gamma} - E_{g,eff})) \quad (5.12)$$

$$= S_{P,cal}^{-90^{\circ},loc} - P_{gen} \left(1 - \frac{E_{\gamma} - E_{g,eff}}{E_{\gamma}} \right) . \quad (5.13)$$

Should the incident ILIT power differ from 1 sun, linear scaling of P_{gen} with the ratio of $J_{sc,meas}/J_{sc,1\ sun}$ is a good approximation. The theoretical considerations in section 5.3.2 concluded that

$$Q_{\text{tot}} = \langle Q_{\text{tot}}^{\text{loc,FELA+Pel}} \rangle . \quad (5.14)$$

The thermalization power can optionally be subtracted by equation 5.13. In conclusion, the emissivity corrected and power calibrated -90° LIT image is either the sum

$$S_{\text{P,cal}}^{-90^\circ,\text{loc}} = Q_{\text{th}}^{\text{loc}} + Q_{\text{Joule}}^{\text{loc}} + Q_{\text{rec}}^{\text{loc}} + Q_{\text{Pel}}^{\text{loc}} , \quad (5.15)$$

or alternatively with subtraction of Q_{th}

$$S_{\text{P,cal,no therm}}^{-90^\circ,\text{loc}} = Q_{\text{Joule}}^{\text{loc}} + Q_{\text{rec}}^{\text{loc}} + Q_{\text{Pel}}^{\text{loc}} . \quad (5.16)$$

The used excitation wavelength for ILIT in this work was always 940 nm. Excitation at shorter wavelength (470 nm, 655 nm) is possible in the used setup but as shown in equation 5.13 this primarily only adds an offset to the images. Since IBC cells collect photogenerated carriers on the rear side, the impact of λ is not as significant as for ILIT on conventional front collecting cells or even tandem cells [202]. For cell BC2, Q_{th} at 1 sun is 7.7 mW/cm² for 940 nm, 30.5 mW/cm² for 655 nm and 60.1 mW/cm² for 470 nm incident radiation respectively.

LIT patterns and contrasts in comparison to luminescence

In the following LIT images of the full cell BC2 are presented and put in qualitative comparison with luminescence images which were treated in chapter 4. Figure 5.9 shows emissivity corrected 0° and power calibrated (equation 5.11) -90° LIT images of cell BC2, this time measured in its entirety and at $f_{\text{lock-in}} = 30$ Hz instead of 120 Hz (see figure 5.10) at all relevant operating conditions. Note that all LIT images are scaled to the same high and low values. Additionally, corresponding EL and PL images are shown on the left.

A crack caused by handling of the cell, marked by the dashed

ellipse in (a), creates a region of high recombination. This crack extended throughout the whole cell due to handling in the LIT measurements which was conducted after the luminescence imaging. The increased recombination at the crack appears as a low EL/PL signal in all images depending on how much it deteriorates cell performance at a given operating condition. The signal of the crack in DLIT/ILIT behaves reciprocally to EL/PL as a high signal due to high recombination power Q_{rec} . The pattern structure from the interdigitated doping however does not have a simple reciprocal behavior to EL/PL. In the dark under forward bias (a), the EL signal is highest in the gap region, since this is where most carriers in this 1 Ωcm cell are injected into the bulk (see figure 4.8). In both DLIT images, the power density is highest over the emitter center with a low signal over the BSF. The conclusion from numerical simulations and measurements at $f_{\text{lock-in}} = 120$ Hz (see figure 5.10 later) was that the overall signal is dominated by surface recombination and that the very low power density over the BSF is caused by intense Peltier cooling.

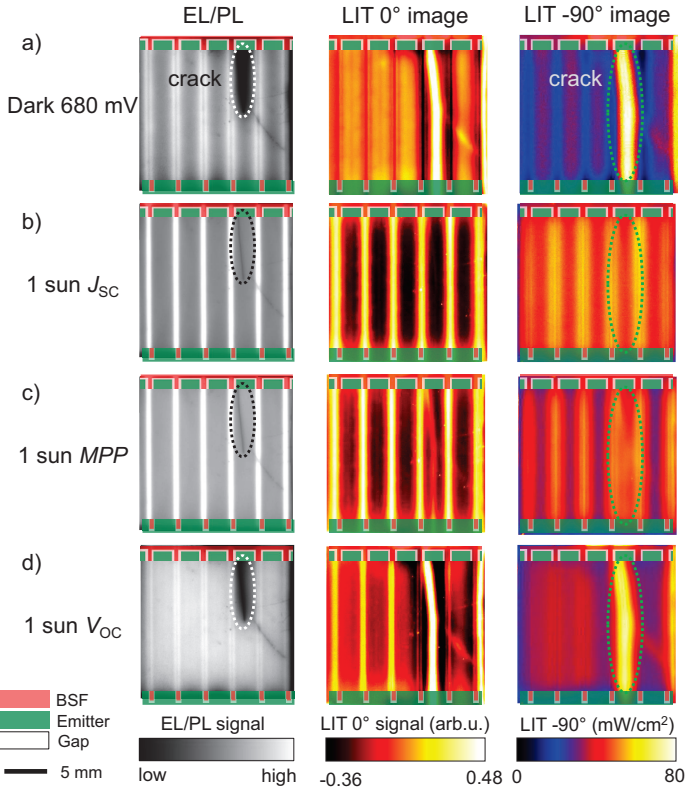


Figure 5.9: Luminescence, 0° LIT and power calibrated -90° LIT (equation 5.11, $f_{\text{lock-in}}=30$ Hz) images of cell BC2 in the dark under forward bias (a), J_{sc} (b), MPP (c) and V_{oc} (d). The cell crack caused by handling visible in EL/PL extended over the whole cell length in the subsequent LIT measurement over the whole cell. At the crack, recombination is high which yields a low EL/PL and high LIT signal. Except for V_{oc} , the regular contrast patterns are not reciprocal as they are heavily influenced by the Peltier effect.

Under J_{sc} conditions (b), the PL image shows bright lines over the BSF from diffusion limited carriers with little quantitative information on recombination. The ILIT images show peaks over gap and BSF region that were interpreted to originate from Joule heating by carriers entering the emitter as well as Peltier heating at the BSF contact.

All *MPP* images (c) are once again similar to J_{sc} both for PL and ILIT. The crack which was barely noticeable at J_{sc} however becomes more clear as a detrimental fault, especially in the LIT images. Note that the ILIT *MPP* -90° signal overall decreased compared to J_{sc} because electrical power is extracted from the cell at *MPP*. Furthermore, a decrease in contrast is observed for all images which for PL is known to be caused by series resistance and likely also in ILIT. The power simulations showed for *MPP* that recombination becomes more dominant than Joule heat, which explains the higher signal from the crack.

Finally, at V_{oc} conditions (d), photogenerated charge carriers diffuse in the cell until they recombine at a surface. For this cell, the J_0^{EM} is just slightly smaller than J_0^{BSF} (see appendix A) and the gap region is well passivated. The PL V_{oc} image in this case shows small PL peaks in the gap region due to the good passivation. In the 0° ILIT image, there is a negative signal surrounding the crack which is a consequence of the negative values in the temperature functions (see figure 2.15).

LIT patterns over fault free unit cells at 120 Hz lock-in frequency

Finally, in analogy to the intensity profile results in luminescence imaging, the following presents an example of intensity profiles of the 0° and -90° images in LIT. The measurements were conducted at unusually high $f_{lock-in}$ of 120 Hz over a sub frame so that thermal diffusion does not blur all interesting features.

Figure 5.10 shows average line scans of 0° (blue) and power scaled

-90° (red, scaled via equation 5.11¹) emissivity corrected LIT images over 5.25 mm across a fault free region of cell BC2 for all relevant operating conditions. The same cell was shown earlier in figure 5.9 and it was the base model for the simulation results.

It is noticeable that several small features in the 0° image are strongly blurred in the -90° image. The -90° line scans offer an impression of the thermal blurring at $\Lambda = 500 \mu\text{m}$. Since $\Lambda/d = 0.36$, the sample cannot be considered thermally thin anymore and the equations in table 2.2 are not fully applicable to describe the thermal waves. The ILIT image graphs contain a dashed line to indicate the 7.7 mW/cm^2 offset in thermalization power density. The rest is a combination of Joule, recombination and Peltier heating. Qualitatively, the trends of the simulated power density profiles under consideration of the Peltier effect (figure 5.7, $Q_{\text{tot}}^{\text{FELA+Pel}}$, red) better resemble the peaks observed in the experimental -90° line scans than the standard FELA model ($Q_{\text{tot}}^{\text{FELA}}$, black).

¹The power calibration was performed via an image of the whole cell.

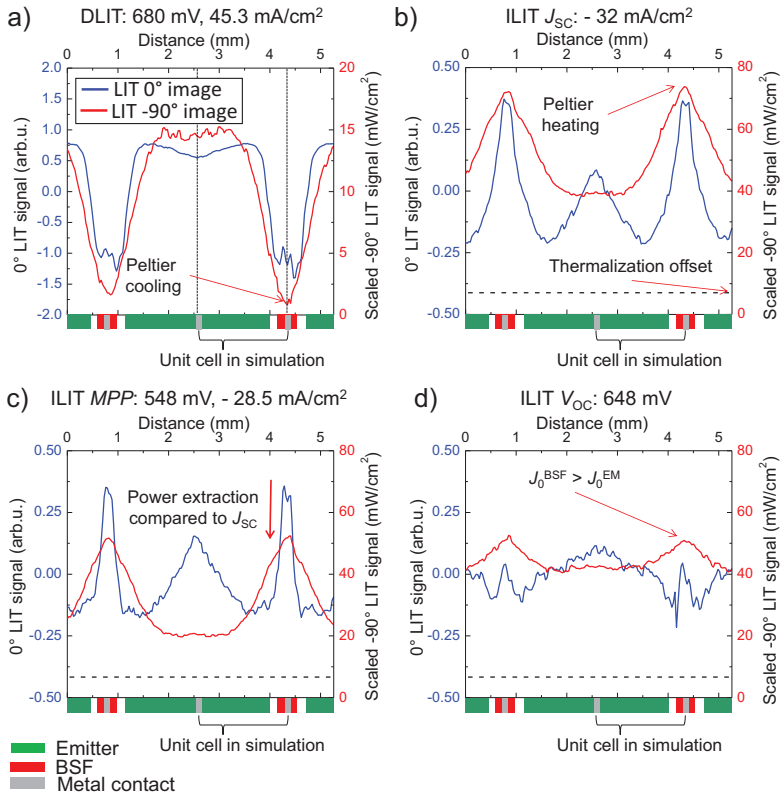


Figure 5.10: Averaged line scans of experimental, emissivity corrected, 0° (blue) and power scaled (equation 5.11) -90° (red) LIT images over 5.25 mm across a fault free region of cell BC2 in the dark under forward bias (a), J_{sc} (b), MPP (c) and V_{oc} (d) at unit120Hz $f_{lock-in}$. Several distinct features in the 0° image disappear in the -90° image due to thermal blurring.

A direct quantitative comparison between the simulated power profiles (figure 5.7, $Q_{tot}^{FELA+Peltier}$) and power calibrated -90° LIT images is not fruitful because the simulated profiles do not take the thermal wave propagation during the LIT experiment into account. There is literature with analytical equations to deconvolute experimental data and reduce thermal blurring [216].¹ A software package

¹Once again the fact that the sample is neither thermally thin nor thermally thick also poses problems for the analytical thermal wave propagation models in

named DECONV has been developed by Breitenstein et al. for this purpose [194] but deconvolution comes at the expense of SNR. The sharpness of the simulated power density profiles is thus not achievable experimentally with state-of-the-art LIT equipment.

However, some interesting tentative conclusions can be made on features found in the $Q_{\text{tot}}^{\text{FELA+Pel}}$ simulations that can be identified in the power scaled experimental -90° images. In figure 5.10 (a), the power over the BSF contact is almost 0 mW/cm^2 although it is known to be an area of high recombination. This is likely caused by the high Peltier cooling in this area. Without the Peltier effect, the -90° signal would show two peaks. A local net cooling effect (signal < 0) in the dark e.g. over the BSF contact area is not observed though, likely because of thermal blurring. In the J_{sc} image (b), a wide peak over the BSF contact is observed. This is a combination of Joule heat at the emitter edge and Peltier heating over the BSF contacts. In comparison, the *MPP* image (c) is very similar to J_{sc} but shows a lower offset and mean power density because 15.6 mW/cm^2 are extracted from the cell. Finally, the V_{oc} image only shows very little contrast but the peak is over the BSF and BSF contact region, because $J_0^{\text{BSF}} > J_0^{\text{EM}}$. This is inverse to the luminescence profile where $J_0^{\text{BSF}} > J_0^{\text{EM}}$ results in a lower PL signal. Since the Peltier effect was found to be negligible at V_{oc} conditions, it can be concluded that a power calibrated (equation 5.13) ILIT V_{oc} image yields thermally blurred but quantitative information on local recombination activity.

Summary

After reviewing the presented simulations and experimental data, an improved understanding for the origins of the LIT images as a function of locally generated power was achieved. The simulations revealed that the Peltier effect plays a significant role in IBC cells under all operating conditions except at V_{oc} . A power calibration and local free-energy loss analysis is therefore not possible in order to study fault free IBC cells with LIT. The fact that IBC cells behave

very differently in the dark than under illumination also means that a 'Local I-V' analysis using DLIT according to Breitenstein et al. [213] can also not be applied.

This complexity however does not render LIT useless for IBC solar cell characterization. The following chapter elaborates on the capability of LIT to characterize local ohmic shunting faults, where LIT is still superior to EL/PL. A summary of the findings on experimental LIT images in this chapter is presented in the discussion chapter 7. Another brief summary of this chapter is presented in chapter 8.

Chapter 6

Detection of local processing faults

Highest efficiency IBC solar cells in industrial and laboratory processing are increasingly sensitive to local performance limiting faults which are best characterized by spatially resolved characterization techniques. The primary use of spatially resolved characterization in photovoltaics is to identify and assess such local faults that occurred during the fabrication process. Unambiguous identification of local problems is essential for fast improvement of the solar cell process. The previous three chapters focused on experimental results of fault free IBC cells and the consequences of the interdigitated doping pattern for SR-LBIC (chapter 3), luminescence imaging (chapter 4) and lock-in thermography (chapter 5). Based on that knowledge, this last results chapter presents investigations on some of the local faults on finished solar cells that are highly relevant in IBC cell processing. The term 'fault' refers to performance degrading problems that are not inherent to cell design but instead caused by imperfections of the processing equipment such as holes in the passivation layer or metallization interruptions.¹

¹Defects in the silicon wafer material are not considered in the scope of this work.

The goal is to obtain the guidelines presented in the discussion section 7.2 that assess which imaging techniques are best suited to identify each fault type. In section 6.1, a literature overview of spatially resolved characterization of processing faults in silicon solar cells is presented. Section 6.2 deals with local series resistance faults, in particular contact resistance and finger interruptions. Section 6.3 describes results on faults related to local shunting. Section 6.4 briefly discusses faults of the front side's optics and passivation losses. Finally, section 6.5 demonstrates breakdown patterns in IBC cells.

The experimental data in this chapter was obtained in collaboration with K. Hagedorn and H. Chu in the scope of their respective Master's thesis under supervision by the author. Results from section 6.2 were published in [112] and [114]. A part of the analysis on breakdowns in section 6.5 was published in [152] in a collaboration with R. Müller.

6.1 Literature overview

The following presents an overview of literature on spatially resolved analysis of the processing faults in solar cell manufacturing treated in this work. The focus is set on luminescence imaging and lock-in thermography. Where these techniques are insufficient also microscopic characterization is mentioned. Since all imaging techniques have drawbacks and risk of misinterpretation when characterizing certain processing faults, only a combination of techniques yields a holistic analysis, as recently reviewed by Michl et al. [218] and the author, and applied by Peloso et al. [219]. An overview of imaging techniques utilized to characterize meta-stable defect impurities in silicon, which is beyond the scope of this work, was published by Schubert et al. [220]. Microcracks are other handling related faults that were not investigated in this work. Such faults have been characterized by Demant et al. [221] and Köntges et al. [124].

Series and contact resistance

Measurements of contact resistance are typically carried out on test structures in parallel to cell processing, by using the transmission line method (TLM) developed by Berger [222] or the three point probe method (TPP) by Vinod [223]. Vinod further reviewed these techniques in [224]. In 2000, the 'Corescanner' was introduced by Van der Heide et al. to map the contact resistance using probes [225, 226]. This approach requires direct contact between needles and the cell for each image pixel though, is destructive, and slow. The Corescanner has become obsolete in the advent of luminescence imaging, which provides a fast and non-destructive alternative. Quantification of local contact resistances on finished silicon solar cells has thus far not been achieved with luminescence imaging or thermography. Luminescence does not directly provide the local contact resistance but local series resistance, which may be sufficient for practical use.

Shunts and shunt imaging

Shunts in solar cells are the result of processing faults that lead to unwanted parasitic current losses, mostly described by the parallel resistance R_p in the diode model and hence ohmic losses. This is why R_p is often called 'shunt resistance' in literature. However, Breitenstein et al. has classified shunts more broadly by their I-V characteristic into linear ohmic shunts (R_p) and non-linear diode-like shunts (J_{01} , J_{02}) [208], which act on local saturation current densities or ideality factors [227]. Steingrube et al. discussed the connection between the diode model interpretation of shunts and the actual physical SRH recombination mechanisms occurring in the semiconductor [228].

Fast and reliable imaging of shunts (which includes pinholes and spikes) for silicon solar cells has seen great advances in the last decade. Dark lock-in thermography has been successfully established by Breitenstein et al. as the most reliable method to detect shunts in silicon solar cells [70, 122, 206]. The transfer of DLIT for in-line shunt detection was investigated by Kasemann et al. [229] and Seren et al. [209]. On the other hand, luminescence imaging was investigated by

Kasemann et al. [230] and Augarten et al. [231] to be in principle capable to detect shunts but quantitative analysis has thus far not been successful as the signal is heavily influenced by the injection level and surrounding resistances yielding injection dependent lateral balancing currents.

Pinholes

Pinholes refer to holes in thin films that locally disable its passivating and insulating properties. They are known problems since the early days of semiconductor manufacturing. Reviews on detection and characterization of pinholes on integrated circuits were published by Kern et al. [232, 233] and in theoretical work by Belousov et al. [234]. In silicon solar cells, pinholes are a processing fault especially known from thin films deposited by chemical vapor deposition (CVD) type processes [235] such as SiN, SiO₂ and Al₂O₃. They can be caused e.g. by mechanical stress [236] and presumably dust particles [237]. In solar cells, pinholes not only present areas of increased recombination but also present an opening for metal to contact the cell's base which, in the worst case, might lead to a short-circuit of the SCR. Completely insulating or rather pinhole-free thin films are particularly important for IBC solar cells with SCR overlapping metallization (see figure 2.10), as pinholes can quickly diminish the efficiency of such cells. Work on this issue was recently published by Reichel [54] and by Keding et al. [237], whose solar cells are also investigated in this chapter. A review on relevant microscopic characterization methods of pinholes was published by Saint-Cast et al. [238].

Spikes

The term 'spikes' and 'spiking' is used in the silicon photovoltaics community referring to pyramids of aluminum metallization that grow into the silicon base at elevated temperatures due to the high solubility of aluminium in silicon [239, 240]. The electric properties of such spikes in silicon in solar cell operation is complex and can

have both ohmic and schottky type contact properties resulting in short-circuited junctions [241]. Recent work focused on the microscopic characterization of nickel-silicide spikes on conventional cells using SEM, DLIT, reverse bias EL (Kluska et al. [242] and Büchler et al. [243, 244]) and μ LBIC (Heinz et al. [245]). As aluminum metallization presents a low cost alternative for high efficiency IBC cells, Keding et al. used an aluminium metallization containing silicon. In these cells, spikes were observed in SEM micrographs of cross-sections [237, 246]. This type of cell is investigated in section 6.3.2 of this work.

Breakdowns

Early studies of breakdowns in silicon pn junctions have been presented by Chynoweth et al. [247–249]. The emission spectrum was found to be much broader than regular photoluminescence and it ranges into the visible light spectrum. Breakdowns at particular sites may occur due to crystal defects or other faults that lead to the Zener effect (tunneling of charge carriers through the bandgap) or the avalanche effect (caused by impact ionization of electron-hole pairs) [250, 251]. Conventional global characterization of breakdowns is done through analysis of the reverse bias I-V curve and its temperature dependence. Spatially resolved characterization of breakdowns using a wide range of techniques, including luminescence [252] and LIT has been conducted in recent years on silicon solar cells. Proposals to classify breakdown types in silicon by their I-V characteristic and relation to cell technology were published by Kwapil et al. [253], Call et al. [254], Kasemann et al. [9] and summarized by Breitenstein et al. [210]. Breakdowns were also studied in relation with hot spot formation and possible damages to solar modules [191, 255, 256].

IBC cells and context in this work

This work uses the broad characterization knowledge from the cited works on conventional solar cells and applies it on IBC specific issues. Guo et al. [57] presented work on IBC cells suffering from

faults related to the cell's shunt resistance using global I-V and microscopic analysis. There is no published research which explicitly utilizes luminescence and lock-in thermography based characterization to investigate processing faults in IBC cells except by the author. Recently though, work has been published on breakdowns in IBC cells by Müller et al. [152] in collaboration with the author and also by Chu et al. [153], who formerly co-worked with the author.

6.2 Local series resistance faults

This section contains a discussion on the processing faults related to contact resistance and finger interruptions in the IBC solar cell structure. Using experimental and simulated current-voltage measurements and luminescence images, this section explores the strongly non-linear effect of poor local contact resistances on the global series resistance, fill factor, short-circuit current density and efficiency. Good agreement between global and spatially resolved characterization of faults is found and potential artifacts are discussed. Seven cases of contacting faults in IBC cells with distinct characteristics are identified using a flow chart of experiments presented in the guideline section 7.2. This should assist silicon solar cell manufacturers in localizing and quantifying local contacting faults that reduce the cell efficiency in industrial and R&D processing of IBC and other complex solar cells.

6.2.1 Simulated I-V and luminescence characteristics

After introducing the special IBC model used throughout this section, the following shows how a locally poor contact resistance affects the global I-V performance and how it is observed by luminescence imaging. A comparison of several base materials and thus injection dependencies is presented as well as a discussion of how well the mean R_s imaging results agree with the globally obtained values. All

data in this sub section is obtained from numerical simulations using Quokka (see section 4.4).

Solar cell model with local R_c faults

The reference structure for all simulations in this work was modeled closely after the 4 cm² IBC cell CF1 presented in [257] and later shown in figure 6.7. A schematic of the 180 μm thick n-type cell is depicted in figure 6.1. The model consists of five unit cells. One unit cell features a pitch distance of 2200 μm. The cell model allows for increasing the contact resistance of a specific emitter or BSF contact, hence the label '1/5' is used throughout this work. In an industrial 156 cm² cell with ~ 100 fingers, this would mean that every fifth finger is affected by this contacting fault. Each unit cell has a full area doped n^+ front-surface-field (FSF), 1900 μm wide p^+ emitter and 300 μm wide n^+ back-surface-field (BSF) each with 20 μm wide contact openings at the center. The contact resistance R_c on all contacts of the cell was set to a low reference value of 1 mΩcm². Furthermore $J_0^{\text{EM}} = 24 \text{ fA/cm}^2$, $J_0^{\text{BSF}} = 370 \text{ fA/cm}^2$, $J_0^{\text{FSF}} = 10 \text{ fA/cm}^2$, $R_{\text{sh}}^{\text{EM}} = 73 \Omega/\text{sq}$, $R_{\text{sh}}^{\text{BSF}} = 39 \Omega/\text{sq}$, $R_{\text{sh}}^{\text{FSF}} = 440 \Omega/\text{sq}$. The gap between emitter and BSF in all schematics is only to better distinguish emitter and BSF visually.

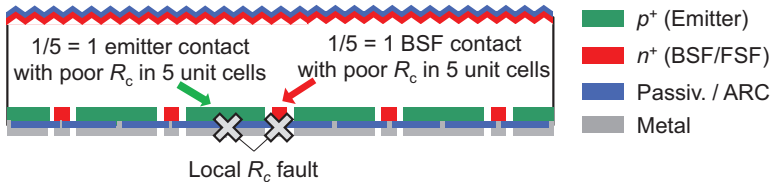


Figure 6.1: Schematic of the simulated IBC cell structure where 1 out of the 5 emitter or BSF contact resistances can be individually increased.

Ultra high purity, Auger-limited n-type silicon was assumed for all base materials in order to eliminate influences of bulk defects. Various base resistivities (ρ^{base}) were simulated in order to cover a wide range of injection effects at MPP from 0.2 Ωcm ($N_D = 3.2 \cdot 10^{16} / \text{cm}^3$,

'low injection'), $1 \text{ } \Omega\text{cm}$ ($N_D = 5 \cdot 10^{15} / \text{cm}^3$, 'medium injection') to $100 \text{ } \Omega\text{cm}$ ($N_D = 4.4 \cdot 10^{13} / \text{cm}^3$, 'high injection'). In the following simulated IBC cells with high effective lifetimes, this leads to mean excess carrier densities at *MPP* conditions of up to $3.2 \cdot 10^{14} / \text{cm}^3$, $6.5 \cdot 10^{14} / \text{cm}^3$ and $1.8 \cdot 10^{15} / \text{cm}^3$ respectively according to the numerical simulations. Normally, a change of ρ^{base} would require a different geometric design to achieve optimal performance. For the sake of comparability, all geometries were left unaltered though. For optical excitation, a generation profile for a AM1.5G spectrum calculated using a PC1D model of the cell's front surface texture was used as input for Quokka yielding $J_{\text{gen}} = 41.96 \text{ mA/cm}^2$. The simulated I-V, effective lifetime (τ_{eff}) and Suns- V_{oc} results for the three base resistances are shown in table 6.1. R_s^{global} was determined from simulated I-V curves using the double-light method [37]. As expected, a lower base resistance increases the lifetime (reduced Auger limitation) in the material and yields higher J_{sc} and V_{oc} but lower *FF* due to a decrease in base conductivity and hence an increase in internal, lateral series resistance losses from carrier transport.

Table 6.1: Simulated I-V results for the reference cell structures.

$\rho^{\text{base}} (\Omega\text{cm})$	τ_{eff} at J_{sc} (ms)	V_{oc} (mV)	J_{sc} (mA/cm^2)	<i>FF</i> (%)	<i>pFF</i> (%)	R_s^{global} (Ωcm^2)	η (%)
0.2	0.14	690	35.9	81.3	84.4	0.6	20.2
1	0.85	695	41	80.2	84.4	0.76	22.9
100	28.56	696	42	79	84.3	0.97	23.1

Global I-V characteristics: asymmetric response to globally and locally poor contacts

Before exploring the impact of local contact resistance faults, it is important to briefly review the well-known case of how a typical solar cell performance responds if the resistance between silicon and metal is undesirably high on all contacts of the cell (i.e. '1/1'). Sample

I-V results of globally increased R_c^{EM}/R_c^{BSF} in comparison to the reference R_c value are listed in table 6.2.

Table 6.2: I-V simulation results for the $1\ \Omega\text{cm}$ reference cell and the case of globally poor R_c^{EM}/R_c^{BSF} of $10\ \text{m}\Omega\text{cm}^2$ which result in an identical performance loss.

Simulation ID	J_{sc} (mA/cm ²)	FF (%)	η (%)
Reference $R_c = 1\ \text{m}\Omega\text{cm}^2$			
Reference	41.1	80.2	22.9
Globally poor contact $R_c = 10\ \text{m}\Omega\text{cm}^2$			
Globally poor R_c^{EM}	41.0	74.9	21.4
Globally poor R_c^{BSF}	41.0	74.9	21.4

When either an emitter or BSF contact is homogeneously (globally) poor over the whole cell, the impact on J_{sc} and FF is identical because the faults act only as a lumped global series resistance. First, the cells FF decreases dramatically and after a critical R_c value, J_{sc} begins to decrease as well until the solar cell cannot extract any excess carriers even under short-circuit conditions. The illuminated I-V curve becomes linear and the FF saturates at 25%.

An identical I-V performance response from poor emitter or BSF R_c is not observed anymore once only a single contact resistance is increased. Figure 6.2 shows I-V data for two different IBC cells. Cell 1 (a) is the $1\ \Omega\text{cm}$ reference structure from table 6.1 and Cell 2 (b) is a hypothetical design with identical geometry but with a front floating emitter (FE) and different base and sheet resistances. For each cell, figure 6.2 shows I-V data without R_c faults and two cases where one out of five (1/5) emitter/BSF R_c was increased to $0.1\ \Omega\text{cm}^2$.

In Cell 1, the cell's R_s^{global} more than doubles with a $0.1\ \Omega\text{cm}^2$ emitter contact fault while for the poor BSF case R_s^{global} only slightly increases. In contrast, in Cell 2 the FF is more sensitive to a poor BSF contact. This can be understood when studying the lateral

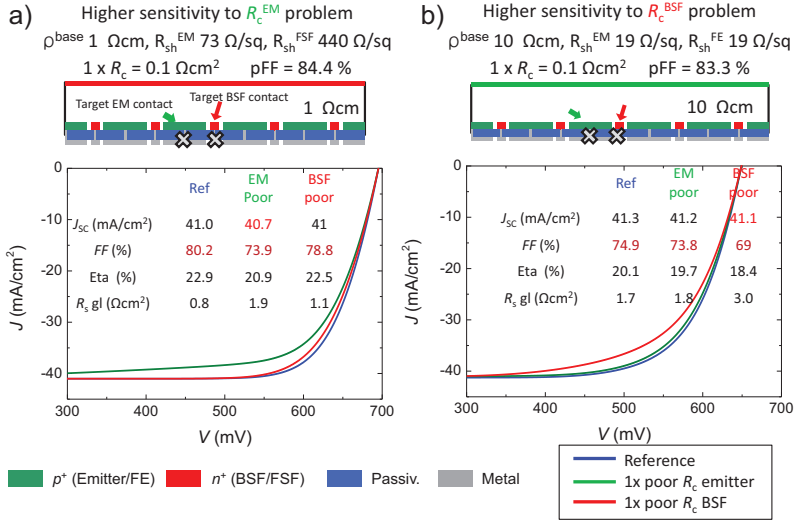


Figure 6.2: I-V simulation results of two IBC cell designs where a locally poor R_c has a very different impact on FF depending on whether an emitter or a BSF contact is affected.

resistances that electrons and holes are exposed to when the nearest contact resistance increases. For Cell 1, the electrons are subjected to a lower base resistance and have the FSF as an alternative current path towards the next BSF contact. On the other hand, in Cell 2 which has a front floating emitter, the n-type base resistance is much higher and in this case, no FSF as an alternative current path for electrons is available. At the same time, holes benefit from a higher base lifetime and may also flow through the floating emitter as an alternative current path to be extracted [50, 51].

From this comparison, one can conclude that complex cells with high lateral current transport respond asymmetrically to local p or n R_c faults. Note that the cell's V_{oc} and also pFF is never altered by a change in local contact resistance, because the simulations assume no impact of R_c on surface recombination. In experiments, e.g. an incomplete opening of the passivation however may be linked to a reduced contact recombination and higher pFF and V_{oc} .

Global I-V characteristics: locally poor contacts J_{sc} and FF evolution

The following presents more detailed results on how local contact resistance faults affects the global J_{sc} , FF and efficiency when measured with a conventional sun simulator or flash tester experiment. Note that V_{oc} and pFF remain constant as the recombination properties were not changed with varying R_c . The analysis is extended to the consequences of different injection conditions at MPP by varying ρ^{base} . Figure 6.3 depicts J_{sc} (top graphs), FF (middle graphs) and efficiency η (bottom graphs) as a function of local R_c for a single poor emitter (1/5, green) and a single poor BSF (1/5, red) contact in 5 unit cells. The graphs in figure 6.3 (b) with open symbols will be addressed later. Figure 6.4 depicts graphical schematics for the following discussion.

Various detrimental effects on J_{sc} and FF and ultimately on efficiency can be observed. Figure 6.3 (a) represents the case of an extremely low base resistance for electrons (majority carriers), low level injection for holes and also fairly low minority carrier lifetime in the base due to Auger recombination. The increase in 1 BSF R_c in 5 unit cells (red) has no impact on J_{sc} and only a marginal influence on FF and thus global efficiency. The extremely high base conductivity makes the cell very insensitive to local fault related series resistance losses from lateral base transport. In contrast, for 1/5 poor emitter R_c (green), the FF for the whole cell drops continuously from 81% to 72% at $1/5 R_c^{EM} = 0.1 \Omega\text{cm}^2$ as one would expect from an increasing lumped series resistance. This is labeled as 'Poor contact resistance' regime. However, beyond $0.1 \Omega\text{cm}^2$, the cell's J_{sc} begins to decrease dramatically because hole extraction even at short-circuit condition is locally deteriorated. At this point, the measured FF begins to recover again until it ultimately reaches its initial reference value. This regime is labeled as 'Poor current collection' as a consequence of extremely high contact resistance. The efficiency declines continuously until it reaches a minimum beyond $R_c > 3 \Omega\text{cm}^2$ where all I-V parameters saturate. In this case, J_{sc} dropped by 18.4 %_{rel} from 36.0 mA/cm² to 29.4 mA/cm² which is close to the worst case sce-

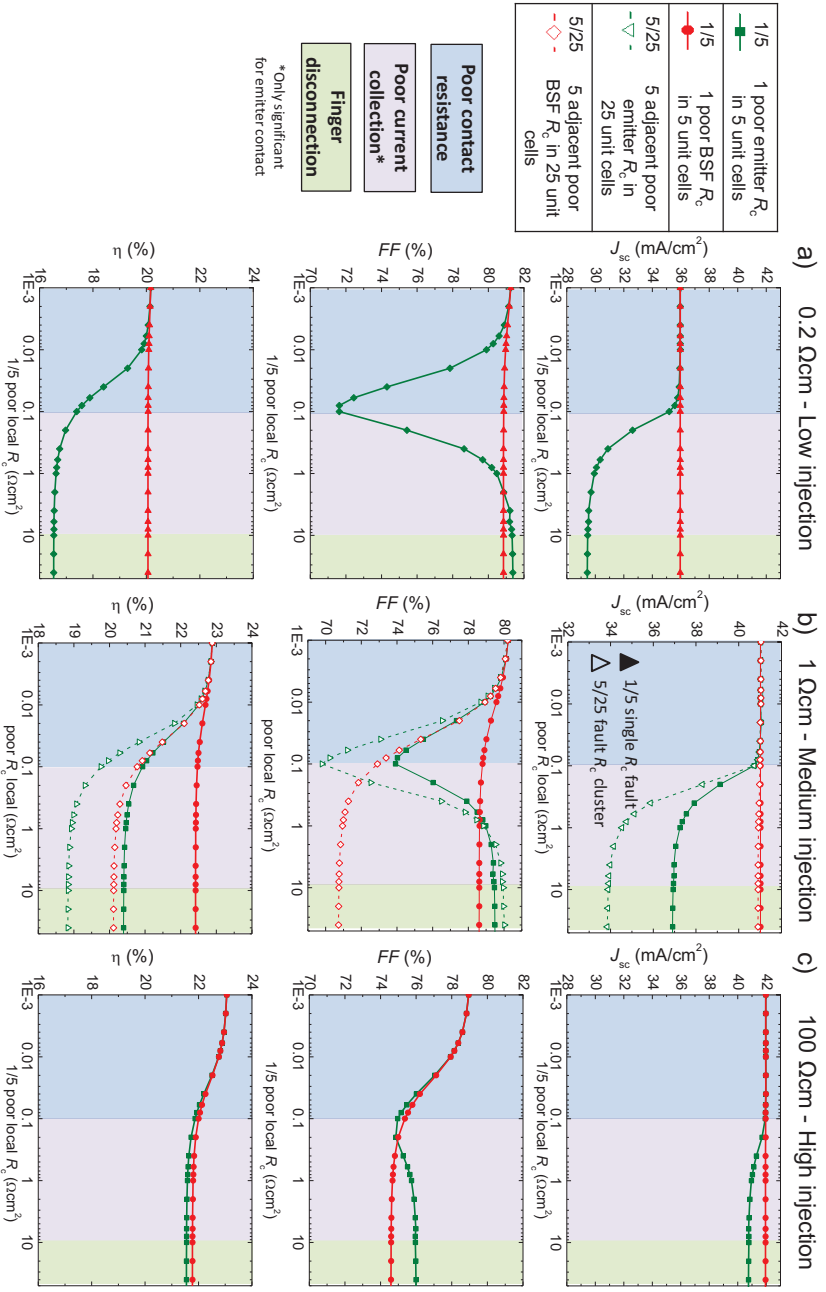


Figure 6.3: Impact on J_{sc} , FF and efficiency of locally increasing emitter (green) or BSF (red) R_c for an IBC solar cell operating at low (a) (0.2 Ωcm), medium (b) (1 Ωcm) and high injection (c) (100 Ωcm).

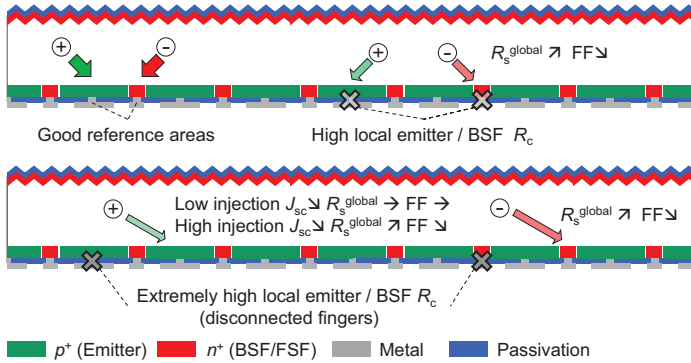


Figure 6.4: Schematic of electron and hole current flows with indications of primary I-V impact for the cases of a high local R_c (top) and extremely high local R_c (bottom).

nario when 20 % of the emitter contacts are unable to extract holes. This is labeled as 'Finger disconnection' since no current can be extracted or injected over that contact. An important consequence of these results is that solar cells in processing may have varying FF and J_{sc} values which may both be caused by local contact resistance faults. An important conclusion is that without spatially resolved analysis, it is not possible to tell if a local R_c is responsible for a drop of J_{sc} .

For low base doping (100 Ωcm) which implies much higher effective lifetimes than (0.2 Ωcm), figure 6.3(c) shows the case of extremely high injection because of reduced Auger recombination. In the 1/5 poor emitter case J_{sc} is also reduced but now only up to 3 %_{rel} despite 20 % of inactive emitter contacts. This is because the extremely high base lifetime (≈ 29 ms) yields a sufficiently high diffusion length for holes to reach the next neighboring emitter region. In the 1/5 poor BSF R_c case, J_{sc} is unaffected despite the high injection. The FF drop for 1/5 poor R_c emitter in the 100 Ωcm high injection case behaves analogous to the 0.2 Ωcm low injection case. However, the FF only slightly recovers even after complete finger disconnection. Therefore, an increased global series resistance is present at MPP which means that holes are subjected to resistance losses. With or

without FF recovery to the initial value, the global efficiency (bottom graphs) in all cases smoothly decreases with increasing local R_c until saturating. Finally, (b) shows the reference $1 \Omega\text{cm}$ case with moderate injection as an intermediate case between (a) and (c). Typically, a base resistivity between 1 and $10 \Omega\text{cm}$ is used for highest efficiency IBC cells [258]. Therefore, high injection effects are indeed relevant.

Global I-V characteristics: fault clustering

Thus far, only the I-V signature of a single local R_c fault in a model cell consisting of 5 unit cells was discussed. Nominally this fault impacts 20 % of the cell. However, series resistance faults may have a different impact on performance when clustered close to each other. This is demonstrated in figure 6.3 (b), where the I-V results for the $1 \Omega\text{cm}$ case with 1 local fault in a 5 unit cell IBC device (1/5, solid lines, full symbols) is compared with the case of 5 adjacent ('clustered') local faults in a 25 unit cell IBC device (5/25, dashed lines, open symbols). In both cases, 20 % of the contact fingers are affected but having several disconnected fingers next to each other increases the required path length for charge carriers to flow through the path of lowest resistance. The impact can be seen in the J_{sc} of the poor emitter case (37 mA/cm^2 for 1/5 and 34 mA/cm^2 for 5/25). Also, the electron flow to the BSF which was almost unaffected by a single disconnected finger shows severe losses in FF when 5/25 adjacent fingers are affected. In experimental application, luminescence imaging allows to quickly localize faults and identify whether the cell faults are individual or clustered. In conclusion, clustered R_s faults are much more detrimental for I-V performance than single faults.

Signature of local R_c faults in R_s^{loc} imaging

In this section, spatially resolved local series resistance (R_s^{loc} , section 4.6) analysis by luminescence imaging is incorporated to study the signature of local R_c faults. Further, the agreement between mean values of R_s images and global values and how taking into account a local short-circuit current density (J_{sc}^{loc} , chapter 3) influences the

results is discussed. These simulations will greatly facilitate the interpretation of experimental results later. The applicability of conventional series resistance imaging using luminescence e.g. by Trupke et al. [137] on IBC cells was demonstrated in section 4.6. The regular contrast pattern of R_s^{loc} profiles in IBC cells can be attributed to lateral transport limitations of both electron and hole transport. The luminescence imaging model, voltage calibration, local series-resistance calculation used in this work was also discussed in detail in sections 4.4 and 4.6. The main equation for R_s^{loc} is 4.11.

Figure 6.5 shows simulated R_s^{loc} profiles of the 1 Ωcm IBC cells for cases where R_c emitter or BSF are homogeneously increased (a), and where 1/5 emitter or BSF contacts suffers from an R_c of 0.01 Ωcm^2 (b), 0.1 Ωcm^2 (c) and 1000 Ωcm^2 (d). Each graph depicts a reference without local fault (black), a locally poor emitter case (green), BSF case (red) and FF data from global I-V simulations. The dashed lines show results including a spatially resolved J_{sc}^{loc} for the denominator in equation 4.11. Even in fault free IBC cells, J_{sc} is typically not homogeneous across the cell due to 'electrical shading' (see section 3.5). From figure 6.5 (a) one can conclude that if all contacts have an elevated R_c , the R_s^{loc} profile receives an offset. Like in the global I-V characteristic, the response of R_s^{loc} profile to a homogeneous R_c^{EM} or R_c^{BSF} fault is identical. The luminescence analysis therefore does not allow a distinction of emitter or BSF problems when R_c of one polarity is globally poor.

In all graphs of figure 6.5 with only locally deteriorated R_c (b-d), a clear spatial symmetry is apparent where the highest R_s^{loc} values occur centered above the fault. This implies that signal symmetry analysis can help in the interpretation of experimental results. The trend of the R_s^{loc} peak values reciprocally follows the FF changes. This includes the asymmetric sensitivity to local emitter and BSF R_c faults. Once the local R_c is practically infinite (d), the BSF fault yields the larger R_s^{loc} effect and thus FF deterioration just as in the global I-V. The inclusion of local J_{sc} information (dashed lines) has only a minor effect on R_s^{loc} profiles for fault characterization with the

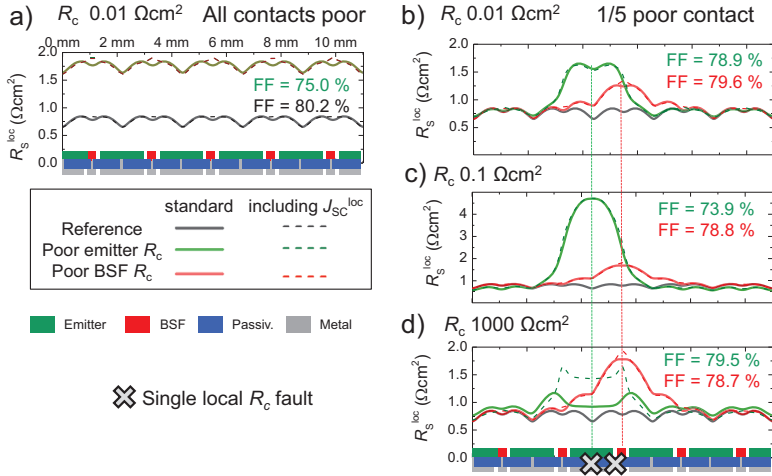


Figure 6.5: R_s^{loc} signature profiles of globally affected R_c emitter (green) or BSF (red) values (a), 1/5 local emitter or BSF fault with various R_c values (b-d). Dashed lines show results with inclusion of spatially resolved $J_{\text{sc}}^{\text{loc}}$ in equation 4.11. The $1 \Omega\text{cm}$ cell is modeled after cell CF1.

exception of the disconnected emitter case (d) where $J_{\text{sc}}^{\text{loc}}$ over the fault is greatly reduced. A smaller $J_{\text{sc}}^{\text{loc}}$ value reduces the denominator value in equation 4.11 and numerically increases the R_s^{loc} . This can have a large effect on R_s^{loc} , especially for cells that are sensitive to local current collection faults. An extremely high R_s^{loc} might lead to contradictions to the global data. By using comparisons to global values, these contradictions will be discussed in the following.

Agreement with global values

Figure 6.6 summarizes the global and mean R_s values obtained from simulations for all three base resistances. Agreement of mean R_s^{loc} with global values by Suns- V_{oc} vs. light-IV method was already shown for fault free IBC cells in figure 4.23. Now a comparison of simulated results obtained by the double-light method (DLM, solid) [37], Suns- V_{oc} vs. light I-V curve (horizontal mesh) [37] and arithmetically averaged R_s^{loc} according to Trupke et. al [137] is presented. For

the latter, homogeneous J_{sc} values are assumed (diagonal lines) or a simulated J_{sc}^{loc} map is used (diagonal mesh). From left to right in figure 6.6, the results for the reference simulations are shown, followed by local R_c values for 0.01, 0.1 and 1000 Ωcm^2 respectively.

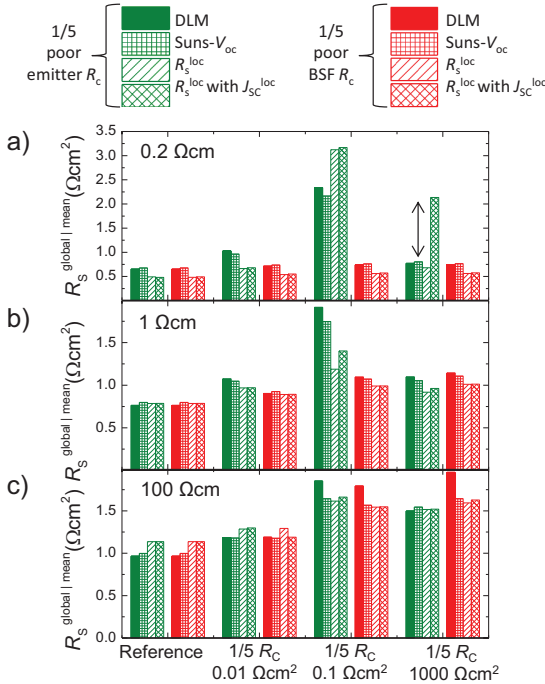


Figure 6.6: Simulated R_s^{global} values using the double-light method, Suns- V_{oc} vs. light I-V method and arithmetic means of R_s^{loc} images without use of J_{sc}^{loc} and with J_{sc}^{loc} for various local emitter (green) and BSF (red) faults and three ρ^{base} values.

The deviations between R_s^{loc} -mean and R_s^{global} are in most cases within the margin of error of physical experiments and thus good agreement is achieved. The agreement between the simulations is however never perfect. As was shown in section 4.6, already the fault free reference case show disagreements between both R_s^{global} and the averaged values from imaging. The discrepancies are thus inherent to these R_s determination methods or the used definition of R_s . All

mean values from the R_s imaging follow the trend observed in the global FF with varying disagreement between 10 and 30 %_{rel}. No systematic behavior of the imaging approaches to exhibit higher or lower R_s^{mean} values than the R_s^{global} methods is observed. The overall agreement is best for the $\rho^{\text{base}} = 100 \Omega\text{cm}$ simulations, which implies that these methods can be used under extremely high injection conditions. The disagreement is highest for $\rho^{\text{base}} = 0.2 \Omega\text{cm}$, where a laterally strongly varying $J_{\text{sc}}^{\text{loc}}$ further influences the signal. As known from I-V simulations, the infinite R_c fault is a resistive fault that is not observed in R_s^{global} but in low J_{sc} . The near zero $J_{\text{sc}}^{\text{loc}}$ increases R_s^{mean} out of proportion (marked by the double-arrow in (a)). If one considers R_s^{global} as a 'correct' reference, the use of a $J_{\text{sc}}^{\text{loc}}$ map leads to contradictions between local and global analysis. However, the use of a $J_{\text{sc}}^{\text{loc}}$ map identifies a resistance fault as the root-cause of the problem. In the end, since only solar cells with ρ^{base} equal to or above $1 \Omega\text{cm}$ are realistic for mass production, one can safely conclude that the R_s^{loc} imaging by PL approach for fault characterization yields sufficiently good agreement with global values to allow quantitative characterization.

6.2.2 Experimental verification

In this section, local series resistance faults are categorized and experimental verification for the conclusions drawn from the previous simulation section is provided. In the real case of solar cell processing, the local resistance related manufacturing faults can be grouped into interrupted or too thin fingers, high contact resistances and ohmic losses from inhomogeneous base or surface diffusions. Since the latter faults occur rarely only locally, only metallization interruptions and contact resistance faults are discussed. Finger interruptions are common when a fine grid metallization is applied e.g. using screen printing [259] or dispensing [260]. High contact resistances are typically caused by poor contact formation between metal and silicon due to inaccurate temperature conditions during contact formation or low doping levels in silicon. The case of an infinite contact resis-

tance occurs when the contact opening of e.g. SiN_x by etching or laser ablation was locally unsuccessful. The luminescence and I-V measurements were carried out in the setup described in section 4.2.

Before presenting solar cells with R_s faults due to unintended inhomogeneous processing, the luminescence imaging signature of well-defined problems is explored. The $1\ \Omega\text{cm}$ solar cells studied here are comparable to the simulation model. Figure 6.7 (a) shows the metallization schematics of cell CF1 that was especially modified for this purpose. The I-V data for the following three states is shown in table 6.3. From the initial state (top), which showed no significant local R_s faults, a $1.2\ \mu\text{m}$ wide interruption at the center of one emitter and of one BSF finger was created by photolithographic patterning and subsequent etching of the Al fingers. Finally the individual emitter/BSF finger were completely etched away (c), thus creating a case of disconnected fingers and hence practically infinite local R_c .

Table 6.3: I-V data for the specially prepared cell CF1 in the initial state, after finger interruption and complete etching of one emitter and one BSF finger. The complete finger disconnection leads to a loss in J_{sc} rather than increased R_s as expected from simulations.

	J_{sc} (mA/cm^2)	V_{oc} (mV)	$\Delta pFF - FF$ (%)	R_s Suns- V_{oc} (Ωcm^2)	$R_s^{\text{loc mean}}$ (Ωcm^2)
Initial	39.2	665	1.9	0.46	0.41
Interrupted	39.3	667	3.1	0.73	0.85
Disconnected	37.2	664	2.6	0.67	0.76

One can observe that the finger interruption does not affect the cell's J_{sc} but significantly increases the $pFF-FF$ difference and R_s^{global} , respectively. The finger disconnection however lowers the cell's J_{sc} . As predicted in the I-V simulations (figure 6.3), the decrease of global J_{sc} results in a partial recovery to the original FF and thus in a decrease in R_s^{global} . Since in both steps an emitter and a BSF finger was etched at the same time, a complete separation of the individual finger's effects on global I-V is not possible in this particular experiment.

Figure 6.7 depicts the luminescence images at J_{sc} (b), MPP (c), V_{oc} (d), R_s^{loc} (e) and an EL image at an elevated forward bias (f) for the 3 states. Image interpretation for the fault free areas can be found in section 4.3. For the evaluation of R_s^{loc} , a constant J_{sc} for equation 4.11 and hence no J_{sc}^{loc} was used, which will be addressed later. The EL images (e) under forward bias clearly show the regions of reduced electrical activity, as charge carrier injection is drastically lowered due to the increased resistance. The finger interruptions are marked by red crosses in (e). The areas within the blue dashed rectangles have been rescaled to allow for observing the vastly increased signal intensities caused by several of the local faults.

The case of finger interruption at J_{sc} condition shows a slightly elevated PL signal in the region of interest 1 (ROI 1) above the emitter finger interruption and no significant effect on the BSF side (ROI 2). At MPP (b) conditions, the PL signal is extremely elevated in ROI 1 and slightly elevated in ROI 2. This indicates severe and slight additional series resistance losses at MPP in the respective regions. The result can be seen in the R_s^{loc} images (e) where the peak value above the impacted regions reaches an R_s^{loc} of $4.8 \Omega\text{cm}^2$ for the emitter and of $0.94 \Omega\text{cm}^2$ for the BSF which is both much higher than the mean of $\approx 0.4 \Omega\text{cm}^2$ in the initial state. As expected, a finger interruption only affects the region away from the respective busbar. Hence, the closer the interruption is located to the busbar the worse the effect on the overall performance will be. At interrupted fingers in the range of the emitter, the detected effects are explained as follows: the total current collected in the affected region has to bypass the metal interruption by flowing through the emitter underneath the metal interruption before reentering the metal finger guiding to the busbar. This non-ideal electrical path causes a high resistive loss in the affected region. Therefore one can conclude, that the longer the finger interruption and the higher the sheet resistance, the more severe the effect of finger interruption will be. Note that metal fingers featuring unintentionally low cross sections (e.g. constricted fingers, thin fingers, narrow fingers) will have a similar basic signature as an interrupted finger.

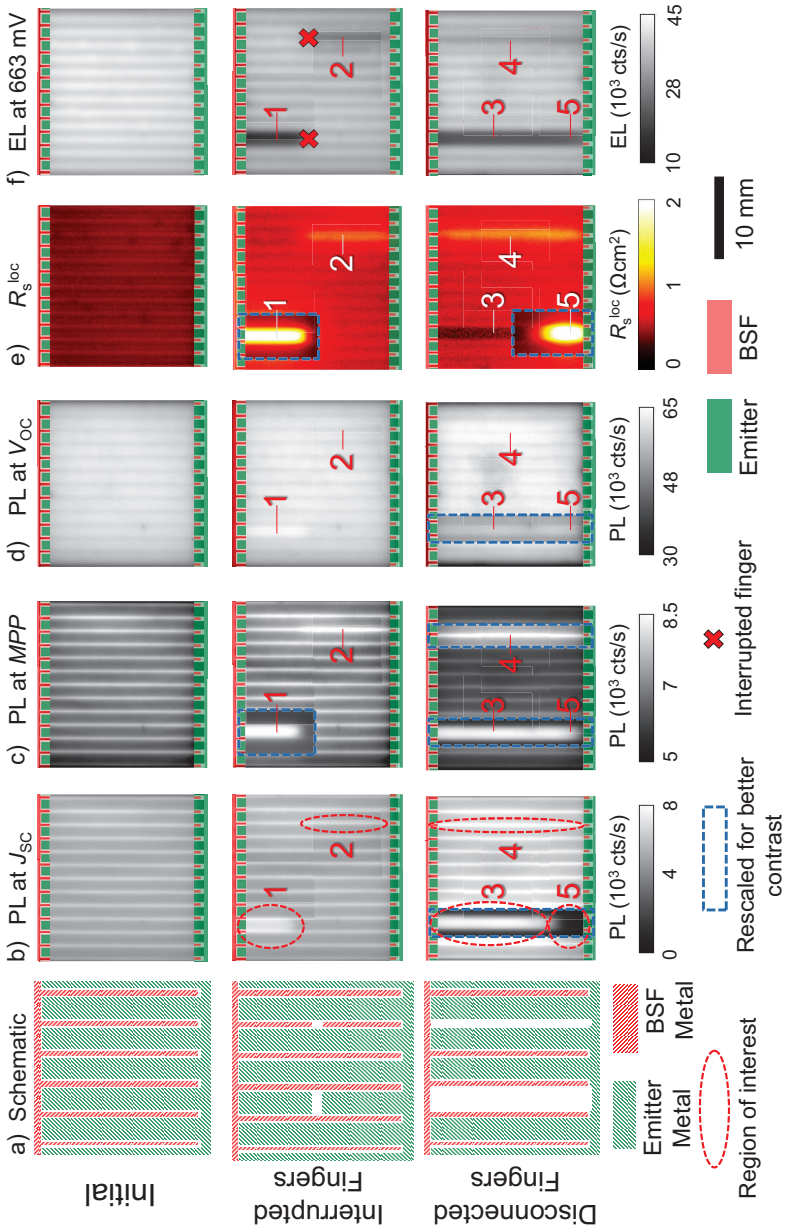


Figure 6.7: Schematics (not to scale) (a) and images of initial, interrupted and final state image of PL at J_{sc} (b), PL at MPP (c), PL at V_{oc} (d), R_s^{loc} (e) and electro luminescence (f). The comparison between J_{sc} and MPP image shows how a completely disconnected finger reduces carrier extraction and thus J_{sc} at short-circuit. This fault in neither observed as an R_c fault in the cell's FF nor in the R_s^{loc} image.

The finger disconnection (infinite R_c along the entire contact opening) acts differently. The PL signal at MPP is extremely high along the entire disconnected fingers both for the emitter (ROI 3+5) and BSF case (ROI 4). The R_s^{loc} image (d) shows an elevated signal all along the disconnected BSF finger. However, for the emitter finger only the last ~ 5 mm before the busbar show an elevated signal (ROI 5), while the rest of the finger (ROI 3) resulted in smaller R_s^{loc} values than the fault free regions and even some negative pixel values which is physically not sensible. As Trupke et al. pointed out, their method is only applicable when the R_s^{loc} values do not significantly alter local J_{sc} extraction [137]. This begins at values of above $\sim 15 \Omega\text{cm}^2$ (see figure 2.5). Thus, the underlying R_s^{loc} values of ROI 3 are expected to be at least higher than $16 \Omega\text{cm}^2$. In ROI 5, just before the emitter busbar, the sheet resistance of the emitter is sufficiently low to extract carriers at short-circuit though. Therefore, ROI 5 acts similarly to an interrupted finger. The behavior of the disconnected emitter in ROI 3 can be understood by the PL image at J_{sc} . In the PL image at J_{sc} , the signal until the last 5 mm before the emitter busbar is extremely high because the cell is locally not actually under short-circuit condition. This is also confirmed by the reduced global J_{sc} from table 6.3. In a first approximation, the R_s^{loc} image is proportional to $\text{PL}_{MPP} - \text{PL}_{J_{\text{sc}}}$. The difference is close to zero in ROI 3 which is why R_s^{loc} is near zero. This could arguably be considered an artifact, since the fault is in fact related to a resistance (here a contact resistance). On the other hand, a low R_s^{loc} in ROI 3 is in accordance to the observations in the global I-V (see figure 6.3), where a disconnected emitter finger does not lead to a higher R_s^{global} . The ambiguity of R_s^{loc} values in regions such as ROI 3 are thus prone to misinterpretations in all R_s^{loc} methods based on the conventional voltage calibration. Note that the global V_{oc} of the cell was virtually unaltered by the etching procedures. However, elevated signals in the emitter regions that became electrically isolated from the metal grid after etching is observed in the PL images. This is not an effect of an actual change in recombination activity at these surfaces, but a

reduction of balancing currents and thus of balancing voltages along the metal fingers [149].

Figure 6.8 shows PL images at J_{sc} of the disconnected fingers under different illumination intensities of below 1 sun. This allows for further understanding the resistive effects of missing metal fingers. Upon reducing the illumination to e.g. 0.32 sun (a), the reduced carrier extraction appears further away from the emitter busbar. This continues for 0.13 sun (b) until at 0.07 sun (c) no sign of fault induced J_{sc} extraction problems is left. A SR-LBIC external quantum efficiency map at 940 nm excitation taken at J_{sc} conditions without bias-light (d) consequently also shows no signs of the etched metal fingers. The lack of bias-light in our setup makes the cell operate at globally very low current. Therefore, the SR-LBIC J_{sc}^{loc} mapping procedure presented in [74] will not result in correct local J_{sc} values under 1 sun illumination which is why using a J_{sc}^{loc} map in equation 4.11 obtained by SR-LBIC according to section 3.3 will not correctly consider the actual fault.

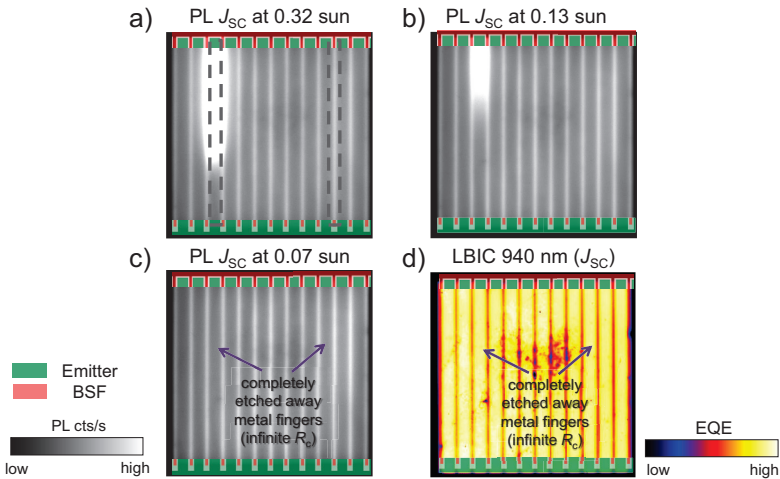


Figure 6.8: Images of a cell with locally disconnected fingers in PL at J_{sc} condition for varying illumination intensities (a-c) and the SR-LBIC EQE at a wavelength of 940 nm (d) measured without bias-light.

Application examples

The findings from the latter experiments and simulations enable to interpret the processing faults of several solar cells fabricated at Fraunhofer ISE with various processing techniques. Figure 6.9 shows luminescence images like in figure 6.7 at the relevant operating conditions, resulting R_s^{loc} as well as a schematic of the local processing faults that are interpreted from these images. The R_s^{loc} graphs contain mean values and globally obtained values which show excellent agreement for all three sample cells.

Figure 6.9 (a) shows cell CF2, a case of locally interrupted BSF fingers, combined with poor local contact resistance of some highlighted BSF contact regions. The PL image at J_{sc} is homogeneous while at MPP , note the strongly increased signals in ROI 6 (equivalent to ROI 2 in figure 6.7). Furthermore, there are several spots in the PL at MPP image (ROI 7), which indicate a locally increased contact resistance. By determining the location of peak signals within the doping pattern of the cell, e.g. using the software ImageJ [261], revealed that these are likely poor BSF contact faults. The R_s^{loc} image quantifies the increase in series resistance at the regions of interest.

In figure 6.9 (b), cell Fi2 with locally poor emitter and BSF contacts is shown. Once again the PL image at J_{sc} appears homogeneous. Using spatial symmetry analysis, one finds that the increased PL at MPP and local R_s signals in ROI 9 can be attributed to increased BSF R_c values while ROI 8 is indicative for an R_c^{EM} fault superposed with an R_c^{BSF} fault. The locally high R_s is much more prominent in ROI 8 than 9, which is why a local rescaling (blue rectangle) was necessary. Further Quokka simulations by the author of this work show that this solar cell design (geometry, base- and sheet resistances) is much more sensitive to R_c^{EM} emitter than to R_c^{BSF} faults.

Lastly, figure 6.9 (c) shows cell CF4, a $1 \Omega\text{cm}$ cell with severe local R_c^{EM} problems. This is an example of extremely poor R_c that even leads to a local disconnection as indicated by the high PL at J_{sc} signal (ROI 10). Locally, the PL at J_{sc} signals of the two leftmost emitter fingers are high but not identical to the PL MPP image as it

was the case for the etched away fingers in figure 6.7. The R_s^{loc} image shows increased R_s over the whole region. However, this is mixed with small dips of lower R_s (ROI 11) where the PL at J_{sc} signal was highest. According to the interpretation in the global I-V simulations, an extremely high local emitter R_c results predominantly in a drop in J_{sc} and not in FF and is hence a current collection and not an ohmic resistance problem.

Section 7.2 presents a comprehensive summary of contacting faults in IBC cells that were classified in this section. These are detailed in a bottom-up (starting from the fault, see figure 7.7) and top-down flowchart approach (starting from I-V measurements, see figure 7.8).

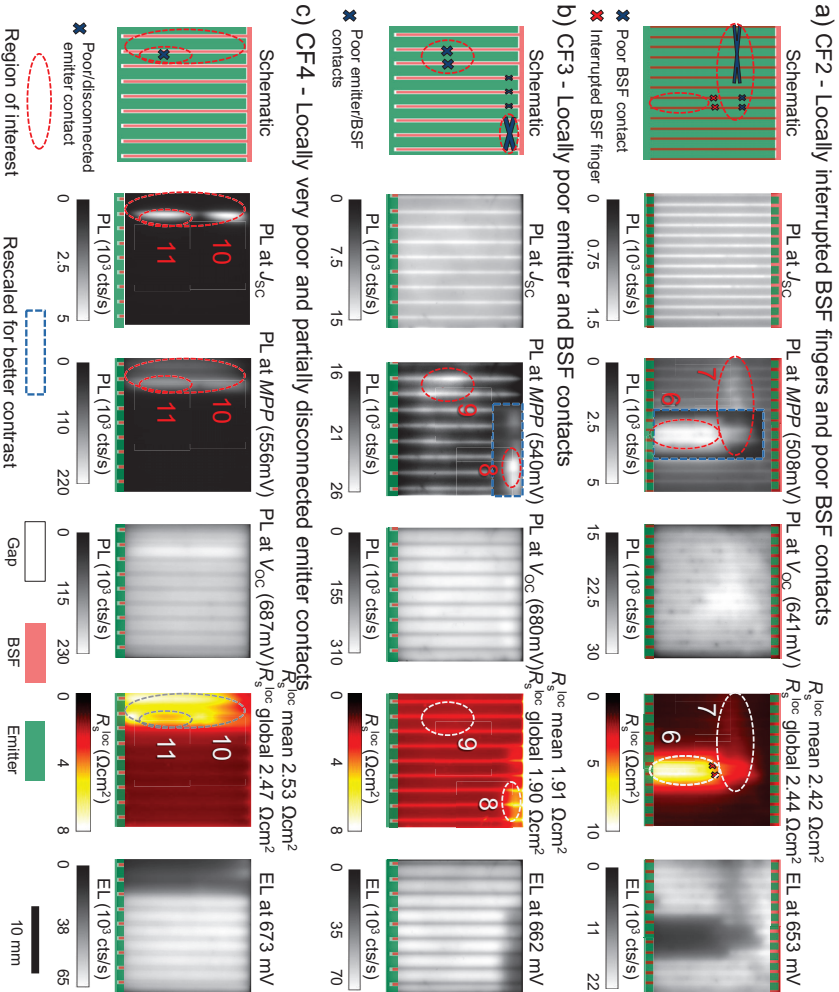


Figure 6.9: Images of PL at J_{SC} , PL at MPP , PL at V_{OC} , $R_{S,loc}^{\text{loc}}$, EL and schematics of the identified local faults for IBC cells with locally interrupted BSF fingers (CF2, a), locally poor emitter and BSF contacts (CF3, b) and locally very poor and partially disconnected emitter contacts (CF4, c).

6.3 Local shunting faults

In this section, two types of typical shunting faults are investigated. Firstly, pinholes in the passivation layers of IBC cells with point-shaped BSF regions (see figure 2.10) are studied with conventional dark lock-in thermography (DLIT). Furthermore, alternative identification by illuminated lock-in thermography and luminescence imaging is attempted. Secondly, a measurement series on spiking is presented where the detrimental effects of growing Al-Si spikes driven by continuous annealing is demonstrated in global I-V data, luminescence imaging and lock-in thermography. Other shunt inducing faults such as cracks and edge shunts are known to be capable of shunting but are not dealt with in this work. All lock-in thermography measurements in this section were performed at $f_{\text{lock-in}} = 30$ Hz (see section 2.3.2).

6.3.1 Pinholes

As introduced in section 2.2, IBC cell passivation layers can be used to electrically isolate BSF metal contact fingers that overlap the emitter regions. This architecture allows for significantly higher emitter coverage fractions at low pitch distances than IBC cells without insulation layers [55]. This design comes with the risk of metallized pinholes that short-circuit the SCR in the case of BSF metal fingers which overlap the SCR. A schematic of pinholes in the cross section of a point-contact IBC cell (figure 2.9 type C) is depicted in figure 6.10. Pinholes are small cracks or holes in the isolation layer that may become filled with metal during metallization. These metallized pinholes can create a direct metal path between emitter and BSF doping and, in consequence, a short circuit of the SCR inducing a strongly detrimental shunt.

The following measurement series was performed on type C cell P1 with overlapping metallization. This cell has square shaped individual 'point' BSF structures. The unit cell has a full pitch of 1000 μm , 460 μm emitter width, 310 μm wide BSF square width and a 115 μm wide gap between emitter and BSF. The BSF and emitter metal fin-

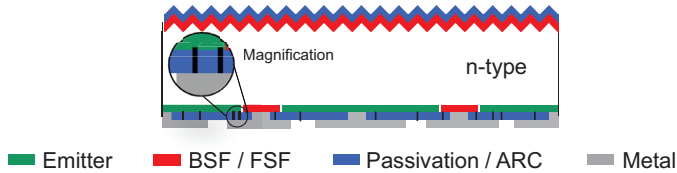


Figure 6.10: Schematic of an IBC cell with pinholes in the rear side passivation layer. The pinholes between the BSF contact fingers that overlap emitter regions may cause shunts.

gers are $340\ \mu\text{m}$ wide, thus an overlay between the BSF metallization and the emitter doping exists which is only separated by the $20\ \text{nm}$ ALD Al_2O_3 , $1500\ \text{nm}$ PECVD SiO and $80\ \text{nm}$ PECVD SiN passivation layer [237]. The global I-V curve, Suns- V_{oc} curve and resulting I-V parameters of cell P1 are shown in figure 6.11. Note that the cell has a very low pFF of $58.2\ \%$ as well as a low V_{oc} compared to the other cells of this cell type, which have a V_{oc} of approximately $650\ \text{mV}$. The I-V data clearly points towards a low parallel resistance R_{p} as the main cause for the low FF and efficiency, according to the diode model (see figure 2.5). According to the low value of R_{s} , the series resistance has only a negligible impact on the FF .

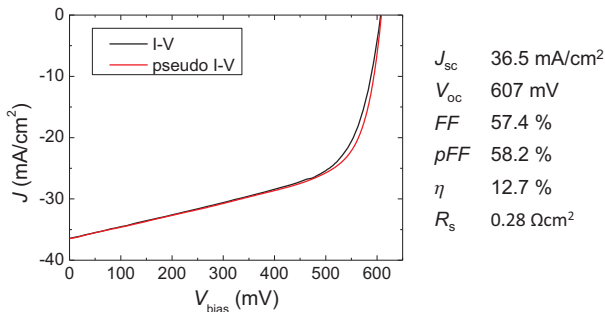


Figure 6.11: I-V and pseudo I-V curve of cell P1 under 1 sun illumination. The linearity of the curves up to $500\ \text{mV}$ and the low pFF indicate severe shunting faults in form of a low R_{p} in the diode model.

Determination of shunt characteristic and local R_p

The standard approach to identify local ohmic shunting on conventional industrial silicon solar cells is to compare current or power calibrated -90° DLIT images¹ at $+500$ mV and -500 mV [206]. Typically $+500$ mV forward bias is sufficiently low so that the DLIT signal from an ohmic shunt does not get mixed with diode-like dark currents (J_0) and -500 mV reverse bias is too low for breakdown behavior (see section 6.5). Figure 6.12 shows the resulting -90° DLIT images. Qualitatively, all spots with a high DLIT signal under reverse bias (a) also appear under forward bias (b) which indicates an ohmic type shunting effect. The images were power calibrated with the procedure explained in section 5.4. A power or current calibration is not mandatory for qualitative identification though. The absence of front side metallization on IBC cells allows an unobstructed quantitative access to the DLIT signal. Emissivity contrasts from the doping structure where found to be negligible in this case.

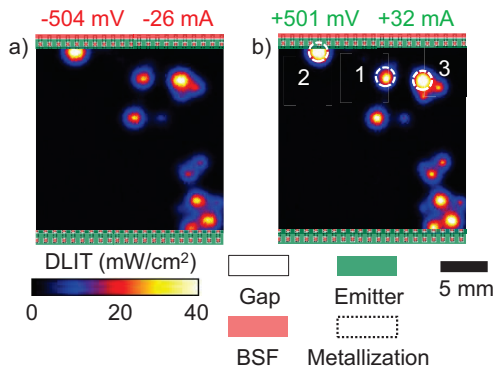


Figure 6.12: Qualitative ohmic shunt detection for cell P1 by comparing the -90° DLIT intensity at -504 mV (a) reverse bias and (b) $+501$ mV forward bias.

The following analysis uses the approach of quantifying the local R_p proposed and conducted by Kasemann [9] on conventional cells. In order to verify the linear I-V behavior and extract an R_p value of

¹See section 2.3.2

the alleged shunts, the mean current densities of the marked circular spots in figure 6.12 for six voltages between -2000 mV and 597 mV are plotted in figure 6.13. The local current density is obtained by dividing the power calibrated image by the applied bias voltage. R_p is then the inverse slope in the linear regime of each curve. The resulting R_p values of this analysis are a function of the chosen diameter of the spot, so spot diameters must be chosen consistently for R_p values to be comparable.¹ A radius equivalent to the thermal diffusion length Λ is suggested by the author (here 1 mm, see table 2.1).

Each shunt resulted in a different parallel resistance with shunt 2 and 3 being more severe than shunt 1. The globally low R_p values are assumed to be caused by pinholes. This assumption is reinforced by the additional imaging analysis in the following. Further confirmation can also be obtained by microscopic analysis at the expense of destruction of the sample [238].

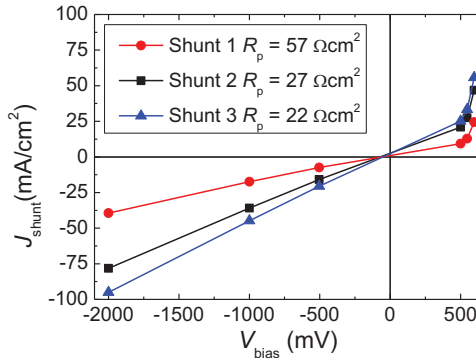


Figure 6.13: Determination of shunt characteristic (here ohmic) and R_p for the 3 shunts marked in figure 6.12. The severity of the shunts can be put quantitatively in comparison with each other.

Since this solar cell is only 4 cm² large, the observed shunts are too detrimental to legitimize installment in a solar module. However, these same shunts in a 243 cm² solar cell could pass I-V flash tester quality control but present a severe risk for hot spots on the field

¹Choosing a larger ROI diameter reduces the mean current density of the spot and thus result in a higher (better) R_p value.

[191]. Importantly, spatial inhomogeneities from the local Peltier effect present in DLIT (see section 5.3) were not found to be an obstacle for this fault analysis. This is likely, because significant current densities are only flowing through the shunts of this cell.

Sensitivity of PL, EL and ILIT measurements to pinholes

The previous sub section established DLIT as the reference technique for ohmic shunt detection also for IBC cells. The following results present an analysis on the sensitivity of PL and ILIT for the detection of these ohmic shunts. The results are summarized in figure 7.9 of discussion section 7.2.

Literature with focus on conventional solar cells shows that luminescence imaging techniques are in principle sensitive to detect shunts but an accurate quantification in practical application has not been achieved yet. Shunts act as recombination sites into which a recombination current flows, effectively reducing the surrounding excess charge carrier density and thus PL signal. The drop in the PL signal is however a function of the injection level and resistivity of the surrounding base and surfaces [262]. Again for IBC cells, the luminescence signature of a shunt is not obstructed by a metal finger on the rear side.

Figure 6.14 depicts PL images under 1 sun illumination at J_{sc} (a), MPP (b), V_{oc} (c), and EL under forward bias (d). The J_{sc} and MPP image are not sensitive to the shunts and only show diffusion limited carriers and R_s effects, but no local faults (see section 4.3.1). Not being able to see the shunts under these conditions does not mean that they are not active, since the I-V performance is particularly affected by ohmic shunts at MPP or pseudo MPP , as was shown in figure 6.11. A tentative explanation for this phenomenon is that the injection level at J_{sc} and MPP is low enough, so that lateral balancing currents within the emitter (which is entirely connected for cell type C) pin the carrier density to a set level. This makes the individual shunts not resolvable.

In the PL V_{oc} image (c) as well as EL (d), the shunts known from DLIT are visible as dark spots. When comparing the signal

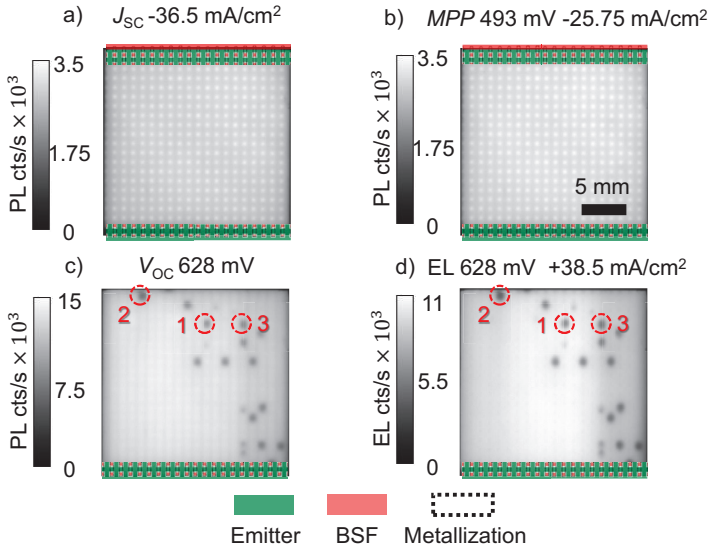


Figure 6.14: PL images of cell P1 at J_{sc} (a), MPP (b) V_{oc} (c) under 1 sun illumination and EL under forward bias (d). Only the V_{oc} and EL images are sensitive to the pinhole shunts but quantitative correlation with the R_p analysis presented in figure 6.13 failed.

intensity of shunts 1, 2 and 3 quantitatively with figure 6.13, the signal intensity could not be correlated to the differing R_p values. The three shunts have an equally low PL/EL signal, although figure 6.13 showed a clear difference between e.g. shunt 1 and shunt 2.

To further explore the sensitivity of the available imaging techniques to pinholes, figure 6.15 shows Illuminated lock-in thermography (ILIT) images at 0.5 sun (a), 0.14 sun (b) and PL V_{oc} images at 0.5 sun (c) and 0.2 sun (d). On standard silicon solar cells, ILIT at V_{oc} conditions is known to be sensitive to ohmic shunts [70]. The shunts in cell P1 identified from DLIT in figure 6.12 are also visible in V_{oc} ILIT, because the recombination sites lead to local heating. Under 0.14 sun (b), hence low illumination intensity, these shunts appear as well. The lower signal to noise ratio (SNR) in (b) is due to the reduced total generated carrier density that recombines. Furthermore, as demonstrated in simulations in section 5.3.2, the V_{oc} condition is

the least influenced by the Peltier effect and thus not a concern for this qualitative data analysis. Therefore, contactless detection of local shunts using ILIT is an applicable alternative to DLIT for IBC cell analysis.

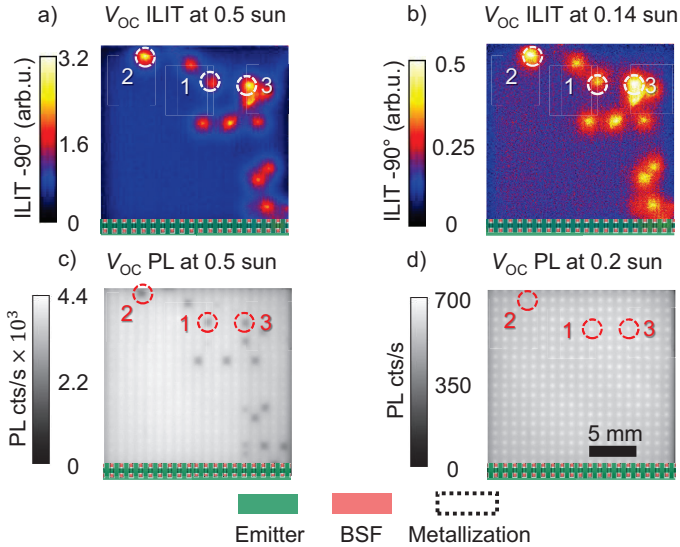


Figure 6.15: ILIT and PL images of cell P1 under V_{oc} conditions for several illumination intensities below 1 sun. The shunts are always detectable using ILIT whereas using PL, the lateral balancing currents are thought to blur the dark spots at low injection conditions.

For the injection dependent V_{oc} PL measurements, the dark spots observed under 1 sun illumination are also observed at 0.5 sun (c), but at 0.2 sun (d) no signs of pinholes are visible in the image. The I-V data and the ILIT images prove that these shunts are active. The seeming absence of shunts in the V_{oc} PL image at 0.2 sun further suggests that low injection conditions also completely blur the recombination effect in the image, which may lead to the contradictory conclusion that no shunts are present in the active cell area. This suggests the usage of high illumination intensities of at least 1 sun to detect pinhole and other ohmic shunting using PL at V_{oc} conditions. Thus PL V_{oc} and EL measurements can be utilized to qualitatively

detect pinholes, but not for a quantitative analysis as it was also found for conventional silicon solar cells [230].

Precise localization of pinholes

High spatial resolution is typically desired when studying local processing faults, especially in the case of microscopic pinholes. Compared to PL, DLIT was demonstrated to be superior for the quantitative evaluation of ohmic shunts. However, the trade-off between thermal blurring and SNR (see section 5.2) make PL the superior technique for precise localization of shunts if visible in the images. That is because in PL one may profit from the regular pattern of the J_{sc} PL image that indicates the exact BSF locations from the diffusion limited carriers (see section 4.3.1).

Figure 6.16 shows an overlay of the PL J_{sc} and V_{oc} images at 1 sun. The quantitative information is lost from overlaying but it becomes clear that the dark spots are only located between two BSF dopings and along the BSF metal fingers as expected for pinholes creating ohmic shunts. Such high quality spatial correlation is difficult and time consuming to achieve using LIT. Note that there may be more pinholes on other parts of the passivation layer that do not induce ohmic shunts.

6.3.2 Spikes

The high solubility of silicon in aluminum may lead to an undesired issue in IBC cells metallized with aluminum: the so called 'spikes'. Spikes originate from a thermally activated dissolution of silicon in aluminum and a penetration of aluminum into silicon in consequence [240]. Thermal processes after metallization are often a necessity to activate the passivation layers and to form the contacts between electrodes and the semiconductor [263]. The growth of spikes may also influence contact formation [241]. However, these spikes may also grow beyond the heavily doped layers into the base and induce shunting. The latter effect is observable in a reduced V_{oc} and pFF . Spikes may penetrate towards the space charge region of a solar cell

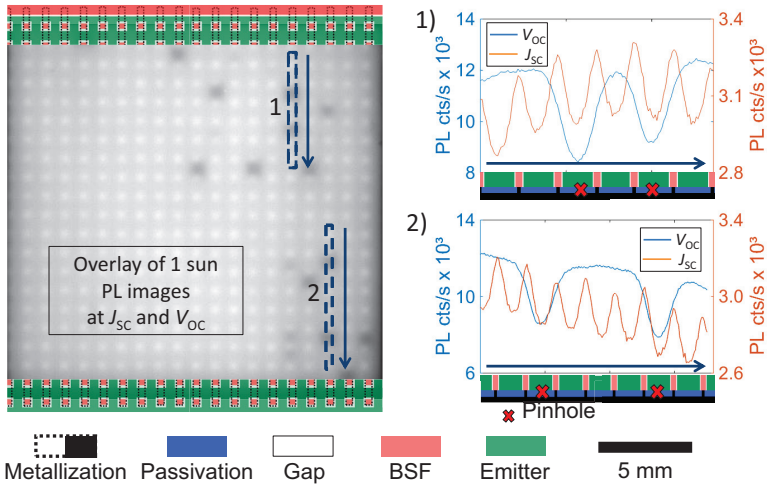


Figure 6.16: Shunt location determination by overlaying a PL V_{oc} with a PL J_{sc} image. The line scans of ROI 1 and 2 further confirm that the pinholes are only located between two BSF diffusions and along the BSF metal fingers.

device and are therefore able to induce a major ohmic shunt. In case of spiking towards a high/low junction (BSF/base) an increase in recombination underneath the metal contact might be expected. First, due to the increase in the metallized surface, second, due to the short-circuit of the field effect passivation.

Figure 6.17 shows a schematic cross section of IBC cells with 'shallow doping' (a) and 'deep doping' (b) and an SEM micrograph (c) of an IBC cell cross section where a few small and one large spike can be identified from the image contrast. When the diffusion profiles reach several μm into the cell, shunting is less likely to occur. The SEM micrograph was adapted from Keding et al. [237], whose solar cells are investigated by the author in the following.

Experiment

In the following measurement series, two cells with doping profiles differing in depth are investigated. Cell S1 is a co-diffused IBC solar cell produced by R. Keding as described in [55, 237]. Cell S2

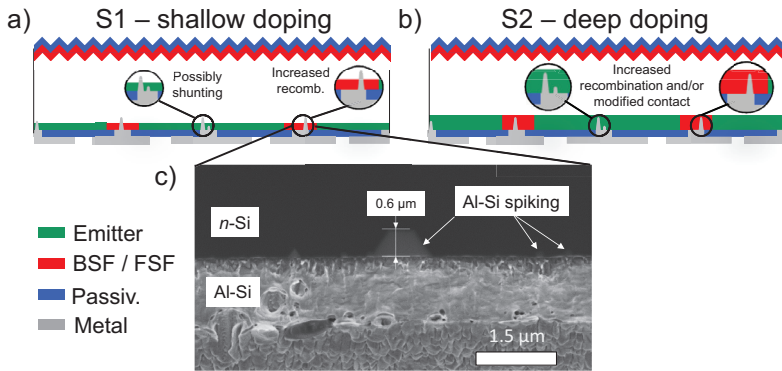


Figure 6.17: Schematics of Al spikes growing from the electrode towards the contact opening into the silicon base of the IBC cell S1 - shallow doping (a), cell S2 - deep doping (b), and an SEM micrograph (c) adapted from Keding et al. [237] depicting the cross section of an IBC cell as those investigated in the following.

was produced in the same way but experienced an additional high temperature 'drive-in' process that deepens the doping profile and decreases the surface doping concentration. In this particular case the emitter depth is increased from about $0.6 \mu\text{m}$ to $0.8 \mu\text{m}$. Before the measurement series, both cells were tempered once to achieve a good contact resistance and passivation quality according to experiments by R. Keding. For this, cell S1 was tempered for 2 minutes at $385 \text{ }^\circ\text{C}$ and cell S2 for 2 minutes at $400 \text{ }^\circ\text{C}$. This marks the initial '0 minutes' state. The objective of this experiment is to induce the growth of spikes through additional temper steps and understand how the impact of spiking on the global I-V performance can be observed in luminescence and lock-in thermographic imaging. The additional temper steps were carried out on a hotplate at a temperature of $400 \text{ }^\circ\text{C}$. Global I-V and spatially resolved measurements were conducted in the initial state and after a time of 1, 2 (+1), 4 (+2), 8 (+4), 12 (+4) and 16 (+4) minutes on the hotplate.

Current-voltage results and analysis

Figure 6.18 shows the development of the global current-voltage parameters J_{sc} (a), V_{oc} (b), FF (c), pFF (d), R_s^{global} from $Suns-V_{oc}$ (e) and η (f) as a function of the additional annealing time t_{HP} . The I-V performance of both cells changes over time, but for S1 with its shallow doping, the efficiency decreases severely.

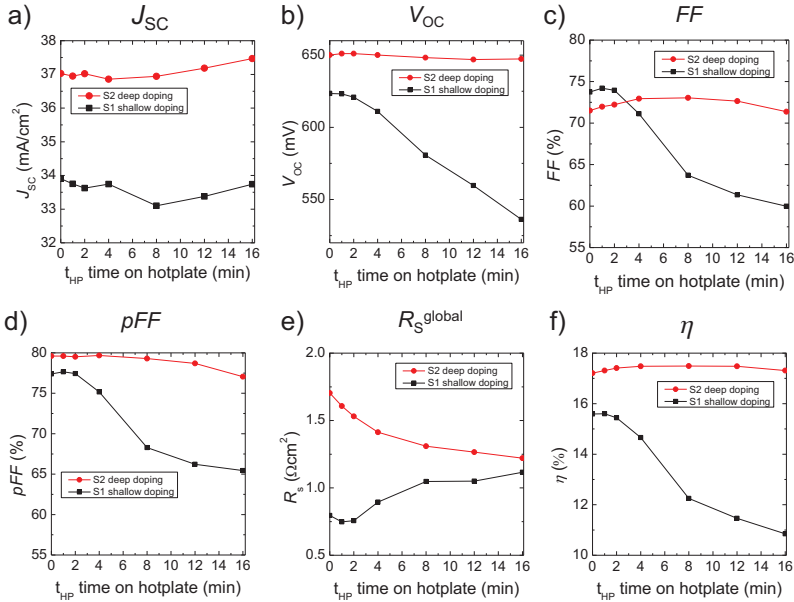


Figure 6.18: Global I-V performance development of cell S1 (shallow doping, black) and S2 (deep doping, red) over the time on the hot plate at 400 °C. The shallowly doped cell quickly suffers a massive performance loss from increased recombination (low pFF , V_{oc}). The deeply doped cell first improves in FF , most likely by a reduced contact resistance, before eventually showing increased recombination as well.

After an annealing time of one minute, S1's V_{oc} decreases steadily as does its pFF and hence also its FF . Compared to these significant correlations, the J_{sc} remains almost constant.¹ The overall efficiency

¹Note measurement uncertainties which originate from e.g. the calibration of the UV-lamp, temperature, placement of the cell on the measurement chuck and the number of measurement cycles of the particular cell over several days.

drops from 15.6 % to 10.9 %. Cell S2 on the other hand shows no significant decrease in V_{oc} and the pFF only begins to decrease after 8 minutes on the hotplate. In fact, the efficiency slightly increases during the first 8 minutes because of the increasing FF , presumably caused by improved contact formation (lower R_c , see R_s^{global} (e)). However, the global series resistance of S1 does not decrease and increases instead, likely because of a deterioration of the contact quality. Note that S1 starts at a much lower R_s^{global} value than S2, presumably because S2 has a lower surface doping concentration and therefore a higher R_c .

Shunting is typically observed in the global I-V curve as a low parallel resistance if it is ohmic or a high J_{02} if it is non ohmic. Either way this impacts foremost the pFF . The decreasing pFF and the fact that the shallowly doped cell was deteriorated much quicker than the deeply doped cell is a strong indicator for spiking. Dark-IV measurements at 0.5 V forward bias of cell S1 yielded 2 mA/cm² in the initial state and 17 mA/cm² after 16 minutes on the hotplate. At the same time, the current at -0.5 V reverse bias remained < 2 mA/cm². Equivalent values were measured for cell S2. Therefore, the presumed shunting due to spikes does not bear an ohmic but rather a diode-like behavior as in a Schottky barrier [41].

PL imaging results and analysis

In the following, PL imaging results are presented that were acquired in parallel to the I-V measurements in order to observe the creation of spike induced shunting through imaging analysis.

Figure 6.19 shows PL images under V_{oc} conditions for the shallow doped cell S1 in the initial state (a), after 1 minute (b), 2 minutes (c) and 4 minutes (d). The graphs below each image contain averaged line scans over the marked ROI across several representative unit cells. Note that all images are scaled to the same counts per second (cts/s). The contrasts across the doping structures are related to the differences in surface recombination (J_0) as explained in section 4.3.1. Note that the signal over the emitter is already lower than the signal over the BSF in the 'initial' state (a), although lifetime

samples had predicted $J_0^{\text{EM}} = 92 \text{ fA/cm}^2 < J_0^{\text{BSF}} = 127 \text{ fA/cm}^2$ (see appendix A). This indicates that spiking may have already started after the default thermal process to activate passivation. No individual dark spots appear over time but instead the absolute signal begins to decrease significantly after 2 minutes. After 4 minutes the line scans reveal that not only the signal decreased everywhere, but that there is also an increasing contrast between emitter and BSF region. τ_{eff} over the emitter region appears to have dropped, which could be caused by spikes passing through the emitter diffusion. It is likely that these spikes emerged at a high density, which could not be spatially resolved by macroscopic PL imaging. Note that while emitter contact spiking is always more detrimental, this analysis does not prove whether spikes at the BSF contact also lead to increased recombination. No further images of cell S1 are presented in this work, as they all show this 'homogeneous' deterioration.

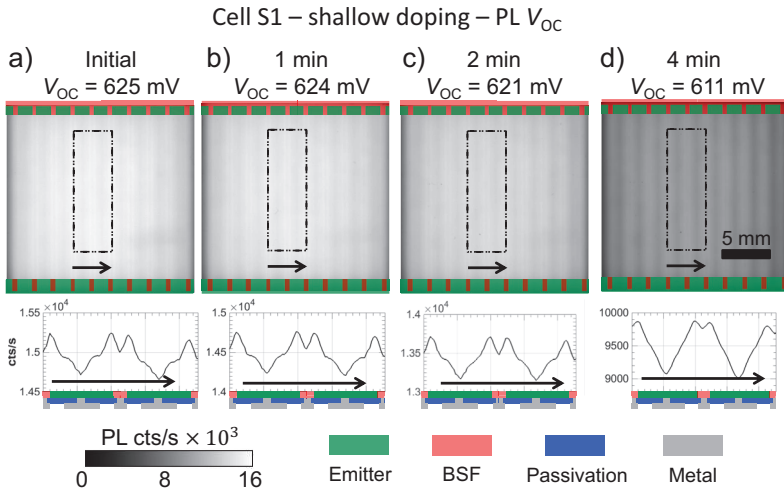


Figure 6.19: V_{oc} PL images of cell S1 (shallow doping) in the initial state (a) and after an annealing time of 1 (b), 2 (c) and 4 minutes (d) on the hotplate at $400 \text{ }^\circ\text{C}$. The PL signal over the emitter contact decreases and the contrast between emitter and BSF contact increases with the tempering time, most likely due to spikes penetrating through the emitter diffusion and inducing shunts.

In figure 6.20, the equivalent V_{oc} PL images for deep doped cell

S2 are depicted in the initial state (a) and after 4 minutes (b), 8 minutes (c) and 16 minutes (d) respectively. The rectangular ROI marks the averaging area for the line scans. Some dark spots of increased recombination are already noticeable in the initial state. After 4 minutes, when cell S1 was already greatly deteriorated, cell S2's V_{oc} and pFF remain stable. V_{oc} and the PL intensity increase slightly. This is expected to be caused by a slight increase in the passivation quality. After 8 minutes (c), first indications of increasing recombination at some emitter contact areas appear (see ROI 1 and 2). After 16 minutes, line-shaped areas that were barely noticeable in the luminescence image after 8 minutes become dominant (see ROI 1 and 3). These critical areas appear as dark lines and are likely the first spikes that pierce the emitter and induce a locally increased recombination. The rectangular ROI shows an example of a line with gradually decreasing PL signal over the emitter contact, as it occurred everywhere in cell S1. The spikes appear without a clear pattern, as their formation is expected to be highly sensitive to the local composition of the Al, the local depth of the doping profile, the local topography of the interface between Al and Si, and local non-idealities like residuals at the interface. Note that the global V_{oc} is unaffected within the margin of error and only the pFF decreases significantly. This is yet another indicator of shunting behavior.

PL images at J_{sc} conditions of both cells only showed typical diffusion limited carrier patterns (see section 4.3.1) and no significant changes of these patterns over t_{HP} was observed (images not shown). This is also in accordance with the global I-V measurements. The PL MPP and R_s^{loc} images however revealed various features for cell S2. Figure 6.21 shows the PL MPP (left) and R_s^{loc} images for cell S2 again in its initial state (a) and after 4 minutes (b), 8 minutes (c) and 16 minutes (d) on the hotplate at 400 °C. The R_s^{loc} images were obtained as described in section 4.6. As introduced in section 4.3.1, the PL MPP image exhibits here effects of contact resistance and also recombination due to the spikes. Also, the PL MPP signal decreases

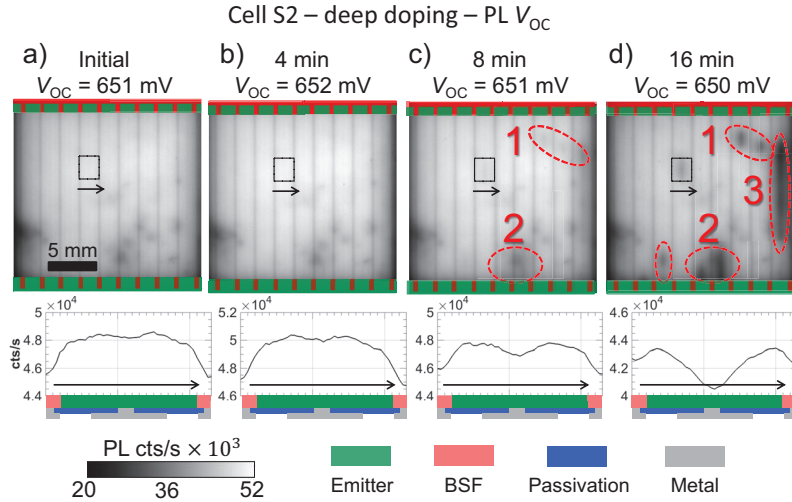


Figure 6.20: V_{OC} PL images of cell S2 (deep doping) in the initial state (a), after 4 minutes (b), 8 minutes (c) and 16 minutes (d) on the hotplate at 400 °C. After 8 minutes, dark lines of increased recombination begin to appear over the emitter contact. This increased recombination effect indicates spiking, as also the cell's pFF decreases.

after the hotplate step.¹ This decrease in PL signal could be caused by improvements in series resistance as well as deterioration of the pFF . The global pFF and R_s^{loc} values in the figure show that both effects happen in parallel: the recombination increases slightly while the series resistance decreases significantly. Also, the PL image after 16 minutes exhibits some of the dark lines observed in the PL V_{OC} image from figure 6.20 (d) marked in red. Note that the PL intensity at MPP and the pFF decrease with the temper time. The global V_{OC} on the other hand stays nearly constant. This indicates that the deterioration is, as expected, most severe at low illumination levels as expected from spiking defects in the SCR, which can be described by an increased J_{02} .

¹Note that PL MPP images (c,d) are scaled differently than (a,b).

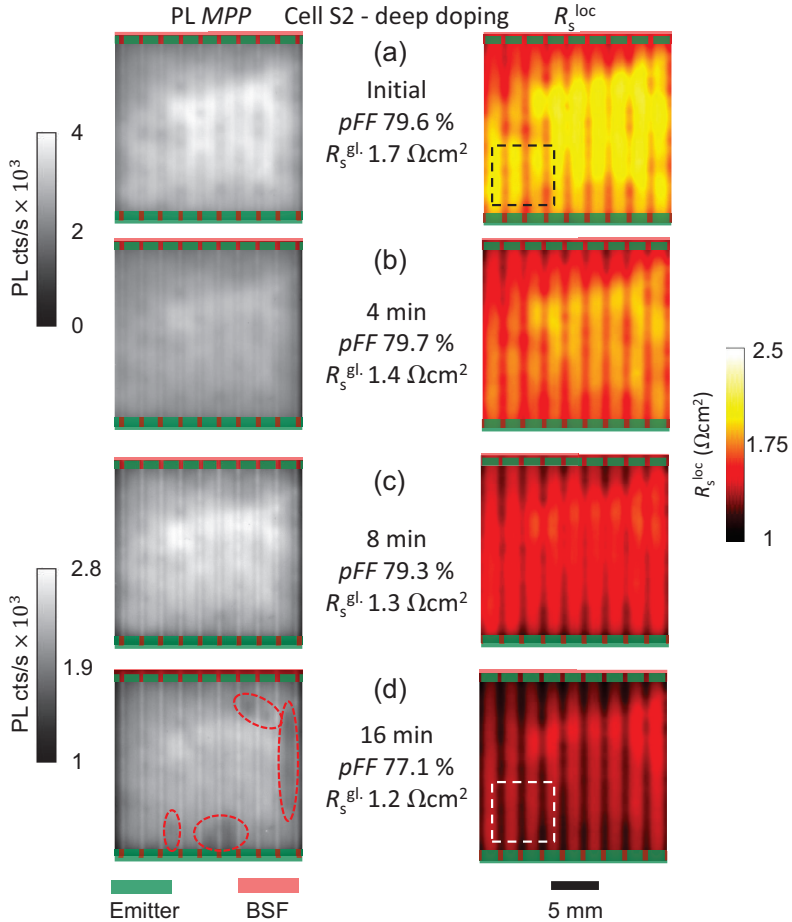


Figure 6.21: PL MPP (left) and R_s^{loc} (right) images of cell S2 (deep doping) in the initial state (a), after 4 minute (b), 8 minutes (c) and 16 minutes (d) on the hotplate at 400 °C. The R_s^{loc} analysis confirms the improved contact formation for the deep doped cell, which correlates with the FF and R_s^{global} improvements.

A separation between recombination and resistance effects at *MPP* becomes possible with the R_s^{loc} image analysis on the right of figure 6.21. The images show how in the initial state, the local contact resistances were high and also not homogeneous. As the temper process continues, the local contact resistance decreases everywhere and becomes more homogeneous as can be seen in the regular patterns (compare dashed rectangle in (a) with (d)). This analysis explains the initial increase in FF due to lower R_s^{loc} and later decrease due to the lower pFF . The highest efficiency of cell S2 was achieved after 8 minutes on the hotplate. Given that the pFF only slightly changed, the major decrease in PL signal at *MPP* is likely dominated by lower series resistance hence improved charge carrier collection.

EL and DLIT imaging results and analysis

PL imaging has successfully proven its capability for the local detection of shunts such as spikes. Moreover, the PL images correlate very well with the global I-V data of the IBC cell. In the following, EL imaging as well as DLIT is applied to cell S2 to assess these alternative imaging techniques' sensitivity to spikes. Figure 6.22 shows an EL image of cell S2 under forward bias (a), a DLIT 0° image (b), and corresponding power scaled DLIT -90° (c) image under forward bias as well as $f_{\text{lock-in}} = 30$ Hz of cell S2 after 16 minutes on a hotplate at 400°C . As observed for the pinhole shunts in section 6.3.1, the EL image shows dark lines in regions of high recombination which are similar to V_{oc} PL images. The power calibrated DLIT -90° image (c) indicates regions of increased dark recombination (ROI 1, 2 and 3). Unlike luminescence, this yields a quantitative value to the local power dissipation under these operating conditions.

Although it has little quantitative information, the DLIT 0° image bears a very high spatial resolution and is sensitive to the spikes, as they are point or line heat sources (see section 5.4). The reverse bias DLIT images resulted in no signal, since as mentioned earlier, these spikes do not behave ohmically and show no significant current flow under reverse bias. The DLIT images also show other regions of increased and inhomogeneous power dissipation (ROI 4). This

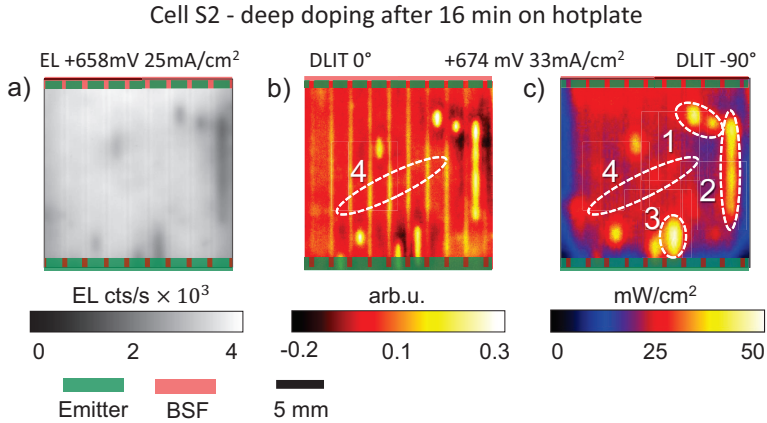


Figure 6.22: EL image at 658 mA/cm² forward bias (a), DLIT 0° image (b) and corresponding power scaled DLIT -90° (c) image at 674 mV and $f_{\text{lock-in}} = 30$ Hz of cell S2 after 16 minutes on a hotplate at 400 °C. The spikes appear as dark stripes in EL and bright spots in DLIT. The DLIT 0° image allows qualitative identification of these lines at high spatial resolution.

however is very likely not a spiking effect but a consequence of inhomogeneous R_s^{loc} , as determined in figure 6.21. It is known that areas with a high R_s^{loc} are correlated with a low DLIT signal, because less current is injected in those areas. This effect makes DLIT prone to misinterpreted inhomogeneities [122]. It can be concluded that PL, EL and DLIT is suitable for qualitative identification of local spiking. An overview of sensitivities and recommendations for practical application is presented in section 7.2.

6.4 Optical and passivation faults

Thus far in this chapter, resistive (section 6.2) and shunting type (section 6.3) processing faults were investigated. Another very common group of faults are related to the local passivation quality and optical reflection. In this regard, the IBC cell structure yields no significant difference to conventional solar cells because it is not directly related to IBC charge carrier distribution and current flow. This is why this topic is only treated briefly in this work.

First a brief introduction with established knowledge from literature: Inhomogeneities of front or rear side SiO_2 or Al_2O_3 passivation layers with non-homogeneous layer thickness, surface charges and/or scratches result in locally increased recombination as a function of the injection level, wafer and passivation material [103]. On a global level, Suns- V_{oc} measurements are a common way of assessing passivation quality of finished cells. However, it is challenging to distinguish between shunting and passivation quality, because both increase recombination. On a local level, passivation quality can be assessed by PL imaging at V_{oc} conditions.¹ To some extent, the IBC cell structure allows a distinction of front and rear side faults because low signals precisely along lines located over the emitter contact center are unlikely to originate from front side effects (see figure 6.20). A poor front side passivation quality also affects J_{sc} and is hence observable in SR-LBIC, especially for cells with a minority carrier collecting pn-junction located at the rear side like IBC cells.

On the other hand, inhomogeneous deposition of layers and/or scratches of a SiN_x anti reflective coating (ARC) reduce the local current generation, thus affecting J_{sc} . These two processing faults are often interrelated, as hydrogen in SiN_x can enhance the surface passivation quality [264–266]. Faults related to ARC and/or surface texturing are best studied with EQE and reflection measurements, because optical parameters of the front and rear side can be obtained by fitting of the reflection curve's data. SR-LBIC mapping yields higher spatial resolution than conventional monochromatic EQE and reflectivity setups at the expense of a limited number of wavelengths. As was shown in an extreme example in figure 3.3, SR-LBIC and the developed $J_{\text{sc}}^{\text{loc}}$, pseudo- $J_{\text{sc}}^{\text{loc}}$ and optical reflection loss mapping is an excellent tool for the detection of optical inhomogeneities as well as their impact on J_{sc} .

¹An increased surface recombination lowers the PL intensity, as was shown in the sensitivity analysis in section 4.5.1.

Example

In the following, an example of an IBC cell is presented where both optical and recombination losses from severe scratches on the front side are studied using luminescence, SR-LBIC and simple photography. Figure 6.23 shows an IR photograph in the PL setup (a), PL image at V_{oc} (b), SR-LBIC reflection at 780 nm (c) and SR-LBIC EQE at 780 nm of cell OP1. The IR photograph was taken inside the luminescence setup as described in section 4.2.

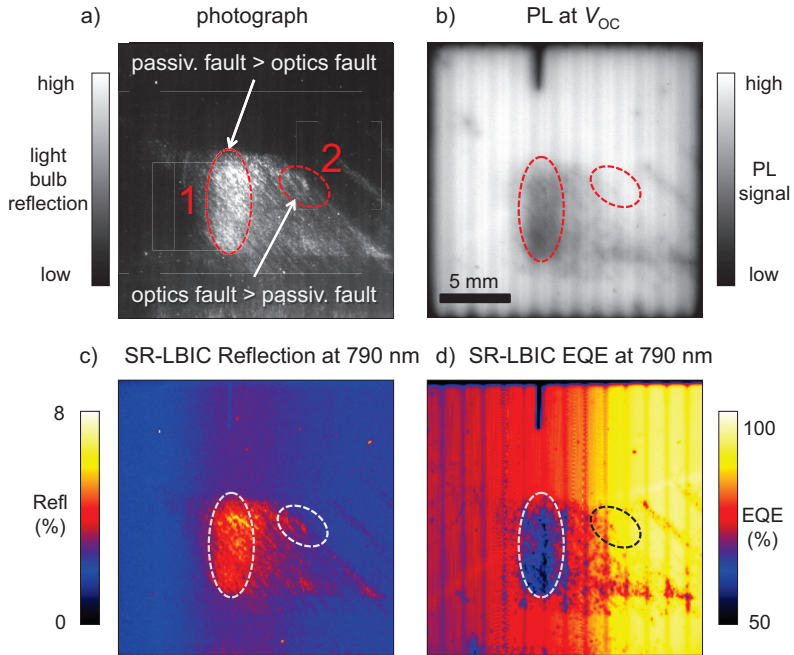


Figure 6.23: IR photograph taken in the PL setup (a), PL image at V_{oc} (b), SR-LBIC reflection at 780 nm (c), SR-LBIC EQE at 780 nm (d) of cell OP1. Severe scratches are noticeable in the photograph and the reflection map. Some of them increase local recombination and thus lower V_{oc} and also lower EQE.

Clearly, ROIs 1, 2 (dashed ellipses) and several other regions of the cell show an increased reflection. The high reflections in (a) presumably stem from scattered reflection on a scratched surface. Scratched

areas can influence both optics and passivation quality. In the PL V_{oc} image (b) contrasts in the scratched areas are visible but the scratches of ROI 2 do not appear as a contrast in the PL image. This indicates that ROI 1 is more detrimental to V_{oc} than ROI 2. Higher reflection is also noticeable as an increased signal in the SR-LBIC reflection from about 2 %_{abs} to 5 %_{abs} (c). The SR-LBIC EQE map at 780 nm¹ (d) however shows much higher contrasts than the reflection image, where the EQE in ROI 1 drops from 70 %_{abs} in reference emitter areas down to 55 %_{abs} and thus by over 25 %_{rel}. Consequently, the IQE map of this cell looks mostly like the EQE map and the cell has predominantly a passivation rather than an optical problem.² The PL V_{oc} image shows a good qualitative correlation with the EQE map. When using PL imaging, the signal contrast may stem from inhomogenous generation so there is a small risk of misinterpreting optical faults and passivation faults.

In conclusion, SR-LBIC EQE and reflection measurements are the recommended methods to assess optical and passivation faults, because of the incorporated quantitative reflection information. PL imaging is a useful alternative to SR-LBIC. The use of further visual inspection tools [267] can prevent misinterpretations.

¹Chosen for best comparison with the optical PL excitation at 790 nm

²Note that the increase in EQE in (d) from left to right across the cell is likely an artifact from instability of the measurement system.

6.5 Breakdown patterns

To conclude this chapter on local faults in IBC solar cells, this section deals qualitatively with pn junction breakdowns observed in luminescence imaging. Local breakdowns under reverse bias voltage can be extremely sensitive to processing inhomogeneities. These inhomogeneities do not necessarily have a detrimental impact on the global I-V data of the cell under forward bias. However, it is useful to characterize the breakdown behavior of solar cells because under partial shading conditions in a solar module, breakdowns may lead to irreversible damage to the solar cells due to e.g. hotspots [191, 255, 256]. This section explores basic qualitative relationships between IBC doping and breakdown patterns. An analysis with focus on the origin of the observed breakdown, e.g. via temperature dependence (tunnelling, avalanche), is beyond the scope of this work.

Breakdown imaging using EL

Once again, the advantage of applying imaging techniques consists in distinguishing between highly localized and homogeneous effects. It is well known from literature on conventional silicon solar cells that breakdowns can be detected with lock-in thermography and luminescence imaging [210]. The method of choice in this work is reverse-biased electroluminescence (RebEL) because PL under reverse bias only yields a superposition of breakdown imaging with diffusion limited carrier patterns (see J_{sc} conditions in section 4.3.1) and thermography offers insufficient resolution for the clear visualization of the small-size structures under investigation. The emitted light from breakdowns in silicon pn junctions is known to have a spectrum extending to visible light so that imaging without long pass filters before the silicon CCD camera could result in very high SNR. However, since pn junction breakdowns occur exclusively on the rear side of an IBC cell, light from the visible spectrum is reabsorbed by the base before it can reach the camera.

Figure 6.24 depicts a reverse bias I-V curve in a linear (a) and semi-logarithmic scale (b) of cell BD1 as well as EL images under in-

creasing reverse bias (c-e), each normalized to the highest signal. The semi-logarithmic I-V curve indicates an exponential 'pre-breakdown' and another exponential 'breakdown' voltage range. The EL image at -6.15 V (a) shows bright rhomb shaped spots with dark centers distributed along lines that are correlated with the unit cell pitch and the BSF doping. Some spots are brighter than others which indicates that some spots break down earlier than others. In the other two images, as the reverse bias voltage and reverse current density increase, more bright spots appear until in (e) a fairly continuous pattern has established. Like for conventional solar cells, EL imaging can thus be used to characterize the location of breakdown sites as a function of the applied voltage.

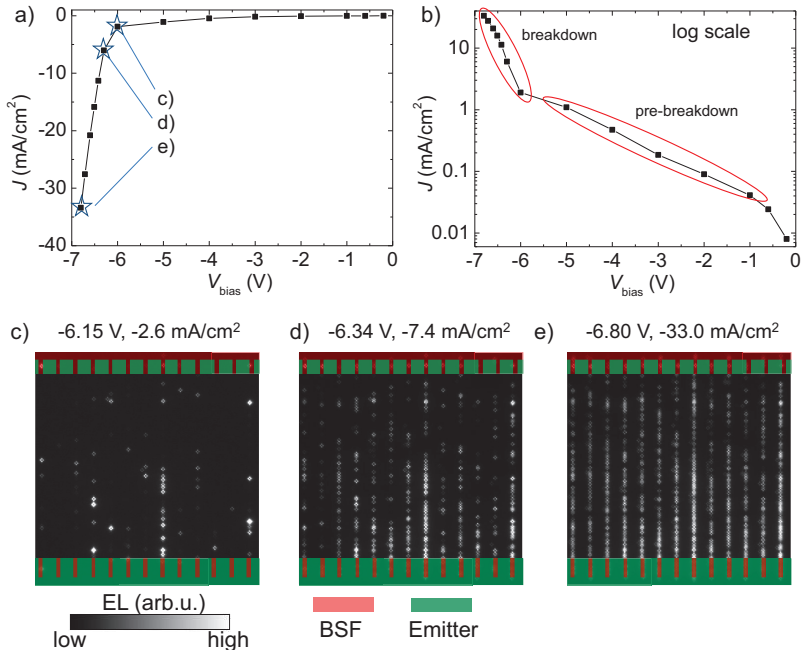


Figure 6.24: Reverse bias I-V curve without illumination of cell BD1 (a,b) and RebEL images at three biases indicated in (a). Breakdowns appear locally along lines at voltages beyond -6.15 V. With increasing voltage and currents, the pattern becomes more homogeneous towards continuous lines of densely spaced breakdown sites.

Figure 6.25 shows two magnifications of a distributed IBC breakdown pattern similar to 6.24 with a high magnification of a single breakdown site. The images were taken with the available macro lens for the setup. All breakdown sites that are individually detected in EL imaging show a symmetry of four bright spots, which can be explained by geometrical optics sketched in figure 6.25 (b). The facets of densely spaced random pyramids are tilted at 54.7° against the flat rear side of the cell. The breakdowns must occur on the bottom of the IBC cell where the pn junctions are located. Light rays which are emitted from there are refracted on the front side's texture featuring random pyramids. Only the light rays with a specific range of incident angles is transmitted perpendicularly to the pyramid facets. Those light rays ultimately reach the camera.¹ At a cell thickness of $200\ \mu\text{m}$, this results in a rhombus symmetry of bright spots at a lateral distance of about $150\ \mu\text{m}$ away from the actual point source. The resolution of up to $13\ \mu\text{m}$ per pixel of the used lens is sufficient to localize a breakdown site and enables further comparison with cross sectional analysis using SEM, EBIC or μLBIC .

Breakdown patterns and hot spot risk

The reverse bias voltage at which a pn junction breaks down is known to be a function of the width of the space charge region (SCR), where a thin SCR, induced by high doping-levels in p- and n-Si for instance, results in a breakdown at a low voltage [41]. Also defects in the silicon crystal and the space charge region may promote breakdown [210]. Compared to conventional solar cells, there can be direct contact between a highly p-doped emitter and a highly n-doped BSF in IBC cells. Therefore, breakdowns may occur between the emitter and the base as well as emitter and BSF. As a consequence, breakdown patterns in IBC cells are a function of the doping structure and also the technology used to create the doping structure (e.g. diffusion compared to ion-implantation [257]).

¹This particular camera setup accepts an incident light cone of $\sim 6^\circ$ [116]

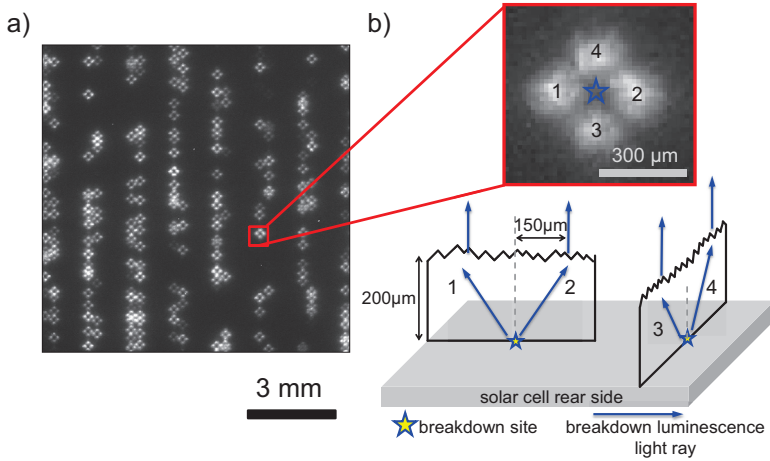


Figure 6.25: Reverse bias EL image of local breakdowns in an IBC cell (a) and schematic of the luminescence light rays that reach the camera (b). The front side's texture featuring randomly arranged pyramids results in a rhombus symmetry of the luminescence signal from each breakdown site.

Three classes of breakdown patterns were identified in this work. Examples for these are shown in figure 6.26, where (a, cell BD2) shows a 'single point breakdown' of an IBC cell produced by R. Keding [55]. The cell has well defined gap regions and therefore breakdowns should only occur locally between emitter and the base. Such breakdowns can occur anywhere across the emitter doping and not necessarily at the edges. Figure 6.26 (b, cell BD3) shows an IBC cell produced by R. Müller using a diffused boron emitter that was locally blocked by ion-implanted phosphorous [257]. This fabrication technique leads to a directly adjacent emitter and BSF doping. The breakdowns occur on spots all along the pn junction's meander between emitter and BSF and are thus labeled 'homogeneous breakdown'. The high density of the breakdown sites makes the rhombus patterns blur into lines. Figure 6.26 (c) depicts cell S2 which has no intended gap in the cell design. Nevertheless, the breakdown sites are inhomogeneously distributed as for cell BD1. The magnification in (c) shows that the breakdown sites are located along two lines, which are located at the left and the right border of each BSF doping region. Since

breakdowns are highly sensitive to the band bending caused by doping near the SCR, a change of a few nm in the width of the SCR impacts the breakdown behavior. Thus, the shape of the breakdown pattern is extremely sensitive to process related uncertainties such as alignment. For example, the breakdowns in figure 6.24 (c-e) occur only on one side of the BSF doping. Cell S2 in figure 6.26 (c) can be compared to 6.20 (d).¹ No spatial correlation between the observed spikes in PL at V_{oc} conditions and breakdown patterns was observed. Thus, the spiking issue is not assumed to be responsible for the detected ReBEL spots.

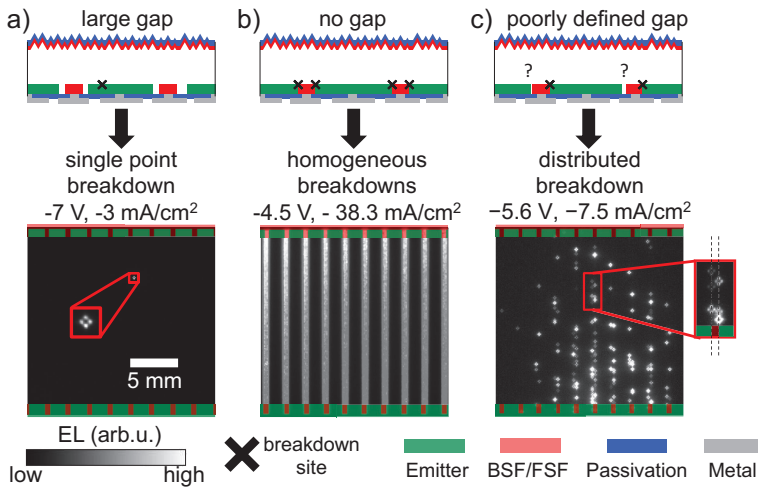


Figure 6.26: Breakdown distribution types: 'single point breakdown' of a cell with large gaps between emitter and BSF (a, cell BD2), 'homogeneous breakdowns' of a cell with no gaps (b, cell BD3) and 'distributed breakdowns' of a cell with a poorly defined gap (c, cell S1). The spatial correlation between the highly doped emitter and BSF defines the breakdown locations. Single point breakdowns are more likely to result in hot spots during operation under reverse bias, while homogeneous breakdowns present integrated by-pass diodes.

The product of cell current and voltage during breakdown defines the dissipated power within the cell. Whether the power is dissipated in a single point or a larger area is crucial for the generation of hot

¹The ReBEL images were taken after 16 minutes on the hotplate.

spots. In a conventional silicon solar module with 60 cells divided into 3 strings, power by a reverse bias of more than 12 V and current of 40 mA/cm² can dissipate. In a completely shaded solar cell, such an electrical power is a risk for severe and irreversible damage for cells such as BD2 (see figure 6.26 (a)) with a gap, because the electrical power is concentrated at break down sites and leads to high local temperatures. 'Homogenous' and early breakdown characteristics such as in BD3 (see figure 6.26 (b)) are hence preferred [47], because the local temperature increase, measured by thermography under worst case conditions for this cell, was found to be less than 35 °C (see [152]). Cells with homogeneous breakdown can be considered as cells with 'integrated by-pass diodes', a concept also found in MWT cells [268]. A brief summary of this chapter is presented in chapter 8.

Chapter 7

Discussion and guidelines for IBC cell characterization

This chapter presents a summarizing discussion on the findings from the experiments and simulations throughout the result chapters 3, 4, 5 and 6. All key interpretations made in the previous chapters are now summarized in comprehensive tabular and flowchart guidelines for spatially resolved characterization of IBC cells. The goal is to enable quick reference for future practical work on IBC cell analysis and other high efficiency silicon solar cells. This chapter also notes conclusions on what distinguishes spatially resolved characterization of IBC from conventional Al-BSF solar cells with front side metalization.

Section 7.1 summarizes the interpretations for patterns and contrasts in SR-LBIC, luminescence and lock-in thermography and comments on the usefulness of images at each of the key operating conditions J_{sc} , MPP , V_{oc} under 1 sun illumination as well as under high forward bias in the dark. Section 7.2 introduces a master flowchart that suggests which spatially resolved characterization methods should be

applied in order to further investigate the observations in the global I-V curve. Also, a summary on which characterization technique is applicable for each of the investigated fault types is given. Finally, section 7.3 offers some critical remarks on the limitations of the new methods presented in this work. A preliminary version of the master flowchart was created in collaboration with K. Hagedorn in the scope of his Master's Thesis under supervision by the author. The overview table and flowchart for series resistance fault identification was published by the author in [114].

7.1 Guidelines for pattern and contrast interpretation

In the following, for each of the spatially resolved characterization techniques and operating conditions, a table summarizes the usefulness of the image/map, the origin of the regular pattern in a typical fault free line-structured IBC cell, the meaning of 'bright areas' (high signal) and 'dark areas' (low signal). Each table also states the sections of this work in which such results were presented.¹ The tables are subdivided into methods utilized for qualitative and quantitative analysis. Based on the author's experience, the 'useful for' column states the major practical application that imaging at each operating condition is suggested for. The colored backgrounds of 'useful for' remark the author's personal judgment. Green indicates a clear recommendation, yellow that it is applicable but either not very sensitive or prone to artifacts and red that the image is not of much use and/or may lead to misinterpretations.

SR-LBIC

Figure 7.1 shows the summary of patterns and contrasts as well as the usefulness of utilizing SR-LBIC for IBC cell characterization. Unlike luminescence and LIT, SR-LBIC only operates at J_{sc} conditions. A

¹In some minor cases, no data was presented in this work for the sake of brevity.

manipulation of the operating conditions is only possible by varying the excitation wavelength λ . All SR-LBIC results (EQE and R) are calibrated with the results of global measurements, so analyses can always be performed quantitatively. However, all currently commercially available SR-LBIC measurement setups work without a bias light due to technical limitations. In case of non-linear spectral response caused by injection dependent lifetime [269], EQE calibration from global EQE should be performed with a bias light. In rare cases of highly inhomogeneous injection dependent lifetime across the cell, this can still bear errors though[75].

SR-LBIC EQE mapping has been an established technique for conventional cells and has also been applied to IBC cells in the past without concerns. Reflection mapping is also an established technique for characterizing local reflection losses. For both EQE and particularly R , short wavelengths with high absorption coefficients ($\lambda \sim 400 \text{ nm} - 800 \text{ nm}$, $l_{\text{Si}} \sim 0.1 \mu\text{m} - 10 \mu\text{m}$) are more sensitive to front side effects while $\lambda > 800 \text{ nm}$ is better representative for rear side effects. In this work, the $J_{\text{sc}}^{\text{loc}}$ mapping method was established which for the first time accurately quantified local J_{sc} losses at STC comparable conditions in IBC or any other silicon solar cells. When performing IQE mapping (equation 3.5), conventional front side metallization fingers are prone to artifacts because at the fingers low EQE and high reflection can lead to inaccurate and even diverging IQE values. This problem does not exist in IBC cells.

There, the only image that needs to be evaluated with caution is the reflectance at long wavelengths. Usually, low reflection signals at long wavelengths are interpreted as a positive performance indicator in a high efficiency solar cell, as more light must have been absorbed. However, light absorption may be caused by undesired parasitic absorption which is an optical but not an optical reflection loss. A careful analysis of EQE, IQE and reflectivity is needed for correct interpretation as was presented in an example in section 3.5. The main application of SR-LBIC on IBC cells is quantifications of 'electrical shading' losses.

SR-LBIC on IBC cells

Operating condition	Useful for	Origin of pattern	Bright areas	Dark areas	Sections
Calibrated EQE, R images					
EQE at $\lambda \approx 400 - 800 \text{ nm}$	Recombination in base, front and back side	Electrical shading	High EQE	Low EQE	3.5
R at $\lambda \approx 400 - 800 \text{ nm}$	Front side optics	no pattern	High optical reflection	Low optical reflection	3.5
EQE at $\lambda \approx 800 - 1100 \text{ nm}$	Recombination at front and back side + parasitic absorption	Electrical shading	High EQE	Low EQE	3.5
R at $\lambda \approx 800 - 1100 \text{ nm}$	Reflectivity of rear side ¹	Rear side reflectance and parasitic absorption	High optical reflection	Low optical reflection	3.5
J_{sc}, pseudo-J_{sc} and optical reflection loss mapping					
J_{sc}^{loc} map	Quantified local J_{sc} losses at STC spectrum	Electrical shading	High J_{sc}	Low J_{sc}	3.3 3.4 3.5
Pseudo-J_{sc}^{loc} map	Local J_{sc} potential of cell without ORL ²	Electrical shading	High pseudo- J_{sc}	Low pseudo- J_{sc}	3.4
Optical reflection loss map	Quantified J_{sc} losses from reflection at STC spectrum ¹	Rear side reflectance	High J_{sc} losses from optical reflection	Low J_{sc} losses from optical reflection	3.4 3.5

Legend		
Useful	Useful with precaution	Not useful or potentially misleading

Figure 7.1: Pattern and contrast interpretations as well as usefulness of SR-LBIC characterization of IBC cells. SR-LBIC is an excellent technique for characterizing local electrical and optical current losses, yields wafer penetration depth dependent information as well as net effects under conditions comparable to STC. Remarks - 1: Parasitic absorption is an optical loss that is not detected in R mapping. 2: IQE maps are prone to artifacts for conventional cells due to front side metallization.

Luminescence imaging

Figure 7.2 shows the summary of patterns and contrasts as well as the usefulness of utilizing luminescence imaging for IBC cell characterization. Applying EL/PL imaging on IBC cells was a more complex endeavor than it was for SR-LBIC. In this work, by using experiments and extensive numerical simulations, signals at all operating conditions could be interpreted and luminescence imaging can now be used as a fast and versatile technique to characterize IBC cells with and without processing faults. Luminescence imaging allows to study local IBC cell physics under arbitrary illumination levels and voltage biases.

Many features of a global I-V curve can be observed in PL imaging. PL imaging is however often more sensitive than global data because instead of a zero-dimensional voltage and current value, each operating condition yields two-dimensional data. Also, unlike in conventional cells, in IBC cells there is no obstruction of emitted luminescence light due to front side metallization, so that access to the luminescence signal at the metal contacts of an IBC cell is inherently provided. This also makes averaging procedures of image data over the whole cell more reliable.

The regular patterns of EL images are not representative for the cell's operation under illumination and not found to be useful for cell analysis. On a qualitative level however, EL is suited to detect contacting faults, shunting faults as well as breakdown patterns with good spatial resolution. PL at V_{oc} conditions is an excellent means for a fast (contactless and typically with integration times < 1 s) assessment of the homogeneity of the manufacturing process. The patterns of PL images at J_{sc} conditions offer little useful qualitative information, but it may help understanding cases of extreme local emitter contact resistance faults (see figure 6.7 (c)). PL images at *MPP* conditions are the basis for R_s^{loc} calibration. However, the PL J_{sc} image must be subtracted from the *MPP* image to remove artifacts from diffusion limited carriers since they do not contribute to R_s^{loc} . This method then becomes inapplicable (see figures 2.5 (a) and 6.7) (c). The main applications of luminescence imaging are the

qualitative analysis of surface recombination and breakdown patterns and as well as the quantitative and qualitative analysis of local series resistance.

Luminescence imaging of IBC cells

Operating condition	Useful for	Origin of pattern in fault free line-structure cells	Bright areas	Dark areas	Sections
Qualitative analysis					
Dark					
EL fwd bias	Qualitative detection of contacting faults	Primary location of carrier injection in the dark	High excess carrier density	Low excess carrier density	4.3.2
EL low rev bias	Not useful	no signal	no signal	no signal	Data not shown
EL high rev bias	Breakdown patterns at very high spatial resolution	Overlap between emitter and BSF regions	Breakdown locations	Rest of the cell	6.5
Illuminated					
PL J_{sc}	Rarely useful. Required for voltage calibration	Diffusion limited carriers and 'electrical shading'	Diffusion limited carriers	High carrier extraction or recombination	4.3.1 6.2.2
PL MPP	Indicator of high R_s^{loc} regions ¹	Lateral transport limitations	Regions of high R_s^{loc} to terminal	Regions of low R_s^{loc} to terminal	4.3.1 6.2.2
PL V_{oc}	Local surface recombination variations and effective lifetime	Varying J_0 of emitter, gap and BSF regions	Low surface rec., high τ_{eff}	High surface rec., low τ_{eff}	4.3.1 6.2.2
Quantitative methods					
PL R_s^{loc}	Quantify local R_s values and contacting faults	Lateral transport limitations	High R_s^{loc}	Low R_s^{loc}	4.6 6.2

Legend		
Useful	Useful with precaution	Not useful or potentially misleading

Figure 7.2: Pattern and contrast interpretations as well as usefulness of luminescence imaging characterization of IBC cells. Luminescence is an excellent means for characterizing local recombination caused by passivation faults, series resistance losses as well as breakdown patterns at good spatial resolution. Remarks - 1: A PL J_{sc} image should be subtracted from the corresponding PL MPP image so that R_s^{loc} information is not blend with diffusion limited carriers.

Lock-in thermography

Finally, figure 7.3 shows the summary of patterns and contrast interpretations as well as usefulness of utilizing lock-in thermography on IBC cells. Thermography poses by far the biggest challenges of the investigated imaging techniques in terms of interpretation and experimental limitations of spatial resolution due to thermal blurring and SNR. As was elaborated by device simulations in section 5.3, Peltier heating and cooling significantly influences the local power densities and hence LIT patterns of fault free cells so that power calibrated images cannot be directly interpreted as local free-energy losses.

This however does not render LIT useless for cell characterization because, like for conventional cells, dark lock-in thermography is an excellent means of identifying shunts and distinguishing whether they have ohmic or diode like properties. R_p values may be attributed to individual ohmic shunts and compared between each other quantitatively. In general, -90° LIT images do represent local power density, so that signals at individual processing faults should be proportional to local power losses. LIT allows a visualization of breakdowns under reverse bias with higher quantitative relevance than EL, but greatly reduced spatial resolution.¹ ILIT images at J_{sc} and MPP conditions are problematic, because of high signals from Peltier and thermalization heat. Peltier effects also exist in conventional cells, but Peltier heating and cooling cancel out within each pixel [70]. Like for conventional cells, ILIT V_{oc} ² still serves the purpose of identifying locally increased recombination, independently of whether it is caused by passivation or shunting faults. Unlike luminescence, ILIT at V_{oc} is very sensitive to local shunts at any illumination level.

¹Data not shown in this work. For an example comparison on a conventional cell see [244]

²Where Peltier and Joule heating is negligible.

Lock-in thermography on IBC cells

Operating condition	Useful for	Origin of pattern in fault free line-structure cells	Bright areas	Dark areas	Section	
Qualitative analysis						
Dark						
DLIT fwd bias	Diode like shunts	Location of highest recombination currents or Peltier cooling	High J_{01} or J_{02} recombination currents or low Peltier cooling	Low recombination currents or high Peltier cooling	5.3 5.4 6.3	
		Ohmic shunts	no pattern	ohmic shunts	rest of cell	6.3
		Breakdown patterns at low resolution but quantitative in power	no pattern	Breakdown regions	rest of cell	Data not shown
Illuminated						
ILIT J_{sc}	Thus far not helpful due to Peltier heat	Joule and Peltier heat	High joule or Peltier heat	Low joule or Peltier heat	5.3 5.4	
ILIT MPP	Thus far not helpful due to Peltier heat	Peltier heat coupled with R_s^{loc} effects	High joule and Peltier heat	Low joule or Peltier heat or high R_s^{loc}	5.3 5.4	
ILIT V_{oc}	High recombination, shunting even at low illumination at low resolution	Varying J_0 of emitter, gap and BSF regions	High surface recombination, low τ_{eff}	Low surface recombination, high τ_{eff}	5.3 5.4	
Quantitative methods						
Local R_p	Quantitative comparison by linear J_{shunt} fit ¹	n/a	low R_p	rest of cell	6.3.1	
'Local I-V' analysis	Not applicable because of Peltier heat and poor dark/light I-V superposition	n/a	n/a	n/a	-	
Legend						
Useful		Useful with precaution		Not useful or potentially misleading		

Figure 7.3: Pattern and contrast interpretations as well as usefulness of lock-in thermographic characterization of IBC cells. The images of fault free cells can be misleading because, due to inhomogeneous Peltier heating and cooling, power calibration does not well represent free-energy losses. However, LIT is more suited for the detection of ohmic and diode like shunts compared to PL. Remarks - 1: Quantification of power losses requires current calibration over the whole cell and same sized ROIs for each shunt.

7.2 Guidelines for identification of local processing faults

This section provides guidelines and recommendations for the analysis of local processing faults, which is highly relevant for practical application. The goal is to answer the questions:

1. Which imaging techniques / analysis methods are sensitive and best suited to each fault type?
2. Based on global I-V data, how can reasons for poor performance be quickly traced by spatially resolved characterization?

Figure 7.4 presents a graphical representation of the 'top-down', 'bottom-up' principle of flowcharts and tabular overviews presented in this section. Note that the list of investigated production faults in this work is not exhaustive. Other inhomogeneous losses that were not discussed in the scope of this work or only briefly mentioned include edge losses¹, short-circuits between metal fingers of the rear side metallization, faults underneath the busbars (not visible in the 4 cm² cells in this work)², cracks within silicon, effects of inhomogeneous finger resistance and more. Note again that a homogeneous and high quality n-type silicon wafer material was always assumed.

An important advantage of using spatially resolved characterization for fault detection is that the two-dimensional images at every operating condition are more sensitive to small performance degrading effects than the zero-dimensional current value at a given voltage. For example, small variations in surface passivation quality may cause variations in V_{oc} of a few mV, which is near the estimated error of V_{oc} measurements.

¹Treated in a co-authored publication in [270]

²Shaded during measurements by the designated aperture area.

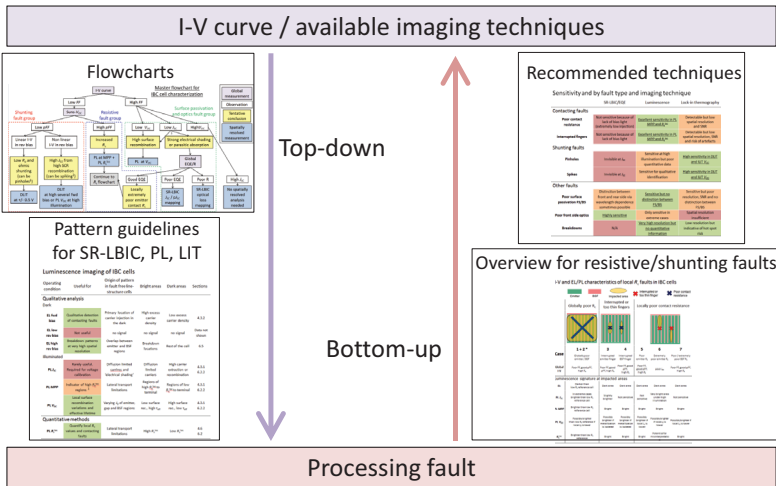


Figure 7.4: Schematic principle of the 'top-down' and 'bottom-up' guidelines for IBC cell characterization introduced in this chapter. Top-down means starting with I-V data and available imaging techniques and working down to the fault type. Bottom-up means starting from suspected faults and verifying the signature using diverse measurement techniques.

Recommended techniques

To answer question 1, based on the experiments in this work and knowledge on conventional silicon solar cells, figure 7.5 shows an overview of the imaging techniques' sensitivity to detect processing faults like contacting, shunting, and other faults. An important conclusion is that no imaging technique is well-suited for all fault types but for every fault there is a well-suited technique. The imaging techniques SR-LBIC, luminescence, and lock-in thermography are compared. For a review of state-of-the-art methods for conventional material and cell characterization, refer to [271] which is co-authored by the author of this work. In several cases, more than one imaging technique is sensitive (orange or green) to the fault. In such cases, the underlined text indicates the most recommended technique, based on the author's experience. Luminescence imaging is the most versatile technique for fault detection, followed by LIT and SR-LBIC.

Regarding surface passivation, the flexibility of SR-LBIC excitation wavelength partially allows a distinction between front side (FS) and back side (BS) effects. However, since SR-LBIC operates as J_{sc} conditions, it is not highly sensitive to passivation effects. Luminescence on the other hand is sensitive but experimentally constrained to optical excitation below 850 nm. LIT does not have this excitation constraints but has poor resolution and SNR.

Sensitivity and by fault type and imaging technique

	SR-LBIC/EQE	Luminescence	Lock-in thermography
Contacting faults			
Poor contact resistance	Not sensitive because of lack of bias light (extremely low injection)	<u>Excellent sensitivity in PL</u> MPP and R_s^{loc}	Detectable but low spatial resolution and SNR
Interrupted fingers	Not sensitive because of lack of bias light (extremely low injection)	<u>Excellent sensitivity in PL</u> MPP and R_s^{loc}	Detectable but low spatial resolution, SNR and risk of artefacts
Shunting faults			
Pinholes	Invisible at J_{sc}	Sensitive at high illumination for qualitative identification	<u>High sensitivity in DLIT</u> and ILIT V_{oc}
Spikes	Invisible at J_{sc}	Sensitive for qualitative identification	<u>High sensitivity in DLIT</u> and ILIT V_{oc}
Other faults			
Poor surface passivation FS/BS	Distinction between front and rear side via wavelength dependence sometimes possible	<u>Sensitive but no distinction between</u> FS/BS	Sensitive but poor resolution, SNR and no distinction between FS/BS
Poor front side optics	<u>Highly sensitive</u>	Only sensitive in extreme cases	Spatial resolution insufficient
Breakdowns	n/a	<u>Very high resolution but no quantitative information</u>	Low resolution but indicative of hot spot risk
Legend			
<u>Most recommended technique</u>	Sensitive and useful	Sensitive but not highly recommended	Not sensitive and/or risk of artefacts

Figure 7.5: Sensitivity of the three major imaging techniques to the processing faults investigated in this work. Luminescence imaging is the most versatile option. No technique is well-suited for all faults but every fault has a well-suited technique to be analyzed with.

Master flowchart

To answer question 2, figure 7.6 shows a master flowchart for the global and spatially resolved analysis of IBC solar cells. The word 'IBC' was left out of the title, as in most cases the procedure is directly transferable to other silicon solar cell architectures. The premise is that all spatially resolved investigations should be based on a global I-V curve, the performance parameters FF , J_{sc} , V_{oc} and optionally a pseudo I-V curve and pFF from Suns- V_{oc} . Global I-V measurements with a flash tester or sun simulator are a necessity and a routine part of solar cell fabrication in PV manufacturing and R&D.

Common analyses of solar cell precursors such as lifetime, SIMS/ECV, sheet and contact resistance samples as well as numerical device simulations yield an expected performance of the finished cell. Observations (white boxes) of e.g. *Low FF* or *High V_{oc}* are thus relative to the values that were expected or relative to other cells in the same batch. Global I-V, Suns- V_{oc} and sometimes EQE/R measurements (purple boxes in figure 7.6) are typically faster than PL, LIT and especially SR-LBIC (yellow boxes). Global data is also easier to process and analyze in established routines from decades of research.

The combination of observations leads to tentative conclusions (blue boxes). Because only the most likely reasons for the poor performance are considered, those reasons are referred to as *tentative conclusions*. The dashed lines separate the fault types into categories. These are shunting faults, best studied with LIT, resistive faults, best studied with EL/PL, and surface recombination and optics faults, best studied with SR-LBIC or PL. Note that solar cells often perform worse than expected for several reasons (i.e. low FF and low V_{oc}). This flowchart guides the user towards the fault that is the dominating loss factor of the solar cell.

An example for the use of the master flowchart: The global measurement reveals a solar cell with a low FF . Afterwards a Suns- V_{oc} pseudo I-V measurement is performed which results in a rather high pFF . The tentative conclusion of these global measurements is that the solar cell suffers from series resistance losses. Thus, a spatially

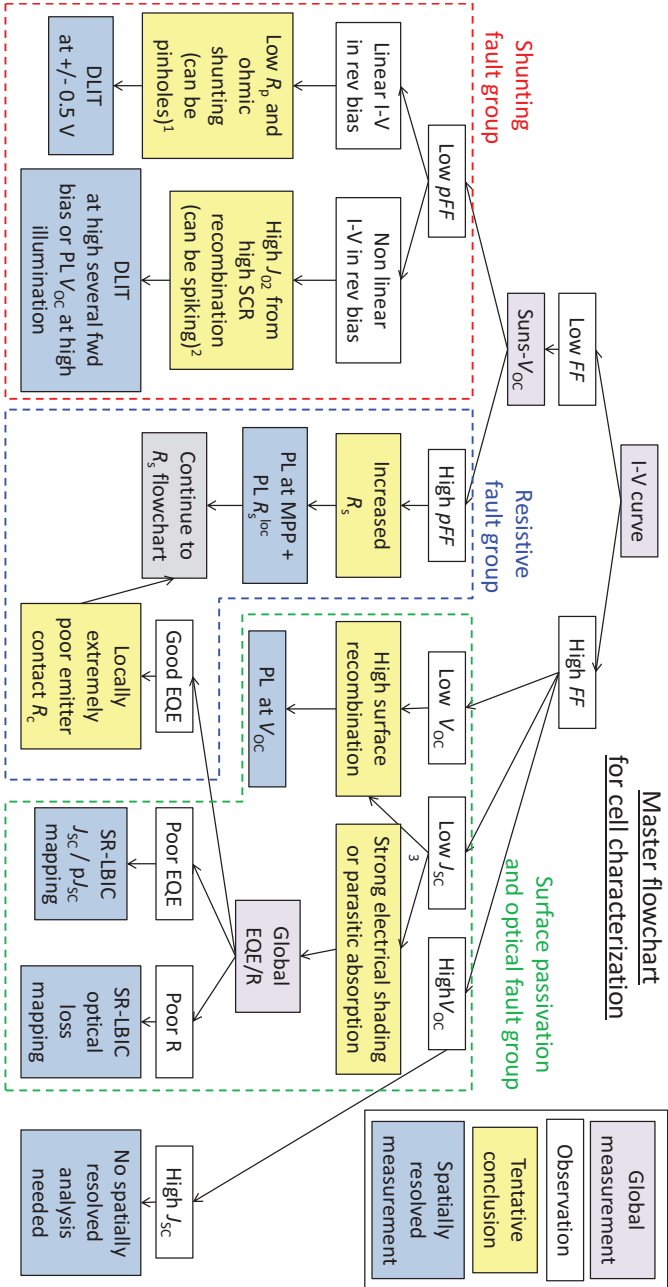


Figure 7.6: Master flowchart for IBC solar cell characterization based on observations in global I-V curve results. This flowchart guides towards tentative conclusions over the dominant loss inducing faults and towards the best suited imaging method for spatially resolved analysis. The observation of low or high values is relative to the values expected from comparable cells, solar cell precursors and/or numerical simulations. Remarks - 1: Low R_p values always indicate ohmic shunting, but pinholes are only relevant in point-structured IBC cell designs. 2: J_{02} type recombination can be caused by diverse other problems in the SCR. Spiking is only relevant for certain metallizations. 3: Both reasons are possible. At a high FF , a low J_{sc} might be related to electrical shading and high surface recombination. Moreover, high surface recombination is known to enhance the electrical shading effect, because of the correlation between diffusion length and effective lifetime.

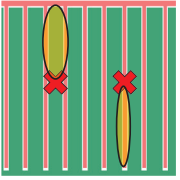
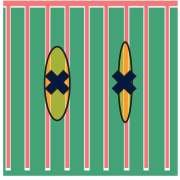
resolved PL measurement under *MPP* conditions is proposed for further analysis of the main loss factor (continued in R_s flowchart in figure 7.8).

Resistive fault group

The resistive fault group (within the blue dashed lines in figure 7.6) were investigated in detail in section 6.2 and published in [114]. A series of experiments and numerical simulations allowed distinguishing seven different types of global and local contacting faults divided into three groups. The three groups of faults are globally high contact resistance R_c , locally high R_c and interrupted fingers, whereby the latter two groups features a distinction between emitter and BSF contacts.

Figure 7.7 presents a bottom-up guideline starting from the fault level. The fault types are sketched in a schematic containing location (cross) and the area impacted by it (yellow ellipsoid). Each case lists the signature in global I-V, PL imaging at 1 sun and EL. Some luminescence images are sensitive to local faults, e.g. all PL *MPP* images, while e.g. PL images at J_{sc} are only sensitive to cells featuring an extremely poor local emitter contact resistance. Note that global contact resistance problems from emitter or BSF can neither be distinguished by an I-V measurement nor by luminescence imaging. By including a PL image at J_{sc} into the analysis, a qualitative assessment can be made whether misinterpretations could occur like in ROI 3 of figure 6.9.

I-V and EL/PL characteristics of local R_c faults in IBC cells

	 Emitter	 BSF	 Impacted area	 Interrupted or too thin finger	 Poor contact resistance	
	Globally poor R_c		Interrupted or too thin fingers		Locally poor contact resistance	
						
Case	1 + 2 * Globally poor emitter / BSF (indistinguishable)	3 Interrupted emitter finger	4 Interrupted BSF finger	5 Poor emitter R_c	6 Extremely poor emitter R_c	7 Poor / extremely poor BSF R_c
Global I-V	Poor FF , good pFF , high R_s	Poor FF , good pFF , high R_s	Poor FF , good pFF , high R_s	Poor FF , good pFF , high R_s	poor J_{sc}	Poor FF , good pFF , high R_s

Luminescence signature at impacted areas

EL	Darker than low R_s reference cell	Dark area	Dark area	Dark area	Dark area	Dark area
PL J_{sc}	In extreme cases brighter than low R_s reference cell	Slightly brighter	Not sensitive	Not sensitive	Very bright under high illumination	Not sensitive
PL MPP	Brighter than low R_s reference cell	Bright	Bright	Bright	Bright	Bright
PL V_{oc}	Possibly brighter than low R_s reference if local J_0 is lower	Possibly brighter if metallization is isolated	Possibly brighter if metallization is isolated	Possibly brighter if local J_0 is lower	Possibly brighter if local J_0 is lower	Possibly brighter if local J_0 is lower
R_s^{loc}	Brighter than low R_s reference	Bright	Bright	Bright	Potential for misinterpretation	Bright

Figure 7.7: Bottom-up guideline of global I-V characteristic and sensitivity of luminescence images at J_{sc} , MPP , V_{oc} , EL and in R_s^{loc} imaging for the seven cases of global and local resistive faults in IBC cells. *: Cases 1 and 2 are experimentally indistinguishable

In practical application, investigations start with the global I-V measurement and end with the determination of the specific fault. A *low FF* paired with a *high pFF* observation in the master guideline 7.6 implies a high series resistance, which points to a subsequent flowchart (grey box in figure 7.6). Figure 7.8 shows a top-down flowchart allowing the identification of local contacting faults. White boxes mark experimental observations and blue boxes conclusions. Yes/no answers ultimately lead to either the conclusion of a global problem (case 1+2) or one of the five other cases elaborated in figure 7.7. For fault identification, J_{sc}^{loc} mapping was not found to be necessary (see section 4.6 and 6.2). As for the luminescence imaging procedure to obtain R_s^{loc} , the approach of Trupke et al. [137] Kampwerth et al. [138], and Glatthaar et al. [139] will yield similar results and confirm the nature of the fault, because all of these methods are based on the same voltage calibration principle. The limitation of applying the flowchart in figure 7.8 to all problems is that in practical application various faults can be mixed in the same device (e.g. poor and very poor emitter R_c , adjacent emitter and BSF regions with poor R_c). A careful study of the raw luminescence data as described in figure 7.7 and 7.8 should yield helpful information for finding the technological causes of local faults and for estimating their impact on the efficiency of the solar cell.

Shunting fault group

The shunting fault group (within red dashed lines in figure 7.6) was investigated in section 6.3 of this work. Shunting is typically always a local effect where increased recombination currents flow either with a linear current-voltage characteristic (ohmic shunts, low R_p) or an exponential characteristic (diode like shunts, typically high J_0 or J_{02}). In IBC cells, like in conventional Al-BSF cells, the distinction between ohmic and diode like shunts can be made by comparing DLIT images at low forward and reverse bias voltages. The manifestation of the Peltier effect may influence the magnitude of the DLIT signal, especially at high forward bias but should pose no complication for the determination of the shunt type.

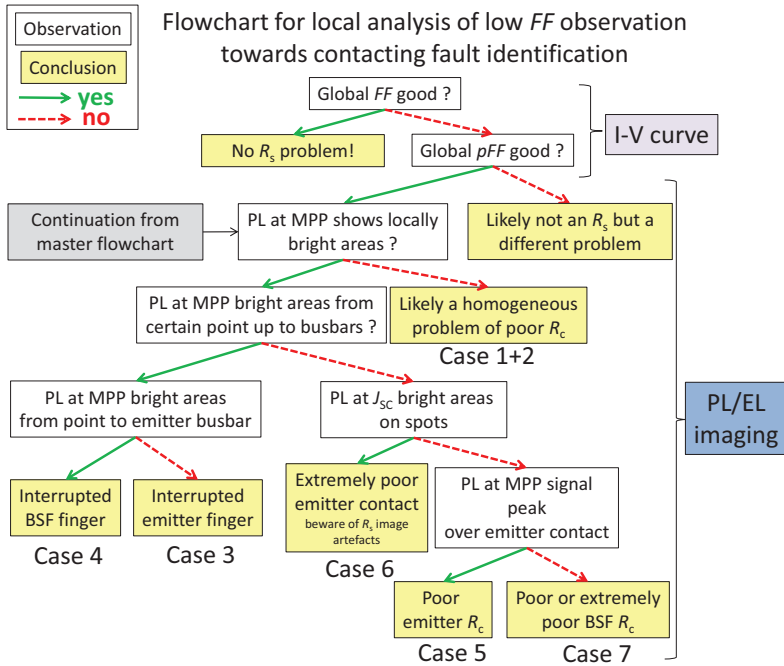


Figure 7.8: Top-down flowchart for experimental identification of local and global FF problems, starting with global I-V characterization and continuing with PL imaging. The case numbers refer to figure 7.7.

In analogy to the resistive fault overview, figure 7.9 depicts an overview of the pinhole and spike shunting types investigated in this work with the signature of all the characterization methods that are sensitive to these faults. It was argued in section 6.3.1 that pinholes (left column) only induce relevant shunting in cells with metal fingers overlapping the SCR (e.g. BSF isles in 'point-structured' cells), but can be very detrimental to the cell performance. Thus, a strong reduction in V_{oc} and particularly pFF might be the consequence of those shunts.¹ DLIT clearly resulted to be the preferred technique for the analysis including the possibility of quantitative assessments of shunt's R_p values. However, the more widely spread availability

¹See figure 6.11 and the dissertation by C. Reichel [54].

of PL and its speed¹, ease of measurement and good spatial resolution presents a valuable qualitative alternative. This however requires that the optical excitation intensity in PL imaging is sufficiently large to counter a complete blurring artifact in the image due to lateral balancing currents (see figure 6.14). The experience thus far showed that the light intensity of 1 sun (standard illumination) is sufficient though. Furthermore, exact localization of pinholes was demonstrated with a method of overlaying the J_{sc} and V_{oc} image at 1 sun illumination intensity (see figure 6.16). The detrimental pinholes were unambiguously traced to occur at locations where BSF metal fingers overlap the SCR. ILIT at V_{oc} conditions was shown to present another contactless alternative to pinhole identification, also at low illumination intensities.

¹Integration times of a PL measurement at V_{oc} is typically < 1 s for good SNR while this is of the order of minutes for DLIT.

Global I-V, LIT and luminescence characteristics of ohmic pinholes and non-ohmic spikes in IBC cells

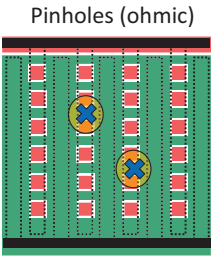
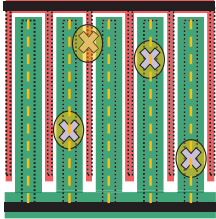
			
		 <p style="text-align: center;">Pinholes (ohmic)</p>	 <p style="text-align: center;">Spikes (typically non-ohmic)</p>
Global I-V		Low FF , pFF and V_{OC} + low R_p	Low, FF , pFF and V_{OC} + high J_{O2}
Lock-in thermography			
DLIT fwd		Bright spots at impacted areas	Bright areas (lines) along contact openings (more harmful at emitter)
DLIT rev		Bright spots at impacted areas. Same intensity in forward an reverse bias (at +0.5 V and -0.5 V)	No signal
ILIT V_{OC}		Bright spots at impacted areas	Bright areas (lines) along contact openings (more harmful at emitter)
Luminescence imaging			
EL fwd		Dark spots	Dark areas
PL V_{OC}		Dark spots but only above an illumination intensity threshold	Dark areas

Figure 7.9: Bottom-up guideline of global I-V characteristic and the imaging techniques sensitive to shunting from pinholes and spikes in IBC cells. DLIT is the suggested method for quantitative analysis but PL at V_{OC} conditions, with precaution, is a fast qualitative alternative with good spatial resolution.

Regarding spikes, it has been shown in section 6.3.2 that spikes in the emitter region are detrimental as soon as they penetrate the pn junction. Note that spiking towards the BSF contact openings is possible as well. It was confirmed that spikes act as recombination centers and reduce the pFF , consequently the FF , and the V_{oc} of a cell. In the case of a cell with a deep doping profile (S2, figure 6.18), the global R_s decreased over time on the hotplate, presumably due to improved contact formation. It has been shown that in PL imaging, spikes are observed as lines along the contact openings rather than as single spots. In the case of a shallowly doped cell (S1, figure 6.19) featuring a high density of spikes penetrating the pn junction simultaneously, they even cause a homogeneous pattern (periodically low signal at the emitter contact despite an *initially* lower J_0 than the BSF region) in PL images at V_{oc} . Furthermore, like for pinholes, DLIT under forward bias was also found to be suitable for spike detection. Again, qualitative analysis is possible with forward-biased EL measurements.

Surface passivation and optical fault group

Section 6.4 briefly addressed surface recombination and optical faults in IBC cells. IBC cells do not pose any additional challenges to the identification and quantification of these fault types compared to conventional solar cells. No separate bottom-up passivation and optical fault guideline is provided in this work. A recommended flowchart for fault identification is shown between the dashed green lines in figure 7.6.

Unlike contacting and shunting faults, optical and surface passivation faults can occur anywhere on the cell and affect its nearby surroundings. A clear distinction between front side passivation and optical effects by luminescence is not always possible, because a low signal of PL at V_{oc} conditions can be caused by high recombination and/or high reflection of the excitation light. For a clear distinction, additional measurements of the EQE and the reflection with global and SR-LBIC techniques is recommended.

7.3 Review and limitations of the proposed methods

The final section of this chapter critically reviews the novel characterization methods and approaches proposed in this work. This includes remarks on the limitations found thus far and on factors that may compromise their accuracy and reliability.

Note that all of the investigated IBC solar cells in this work were rather small, featuring an active area of 2 cm x 2 cm (4 cm²). Industrial size solar cells are typically 12.5 cm x 12.5 cm (156 cm²) or 15.6 cm x 15.6 cm (243 cm²) large. To fulfill the aim of this work, 4 cm² sized cells have the advantage of allowing imaging features of ~ 100 μm size but still capture the entire cell in the same image. The device physics related to the interdigitated doping structure in a 156 cm² or 243 cm² IBC cell are the same as on a 4 cm² cell, so all findings are transferable. Finger resistance plays a larger role in large cells and the busbar design is part of the active cell area [58], which can lead to a more prominent appearance of the 'electrical shading' (section 3.5), resistive losses in lateral transport out of the busbar area (section 4.6) and along fingers and finger interruptions (section 6.2) compared to small cells.

J_{sc} , pseudo- J_{sc} and optical reflection loss mapping

Chapter 3 of this work introduced a simple and robust method of generating $J_{\text{sc}}^{\text{loc}}$ maps for arbitrary irradiance spectra using commercially available SR-LBIC instruments by interpolation of local quantum efficiency and integration with the AM1.5G spectrum. The method offers numerous application possibilities for local current loss analysis beyond IBC silicon solar cells with a high resolution, limited by the laser spot size. Purely electrical device properties can now be studied more exclusively with a newly introduced pseudo- $J_{\text{sc}}^{\text{loc}}$ map obtained from IQE measurements, which can separate electrical and optical reflection losses. All of these results can be extracted from one set of SR-LBIC maps, without compromising on any of the depth-resolved

information SR-LBIC is often used for. In addition, the resulting images are of interest for all established luminescence and lock-in thermography characterization methods that use the assumption of a homogeneous J_{sc}^{loc} such as PL based R_s^{loc} (as demonstrated in section 4.6) but also for Breitenstein et al.'s Local I-V method [213]. To what extent the usage of J_{sc}^{loc} maps improves lock-in thermography imaging results remains to be demonstrated.

This method was found to exhibit a good agreement between average J_{sc}^{loc} and globally obtained values for the investigated variety of mostly non-IBC solar cells. This agreement does not definitively prove the accuracy at each pixel. Aspects that may induce errors in these methods include

- Interpolation errors of the EQE and reflection curve at each pixel
- The additionally introduced interpolation points in the UV- and the IR-regime of the silicon EQE are not sufficiently representative at each pixel (see figure 3.1 and equations 3.3, 3.4)
- Divergent IQE values on grid fingers for conventional cells
- Lack of bias light in SR-LBIC measurements in cases of inhomogeneous injection dependent lifetime (see figure 8 in [75])
- A lack of bias light in SR-LBIC measurements may leave cases of extremely high R_c unnoticed despite their impact on global J_{sc} (see figure 6.8)
- Imperfect spatial alignment of the different SR-LBIC laser spots on the sample falsely blur the J_{sc}^{loc} image
- Poor focusing of the SR-LBIC laser spots

In the recent publication of Fertig et al., co-authored by the author of this work, a comprehensive summary of SR-LBIC based J_{sc}^{loc} mapping in comparison to the other recently proposed J_{sc}^{loc} imaging techniques is presented [75]. This includes a tabular overview on accuracy, advantages, drawbacks, limitations and robustness of each method.

Simulation of experiments

Electrical device simulations and the simulation of experiments was a key approach for the success of this work. Simulations lead to the primary results on luminescence patterns and SRVs (sections 4.3 and 4.5), series resistance imaging (section 4.6), local Peltier heating and cooling (section 5.3) and signatures of contacting faults (section 6.2). Also the approach by Reichel et al. to simulate SR-LBIC maps [99] was implemented and used in section 4.6. The use of a conductive boundary model with the software Quokka allowed the large number of simulations in this work with reasonable computational time. With the conductive boundary approach, J_0 and R_{sh} parameters could be varied independently which is not possible with conventional doping profiles because J_0 and R_{sh} are in reality always related. Global I-V and luminescence simulations of local processing faults allowed understanding the signature of a locally poor contact resistance and the different impact of single compared to clustered faults on J_{sc} , FF and η .

When simulating experiments, a distinction between simulation towards general device understanding and towards quantitative extraction of parameters is needed. The latter was only used for obtaining SRVs by modeling PL imaging near V_{oc} conditions in section 4.5. While the simulation of luminescence was overall very fruitful, simulations of lock-in thermography experiments by combining stationary electrical and dynamic thermal simulations in COMSOL Multiphysics was attempted in the scope of the Master's Thesis by M. Selinger. Thus far however, results yielded no additional knowledge for this discussion [187] (results not presented in this work).

Simulating experimental results of two or three-dimensional images is more challenging than the typical simulation of I-V curves. For example, V_{oc} is a zero dimensional figure of merit that can be matched with a variety of input parameters, but the PL intensity profiles over a unit cell presents one or two-dimensional information about individual cell regions. Limitations to the success of simulat-

ing SR-LBIC, luminescence and lock-in thermography experiments include

- Insufficient accuracy of the implemented physical models such as injection dependent lifetime, inversion layers, passivated contacts, tunneling etc.
- Even when the electrical device modelling is accurate, simulated reproduction of experimental factors such as the exact cell temperature and sharpness of the lens are challenging
- Uncertainties of many required input parameters including basic parameters such as $n_{i,\text{eff}}$, which the results are sensitive to
- Uncertainty of whether a conductive boundary (Quokka, CoBo) approach is sufficiently accurate for the specific simulation
- Long computer calculation times when using advanced software like Sentaurus Device or ATLAS, particularly for three-dimensional simulations

Surface recombination parameters from modeled luminescence images

In section 4.5 of this work, it was proposed that matching experiments and simulated luminescence intensity profiles at V_{oc} conditions yields accurate data on the individual surface recombination velocities of the surfaces that are used as inputs in the simulations. The simulations started with values obtained from typical test structures and it remains to be demonstrated how well all parameters could be obtained from initial guess values. Conclusions can however be drawn for the metal contact areas, for which no SRV data from test structures is available. It also remains to be demonstrated whether perfect matching of experiments with simulations is feasible in practical application, which is only possible if all experimental circumstances are extremely well modeled.

The sensitivity analysis has shown that each SRV has a particular influence on the PL intensity and hence also the signature of faults,

but the six-dimensional parameter space (see figure 4.16) opens a broad range of parameter combinations to sweep through. Practical application of this method will require computer based optimizer algorithms to determine the best and most realistic combination to match the experimental data. The proposed method is most valuable for cells that are limited by large differences in surface recombination, because V_{oc} of highly efficient IBC cells like the recent achievements by SunPower corporation are limited by bulk recombination [4] and are expected to show very minor variations in PL intensity profiles.

Luminescence based series resistance imaging on IBC cells

A major achievement of this work was the adapted interpretation of luminescence R_s^{loc} imaging on IBC cells in section 4.6. The method was chosen to be based on the approach by Trupke et al. [137] and was adapted to include a J_{sc}^{loc} map from SR-LBIC as input instead of assuming a homogeneous J_{sc}^{loc} . This adapted method was found to show good agreement between average J_{sc}^{loc} and globally obtained values for the investigated variety of solar cells. This agreement does however not definitively prove the accuracy at each pixel, because the use of a J_{sc}^{loc} input map was not found to influence the average R_s^{global} value significantly, but only the image contrast. In the case of R_s , there is not even a universally accepted global determination method. Unlike what is assumed in the diode models, R_s^{global} can be a sensitive function of operating conditions such as injection dependent lifetime and temperature [39, 147].

The inclusion of a J_{sc}^{loc} map from SR-LBIC likely improves the accuracy of the local results though as the constant J_{sc}^{loc} assumption is clearly incorrect (see e.g. figure 3.4 or 4.20). The spatial resolution and blurring effects in SR-LBIC measurements are however very different from those in luminescence imaging. It is unclear which is the physically most sensible way to blur the SR-LBIC map. In practical application however, the interest of spatially resolved characterization lies in fault detection rather than fault free regular patterns. J_{sc}^{loc} mapping was not found to be a necessity for fault detection in this work (see figure 6.6).

Moreover, homogeneous J_0 over the cell surface is assumed, which is inaccurate. Still the approach based on Trupke et al.'s method was chosen for this work to reduce the parameter space of input images compared to Glatthaar et al.'s method [139] that results also in a J_0^{loc} image.¹ Furthermore, any cell parameter value from luminescence based analysis methods is blurred by optical effects² and lateral balancing currents such that the 'real' value at a pixel is always higher by an unknown amount than what the result image suggests. Therefore, the impact of the homogeneous J_0^{loc} assumption is reduced.

¹Glatthaar et al.'s method requires an additional PL image away from maximum power point and closer to V_{oc} conditions.

²Including the choice of filters in front of the camera.

Chapter 8

Summary and outlook

This dissertation presented a comprehensive investigation of spatially resolved characterization of interdigitated back contact silicon solar cells using a range of commercially available imaging and mapping tools. The acquired knowledge through this work enables the study of IBC cells with powerful imaging methods that were prior applied only to simple cell structures like Al-BSF cells. The IBC cell analysis was carried out on a fundamental level and a practical level. On the fundamental level, it was done by studying the inherently inhomogeneous image contrast patterns caused by the interdigitated doping structure and the subsequent three dimensional charge carrier distribution and current flow. On the practical level, it was done by studying the detection of local processing faults that were grouped into resistive, shunting and surface recombination / optical faults. Local cell characteristics were investigated at all important cell operating conditions, namely short-circuit, maximum power point, open-circuit and in the dark under forward- and reverse-bias. Practical guidelines were created to facilitate the implementation of these findings in other R&D and industrial environments. For a deeper understanding of the device physics, in particular numerical modeling of luminescence imaging was developed. This modeling served as a powerful complementary approach to the conventional experimental

work. Beyond providing progress in understanding, new characterization methods were developed in this work. The findings were also successfully applied on large area IBC cells in the frame of a cooperation with an industrial manufacturer, which could not be disclosed in this dissertation.

Chapter summaries

Chapter 3: SR-LBIC for short-circuit current density mapping

A method based on SR-LBIC maps of arbitrary silicon solar cells was introduced, where a pixel by pixel interpolation of EQE, reflection and IQE data, convoluted with an AM1.5G or other desired spectrum, yields spatially resolved J_{sc}^{loc} maps. Furthermore, the pseudo- J_{sc} figure of merit was introduced which enabled a quantification of what the local J_{sc} would be without optical reflection losses. Subtraction of a J_{sc}^{loc} from the pseudo- J_{sc}^{loc} map directly yields local J_{sc} losses from optical reflection. The application of these methods on IBC cells yielded the accurate quantification of the local and integrated 'electrical shading' effect at an illumination spectrum representative for AM1.5G. Additionally, this approach allowed spatially resolved detection of parasitic free-carrier absorption losses that reduced a solar cell's J_{sc} in an IBC cell with an Al emitter.

Chapter 4: Luminescence imaging of local cell characteristics

Understanding of the regular patterns in electro- and photoluminescence imaging of IBC cells was achieved at all important operating conditions. Through representative examples and numerical simulations using Quokka and COMSOL Multiphysics, it was found that the luminescence patterns at short-circuit conditions is dominated by diffusion limited carriers over the BSF regions, at maximum power point by a combination of diffusion limited carriers and series resistance and at open-circuit by lateral variations in surface recombination. Electroluminescence patterns under forward bias were found

to be linked to the individual sheet and base resistance of the cell and the subsequent primary locations of excess carrier injection. A sensitivity analysis of the luminescence patterns to surface recombination parameters was carried out. As a result, a method to extract surface recombination parameters of finished IBC cells by matching experimental and simulated luminescence images was proposed. This approach also enables access to surface recombination at metal silicon interfaces where conventional characterization by QSSPC lifetime test structures is not possible. Series resistance imaging was applied and adapted to IBC cells. Moreover, lateral series resistance losses could be attributed to limitations from electron or hole transport. This series resistance imaging should assist optimization of solar cell technology and design to maximize the fill factor.

Chapter 5: Lock-in thermography of local cell characteristics

An investigation of applying lock-in thermography (LIT) to IBC cells was conducted. Since lock-in thermography measures spatially resolved power densities, the question was raised whether the globally applicable free-energy loss analysis (FELA) could be applied in spatially resolved IBC cell analysis. Theoretical considerations on the released energy during thermalization, bulk and surface recombination of charge carriers lead to a model to simulate spatially resolved power density with and without consideration of the Peltier effect. Peltier effects in a typical IBC cell were identified and implemented into numerical device modeling based on electrical simulations using the program Quokka. These effects arise from ten electron and hole current contributions. According to the proposed model, the local power density profiles were found to be significantly influenced by the Peltier effect at all important operating conditions except at open-circuit. Consequently, power calibration of LIT images of IBC cells is possible but contains artifacts. A method for power calibration of illuminated lock-in thermography images was proposed. Experimentally observed patterns on a example IBC cell were qualitatively associated with findings in the simulations where e.g. local Peltier

cooling was identified as a potential source of signal misinterpretation.

Chapter 6: Detection of local processing faults

In practical application, imaging and mapping techniques are primarily used to detect and quantify local processing faults. The focus was set on some of the most common processing faults in IBC cells and the signature of these faults in global current-voltage characteristic, luminescence imaging and lock-in thermography. These faults were grouped into resistive, shunting and surface passivation / optical faults.

The investigated resistive faults comprised of namely globally high emitter/BSF contact resistance (R_c), locally high emitter R_c , locally high BSF R_c , locally extremely high emitter R_c (noticeable in reduced J_{sc}) and interrupted emitter and interrupted BSF metal fingers. Current-voltage simulations demonstrated that faults such as a single disconnected emitter finger cannot be correctly identified with global data but require imaging analysis. The more severe impact on cell performance of a clustered R_c faults compared to several local R_c faults was demonstrated through simulations.

The investigated shunting faults were pinhole shunts in isolation layers of 'point-structured' IBC cells¹ with an ohmic behavior and spiking shunts in aluminum metallized IBC cells with non-ohmic behavior. Identification and quantification of ohmic shunts from pinholes was achieved through conventional dark lock-in thermography analysis at forward and reverse bias. Precise spatial localization of pinhole shunts was accomplished through luminescence images. Spiking was investigated on a solar cell with a shallow and one with deep doping profile by gradual formation of spikes on hot plate temperature steps. The evolution of global current-voltage parameters could be well associated with all effects observed in luminescence imaging. The sensitivity of both LIT and luminescence imaging towards shunt-

¹See figure 2.10

ing faults was investigated and LIT was found to be well suited for the detection of shunting faults, despite the Peltier effect.

Furthermore, breakdown patterns were investigated with reverse-bias electroluminescence. It was found that breakdowns depend on whether or not there is a defined gap between emitter and BSF doping on the rear side. This yields information on the risk for hot spots in module application.

Chapter 7: Guidelines for IBC cell characterization

Finally, the conclusions on the origin of regular patterns in SR-LBIC, luminescence, and LIT images were summarized in user-friendly tabular overviews at all important operating conditions of the solar cell. Remarks on the usefulness of each image at each operating condition as well as recommendations on the most suitable method to study specific processing faults were provided. Guidelines for the investigation of local processing faults were summarized in 'top-down' flowcharts that start from basic current-voltage data and in 'bottom-up' tabular overviews that start from the processing fault and describe the fault's signature in current-voltage and imaging characteristic. Critical remarks on the new methods' limitations were stated.

Main achievements of this work

The main achievements of this dissertation can be summarized as follows:

1. Based on SR-LBIC, a robust quantitative analysis method was developed to determine spatially resolved short-circuit current density maps with high resolution as well as a newly defined pseudo- J_{sc} mapping method, which quantifies optical reflection losses. The method is applicable on any silicon solar cell design (chapter 3, published in [74]).
2. A model for simulating luminescence imaging experiments including optical blurring effects was introduced, based on two

or three-dimensional numerical device simulation with the software Quokka or COMSOL Multiphysics. The combination of simulations and experiments allowed thorough understanding of the regular patterns in luminescence imaging caused by the doping structure (section 4.3). Moreover, a method for obtaining local surface recombination parameters was proposed (section 4.5, published in [111]).

3. An adapted version of luminescence based series resistance imaging was validated to be applicable to IBC cells. Through numerical simulations and experiments of series resistance imaging, the impact of lateral electron and hole transport to the image was demonstrated (section 4.6, published in [113]).
4. An experimental study of lock-in thermography on IBC cells was conducted including a detailed analysis of Peltier effects by numerical simulations. It was shown that the Peltier heating and cooling significantly impacts the lock-in thermography images and that an immediate correlation between signal and power losses is not always possible (chapter 5).
5. A detailed understanding of the characteristic I-V and luminescence signature of all relevant contacting faults in IBC cells was achieved. Numerical simulations further enabled quantifying how clustered contact resistance faults impact cell performance more severely than individual faults (section 6.2, published in [112] and [114]).

Outlook

Various topics emerge for future research on further details of IBC cell characterization as well as the transfer of the used methods to other solar cell designs. Regarding IBC cells, this work focused mostly on the most typical cell designs that have line-shaped emitter and BSF regions instead of e.g. square-shaped BSF regions, which makes the unit cell three-dimensional. While the basic findings are the same, slight adaptations of the guidelines for such cells may be required. In

addition, examples of experimental luminescence imaging and lock-in thermography on industrial size IBC cells remain to be published.¹ The large busbar areas in industrial size cells contain highly interesting and more extreme cases of 'electrical shading', very high injection² and series resistance from lateral transport than the standard unit cells.

While adapting the series resistance imaging method based on Trupke et al.'s approach was successful, further research on whether alternative series resistance imaging methods or even voltage calibrations yield more accurate results remains to be conducted. Regarding lock-in thermography, this dissertation provided understanding of the local heating and cooling caused by the Peltier effect in a complex cell structure. More experimental work for verification of the Peltier effect modeling is suggested for the future. Ultimately, a method for quantitative experimental consideration or even correction of this effect in high resolution LIT experiments on complex solar cells has yet to be developed.

The list of investigated processing faults in this work was not exhaustive and various other processing faults could further be studied with respect to the IBC cell's device physics. The guidelines created in this work aimed to help technology oriented researchers in their day to day process of solving quality issues in solar cell manufacturing. Flowcharts and tabular overviews as presented in this work for IBC cells can be expanded upon as well as adapted to other solar cell designs in future work.

Finally, the approach of simulating current-voltage, SR-LBIC and luminescence imaging experiments of fault free silicon solar cells and cells with locally well-defined faults has great potential for future

¹Results obtained on large area IBC cells in the frame of a collaboration with an industrial manufacturer could not be disclosed in this dissertation.

²When excess carrier density is significantly higher than the base doping concentration and the notion of majority and minority carriers is not applicable.

work. The absence of experimental uncertainties and the perfect control over the cell design parameters that are normally too costly or challenging to vary in sample production makes the simulation of characterization experiments an ideal tool for comparison of competing characterization methods.

Deutsche

Zusammenfassung

Diese Dissertation präsentierte eine umfassende Untersuchung über orts aufgelöste Charakterisierung von rückseitig kontaktierten (IBC) Silizium Solarzellen mit einer Auswahl an kommerziell verfügbaren bildgebenden Messverfahren und Messgeräten. Das durch diese Arbeit erlangte Wissen ermöglicht die Analyse von IBC Zellen mit mächtigen bildgebenden Methoden die zuvor nur an einfacheren Zellstrukturen wie Al-BSF Zellen verwendet wurden. Die Zellanalyse wurde auf einer fundamentalen und einer praktischen Ebene durchgeführt. Auf der fundamentalen Ebene wird eine Studie der inhärent inhomogenen Bildkontrastmuster, die durch die interdigitale Dotierstruktur erzeugt werden, durchgeführt. Auf der praktischen Ebene wird eine Studie zur Erkennung von lokaler Prozessfehlern durchgeführt, die gruppiert sind in Widerstands-, Shunt- und Oberflächenrekombinationsfehler. Lokale Zellcharakteristika werden untersucht an den wichtigsten Arbeitspunkten der Solarzelle, d.h. unter Kurzschlussbedingungen, am Punkt maximaler Leistung, im Leerlaufzustand und im Dunkeln unter Vorwärts- und Rückwärtsspannung. Praktische Leitfäden wurden erstellt um die Implementierung der Erkenntnisse dieser Arbeit in anderen Forschungseinrichtungen und Industrieumgebungen zur erleichtern. Für ein tieferes Verständnis über die Zellphysik wurde vor allem die numerische Simulation von Lumineszenz Imaging entwickelt. Diese Modellierung diente als äußerst hilfreicher komplementärer Ansatz zur konventionellen experimentellen Arbeit.

Neben Fortschritten im physikalischen Verständnis wurden auch neue Charakterisierungsmethoden im Rahmen dieser Arbeit entwickelt.

Zusammenfassungen der Kapitel

Kapitel 3: SR-LBIC für orts aufgelöste Kurzschlussstromdichten

Eine Methode basierend auf SR-LBIC für beliebige Silizium Solarzellen wurde eingeführt, bei der eine Pixel für Pixel Interpolation von EQE, Reflektion und IQE Daten, gefaltet mit einem AM1.5G oder anderen gewünschten Spektrum, orts aufgelöste J_{sc}^{loc} Karten ergibt. Darüber hinaus wurde die Kenngröße pseudo- J_{sc} eingeführt, welche eine Quantifizierung von J_{sc} ohne optische Reflektionsverluste ermöglicht. Die Subtraktion einer J_{sc}^{loc} von einer pseudo- J_{sc} Karte ergibt unmittelbar die lokalen J_{sc} Verluste durch optische Reflektion. Die Anwendung dieser Methode auf IBC Zellen ergab die Quantifizierung des lokalen und integrierten 'electrical shading' Effekts unter einem Anregungsspektrum das für AM1.5G repräsentativ ist. Zusätzlich erlaubte dieser Ansatz die orts aufgelöste Detektion von parasitären Absorptionsverlusten, die den lokalen J_{sc} eine IBC Solarzelle mit einem Al Emitter reduziert haben.

Kapitel 4: Lumineszenz Imaging lokaler Zellcharakteristika

Das Verständnis der regelmäßigen Muster in Elektro- und Photolumineszenz Imaging von IBC Zellen wurden an allen wichtigen Arbeitspunkten untersucht. Über repräsentative Beispiele und numerische Simulationen mittels Quokka und COMSOL Multiphysics wurde herausgefunden, dass Lumineszenzmuster unter Kurzschlussbedingungen von diffusionslimitierten Ladungsträgern über den BSF Regionen, am *MPP* durch eine Kombination von diffusionslimitierten Ladungsträgern und Serienwiderstand und bei offenerer Klemmspannung durch Oberflächenrekombination dominiert werden. Elektrolumineszenzmuster unter Vorwärtsspannung wurden in Verbindung gesetzt zu den individuellen Schicht- und Basiswiderstandswerten der Zelle und den daraus folgenden primären Orten der Ladungsträgerinjektion. Eine

Sensitivitätsanalyse der Lumineszenzmuster auf Oberflächenrekombinationsparameter wurde ebenfalls durchgeführt. Als Ergebnis wurde eine Methode vorgeschlagen, welche die Bestimmung von Oberflächenrekombinationsparametern an fertigen IBC Zellen durch den Abgleich von Simulationen und Experimenten ermöglicht. Dieser Ansatz erlaubt auch den Zugang zur Oberflächenrekombination an Metall-Halbleiter Grenzflächen, wo die Anwendung konventioneller QSSPC Lebensdauerteststrukturen nicht möglich ist. Serienwiderstands Imaging wurde zudem angewandt und angepasst auf IBC Zellen, wobei laterale Serienwiderstandsverluste mit Limitierungen durch Transportverluste von Elektron oder Löcherströmen in Verbindung gesetzt werden konnten.

Kapitel 5: Lock-in Thermographie lokaler Zellcharakteristika

Eine Untersuchung der Anwendung von Lock-in Thermographie (LIT) auf IBC Zellen wurde durchgeführt. Da LIT orts aufgelöste Leistungsdichten misst wurde die Frage gestellt, ob die global anwendbare free-energy loss analysis (FELA) auch orts aufgelöst auf IBC Zellen anwendbar ist. Theoretische Überlegungen zu der frei werdenden Energie bei Thermalisierung und Basis- und Oberflächenrekombination von Ladungsträgern führte zu einem Model zur Simulation orts aufgelöster Leistungsdichten mit und ohne Berücksichtigung des Peltier Effektes. Peltier Effekte in typischen IBC Zellen wurden identifiziert und implementiert in numerische Simulationen basierend auf elektrischen Simulationen mit dem Programm Quokka. Diese Effekte entstehen aus zehn Strombeiträgen von Elektronen und Löchern. Es stellte sich heraus, dass die Profile lokaler Leistungsdichte signifikant von Peltier Effekte an allen Arbeitspunkten bis auf den Leerlaufzustand beeinflusst werden. Dies demonstrierte, dass eine Leistungskalibrierung von LIT Bildern von IBC Zellen möglich ist aber Artefakte enthält. Eine Methode zur Leistungskalibrierung von Lock-in Thermographie unter Beleuchtung wurde vorgeschlagen. Experimentell beobachtete Muster an einer Beispiel IBC Zelle wurden assoziiert mit den Erkenntnissen aus den Simulation, bei denen

z.B. lokale Peltier Kühlung identifiziert wurde also Quelle möglicher Fehldeutung von Signalen.

Kapitel 6: Detektion lokaler Prozessfehler

In der praktischen Anwendungen werden bildgebende Methoden primär zur Detektion und Quantifizierung lokaler Prozessfehler verwendet. Der Fokus wurde hierbei auf die häufigsten Prozessfehler in IBC Zellen und der Signatur dieser Fehler in globaler I-V Charakteristik sowie in Lumineszenz Imaging und Lock-in Thermographie gesetzt. Diese Fehler wurden gruppiert in Widerstands-, Shunt- und Oberflächenpassivierungsfehler.

Die untersuchten Widerstandsfehler umfassten global hoher Emitter/BSF Kontaktwiderstand (R_c), lokal hoher Emitter R_c , lokal hoher BSF R_c , loka extrem hoher Emitter R_c (bemerktbar durch reduzierten J_{sc}) sowie unterbrochene Emitter- und unterbrochene BSF Metallfinger. I-V Simulationen zeigten, dass Fehler wie einzelne nicht angeschlossene Emitter Metallfinger nicht korrekt durch globale Daten identifiziert werden können und dafür bildgebende Verfahren benötigen. Die schwerwiegendere Auswirkung auf die Zelleffizienz von gebündelten R_c Fehlern im Vergleich zu mehreren einzelnen R_c Fehlern wurde durch Simulationen demonstriert.

Die untersuchten Shunt Fehler waren Pinhole Shunts in Isolationsschichten von 'punkt-strukturierten' IBC Zellen¹ mit ohmschen Verhalten und Spiking Shunts in Aluminium metallisierten IBC Zellen mit nicht ohmschen Verhalten. Identifikation und Quantifizierung von ohmschen Shunts durch Pinholes wurde durch konventionelle dunkel Lock-in Thermographie Analyse unter vorwärts und rückwärts Spannung erzielt. Eine präzise Lokalisierung der Pinhole Shunts wurde hingegen durch Lumineszenz Imaging erreicht. Spiking wurde an einer Solarzelle mit einem flachen Dotierprofil und einer Zelle mit einem tiefen Dotierprofil durch die schrittweise Erzeugung von Spikes mittels Temperaturschritten auf einer Heizplatte untersucht. Die Entwicklung von globalen I-V Parametern konnte gut assoziiert werden

¹Siehe Abbildung 2.10

mit allen beobachteten Effekten im Lumineszenz Imaging. Die Sensitivität von LIT und Lumineszenz Imaging auf Shunt Fehler wurde untersucht und LIT wurde als geeignete Methode für die Detektion von Shunt Fehlern identifiziert, trotz des Peltier Effekts.

Darüber hinaus wurden Muster von elektrischen Durchbrüchen mittels Elektrolumineszenz Imaging unter rückwärts Spannung untersucht. Es stellte sich heraus, dass die Durchbrüche davon abhängen ob es eine definierte Lücke zwischen Emitter und BSF Dotierung auf der Rückseite gibt. Dies liefert auch Information über das Risiko von Hot Spots in Solarmodulen.

Kapitel 7: Leitfäden für IBC Zellcharakterisierung

Schließlich wurden die Schlussfolgerungen zu den Ursprüngen der regelmäßigen Muster in SR-LBIC, Lumineszenz und LIT Bildern in benutzerfreundlichen tabellarischen Übersichten an allen wichtigen Arbeitspunkten der Solarzelle zusammengefasst. Bemerkungen zur Nützlichkeit der Bilder an jedem Arbeitspunkt sowie Empfehlungen zur bestgeeignetsten Methode zur Untersuchung bestimmter Prozessfehler wurden bereitgestellt. Leitfäden für die Untersuchung lokaler Prozessfehler wurden zusammengefasst in 'top-down' Flussdiagrammen, die mit grundlegenden I-V Daten beginnen und 'bottom-up' Übersichten die vom Prozessfehler starten und dessen Signatur in I-V und Bildcharakteristik beschreiben. Kritische Bemerkungen zu den Limitierungen der neuen Charakterisierungsmethoden wurden benannt.

Zentrale Errungenschaften dieser Arbeit

Die zentralen Errungenschaften dieser Dissertation können folgendermaßen zusammengefasst werden:

1. Basierend auf SR-LBIC wurde eine robuste quantitative Analyseverfahren zur orts aufgelösten Bestimmung von Kurzschlussstromdichten mit hoher Ortsauflösung entwickelt, sowie eine neu definierten pseudo- J_{sc} Kartierungsmethode welche optische Reflektionsver-

luste quantifiziert. Diese Methode ist auf beliebige Silizium Solarzellendesigns anwendbar (Kapitel 3, publiziert in [74]).

2. Ein Model für die Simulation von Lumineszenz Imaging Experimenten inklusive optische Verschmierungseffekte wurde eingeführt, basierend auf zwei oder dreidimensionalen numerischen Simulationen mit der Software Quokka oder COMSOL Multiphysics. Die Kombination aus Simulationen und Experimenten ermöglichte ein gründliches Verständnis der durch die interdigitalen Dotierstrukturen hervorgerufenen regelmäßigen Muster im Lumineszenz Imaging (Abschnitt 4.3). Zudem wurde eine Methode zur Bestimmung lokaler Oberflächenrekombinationsparameter vorgeschlagen (Abschnitt 4.5, publiziert in [111]).
3. Eine angepasste Version von Lumineszenz basierten Serienwiderstands Imaging wurde als anwendbar auf IBC Zelle verifiziert. Über numerische Simulationen und Experimente konnte der Einfluss von lateralen Elektron und Loch Transport auf das Bild demonstriert werden (Abschnitt 4.6, publiziert in [113]).
4. Eine experimentelle Studie von Lock-in Thermographie an IBC Zellen wurde durchgeführt, inklusive der detaillierten Analyse von Peltier Effekten durch numerischen Simulationen. Es wurde gezeigt, dass Peltier Heizen und Kühlen signifikante die Lock-in Thermographie Bilder beeinflusst und dass eine unmittelbare Korrelation zwischen Signal und Leistungsverlusten nicht immer möglich ist (Kapitel 5).
5. Ein detailliertes Verständnis der charakteristischen I-V und Lumineszenz Signaturen aller relevanter Kontaktierungsfehler in IBC Zellen wurden erreicht. Numerische Simulationen haben zudem die Quantifizieren ermöglicht, wie gebündelte Kontaktwiderstandsfehler die Zelle stärker beeinflussen als individuelle Fehler (Abschnitt 6.2, publiziert in [112] und [114]).

Ausblick

Diverse Themen bieten sich für zukünftige Forschungsarbeiten zur detaillierteren IBC Zellcharakterisierung, sowie für den Transfer der verwendeten Methoden auf anderen Solarzellendesigns an. Mit Hinblick auf IBC Zellen fokussierte sich diese Arbeit auf die typischsten Designs mit linienförmigen Emitter und BSF Regionen anstatt z.B. quadratischen BSF Regionen, welche die Einheitszelle dreidimensional machen. Die grundlegenden Erkenntnisse sollten die Selben bleiben, aber leichte Anpassungen an die Leitfäden sind wohlmöglich notwendig. Zudem wurden Beispiele von experimentellen Lumineszenz und Lock-Thermographie Ergebnissen an IBC Zellen mit industrierelevanten Zelldimensionen bislang nicht veröffentlicht. Die großen Busbar Regionen in Industriezellen enthalten hochinteressante und extremere Beispiele des 'electrical shading', Hochinjektion¹ und Serienwiderstand durch lateralen Transport im Vergleich zu Standard Einheitszellen.

Während die Anpassung des Serienwiderstand Imaging basierend auf die Methode von Trupke et al. erfolgreich war, könnte weiterführend erforscht werden, ob alternative Serienwiderstand Imaging Methoden oder sogar Spannungskalibrierungen bei IBC Zellen zu besseren Ergebnissen führen. Mit Hinblick auf Lock-in Thermographie bietet diese Dissertation ein grundlegendes Verständnis für das lokale Heizen und Kühlen, verursacht durch die Peltier Effekte in einer komplexen Zellstruktur aber eine Methode diesen Effekt quantitativ zu bewerten bzw. zu korrigieren ist bislang nicht entwickelt worden.

Die Liste der untersuchten Prozessfehler war nicht umfassend und diverse andere Prozessfehler könnten weitergehen mit Hinblick auf die IBC Zellphysik untersucht werden. Die Leitlinien die in dieser Arbeit entwickelt wurden zielen darauf ab technologieorientierte Forscher bei

¹Wenn Ladungsträgerdichten wesentlich höher sind als die Basisdotierkonzentration und der Begriff der Majoritäten und Minoritäten nicht direkt anwendbar ist.

ihrer täglichen Arbeit zu unterstützen und Qualitätsprobleme bei der Solarzelleherstellung zu lösen. Flussdiagramme und Übersichten, wie in dieser Arbeit präsentiert für IBC Zellen, könnten erweitert und auch auf andere Zelldesigns angepasst werden.

Letztlich hat der Ansatz der Simulation von I-V, SR-LBIC und Lumineszenz Imaging von prozessfehlerfreien Silizium Solarzellen sowie Zellen mit wohldefinierten lokalen Fehlern großes Potential für künftige Arbeiten. Das Fehlen von experimentellen Unsicherheiten und die perfekte Kontrolle über Zelldesign Parameter, die normalerweise zu teuer oder zu anspruchsvoll sind die Probenherstellung für, machen die Simulation von Charakterisierung Experimenten zu einem idealen Werkzeug zum Vergleich von Methoden die in Konkurrenz miteinander stehen.

Appendix A

Details on all investigated solar cells

Turn to the next page for a table with technical information on all IBC silicon solar cells investigated in this work.

Table A.1: Technical information on all IBC silicon solar cells investigated in this work. All J_0 obtained by researchers at Fraunhofer ISE via solar cell precursors. Remarks - 1: Al emitter cell; 2: J_0 values only representative to before the tempering step prior to the 'initial' state in section 6.3.2.

Name	type	material	ρ_{base}	d	pitch	w_{EM}	w_{BSF}	w_{cont}	J_0^{EM}	J_0^{BSF}	J_0^{FSF}	J_0^{ap}
			(Ωcm)							(μm)	(μm)	
A ¹	B	n, Cz	3.5	156	1600	1000	600	200n,1000p	200	146/21*	34	n/a
A1	B	n, Cz	3.2	159	1000	640	360	36	92	127	46	n/a
B ¹	B	n, Cz	3.5	156	1600	1000*	600	200n,800p	200	146/21*	34	n/a
BC1	A	n, Fz	1	160	2200	1600	300	20	235	288	24	176
BC2	A	n, Fz	1	160	3500	2900	300	20	235	288	24	176
BC3	A	n, Fz	10	160	3500	2900	300	20	235	288	24	176
BC4	A	n, Fz	10	160	3500	2900	300	20	235	288	24	176
BC5	A	n, Fz	10	160	2200	1600	300	20	235	288	24	176
BC6	A	n, Fz	10	160	1300	700	300	20	235	288	24	176
BD1	A	n, Cz	5	159	1500	1000	300	27	92	74	40	6
BD2	A	n, Cz	5	156	1500	1000	300	27	116	147	66	6
BD3	B	n, Fz	1	180	1600	1300	300	10	20	550	35	n/a
CF1	B	n, Fz	1	180	2200	1900	300	20	24	370	10	n/a
CF2	B	n, Fz	3.2	159	1500	1140	360	39	92	127	46	n/a
CF4	B	n, Fz	5	180	2200	1600	600	10	11	85	24	n/a
F11	A	n, Fz	1	180	2200	1600	300	10	12	140	29	12
F12	A	n, Fz	1	180	2200	1600	300	10	12	140	29	12
OP1	A	n, Cz	4.3	159	1000	700	300	27	92	127	66	n/a
P1	C	n, Cz	6.1	168	1000	460	310	72n,32p	450	74	66	6
S1 ²	B	n, Cz	4.3	159	2000	1700	300	35	92	127	66	n/a
S2 ²	B	n, Cz	4.2	157	2000	1700	300	35	-	74	40	n/a

Table A.2: *continued from previous page* Technical information on all IBC silicon solar cells investigated in this work.

Name	type	R_{sh}^{EM}	R_{sh}^{BSF} (Ω/sq)	R_{sh}^{FSF}	BS passiv.	Metal
A	B	Al EM	40	200	SiONy	Al
A1	B	692	35	400	F-AlO/SiN	AlSi
B B	Al EM	40	200	SiONy	Al	
BC1	A	19	10	150	SiO ₂	Al+TiPdAg
BC2	A	19	10	150	SiO ₂	Al+TiPdAg
BC3	A	19	10	150	SiO ₂	Al+TiPdAg
BC4	A	19	10	150	SiO ₂	Al+TiPdAg
BC5	A	19	10	150	SiO ₂	Al+TiPdAg
BC6	A	19	10	150	SiO ₂	Al+TiPdAg
BD1	A	39	65	400	O-AlO/SiN	AlSi
BD2	A	73	65	400	P-AlO/SiN	AlSi
BD3	B	90	55	90	Al ₂ O ₃ +SiO _x	Ti+Al
CF1	B	73	39	440	Al ₂ O ₃ +SiO _x	Al
CF2	B	54	20	400	F-AlO/SiN	AlSi
CF4	B	110	225	300	Al ₂ O ₃ +SiO _x	Al+TiPdAg
F11	A	85	10	148	Al ₂ O ₃ +SiO _x	Al+TiPdAg
F12	A	85	10	148	Al ₂ O ₃ +SiO _x	Al+TiPdAg
OP1	A	39	54	400	O-AlO/SiN	AlSi
P1	C	104	41	400	F-AlO/SiO/SiN	AlSi
S1	B	39	54	400	O-AlO/SiN	AlSi
S2	B	53	55	400	O-AlO/SiN	AlSi

Bibliography

- [1] Fraunhofer ISE. Aktuelle Fakten zur Photovoltaik in Deutschland. Technical report, July 2015.
- [2] International Energy Agency. World Energy Outlook. Technical report, June 2015.
- [3] International Technology Roadmap for Photovoltaic (ITRPV). Technical report, 2015.
- [4] D. D. Smith, P. Cousins, S. Westerberg, R. De Jesus-Tabajonda, G. Aniero, and Y.-C. Shen. Toward the practical limits of silicon solar cells. *IEEE Journal of Photovoltaics*, 4(6):1465–9, 2014.
- [5] K. Masuko, M. Shigematsu, T. Hashiguchi, D. Fujishima, M. Kai, N. Yoshimura, T. Yamaguchi, Y. Ichihashi, T. Mishima, N. Matsubara, T. Yamanishi, T. Takahama, M. Taguchi, E. Maruyama, and S. Okamoto. Achievement of more than 25% conversion efficiency with crystalline silicon heterojunction solar cell. *IEEE Journal of Photovoltaics*, 4(6):1433–5, 2014.
- [6] M. A. Green, K. Emery, Y. Hishikawa, W. Warta, and E. D. Dunlop. Solar cell efficiency tables (version 46). *Progress in Photovoltaics: Research and Applications*, 23(7):805–812, 2015.
- [7] Solar Impulse - www.solarimpulse.com, 2015.
- [8] Industry reports found on www.pv-tech.org, 2015.

- [9] M. Kasemann. *What photons tell us about solar cells*. PhD thesis, Universität Freiburg, 2010.
- [10] Peter Würfel and Uli Würfel. *Physics of solar cells: from basic principles to advanced concepts*. John Wiley and Sons, 2009.
- [11] Martin A Green. *Silicon solar cells: advanced principles and practice*. Centre for photovoltaic devices and systems, University of New South Wales, 1995.
- [12] H. Straube. *Quantitatives Verständnis von Lock-in-Thermographie an Dünnschicht-Solarmodulen*. PhD thesis, 2011.
- [13] M. A. Green. Intrinsic concentration, effective densities of states, and effective mass in silicon. *Journal of Applied Physics*, 67(6):2944–54, 1990.
- [14] P. P. Altermatt, A. Schenk, F. Geelhaar, and G. Heiser. Re-assessment of the intrinsic carrier density in crystalline silicon in view of band-gap narrowing. *Journal of Applied Physics*, 93(3):1598–604, 2003.
- [15] A. Schenk. Finite-temperature full random-phase approximation model of band gap narrowing for silicon device simulation. *Journal of Applied Physics*, 84(7):3684–95, 1998.
- [16] D. A. Kleinman. The forward characteristic of the pin diode. *Bell System Technical Journal*, 35(3):685–706, 1956.
- [17] A. Fell. A free and fast three-dimensional/two-dimensional solar cell simulator featuring conductive boundary and quasi-neutrality approximations. *IEEE Transactions on Electron Devices*, 60(2):733–8, 2013.
- [18] J. Giesecke. *Quantitative Recombination and Transport Properties in Silicon from Dynamic Photoluminescence*. PhD thesis, Universität Konstanz, 2014.

- [19] F. Schindler, M. Forster, J. Broisch, J. Schön, J. Giesecke, S. Rein, W. Warta, and M. C. Schubert. Towards a unified low-field model for carrier mobilities in crystalline silicon. *Solar Energy Materials and Solar Cells*, 131:92–9, 2014.
- [20] A. Einstein. Über die von der molekularkinetischen Theorie der Wärme geforderte Bewegung von in ruhenden Flüssigkeiten suspendierten Teilchen. *Annalen der Physik*, 14(S1):182–193, 1905.
- [21] D. A. Clugston and P. A. Basore. Pc1d version 5: 32-bit solar cell modeling on personal computers. In *Proceedings of the 26th IEEE Photovoltaic Specialists Conference*, Conference Record of the Twenty Sixth IEEE Photovoltaic Specialists Conference - 1997, pages 207–10.
- [22] B. Michl. *Material Limits of Multicrystalline Silicon in Advanced Solar Cell Processing*. Phd thesis, Universität Freiburg, 2014.
- [23] Oliver Schultz. *High-efficiency multicrystalline silicon solar cells*. Phd thesis, universität Konstanz, 2005.
- [24] M. Rüdiger. *Analysis and Simulation of Crystalline Silicon Solar Cells*. Phd thesis, Universität Konstanz, 2013.
- [25] W. Shockley and H. J. Queisser. Detailed balance limit of efficiency of p-n junction solar cells. *Journal of Applied Physics*, 32(3):510–9, 1961.
- [26] A. Richter, M. Hermle, and S. W. Glunz. Reassessment of the limiting efficiency for crystalline silicon solar cells. *IEEE Journal of Photovoltaics*, 3(4):1184–91, 2013.
- [27] K. R. McIntosh and P. P. Altermatt. A freeware 1d emitter model for silicon solar cells. In *Proceedings of the 35th IEEE Photovoltaic Specialists Conference*, pages 1–6.
- [28] A. Cuevas and D. Macdonald. Measuring and interpreting the lifetime of silicon wafers. *Solar Energy*, 76(1-3):255–62, 2004.

- [29] R. Brendel. Modeling solar cells with the dopant-diffused layers treated as conductive boundaries. *Progress in Photovoltaics: Research and Applications*, 20(1):31–43, 2012.
- [30] T. Trupke, M. A. Green, P. Würfel, P. P. Altermatt, A. Wang, J. Zhao, and R. Corkish. Temperature dependence of the radiative recombination coefficient of intrinsic crystalline silicon. *Journal of Applied Physics*, 94(8):4930–7, 2003.
- [31] P. P. Altermatt, F. Geelhaar, T. Trupke, X. Dai, A. Neisser, and E. Daub. Injection dependence of spontaneous radiative recombination in c-si: experiment, theoretical analysis, and simulation. In *Proceedings of the 5th International Conference on Numerical Simulation of Optoelectronic Devices*, pages 47–8.
- [32] A. Hangleiter and R. Häcker. Enhancement of band-to-band auger recombination by electron-hole correlations. *Physical Review Letters*, 65(2):215–8, 1990.
- [33] J. Dziewior and W. Schmid. Auger coefficients for highly doped and highly excited silicon. *Applied Physics Letters*, 31(5):346–8, 1977.
- [34] A. Richter, S. W. Glunz, F. Werner, J. Schmidt, and A. Cuevas. Improved quantitative description of auger recombination in crystalline silicon. *Physical Review B*, 86(16):165202, 2012.
- [35] K. Graff. *Metal Impurities in Silicon-Device Fabrication*. Springer Series in Materials Science. Springer, Berlin, 2nd edition, 2000.
- [36] PV Lighthouse - www.pvlighthouse.au.
- [37] M. Wolf and H. Rauschenbach. Series resistance effects on solar cell measurements. *Advanced Energy Conversion*, 3:455–79, 1963.
- [38] K. R. McIntosh. *Lumps, humps and bumps: Three detrimental effects in the current-voltage curve of silicon solar cells*. Phd thesis, university of new south wales, 2001.

- [39] D. Pysch, A. Mette, and S. W. Glunz. A review and comparison of different methods to determine the series resistance of solar cells. *Solar Energy Materials and Solar Cells*, 91:1698–706, 2007.
- [40] O. Breitenstein. An alternative one-diode model for illuminated solar cells. *IEEE Journal of Photovoltaics*, 4(3):899–905, 2014.
- [41] S.M. Sze. *Physics of semiconductor devices*. John Wiley and Sons, Inc., New York, 2nd edition, 1981.
- [42] H. Straube, J. M. Wagner, and O. Breitenstein. Measurement of the peltier coefficient of semiconductors by lock-in thermography. *Applied Physics Letters*, 95(5):052107, 2009.
- [43] G. S. Nolas, J. Sharp, and J. Goldsmid. *Thermoelectrics: basic principles and new materials developments*, volume 45. Springer Science and Business Media, 2013.
- [44] T. H. Geballe and G. W. Hull. Seebeck effect in silicon. *Physical Review*, 98(4):940–947, 1955.
- [45] M. E. Brinson and W. Dunstant. Thermal conductivity and thermoelectric power of heavily doped n-type silicon. *Journal of Physics C: Solid State Physics*, 3(3):483, 1970.
- [46] L. Weber and E. Gmelin. Transport properties of silicon. *Applied Physics A*, 53(2):136–140, 1991.
- [47] D. D. Smith, P. J. Cousins, A. Masad, S. Westerberg, M. Defensor, R. Ilaw, T. Dennis, R. Daquin, N. Bergstrom, A. Leygo, Zhu Xi, B. Meyers, B. Bourne, M. Shields, and D. Rose. Sunpower’s maxeon gen iii solar cell: High efficiency and energy yield. In *Photovoltaic Specialists Conference (PVSC), 2013 IEEE 39th*, pages 0908–0913.
- [48] R. J. Schwartz and M. D. Lammert. Silicon solar cells for high concentration applications. In *Technical Digest of the International Electron Devices Meeting*, pages 350–2, Dicker.

- [49] F. Granek, M. Hermle, D Huljic, O. Schultz-Wittmann, and S. W. Glunz. Enhanced lateral current transport via the front n+ diffused layer of n-type high-efficiency back-junction back-contact silicon solar cells. *Progress in Photovoltaics: Research and Applications*, 17(1):47–56, 2008.
- [50] P. Engelhart, N.-P. Harder, R. Grischke, A. Merkle, R. Meyer, and R. Brendel. Laser structuring for back junction silicon solar cells. *Progress in Photovoltaics: Research and Applications*, 15(3):237–43, 2006.
- [51] I. Cesar, N. Guillevin, A. R. Burgers, A. A. Mewe, M. Koppes, J. Anker, L. J. Geerligs, and A. W. Weeber. Mercury: A back junction back contact front floating emitter cell with novel design for high efficiency and simplified processing. *Energy Procedia*, 55:633–42, 2014.
- [52] T. Ohrdes, U. Römer, Y. Larionova, R. Peibst, P. P. Altermatt, and N.-P. Harder. High fill-factors of back-junction solar cells without front surface field diffusion. In *Proceedings of the 27th European Photovoltaic Solar Energy Conference and Exhibition*, pages 866–9.
- [53] Robert Woehl. *All-Screen-Printed Back-Contact Back-Junction Silicon Solar Cells with Aluminum-Alloyed Emitter*. Phd thesis, Universität Freiburg, 2011.
- [54] C. Reichel. *Decoupling Charge Carrier Collection and Metallization Geometry of Back-Contacted Back-Junction Silicon Solar Cells*. Phd thesis, 2012.
- [55] R. Keding. *Co-diffused Back-Contact Back-Junction Silicon Solar Cells*. Phd thesis, Universität Freiburg, 2015.
- [56] A. Kimmerle. *Diffused Surfaces for Crystalline Silicon Solar Cells - Process Developemnt, Characterization and Modelling*. Phd thesis, Universität Freiburg, 2015.

- [57] J.-H. Guo, P. J. Cousins, and J. E. Cotter. Investigations of parasitic shunt resistance in n-type buried contact solar cells. *Progress in Photovoltaics: Research and Applications*, 14(2): 95–105, 2006.
- [58] M. Hendrichs, M. Padilla, F. Walter, A. Fell, and B. Rech. Screen-printed metallization concepts for large-area back-contact back-junction solar cells. In *Proceedings of the 42nd IEEE Photovoltaic Specialists Conference*.
- [59] M. Rinio. *Untersuchung der prozessabhängigen Ladungsträgerrekombination an Versetzungen in Siliziumsolarzellen*. Phd thesis, Technische Universität Bergakademie Freiberg, 2004.
- [60] R.J. Nelson and R.G. Sobers. Minority-carrier lifetime and internal quantum efficiency of surface-free gaas. *Journal of Applied Physics*, 49:6103–8, 1978.
- [61] J. Giesecke. *Quantitative recombination and transport properties in silicon from dynamic luminescence*. Springer, 2014.
- [62] E. Daub. *Photolumineszenz von Silizium*. Phd thesis, Universität Karlsruhe, 1995.
- [63] M. A. Green. Self-consistent optical parameters of intrinsic silicon at 300 k including temperature coefficients. *Solar Energy Materials and Solar Cells*, 92(11):1305–10, 2008.
- [64] C. Schinke, K. Bothe, P. C. Peest, J. Schmidt, and R. Brendel. Uncertainty of the coefficient of band-to-band absorption of crystalline silicon at near-infrared wavelengths. *Applied Physics Letters*, 104(8):081915, 2014.
- [65] H. T. Nguyen, F. E. Rougieux, B. Mitchell, and D. Macdonald. Temperature dependence of the band-band absorption coefficient in crystalline silicon from photoluminescence. *Journal of Applied Physics*, 115(4):043710, 2014.

- [66] M. Glatthaar, J. Haunschild, R. Zeidler, M. Demant, J. Greulich, B. Michl, W. Warta, S. Rein, and R. Preu. Evaluating luminescence based voltage images of silicon solar cells. *Journal of Applied Physics*, 108:014501, 2010.
- [67] H. Höffler, H. Al-Mohtaseb, J. Haunschild, B. Michl, and M. Kasemann. Voltage calibration of luminescence images of silicon solar cells. *Journal of Applied Physics*, 115(3):034508, 2014.
- [68] J. Wong. Perturbation theory for solar cell efficiency ii - delineating series resistance. *Electron Devices, IEEE Transactions on*, 60(3):917–922, 2013.
- [69] O. Breitenstein, H. Höffler, and J. Haunschild. Photoluminescence image evaluation of solar cells based on implied voltage distribution. *Solar Energy Materials and Solar Cells*, 128(0): 296–299, 2014.
- [70] Otwin Breitenstein, Wilhelm Warta, and Martin Langenkamp. *Lock-in thermography: Basics and use for evaluating electronic devices and materials*, volume 10. Springer Science and Business Media, 2010.
- [71] O. Breitenstein, A. Khanna, Y. Augarten, J. Bauer, J.-M. Wagner, and K. Iwig. Quantitative evaluation of electroluminescence images of solar cells. *Physica Status Solidi RRL*, 4(1-2): 7–9, 2010.
- [72] M. Planck. Über das Gesetz der Energieverteilung im Normalspektrum. *Annalen der Physik*, 309(3):553–563, 1901.
- [73] J. Stefan. *Über die Beziehung zwischen der Wärmestrahlung und der Temperatur*. 1879.
- [74] M. Padilla, B. Michl, B. Thaidigsmann, W. Warta, and M. C. Schubert. Short-circuit current density mapping for solar cells. *Solar Energy Materials and Solar Cells*, 120, Part A:282–8, 2014.

- [75] Fabian Fertig, Milan Padilla, Otwin Breitenstein, Hannes Höfler, Ino Geisemeyer, Martin C. Schubert, and Stefan Rein. Short-circuit current density imaging methods for silicon solar cells. *Energy Procedia*, 77:43–56, 2015.
- [76] C. Donolato. Evaluation of diffusion lengths and surface recombination velocities from electron beam induced current scans. *Applied Physics Letters*, 43(1):120–2, 1983.
- [77] K. L. Luke, O. von Roos, and L.-J. Cheng. Quantification of the effects of generation volume, surface recombination velocity, and diffusion length on the electron-beam-induced current and its derivative: determination of diffusion lengths in the low micron and submicron ranges. *Journal of Applied Physics*, 57(6):1978–84, 1985.
- [78] W. D. Sawyer. An improved method of light-beam induced current characterization of grain boundaries. *Journal of Applied Physics*, 59(7):2361–3, 1986.
- [79] J. D. Zook. Theory of beam-induced currents in semiconductors. *Applied Physics Letters*, 42(7):602–4, 1983.
- [80] M. Stemmer and S. Martinuzzi. Mapping of local minority carrier diffusion length applied to multicrystalline silicon cells. In *Proceedings of the 11th European Photovoltaic Solar Energy Conference*, pages 450–2.
- [81] J. Isenberg, O. Bartels, and W. Warta. Separation of bulk diffusion length and rear surface recombination velocity in sr-lbic mappings. In *Proceedings of the 29th IEEE Photovoltaics Specialists Conference*, pages 328–31.
- [82] V. Schlosser, R. Ebner, J. Summhammer, P. Bajons, and G. Klinger. Lbic investigations of multicrystalline silicon solar cells with the front contact on grain boundaries. In *Proceedings of the 20th European Photovoltaic Solar Energy Conference*, pages 1135–8.

- [83] W. Warta, J. Sutter, B. F. Wagner, and R. Schindler. Impact of diffusion length distributions on the performance of mc-silicon solar cells. In J. Schmid, H. A. Ossenbrink, P. Helm, H. Ehmann, and E. D. Dunlop, editors, *Proceedings of the 2nd World Conference on Photovoltaic Energy Conversion*, pages 1650–3.
- [84] M. Breitwieser, F. D. Heinz, A. Büchler, M. Kasemann, J. Schön, W. Warta, and M. C. Schubert. Analysis of solar cell cross sections with micro-light beam induced current (μ LBIC). *Solar Energy Materials and Solar Cells*, 131:124–8, 2014.
- [85] M. Breitwieser, F. D. Heinz, T. Rachow, M. Kasemann, S. Janz, W. Warta, and M. C. Schubert. Process control and defect analysis for crystalline silicon thin films for photovoltaic applications by the means of electrical and spectroscopic microcharacterization tools. *Photovoltaics, IEEE Journal of*, 4(5):1275–1281, 2014.
- [86] A. Goetzberger, B. Voß, and J. Knobloch. *Sonnenenergie: Photovoltaik - Physik und Technologie der Solarzelle*, volume 2.,. B. G. Teubner Stuttgart, Freiburg im Breisgau, 1997.
- [87] M. De Vittorio, R. Cingolani, M. Mazzer, and D. B. Holt. Sub-micron photocurrent mapping of heterostructures by microprobe optical-beam induced current. *Review of Scientific Instruments*, 70(8):3429–3431, 1999.
- [88] M. Schwalm, C. Lange, W. Rühle, W. Stolz, K. Volz, and S. Chatterjee. Solar cell characterization with high spatial resolution. In *Advanced Photonics and Renewable Energy*, OSA Technical Digest (CD). Optical Society of America.
- [89] Jonathan E. Allen, Daniel E. Perea, Eric R. Hemesath, and Lincoln J. Lauhon. Nonuniform nanowire doping profiles revealed by quantitative scanning photocurrent microscopy. *Advanced Materials*, 21(30):3067–3072, 2009.

- [90] F. Fertig, J. Greulich, and S. Rein. Spatially resolved determination of the short-circuit current density of silicon solar cells via lock-in thermography. *Applied Physics Letters*, 104(20):201111, 2014.
- [91] F. Fertig, J. Greulich, and S. Rein. Short-circuit current density imaging of crystalline silicon solar cells via lock-in thermography: Robustness and simplifications. *Journal of Applied Physics*, 116(18):184501, 2014.
- [92] Otwin Breitenstein, Jan Bauer, David Hinken, and Karsten Bothe. The reliability of thermography- and luminescence-based series resistance and saturation current density imaging. *Solar Energy Materials and Solar Cells*, 137(0):50–60, 2015.
- [93] H. Höffler, O. Breitenstein, and J. Haunschild. Short-circuit current density imaging via pl image evaluation based on implied voltage distribution. *IEEE Journal of Photovoltaics*, 5(2):613–8, 2015.
- [94] F. Dross, E. Van Kerschaver, and G. Beaucarne. Minimization of the shadow-like losses for inter-digitated back-junction solar cells. In *Proceedings of the 15th International Photovoltaic Science and Engineering Conference*, pages 971–2.
- [95] M. Hermle, F. Granek, O. Schultz-Wittmann, and S. W. Glunz. Shading effects in back-junction back-contacted silicon solar cells. In *Proceedings of the 33rd IEEE Photovoltaic Specialists Conference*.
- [96] C. Reichel, F. Granek, M. Hermle, and S. W. Glunz. Enhanced current collection in backcontacted back-junction si solar cells by overcompensating a boron emitter with a phosphorus base-type doping. *Physica Status Solidi A*, 207(8):1978–81, 2010.
- [97] S. Kluska, F. Granek, M. Rüdiger, M. Hermle, and S. W. Glunz. Modeling and optimization study of industrial n-type high-efficiency back-contact back-junction silicon solar cells. *Solar Energy Materials and Solar Cells*, 94(3):568–77, 2010.

- [98] F. Granek, M. Hermle, C. Reichel, A. Grohe, O. Schultzwittmann, and S. Glunz. Positive effects of front surface field in high-efficiency back-contact back-junction n-type silicon solar cells. In *Proceedings of the 33rd IEEE Photovoltaic Specialists Conference*.
- [99] C. Reichel, F. Granek, M. Hermle, and S. W. Glunz. Investigation of electrical shading effects in back-contacted back-junction silicon solar cells using the two-dimensional charge collection probability and the reciprocity theorem. *Journal of Applied Physics*, 109(2):024507, 2011.
- [100] C. Donolato. A reciprocity theorem for charge collection. *Applied Physics Letters*, 46(3):270–2, 1985.
- [101] pv-tools GmbH - www.pv-tools.de.
- [102] B. Fischer. *Loss analysis of crystalline silicon solar cells using photoconductance and quantum efficiency measurements*. PhD thesis, Universität Konstanz, 2003.
- [103] A. G. Aberle, S. Glunz, and W. Warta. Impact of illumination level and oxide parameters on shockley-read-hall recombination at the si-sio₂ interface. *Journal of Applied Physics*, 71(9):4422–31, 1992.
- [104] MathWorks MATLAB - <http://www.mathworks.com/products/matlab>.
- [105] H. Hauser, B. Michl, S. Schwarzkopf, V. Kübler, C. Müller, M. Hermle, and B. Bläsi. Honeycomb texturing of silicon via nanoimprint lithography for solar cell applications. *IEEE Journal of Photovoltaics*, 2(2):114–22, 2012.
- [106] K. R. McIntosh and L. P. Johnson. Recombination at textured silicon surfaces passivated with silicon dioxide. *Journal of Applied Physics*, 105:124520, 2009.
- [107] J. Isenberg and W. Warta. Free carrier absorption in heavily doped silicon layers. *Applied Physics Letters*, 84(13):2265–7, 2004.

- [108] J. Magnés, D. Odera, J. Hartke, M. Fountain, L. Florence, and V. Davis. Quantitative and qualitative study of gaussian beam visualization techniques. *arXiv preprint physics/0605102*, 2006.
- [109] C. Vonesch and M. Unser. A fast thresholded landweber algorithm for wavelet-regularized multidimensional deconvolution. *Image Processing, IEEE Transactions on*, 17(4):539–549, 2008.
- [110] R. Woehl, M. Rüdiger, D. Biro, and J. Wilde. All-screen-printed back-contact back-junction silicon solar cells with aluminum-alloyed emitter and demonstration of interconnection of point-shaped metalized contacts. *Progress in Photovoltaics: Research and Applications*, 23(2):226–237, 2015.
- [111] M. Padilla, H. Höffler, C. Reichel, H. Chu, J. Greulich, S. Rein, W. Warta, M. Hermle, and M. C. Schubert. Surface recombination parameters of interdigitated-back-contact silicon solar cells obtained by modeling luminescence images. *Solar Energy Materials and Solar Cells*, 120, Part A:363–75, 2014.
- [112] M. Padilla, B. Michl, C. Reichel, N. Hagedorn, S. Kluska, S. T. Haag, R. Keding, A. Fell, M. Kasemann, W. Warta, and M. C. Schubert. Characterizing local contact resistances of interdigitated back contact silicon solar cells. In *Proceedings of the 29th European Photovoltaic Solar Energy Conference and Exhibition*, pages 1138–42.
- [113] M. Padilla, B. Michl, N. Hagedorn, C. Reichel, S. Kluska, A. Fell, M. Kasemann, W. Warta, and M. C. Schubert. Local series resistance imaging of silicon solar cells with complex current paths. *Photovoltaics, IEEE Journal of*, 5(3):752–758, 2015.
- [114] M. Padilla, C. Reichel, N. Hagedorn, A. Fell, R. Keding, B. Michl, M. Kasemann, W. Warta, and M. C. Schubert. Contact fault characterization of complex silicon solar cells: a guideline based on current voltage characteristics and lumines-

- cence imaging. *Progress in Photovoltaics: Research and Applications*, (published online), 2015.
- [115] N. Hagedorn. *Luminescence Imaging and Lock-In Thermography for Local Device Fault Analysis of Interdigitated Back-Contact Silicon Solar Cells*. Master's thesis, Universität Freiburg, 2015.
- [116] H. Chu. *Luminescence imaging for the characterization of interdigitated-back-contact silicon solar cells*. Master's thesis, Karlsruhe Institute of Technology, 2013.
- [117] T. Fuyuki, H. Kondo, Y. Kaji, T. Yamazaki, Y. Takahashi, and Y. Uraoka. One shot mapping of minority carrier diffusion length in polycrystalline silicon solar cells using electroluminescence. In *Proceedings of the 31st IEEE Photovoltaic Specialists Conference*, pages 1343–5.
- [118] T. Fuyuki, H. Kondo, T. Yamazaki, Y. Takahashi, and Y. Uraoka. Photographic surveying of minority carrier diffusion length in polycrystalline silicon solar cells by electroluminescence. *Applied Physics Letters*, 86(26):262108, 2005.
- [119] T. Trupke, R. A. Bardos, M. C. Schubert, and W. Warta. Photoluminescence imaging of silicon wafers. *Applied Physics Letters*, 89(044107):1–3, 2006.
- [120] R. A. Sinton and A. Cuevas. Contactless determination of current-voltage characteristics and minority-carrier lifetimes in semiconductors from quasi-steady-state photoconductance data. *Applied Physics Letters*, 69(17):2510–2, 1996.
- [121] T. Trupke, R. A. Bardos, and M. D. Abbott. Self-consistent calibration of photoluminescence and photoconductance lifetime measurements. *Applied Physics Letters*, 87(18):184102, 2005. Using Smart Source Parsing.
- [122] O. Breitenstein, J. Bauer, K. Bothe, D. Hinken, J. Müller, W. Kwapil, M. C. Schubert, and W. Warta. Can luminescence

- imaging replace lock-in thermography on solar cells? *IEEE Journal of Photovoltaics*, 1(2):159–67, 2011.
- [123] M. A. Munoz, M. C. Alonso-García, Nieves Vela, and F. Chenlo. Early degradation of silicon pv modules and guaranty conditions. *Solar Energy*, 85(9):2264–2274, 2011.
- [124] M. Köntges, I. Kunze, S. Kajari-Schröder, X. Breitenmoser, and B. Bjorneklett. The risk of power loss in crystalline silicon based photovoltaic modules due to micro-cracks. *Solar Energy Materials and Solar Cells*, 95(4):1131–1137, 2011.
- [125] M. D. Abbott, J. E. Cotter, F. W. Chen, T. Trupke, R. A. Bardos, and K. C. Fisher. Application of photoluminescence characterization to the development and manufacturing of high-efficiency silicon solar cells. *Journal of Applied Physics*, 100:114514, 2006.
- [126] J. Haunschild, I. E. Reis, J. Geilker, and S. Rein. Detecting efficiency-limiting defects in czochralski-grown silicon wafers in solar cell production using photoluminescence imaging. *Physica Status Solidi RRL*, 5-6:199–201, 2011.
- [127] B. Mitchell, T. Trupke, J. W. Weber, and J. Nyhus. Bulk minority carrier lifetimes and doping of silicon bricks from photoluminescence intensity ratios. *Journal of Applied Physics*, 109(8):083111, 2011.
- [128] S. Herlufsen, J. Schmidt, D. Hinken, K. Bothe, and R. Brendel. Photoconductance-calibrated photoluminescence lifetime imaging of crystalline silicon. *Physica Status Solidi RRL*, 2(6):245–7, 2008.
- [129] J. Giesecke, M. C. Schubert, D. Walter, and W. Warta. Minority carrier lifetime in silicon wafers from quasi-steady-state photoluminescence. *Applied Physics Letters*, 97:092109, 2010.
- [130] J. A. Giesecke, M. C. Schubert, B. Michl, F. Schindler, and W. Warta. Minority carrier lifetime imaging of silicon wafers

- calibrated by quasi-steady-state photoluminescence. *Solar Energy Materials and Solar Cells*, 95(3):1011–8, 2011.
- [131] J. A. Giesecke, B. Michl, F. Schindler, M. C. Schubert, and W. Warta. Minority carrier lifetime of silicon solar cells from quasi-steady-state photoluminescence. *Solar Energy Materials and Solar Cells*, 95(7):1979–82, 2011.
- [132] J. A. Giesecke, M. C. Schubert, and W. Warta. Measurement of net dopant concentration via dynamic photoluminescence. *Journal of Applied Physics*, 112(6):063704, 2012.
- [133] J. A. Giesecke, F. Schindler, M. Bühler, M. C. Schubert, and W. Warta. Accurate determination of minority carrier mobility in silicon from quasi-steady-state photoluminescence. *Journal of Applied Physics*, 113(21):213705, 2013.
- [134] B. Michl, J. Giesecke, W. Warta, and M. C. Schubert. Separation of front and backside surface recombination by photoluminescence imaging on both wafer sides. *IEEE Journal of Photovoltaics*, 2(3):348–51, 2012.
- [135] P. Würfel, T. Trupke, T. Puzzer, E. Schäffer, W. Warta, and S. W. Glunz. Diffusion lengths of silicon solar cells from luminescence images. *Journal of Applied Physics*, 101:123110, 2007.
- [136] Z. Hameiri, P. Chaturvedi, M. K. Juhl, and T. Trupke. Spatially resolved emitter saturation current by photoluminescence imaging. In *Proceedings of the 39th IEEE Photovoltaic Specialists Conference*, pages 0664–8.
- [137] T. Trupke, E. Pink, R.A. Bardos, and M.D. Abbott. Spatially resolved series resistance of silicon solar cells obtained from luminescence imaging. *Applied Physics Letters*, 90(093506):1–3, 2007.
- [138] H. Kampwerth, T. Trupke, J. W. Weber, and Y. Augarten. Advanced luminescence based effective series resistance imaging of silicon solar cells. *Applied Physics Letters*, 93(202102):202102/1–3, 2008.

- [139] M. Glatthaar, J. Haunschild, M. Kasemann, J. Giesecke, W. Warta, and S. Rein. Spatially resolved determination of dark saturation current and series resistance of silicon solar cells. *Physica Status Solidi RRL*, 4(1):13–15, 2010.
- [140] D. Hinken, K. Ramspeck, K. Bothe, B. Fischer, and R. Brendel. Series resistance imaging of solar cells by voltage dependent electroluminescence. *Applied Physics Letters*, 91(182104):1–3, 2007.
- [141] J. Haunschild, M. Glatthaar, M. Kasemann, S. Rein, and E. R. Weber. Fast series resistance imaging for silicon solar cells using electroluminescence. *Physica Status Solidi RRL*, 3:227–9, 2009.
- [142] C. Shen, H. Kampwerth, and M. Green. Spatially resolved photoluminescence imaging of essential silicon solar cell parameters. In *Proceedings of the 38th IEEE Photovoltaic Specialists Conference*.
- [143] H. Höffler, J. Haunschild, R. Zeidler, and S. Rein. Statistical evaluation of a luminescence-based method for imaging the series resistance of solar cells. *Energy Procedia*, 27:253–8, 2012.
- [144] B. Michl, M. Kasemann, J. Giesecke, M. Glatthaar, A. Schütt, J. Carstensen, H. Föll, S. Rein, W. Warta, and H. Nagel. Application of luminescence imaging based series resistance measurement methods in an industrial environment. In *Proceedings of the 23rd European Photovoltaic Solar Energy Conference*, pages 1176–81.
- [145] O. Breitenstein, C. Shen, H. Kampwerth, and M. A. Green. Comparison of dlit- and pl-based local solar cell efficiency analysis. *Energy Procedia*, 38(0):2–12, 2013.
- [146] Chao Shen, Martin A. Green, Otwin Breitenstein, Thorsten Trupke, Muye Zhang, and Henner Kampwerth. Improved local efficiency imaging via photoluminescence for silicon solar cells. *solar Energy Materials and Solar Cells*, 123(0):41–46, 2014.

- [147] K. C. Fong, K. R. McIntosh, and A. W. Blakers. Accurate series resistance measurement of solar cells. *Progress in Photovoltaics: Research and Applications*, 21(4):490–9, 2013.
- [148] O. Breitenstein and S. Rißland. A two-diode model regarding the distributed series resistance. *Solar Energy Materials and Solar Cells*, 110:77–86, 2013.
- [149] C. Shen, H. Kampwerth, and M. A. Green. Photoluminescence based open circuit voltage and effective lifetime images re-interpretation for solar cells: The influence of horizontal balancing currents. *Solar Energy Materials and Solar Cells*, 130:393–6, 2014.
- [150] D. De Ceuster, P. Cousins, D. Rose, D. Vicente, P. Tipones, and W. Mulligan. Low cost, high volume production of >22% efficiency silicon solar cells. In *Proceedings of the 22nd European Photovoltaic Solar Energy Conference*, pages 816–9.
- [151] C. Schinke, F. Kiefer, M. Offer, D. Hinken, A. Schmidt, N.-P. Harder, R. Bock, T. Brendemühl, J. Schmidt, K. Bothe, and R. Brendel. Contacting interdigitated back-contact solar cells with four busbars for precise current voltage measurements under standard testing conditions. *IEEE Journal of Photovoltaics*, 2(3):247–55, 2012.
- [152] R. Müller, C. Reichel, J. Schrof, M. Padilla, M. Selinger, I. Geisemeyer, J. Benick, and M. Hermle. Analysis of n-type ibc solar cells with diffused boron emitter locally blocked by implanted phosphorus. *Solar Energy Materials and Solar Cells*, (published online), 2015.
- [153] Haifeng Chu, Lejo J. Koduvelikulathu, Valentin D. Mihailetchi, Giuseppe Galbiati, Andreas Halm, and Radovan Kopecek. Soft breakdown behavior of interdigitated-back-contact silicon solar cells. *Energy Procedia*, 77:29–35, 2015.

- [154] D. Hinken, C. Schinke, S. Herlufsen, A. Schmidt, K. Bothe, and R. Brendel. Experimental setup for camera-based measurements of electrically and optically stimulated luminescence of silicon solar cells and wafers. *Review of Scientific Instruments*, 82(033706):1–9, 2011.
- [155] D. Walter, A. Liu, E. Franklin, D. Macdonald, B. Mitchell, and T. Trupke. Contrast enhancement of luminescence images via point-spread deconvolution, 3-8 June 2012.
- [156] D. Walter, A. Fell, E. Franklin, D. Macdonald, B. Mitchell, and T. Trupke. The impact of silicon ccd photon spread on quantitative analyses of luminescence images. *IEEE Journal of Photovoltaics*, 4(1):368–73, 2014.
- [157] M. Hermle. *Analyse neuartiger Silizium- und III-V-Solarzellen mittels Simulation und Experiment*. Phd thesis, Universität Konstanz, 2008.
- [158] D. E. Kane and R. M. Swanson. Measurement of the emitter saturation current by a contactless photoconductivity decay method (silicon solar cells). In *Proceedings of the 18th IEEE Photovoltaic Specialists Conference*, pages 578–83.
- [159] J. Haunschild. *Lumineszenz-Imaging-vom Block zum Modul*. Phd thesis, Universität Freiburg, 2012.
- [160] M. Kasemann, W. Kwapil, M. C. Schubert, H. Habenicht, B. Walter, M. The, S. Kontermann, S. Rein, O. Breitenstein, J. Bauer, A. Lotnyk, B. Michl, H. Nagel, A. Schütt, J. Carstensen, H. Föll, T. Trupke, Y. Augarten, H. Kampwerth, R. A. Bardos, S. Pingel, J. Berghold, W. Warta, and S. W. Glunz. Spatially resolved silicon solar cell characterization using infrared imaging methods. In *Proceedings of the 33rd IEEE Photovoltaic Specialists Conference*, .
- [161] COMSOL Multiphysics - www.comsol.com.

- [162] C. Reichel. Comsol multiphysics for analysis and simulation of silicon solar cells. *SiliconForest Workshop*, 2012.
- [163] Synopsys Sentaurus Device - <http://www.synopsys.com>.
- [164] Silvaco Atlas - <http://www.silvaco.com>.
- [165] A. Fell, K. C. Fong, K. R. McIntosh, E. Franklin, and A. W. Blakers. 3-d simulation of interdigitated-back-contact silicon solar cells with quokka including perimeter losses. *Photovoltaics, IEEE Journal of*, 4(4):1040–1045, 2014.
- [166] A. Fell, K. R. McIntosh, M. D. Abbott, and D. Walter. Quokka version 2: selective surface doping, luminescence modeling and data fitting. In *23rd Photovoltaic Science and Engineering Conference, Taipei*.
- [167] A. Fell, D. Walter, X. Yang, S. Surve, E. Franklin, K. Weber, and D. MacDonald. Quantitative surface recombination imaging of single side processed silicon wafers obtained by photoluminescence modeling. *Energy Procedia*, 55:63–70, 2014.
- [168] D. B. M. Klaassen. A unified mobility model for device simulation - i. model equations and concentration dependence. *Solid-State Electronics*, 35(7):953–9, 1992.
- [169] G. A. M. Hurkx, D. B. M. Klaassen, and M. P. G. Knuvers. A new recombination model for device simulation including tunneling. *IEEE Transactions on Electron Devices*, 39(2):331–8, 1992.
- [170] J. del Alamo, S. Swirhun, and R. M. Swanson. Measuring and modeling minority carrier transport in heavily doped silicon. *Solid-State Electronics*, 28(1-2):47–54, 1985.
- [171] A. Kimmerle, A. Wolf, U. Belledin, and B. Biro. Modelling carrier recombination in highly phosphorus-doped industrial emitters. In *Proceedings of the 1st International Conference on Silicon Photovoltaics*, volume 8, pages 275–81. Elsevier Energy Procedia.

- [172] T. Fellmeth, F. Clement, and D. Biro. Analytical modeling of industrial-related silicon solar cells. *IEEE Journal of Photovoltaics*, 4(1):504–13, 2014.
- [173] M. C. Schubert, S. Pingel, M. The, and W. Warta. Quantitative carrier lifetime images optically measured on rough silicon wafers. *Journal of Applied Physics*, 101:124907, 2007.
- [174] M. Schubert. *Detektion von infraroter Strahlung zur Beurteilung der Materialqualität von Solar-Silizium*. Phd thesis, Universität Konstanz, 2008.
- [175] S. Kluska, F. Granek, M. Hermle, and S. W. Glunz. Loss analysis of high-efficiency back-contact back-junction silicon solar cells. In *Proceedings of the 23rd European Photovoltaic Solar Energy Conference*, pages 1590–5.
- [176] A. Cuevas, P. A. Basore, G. Giroult-Matlakowski, and C. Dubois. Surface recombination velocity of highly doped n-type silicon. *Journal of Applied Physics*, 80(6):3370–5, 1996.
- [177] A. Cuevas, M. Stuckings, J. Lau, and M. Petracic. The recombination velocity of boron diffused silicon surfaces. In H. A. Ossenbrink, P. Helm, and H. Ehmman, editors, *Proceedings of the 14th European Photovoltaic Solar Energy Conference*, pages 2416–9. H.S. Stephens and Associates, Bedford, UK, 1997.
- [178] A. W. Blakers and M. A. Green. 20% efficiency silicon solar cells. *Applied Physics Letters*, 48(3):215–7, 1986.
- [179] J. Zhao, A. Wang, and M. A. Green. 24% efficient perl structure silicon solar cells. In *Proceedings of the 21st IEEE Photovoltaic Specialists Conference*, volume 1, pages 333–5. IEEE.
- [180] B. Thaidigsmann, M. Linse, A. Wolf, F. Clement, D. Biro, and R. Preu. The path to industrial production of highly efficient metal wrap through silicon solar cells. *Green*, 2(4):171–6, 2012.

- [181] J. M. Gee, W. K. Schubert, and P. A. Basore. Emitter wrap-through solar cell. In *Proceedings of the 23rd IEEE Photovoltaic Specialists Conference, Conference Record of the Twenty Third IEEE Photovoltaic Specialists Conference - 1993*, pages 265–70.
- [182] H. Murrmann and D. Widmann. Current crowding on metal contacts to planar devices. *IEEE Transactions on Electron Devices*, 16(12):1022–4, 1969. B Electrical and Electronic Engineering.
- [183] M. Glatthaar, J. Giesecke, M. Kasemann, J. Haunschild, M. The, W. Warta, and S. Rein. Spatially resolved determination of the dark saturation current of silicon solar cells from electroluminescence images. *Journal of Applied Physics*, 105: 113110, 2009.
- [184] R. A. Sinton, P. J. Verlinden, R. M. Swanson, R. A. Crane, K. Wickham, and J. Perkins. Improvements in silicon backside-contact solar cells for high-value one-sun applications. In *Proceedings of the 13th European Photovoltaic Solar Energy Conference*, pages 1586–9.
- [185] Y. Yang, G. Xu, K. Zhang, X. Zhang, H. Shen, P. P. Altermatt, Verlinden P. J., and Z. Feng. Analysis of series resistance of industrial crystalline silicon solar cells by numerical simulation and analytical modelling. In *Proceedings of the 28th European Photovoltaic Solar Energy Conference and Exhibition*, pages 1558–61.
- [186] P. P. Altermatt, G. Heiser, A. G. Aberle, A. Wang, J. Zhao, S. J. Robinson, S. Bowden, and M. A. Green. Spatially resolved analysis and minimization of resistive losses in high-efficiency si solar cells. *Progress in Photovoltaics: Research and Applications*, 4(6):399–414, 1996.
- [187] M. Selinger. *Lock-In Thermography and Thermal Modeling of Interdigitated Back-Contact Silicon Solar Cells*. Master’s thesis, Universität Freiburg, 2014.

- [188] O. Breitenstein, W. Eberhardt, and K. Iwig. Imaging the local forward current density of solar cells by dynamical precision contact thermography. In *Photovoltaic Energy Conversion, 1994., Conference Record of the Twenty Fourth. IEEE Photovoltaic Specialists Conference - 1994, 1994 IEEE First World Conference on*, volume 2, pages 1633–1636 vol.2, .
- [189] J. Rappich, M. Mueller, F. Schneider, and H. Tributsch. Thermographic sampling technique applied to microelectronics and photovoltaic devices. *Solar Energy Materials and Solar Cells*, 53(3-4):205–15, 1998.
- [190] O. Breitenstein and M. Langenkamp. *Lock-in Thermography - Basics and Use for Functional Diagnostics of Electronic Components*. Springer Verlag, Berlin/Heidelberg, 2003.
- [191] I. Geisemeyer, F. Fertig, W. Warta, S. Rein, and M. C. Schubert. Prediction of silicon pv module temperature for hot spots and worst case partial shading situations using spatially resolved lock-in thermography. *Solar Energy Materials and Solar Cells*, 120(Part A):259–69, 2014.
- [192] M. Kasemann, B. Walter, C. Meinhardt, J. Ebser, W. Kwapil, and W. Warta. Emissivity-corrected power loss calibration for lock-in thermography measurements on silicon solar cells. *Journal of Applied Physics*, 103:113503, 2008.
- [193] H. Straube and O. Breitenstein. Estimation of heat loss in thermal wave experiments. *Journal of Applied Physics*, 109(6):064515, 2011.
- [194] Max-Planck Innovations GmbH. DECONV, 2013.
- [195] S. Riepe, J. Isenberg, C. Ballif, S. W. Glunz, and W. Warta. Carrier density and lifetime imaging of silicon wafers by infrared lock-in thermography. In B. McNelis, W. Palz, H. A. Ossensbrink, and P. Helm, editors, *Proceedings of the 17th European Photovoltaic Solar Energy Conference*, pages 1597–9.

- [196] M. Bail, J. Kentsch, R. Brendel, and M. Schulz. Lifetime mapping of si wafers by an infrared camera [for solar cell production]. In *Proceedings of the 28th IEEE Photovoltaics Specialists Conference*, pages 99–103.
- [197] J. Isenberg and W. Warta. Spatially resolved evaluation of power losses in industrial solar cells by illuminated lock-in thermography. *Progress in Photovoltaics: Research and Applications*, 12(5):339–53, 2004.
- [198] J. Isenberg, A. S. H. van der Heide, and W. Warta. Investigation of series resistance losses by illuminated lock-in thermography. *Progress in Photovoltaics: Research and Applications*, 13(8):697–703, 2005.
- [199] O. Breitenstein, J. P. Rakotoniaina, A. S. H. van der Heide, and J. Carstensen. Series resistance imaging in solar cells by lock-in thermography. *Progress in Photovoltaics: Research and Applications*, 13(8):645–60, 2005.
- [200] W. Kwapil, M. Kasemann, J. Ebser, S. Rein, and W. Warta. Application of illuminated lock-in thermography to industrial silicon solar cells. In *Proceedings of the 22nd European Photovoltaic Solar Energy Conference*, pages 1596–9.
- [201] O. Breitenstein. Illuminated versus dark lock-in thermography investigations of solar cells. *International Journal of Nanoparticles*, 6(2/3):81–92, 2013.
- [202] H. Straube, M. Siegloch, A. Gerber, J. Bauer, and O. Breitenstein. Illuminated lock-in thermography at different wavelengths for distinguishing shunts in top and bottom layers of tandem solar cells. *Physica Status Solidi C*, 8(4):1339–41, 2011.
- [203] O. Breitenstein, M. Langenkamp, K. R. McIntosh, C. B. Honsberg, and M. Rinio. Localization of shunts across the floating junction of dsbc solar cells by lock-in thermography. In *Proceedings of the 28th IEEE Photovoltaics Specialists Conference*, pages 124–7, .

- [204] O. Breitenstein, M. Langenkamp, J. P. Rakotoniaina, and J. Zettner. The imaging of shunts in solar cells by infrared lock-in thermography. In B. McNelis, W. Palz, H. A. Ossenkopf, and P. Helm, editors, *Proceedings of the 17th European Photovoltaic Solar Energy Conference*, pages 1499–502, Isenberg, . WIP-Munich and ETA-Florence.
- [205] O. Breitenstein, M. Langenkamp, O. Lang, and A. Schirrmacher. Shunts due to laser scribing of solar cells evaluated by highly sensitive lock-in thermography. *Solar Energy Materials and Solar Cells*, 65(1-4):55–62, 2001.
- [206] O. Breitenstein, J. P. Rakotoniaina, and M. H. Al Rifai. Quantitative evaluation of shunts in solar cells by lock-in thermography. *Progress in Photovoltaics: Research and Applications*, 11(8):515–26, 2003.
- [207] M. Langenkamp and O. Breitenstein. Classification of shunting mechanisms in crystalline silicon solar cells. *Solar Energy Materials and Solar Cells*, 72(1-4):433–40, 2002.
- [208] O. Breitenstein, J. P. Rakotoniaina, M. H. Al Rifai, and M. Werner. Shunt types in crystalline silicon solar cells. *Progress in Photovoltaics: Research and Applications*, 12(7):529–38, 2004.
- [209] S. Seren, M. Kaes, G. Hahn, and H. Nagel. Shunt detection with illuminated lock-in thermography on inline relevant time scales. In *Proceedings of the 23rd European Photovoltaic Solar Energy Conference*, pages 1746–8.
- [210] O. Breitenstein. Nondestructive local analysis of current-voltage characteristics of solar cells by lock-in thermography. *Solar Energy Materials and Solar Cells*, 95(10):2933–6, 2011.
- [211] Max-Planck Innovations GmbH. Local I-V 2, 2013.
- [212] S. J. Robinson, A. G. Aberle, and M. A. Green. Departures from the principle of superposition in silicon solar cells. *Journal of Applied Physics*, 76(12):7920–30, 1994.

- [213] O. Breitenstein. Local efficiency analysis of solar cells based on lock-in thermography. *Solar Energy Materials and Solar Cells*, 107:381–9, 2012.
- [214] IRCAM GmbH - www.ircam.de.
- [215] R. Brendel, S. Dreissigacker, N. P. Harder, and P. P. Altermatt. Theory of analyzing free energy losses in solar cells. *Applied Physics Letters*, 93(17):173503, 2008.
- [216] H. Straube, O. Breitenstein, and J. M. Wagner. Thermal wave propagation in thin films on substrate: the time-harmonic thermal transfer function. *Physica Status Solidi B*, 248(9):2128–41, 2011.
- [217] J. Isenberg and W. Warta. Realistic evaluation of power losses in solar cells by using thermographic methods. *Journal of Applied Physics*, 95(9):5200–9, 2004.
- [218] B. Michl, D. Impera, M. Bivour, W. Warta, and M. C. Schubert. Suns-pfi as a powerful tool for spatially resolved fill factor analysis of solar cells. *Progress in Photovoltaics: Research and Applications*, 22(5):581–6, 2014.
- [219] M. P. Peloso, Meng Lei, and C. S. Bhatia. Combined thermography and luminescence imaging to characterize the spatial performance of multicrystalline si wafer solar cells. *Photovoltaics, IEEE Journal of*, 5(1):102–111, 2015.
- [220] M. C. Schubert, H. Habenicht, and W. Warta. Imaging of metastable defects in silicon. *IEEE Journal of Photovoltaics*, 1(2):168–73, 2011.
- [221] M. Demant, S. Rein, J. Krisch, S. Schoenfelder, C. Fischer, S. Bartsch, and Ralf Preu. Detection and analysis of microcracks in multi-crystalline silicon wafers during solar cell production. In *Photovoltaic Specialists Conference (PVSC), 2011 37th IEEE*, pages 1641–6.

- [222] H. H. Berger. Contact resistance and contact resistivity. *Journal of the Electrochemical Society*, 119(4):507–14, 1972.
- [223] P. N. Vinod. Specific contact resistance of the porous silicon and silver metal ohmic contact structure. *Semiconductor Science and Technology*, 20(9):966, 2005.
- [224] P. N. Vinod. Specific contact resistance measurements of the screen-printed ag thick film contacts in the silicon solar cells by three-point probe methodology and tlm method. *Journal of Materials Science: Materials in Electronics*, 22(9):1248–57, 2011.
- [225] A. S. H. van der Heide, A. Schönecker, G. P. Wyers, and W. C. Sinke. Mapping of contact resistance and locating shunts on solar cells using resistance analysis by mapping of potential (ramp) techniques. In H. Scheer, B. McNelis, W. Palz, H. A. Ossenbrink, and P. Helm, editors, *Proceedings of the 16th European Photovoltaic Solar Energy Conference*, pages 1438–42. James and James, London, UK, 2000.
- [226] A. S. H. van der Heide, J. H. Bultman, J. Hoornstra, and A. Schönecker. Error diagnosis and optimisation of c-si solar cell processing using contact resistances determined with the corescanner. *Solar Energy Materials and Solar Cells*, 74:43–50, 2002.
- [227] O. Breitenstein, P. Altermatt, K. Ramspeck, and A. Schenk. The origin of ideality factors $n > 2$ of shunts and surfaces in the dark i-v curves of si solar cells. In *Proceedings of the 21st European Photovoltaic Solar Energy Conference*, pages 625–8, .
- [228] S. Steingrube, O. Breitenstein, K. Ramspeck, S. Glunz, A. Schenk, and P. P. Altermatt. Explanation of commonly observed shunt currents in c-si solar cells by means of recombination statistics beyond the shockley-read-hall approximation. *Journal of Applied Physics*, 110(1):014515, 2011.

- [229] M. Kasemann, D. Grote, B. Walter, T. Trupke, Y. Augarten, R. A. Bardos, E. Pink, M. D. Abbott, and W. Warta. Shunt detection capabilities of luminescence imaging on silicon solar cells. In *Proceedings of the 22nd European Photovoltaic Solar Energy Conference*, pages 394–7, .
- [230] M. Kasemann, D. Grote, B. Walter, W. Kwapil, T. Trupke, Y. Augarten, R.A. Bardos, E. Pink, M. D. Abbott, and W. Warta. Luminescence imaging for the detection of shunts on silicon solar cells. *Progress in Photovoltaics*, 16(4):297–305, 2008.
- [231] Y. Augarten, T. Trupke, M. Lenio, J. Bauer, J. W. Weber, M. K. Juhl, M. Kasemann, and O. Breitenstein. Calculation of quantitative shunt values using photoluminescence imaging. *Progress in Photovoltaics: Research and Applications*, 21(5): 933–941, 2013.
- [232] W. Kern. Detection and characterization of localized defects in dielectric films. *RCA Review*, 34(4):655–90, 1973.
- [233] W. Kern and R. B. Comizzoli. New methods for detecting structural defects in glass passivation films. *Journal of Vacuum Science and Technology*, 14(1):32–9, 1977. Cv607 Times Cited:7 Cited References Count:27.
- [234] I. V. Belousov, A. N. Grib, and G. V. Kuznetsov. The influence of surface defects on the pinhole formation in silicide thin film. *Semiconductor Physics, Quantum Electronics and Optoelectronics*, 9(3):29–34, 2006.
- [235] A. Jones and M. L. Hitchman. *Chemical vapour deposition: precursors, processes and applications*. Royal Society of Chemistry, 2009.
- [236] G. Schmitt, J. W. Schultze, F. Faßbender, G. Buß, H. Lüth, and M. J. Schöning. Passivation and corrosion of microelectrode arrays. *Electrochimica Acta*, 44(21-22):3865–3883, 1999.

- [237] R. Keding, R. Bock, A. Bochow, K. Katkhouda, D. St \ddot{A} we, C. Reichel, F. Clement, R. Woehl, H. Reinecke, and T. Geppert. Study of the electrical insulation of dielectric passivation layers and stacks for back-contact back-junction silicon solar cells. In *Proceedings of the 28th European Photovoltaic Solar Energy Conference and Exhibition*, pages 1321–6, .
- [238] P. Saint-Cast, F. Tanay, M. Aleman, C. Reichel, J. Bartsch, M. Hofmann, J. Rentsch, and R. Preu. Relevant pinhole characterisation methods for dielectric layers for silicon solar cells. In *Proceedings of the 24th European Photovoltaic Solar Energy Conference*, pages 2084–7.
- [239] J. O. McCaldin and H. Sankur. Diffusivity and solubility of si in the al metallization of integrated circuits. *Applied Physics Letters*, 19(12):524–7, 1971.
- [240] K. Katkhouda, A. Martinez-Limia, L. Bornschein, R. Koseva, T. Geppert, A. Grohe, H. J. Krokoszinski, and P. Schaaf. Aluminum-based rear-side pvd metallization for npert silicon solar cells. *Photovoltaics, IEEE Journal of*, 4(1):160–167, 2014.
- [241] D. K. Schroder and D. L. Meier. Solar cell contact resistance - a review. *IEEE Transactions on Electron Devices*, ED-31(5): 637–47, 1984.
- [242] S. Kluska, C. Fleischmann, A. B \ddot{u} chler, W. H \ddot{o} rdt, C. Geisler, S. Hopman, and M. Glatthaar. Micro characterization of laser structured solar cells with plated ni-ag contacts. *Solar Energy Materials and Solar Cells*, 120(Part A):323–31, 2014.
- [243] A. B \ddot{u} chler, S. Kluska, A. Brand, C. Geisler, S. Hopman, and M. Glatthaar. Micro characterization and imaging of spikes in nickel plated solar cells. *Energy Procedia*, 55:624–32, 2014.
- [244] A. B \ddot{u} chler, S. Kluska, M. Kasemann, M. Breitwieser, W. Kwopil, A. H \ddot{a} hnel, H. Blumtritt, S. Hopman, and M. Glatthaar. Localization and characterization of annealing-induced shunts in ni-plated monocrystalline silicon solar cells.

- physica status solidi (RRL) - Rapid Research Letters*, 8(5):385–389, 2014.
- [245] F. D. Heinz, M. Breitwieser, P. Gundel, M. König, M. Hörteis, W. Warta, and M. C. Schubert. Microscopic origin of the aluminium assisted spiking effects in n-type silicon solar cells. *Solar Energy Materials and Solar Cells*, 131:105–9, 2014.
- [246] R. Keding, D. Stüwe, M. Kamp, C. Reichel, A. Wolf, R. Woehl, D. Borchert, H. Reinecke, and D. Biro. Co-diffused back-contact back-junction silicon solar cells. In *Proceedings of the 28th European Photovoltaic Solar Energy Conference and Exhibition*, page to be published, .
- [247] A. G. Chynoweth and K. G. McKay. Photon emission from avalanche breakdown in silicon. *Physical Review*, 102(2):369–76, 1956.
- [248] A. G. Chynoweth and K. G. McKay. Internal field emission in silicon p-n junctions. *Physical Review*, 106(3):418–27, 1957.
- [249] A. G. Chynoweth and K. G. McKay. Light emission and noise studies of individual microplasmas in silicon p-n junctions. *Journal of Applied Physics*, 30(11):1811–3, 1959.
- [250] A. G. Chynoweth and G. L. Pearson. Effect of dislocations on breakdown in silicon p-n junctions. *Journal of Applied Physics*, 29(7):1103–10, 1958.
- [251] S. Mahadevan, S. M. Hardas, and G. Suryan. Electrical breakdown in semiconductors. *phys. stat. sol. (a)*, 8(335):335–74, 1971.
- [252] M. Schneemann, T. Kirchartz, R. Carius, and U. Rau. Spatially resolved reverse biased electroluminescence spectroscopy of crystalline silicon solar cells. In *Proceedings of the 25th European Photovoltaic Solar Energy Conference and Exhibition*, pages 24–8.

- [253] W. Kwapil, M. Kasemann, P. Gundel, M. C. Schubert, W. Warta, P. Bronsveld, and G. Coletti. Diode breakdown related to recombination active defects in block-cast multicrystalline silicon solar cells. *Journal of Applied Physics*, 106(6):063530, 2009.
- [254] N. J. Call, S. W. Johnston, R. K. Ahrenkiel, M. J. Romero, and B. Yang. Imaging of shunts and junction breakdown in multicrystalline silicon solar cells. In *Proceedings of the 34th IEEE Photovoltaic Specialists Conference*, pages 1184–9.
- [255] F. Fertig, C. Willibald, I. Geisemeyer, M. C. Schubert, and S. Rein. Illumination and temperature dependence of breakdown mechanisms in multi-crystalline silicon solar cells. *Energy Procedia*, 38(0):32–42, 2013.
- [256] E. Lohmüller, F. Fertig, S. Werner, I. Geisemeyer, F. Clement, and D. Biro. Reverse bias behavior of diffused and screen-printed n-type cz-si solar cells. *IEEE Journal of Photovoltaics*, 4(6):1483–90, 2014.
- [257] R. Müller, J. Schrof, C. Reichel, J. Benick, and M. Hermle. Back-junction back-contact n-type silicon solar cell with diffused boron emitter locally blocked by implanted phosphorus. *Applied Physics Letters*, 105(10):103503, 2014.
- [258] E. Franklin, K. C. Fong, K. R. McIntosh, Andreas Fell, A. W. Blakers, T. Kho, Daniel Walter, D. Wang, N. Zin, M. Stocks, E. Wang, N. Grant, Y. Wan, Y. Yang, X. Zhang, Z. Feng, and P. J. Verlinden. Design, fabrication and characterisation of a 24.4% efficient interdigitated back contact solar cell. *Progress in Photovoltaics: Research and Applications*, (published online), 2014.
- [259] G. Galbiati, V. D. Mihailetchi, R. Roescu, A. Halm, L. J. Koduvelikulathu, R. Kopecek, K. Peter, and J. Libal. Large-area back-contact back-junction solar cell with efficiency exceeding 21%. *IEEE Journal of Photovoltaics*, PP(99):1–6, 2012.

- [260] M. Pospischil, M. Kuchler, M. Klawitter, C. Rodriguez, A. Padilla, R. Efinger, H. Gentischer, M. König, M. Hörteis, L. Wende, O. Doll, F. Clement, and D. Biro. Ultrafine front side metallization on silicon solar cells by industrial dispensing technology. In *Proceedings of the 29th European Photovoltaic Solar Energy Conference and Exhibition*, pages 1304–6.
- [261] W.S. Rasband. ImageJ - imagej.nih.gov/ij, 1997-2012.
- [262] Y. Augarten, T. Trupke, M. Lenio, J. Bauer, J. W. Weber, M. Juhl, M. Kasemann, and O. Breitenstein. Calculation of quantitative shunt values using photoluminescence imaging. *Progress in Photovoltaics: Research and Applications*, pages 1–9, 2012.
- [263] J. Seiffe, L. Gautero, M. Hofmann, J. Rentsch, R. Preu, S. Weber, and R. A. Eichel. Surface passivation of crystalline silicon by plasma-enhanced chemical vapor deposition double layers of silicon-rich silicon oxynitride and silicon nitride. *Journal of Applied Physics*, 109(3):034105, 2011.
- [264] A. G. Aberle. Surface passivation of crystalline silicon solar cells: a review. *Progress in Photovoltaics: Research and Applications*, 2000(8):473–487, 2000.
- [265] P. Saint-Cast. *Passivation of Si surfaces by PECVD aluminium oxide*. Phd thesis, Universität Konstanz, 2012.
- [266] A. Richter. *Aluminum oxide for the surface passivation of high efficiency silicon solar cells - Technology and advanced characterization*. Phd thesis, Universität Konstanz, 2014.
- [267] B. Sopori, S. Devayajanam, R. Rivero, and P. Rupnowski. Online monitoring for si solar cell manufacturing. In *Proceedings of the 39th IEEE Photovoltaic Specialists Conference*, pages 0939–44.
- [268] B. Thaidigsmann, E. Lohmüller, F. Fertig, F. Clement, and A. Wolf. Characterization and modeling of screen-printed metal

- insulator semiconductor tunnel junctions for integrated bypass functionality in crystalline silicon solar cells. *Journal of Applied Physics*, 113(21):214502, 2013.
- [269] J. Hohl-Ebinger, G. Siefer, and W. Warta. Non-linearity of solar cells in spectral response measurements. In *Proceedings of the 22nd European Photovoltaic Solar Energy Conference*, pages 422–4.
- [270] K. C. Fong, M. Padilla, A. Fell, E. Franklin, K. R. McIntosh, K. Teng, A. W. Blakers, N. Yona, and S. Surve. Perimeter loss characterisation by luminescence imaging. *IEEE Journal of Photovoltaics*, (published online), 2015.
- [271] B. Michl, M. Padilla, I. Geisemeyer, S. T. Haag, F. Schindler, M. C. Schubert, and W. Warta. Imaging techniques for quantitative silicon material and solar cell analysis. *IEEE Journal of Photovoltaics*, 4(6):1502–10, 2014.

List of symbols, abbreviations and physical constants

Physical constants

Constant	Name	Value
k	Boltzmann constant	$1.380 \cdot 10^{-23}$ J/K
q	elementary charge	$1.602 \cdot 10^{-19}$ As
h	Planck constant	$6.625 \cdot 10^{-32}$ Js
ϵ_0	vacuum permittivity	$8.854 \cdot 10^{-12}$ F/m
c	speed of light in vacuum	$2.998 \cdot 10^8$ m/s

List of symbols

Note that 'camera units' are dimensionless

Symbol	Typical units	Meaning
A	camera units	amplitude of lock-in thermography
α	1/cm	absorption coefficient
B	cm ³ /s	radiative recombination coefficient
β	rad	photon emission angle relative to surface
C^{loc}	camera units	local calibration constant for imaging

continued from previous page

Symbol	Typical units	Meaning
$C_{n/p}$	cm^6/s	Auger coefficient for electrons/holes
$\sigma_{\text{SRH},n/p}$	cm^2	capture cross section for electrons/holes
c_p	kJ/kgK	heat capacity
d	μm	cell or wafer thickness
D	m^2/s	diffusion coefficient
Δn	$1/\text{cm}^3$	excess electron density
Δp	$1/\text{cm}^3$	excess hole density
D_n, D_p	$1/\text{eV cm}^3$	electron/hole density of states
E	eV	energy
E_C	eV	conduction band energy
E_g	eV	band gap energy
E_γ	eV	photon energy
$E_{g,\text{eff}}$	eV	effective band gap energy
E_i	eV	intrinsic energy level in SRH rec.
ϵ	1	relative permittivity
ε	1	relative emissivity
EQE^{loc}	1	local external quantum efficiency
η	%	solar cell conversion efficiency
η_{cam}	1	camera quantum efficiency
$\Delta\eta$	eV	quasi-Fermi level splitting $\Phi_{Fn} - \Phi_{Fp}$
E_t	eV	trap energy level in SRH recombination
E_V	eV	valence band energy
$f_{n/p}$	1	Fermi-Dirac distribution of electrons/holes
FF	%	solar cell fill factor
$f_{\text{lock-in}}$	Hz	lock-in frequency in LIT measurement
f_n, f_p	1	Fermi distribution for electrons/holes
G	$1/\text{cm}^3\text{s}$	generation rate
G_λ	$1/\text{nm cm}^3\text{s}$	specific generation rate
IQE^{loc}	1	local internal quantum efficiency
I_{sc}	mA/cm^2	short-circuit current
l_{Si}	μm	photon penetration depth in silicon ($1/\alpha$)
J	mA/cm^2	current density
J_0	fA/cm^2	saturation current density

continued from previous page

Symbol	Typical units	Meaning
J_0^{region}	fA/cm ²	saturation current density of a region
J_{diff}	mA/cm ²	current density from base into surface
J_{gen}	mA/cm ²	photogenerated current density
J^{loc}	mA/cm ²	local current density
\vec{J}_n, \vec{J}_p	mA/cm ²	directed electron/hole current density
J_{rec}	mA/cm ²	recombination current density
J_{sc}	mA/cm ²	short-circuit current density
J_{shunt}	mA/cm ²	current density flowing through a shunt
J_{surf}	1/cm	luminescence photon flux at the surface
$K_{\text{cal,LIT}}$	mW/cm ²	calibration factor for LIT
$K_{\text{cal,PL}}$	1	calibration factor for lum. imaging
k_{th}	W/K m	heat conductivity
λ	nm	photon wavelength
L_{eff}	μm	effective diffusion length
m	1	ideality factor in a one diode model
M_λ	W/μm m ²	specific radiance of a black body
m_n^*, m_p^*	kg	effective electron/hole mass
μ_n, μ_p	cm ² /Vs	mobility of electrons/holes
n	1/cm ³	electron density
n_1, n_2	1	ideality factors in the two-diode model
$N_{\text{A/D}}$	1/cm ³	doping concentration
$N_{\text{C}}, N_{\text{V}}$	1/cm ³	effective density of states
N_{dop}	1/cm ³	doping density
n_i	1/cm ³	intrinsic carrier concentration
$n_{i,\text{eff}}$	1/cm ³	effective intrinsic carrier concentration
\vec{n}	1	normal vector of a surface
N_t	1/cm ³	defect density
ω	1/s	angular frequency
$\text{ORL}_{\text{sc}}^{\text{loc}}$	mA/cm ²	local optical reflection J_{sc} losses
p	1/cm ³	hole density
P	mW/cm ²	power density
pFF	%	pseudo fill factor
P_{gen}	mW/cm ²	illumination power density

continued from previous page

Symbol	Typical units	Meaning
ϕ	$^\circ$	Phase in lock-in thermography
Φ	$1/\text{cm}^2\text{s}$	integrated photon flux
Φ_λ	$1/(\text{nm cm}^3 \text{ s})$	specific photon flux
Π	eV	Peltier coefficient
Π_{maj}	eV	Peltier coefficient of majority carriers
Π_{min}	eV	Peltier coefficient of minority carriers
P_{in}	mW/cm^2	incident illumination power density
$\Pi_{\text{min/maj,n/p}}^{\text{region}}$	eV	minority/majority Peltier coefficient
pseudo- $J_{\text{sc}}^{\text{loc}}$	mA/cm^2	local pseudo short-circuit current density
p^l	mW/cm	power density of a line source
ψ	V	electrical potential
Q	mW/cm^2	power density per surface area
Q_{elec}	mW/cm^2	electrically dissipated/extracted power
$\Phi_{F_{\text{maj}}}$	eV	quasi-Fermi level of the majority carrier
Φ_{F_n}	eV	quasi-Fermi level for electrons
Φ_{F_p}	eV	quasi-Fermi level for holes
Q_{Joule}	mW/cm^2	Joule power density
Q^{loc}	mW/cm^2	local power density
Q_{net}	mW/cm^2	net power density
Q_{rec}	mW/cm^2	recombination power density
Q_{th}	mW/cm^2	thermalization power density
r	cm	radius
R_{Aug}	$1/\text{cm}^3\text{s}$	Auger recombination rate
R_c	Ωcm^2	contact resistance
R_f	1	front side reflectance
ρ	g/cm^3	density
ρ^{base}	Ωcm	base resistivity
ρ_Q	$1/\text{cm}^3$	net charge carrier density
R^{loc}	1	local optical reflectance
R_p	Ωcm^2	parallel resistance
R_r	1	rear side reflectance
r_{rad}	$1/\text{cm}^3\text{nm,s}$	specific radiative recombination rate
R_{rad}	$1/\text{cm}^3\text{s}$	radiative recombination rate

continued from previous page

Symbol	Typical units	Meaning
R_s, R_s^{global}	Ωcm^2	series resistance
R_{sh}	Ω/sq	sheet resistance
R_s^{loc}	Ωcm^2	local series resistance
R_{SRH}	$1/\text{cm}^3\text{s}$	Shockley-Read-Hall recombination rate
R_{surf}	$1/\text{cm}^2\text{s}$	surface recombination rate (SRH)
S	cm/s	surface recombination velocity
S_0	cm/s	S at the physical surface
$S^{0^\circ, \text{loc}}$	camera units	0° LIT signal
$S^{-90^\circ, \text{loc}}$	camera units	-90° LIT signal
S_E	eV/K	entropy
S_{eff}	cm/s	effective surface recombination velocity
$\sigma_{n/p}$	$1/\Omega\text{cm}$	conductivity of electrons/holes
T, T_{cell}	K or $^\circ\text{C}$	cell temperature
t	s	time
T_{amb}	K or $^\circ\text{C}$	ambient temperature
τ_{bulk}	μs	bulk lifetime
τ_{eff}	μs	effective lifetime
$\tau_{n0,p0}$	μs	electron/hole capture time constant
τ_{surf}	s	surface lifetime
T_{cell}	K	cell temperature
T_{filters}	1	filter transmission
t_{HP}	s	temper time on a hot plate
t_{int}	s	integration time
U	eV	inner energy
V, V_{bias}	mV	voltage on the solar cell
$V^{\text{loc}}, V^{\text{loc,imp}}, V_j$	mV	local (implied) voltage
V_{oc}	mV	open circuit voltage
V_T	mV	thermal voltage
V_{term}	mV	solar cell voltage at the terminal
v_{th}	cm/s	thermal velocity
W	μm	unit cell pitch
w^{gap}	μm	width of gap between emitter and BSF
x, y	μm	coordinates on the solar cell area

continued from previous page

Symbol	Typical units	Meaning
x_0, z_0	μm	distance of a point source to surface
z	μm	coordinate in the depth of the cell

Abbreviations

Symbol	Meaning
Al-BSF	aluminum back surface field
ALD	atomic layer deposition
AM1.5G	global 1.5 air mass solar spectrum
ARC	anti-reflective coating
BB	black body
BC-BJ	back contact back junction
BGN	band-gap narrowing
BS	back side
BSF	back surface field
CCD	charge-coupled device
C-DCR	coupled det. of dark sat. current dens. and R_s
CoBo	conductive boundary
cts/s	luminescence counts per second
CVD	chemical Vapor Deposition
Cz	Czochralski grown silicon
DC	direct current
DLIT	dark lock-in thermography
DLM	double-light method for R_s^{global}
ECV	Electro capacitance voltage
EL	electroluminescence
EM	emitter
EQE	external quantum efficiency
EWT	emitter-wrap-through
FCA	free-carrier-absorption
FDM	finite difference method
FE	floating emitter
FELA	free energy loss analysis

continued from previous page

Abbreviation	Meaning
FEM	finite element method
FPA	focal-plane array
FS	front side
FSF	front surface field
fwd	forward
FWHM	full width at half maximum
Fz	float zone
HP	hotplate
IBC	interdigitated back contact
IEC	International Electrotechnical Commission
ILIT	illuminated lock-in thermography
IQE	internal quantum efficiency
IR	infra red
I-V	current-voltage
LBIC	light beam induced current
LFC	laser fired contacts
LIT	lock-in thermography
loc	a pixel value in an xy plane of an image or map
mc	multicrystalline
min/maj	minority/majority
<i>MPP</i>	maximum power point
MWIR	mid-wavelength infrared
MWT	metal-wrap-through
n/a	not applicable
NETD	noise equivalent temperature difference
ORL	optical reflection loss
PECVD	plasma enhanced chemical vapor deposition
PERC	passivated emitter rear cell
PERL	passivated emitter rear locally diffused
PERT	passivated emitter, rear totally diffused
PL	photo luminescence
PV	Photovoltaics
QSSPC	quasi steady state photoconductance

continued from previous page

Abbreviation	Meaning
QSSPL	quasi steady state photoluminescence
R&D	Research and Development
RebEL	reverse bias electroluminescence imaging
Refl, R	reflectance
rev	reverse
ROI	region of interest
SCR	space charge region
SEM	scanning electron microscope
SIMS	Secondary ion mass spectroscopy
SNR	Signal to noise ratio
SP	short pass
SR	spectral response
SRH	Shottky-Read-Hall
SR-LBIC	spectrally resolved light beam induced current
SRV	surface recombination velocity
STC	standard testing conditions (AM1.5G, 1000 W/m ² , 25 °C)

List of Publications

In the following, all photovoltaics related papers published within the framework of this thesis are listed. Some of these publications deal with topics beyond interdigitated back contact silicon solar cells.

Peer-reviewed journals

- **M. Padilla**, B. Michl, B. Thaidigsmann, W. Warta, M.C. Schubert, Short-circuit current density mapping for solar cells, *Solar Energy Materials and Solar Cells* Vol. 120, 282-288, 2014
- **M. Padilla**, H. Höffler, C. Reichel, H. Chu, J. Greulich, S. Rein, W. Warta, M. Hermle, W. Warta, M. C. Schubert, Surface recombination parameters of interdigitated-back-contact silicon solar cells obtained by modeling luminescence images, *Solar Energy Materials and Solar Cells* Vol. 120, 363-375, 2014
- **M. Padilla**, B. Michl, N. Hagedorn, C. Reichel, S. Kluska, A. Fell, M. Kasemann, W. Warta, M. C. Schubert, Local series resistance of silicon solar cells with complex current paths, *IEEE Journal of Photovoltaics*, Vol. 5, Issue 3, 752-758, 2015
- **M. Padilla**, C. Reichel, N. Hagedorn, A. Fell, B. Michl, R. Keding, M. Kasemann, W. Warta, M. C. Schubert, Contact fault characterization of complex silicon solar cells: a guideline from current voltage characteristics to luminescence imaging, *Progress in Photovoltaics*, published online, 2015

- B. Michl, **M. Padilla**, I. Geisemeyer, S.T. Haag, F. Schindler, M.C. Schubert, W. Warta, Imaging Techniques for Quantitative Silicon Material and Solar Cell Analysis, *IEEE Journal of Photovoltaics* Vol. 4, Issue 6 1502-10
- M.C. Schubert, **M. Padilla**, B. Michl, L. Mundt, F. Schindler, J. Hohl-Ebinger, W. Warta, Iron related solar cell instability: Imaging analysis and impact on cell performance, *Solar Energy Materials and Solar Cells* Vol. 138, 96-101, 2015
- P. Saint-Cast, **M. Padilla**, A. Kimmerle, C. Reichel, An analytical model for interdigitated back contact solar cells, *IEEE Journal of Photovoltaics*, Vol. 4, Issue 1, 114-121
- M. Hendrichs, **M. Padilla**, J. Walter, F. Clement, A. Fell, B. Rech, Screen-Printed Metallization Concepts for Large-Area Back-Contact Back-Junction Solar Cells, *IEEE Journal of Photovoltaics*, published online, 2015
- K. C. Fong, **M. Padilla**, A. Fell, E. Franklin, K. Teng, K. R. McIntosh, A. W. Blakers, Characterization of Perimeter Loss via PL imaging, *IEEE Journal of Photovoltaics*, published online, 2015
- R. Müller, C. Reichel, J. Schrof, **M. Padilla**, M. Selinger, I. Geisemeyer, J. Bennick, M. Hermle, Analysis of n-type IBC solar cells with diffused boron emitter locally blocked by implanted phosphorus, *Solar Energy Materials and Solar Cells*, published online, 2015
- S. Mastroianni, F. Heinz, J.-H. Im, W. Veurman, **M. Padilla**, M.C. Schubert, U. Würfel, M. Grätzel, N. Park, A. Hinsch, Analysing the effect of crystal size and structure in highly efficient $\text{CH}_3\text{NH}_3\text{PbI}_3$ perovskite solar cells by spatially resolved photo- and electroluminescence imaging, *Nanoscale*, Vol. 7, 46, 19653-19662, 2015

Conference proceedings

- **M. Padilla**, B. Michl, C. Reichel, N. Hagedorn, S. Kluska, S. T. Haag, R. Keding, A. Fell, M. Kasemann, W. Warta, M. C. Schubert, Characterizing local contact resistances of interdigitated back contact silicon solar cells, *Proceedings of the 29th European Photovoltaics Conference*, Amsterdam, The Netherlands, 2015
- F. Fertig, **M. Padilla**, H. Höffler, I. Geisemeyer, O. Breitenstein, M. Schubert, S. Rein, Short-circuit current density imaging methods for silicon solar cells, *Presented at the 5th International Conference on Crystalline Silicon Photovoltaics*, Constance, Germany 2015, *Energy Procedia* Vol. 77, 43-56 (peer-reviewed)
- M. Hendrichs, **M. Padilla**, J. Walter, F. Clement, A. Fell, B. Rech, Evaluation of Screen-Printed Metallization Concepts for Large-Area BC-BJ Solar Cells, *Proceedings of the 42nd IEEE Photovoltaics Specialists Conference*, New Orleans, USA, 2015
- I. Hädrich, **M. Padilla**, A. Jötten, M. Mundus, W. Warta, H. Wirth, Increasing module power: Detailed experimental and theoretical analysis of finger and ribbon optics, *to be presented at the 30th European Photovoltaics Conference*, Hamburg, Germany, 2015
- M. Pospischil, M. Kuchler, M. Klawitter, C. Rodriguez, **M. Padilla**, R. Efinger, M. Linse, A. Padilla, H. Gentischer, M. König, M. Hörteis, L. Wende, O. Doll, R. Zengerle, F. Clement, D. Biro, Dispensing Technology on the Route to an Industrial Metallization Process, *Presented at the 5th Metallization workshop*, Constance, Germany, 2014, *Energy Procedia* Vol. 67, 138-146 (peer-reviewed)
- M.C. Schubert, J. Schön, A. Abdollahinia, B. Michl, W. Kwapil, F. Schindler, F. Heinz, **M. Padilla**, J. Giesecke, M. Breitwieser,

S. Riepe, W. Warta, Efficiency-Limiting Recombination in Multicrystalline Silicon Solar Cells, *Solid State Phenomena* Vol. 205, 110-117, 2014

- C. Rodríguez, M. Pospischil, A. Padilla, M. Kuchler, M. Klawitter, T. Geipel, **M. Padilla**, T. Fellmeth, R. Efinger, M. Linse, H. Gentischer, M. König, M. Hörteis, L. Wende, O. Doll, F. Clement and D. Biro, Analysis and Performance of Dispensed and Screen Printed Front Side Contacts on Cell and Module Level, to be presented at the *30th European Photovoltaics Conference*, Hamburg, Germany, 2015

Master's thesis supervisions

During the scope of this dissertation, the author supervised the Master's thesis of

- H. Chu - Luminescence Imaging for the Characterization of Interdigitated Back-Contact Silicon Solar Cells, *Karlsruhe Institute of Technology*, 2013
- M. Selinger - M. Selinger titled Lock-In Thermography and Thermal Modelling of Interdigitated Back-Contact Silicon Solar Cells, *Universität Freiburg*, 2014
- K. Hagedorn - Luminescence Imaging and Lock-In Thermography for Local Device Fault Analysis of Interdigitated Back Contact Silicon Solar Cells, *Universität Freiburg*, 2015

Acknowledgements

I would like to express my sincere gratitude to all the people who supported me over the past years towards the completion of this dissertation. In particular, I would like to thank

- Prof. Dr. Eicke Weber and Prof. Dr. Leonhard Reindl for the academic supervision of this thesis,
- the Reiner Lemoine Foundation for scholarship support,
- my immediate supervisors Martin Schubert and Wilhelm Warta for giving me the opportunity to work in such an excellent environment, for their integrity and their great support,
- the head of my department Prof. Dr. Stefan Glunz for his leadership, advice and sense of humor,
- Haifeng Chu, Marisa Selinger and Nikolaus Hagedorn for being excellent Master's thesis students,
- Christian Reichel, Bernhard Michl, Roman Keding, Martin Kasemann, Sven Kluska, Ino Geisemeyer, Jochen Hohl-Ebinger, Johannes Greulich, Hannes Höffler, Fabian Fertig, Otwin Breitenstein, Johannes Giesecke, Thomas Hultzsich, Martin Hermle, Achim Kimmerle, Max-Sebastian Hendrichs, Pierre Saint-Cast, Ralph Müller, Martin Bivour (Hetero-Papst), Bernd Steinhauser, Frank Feldmann, Manuel Schnabel, Alexander Krieg, Alois Kabelschacht, Benjamin Thaidigsmann, Ingrid Hädrich, Anna Jötten, Markus Mundus and many other colleagues from Fraun-

hofer ISE and other institutes with whom I collaborated and had fruitful discussions,

- once again Christian Reichel for his immeasurable helpfulness for proof-reading and for inspiring me to focus on this fascinating solar cell concept,
- once again Roman Keding for providing solar cells with highly diverse processing faults and for this technological wisdom,
- Andreas Fell from ANU for creating the solar cell simulator Quokka, which is an outstanding contribution to my work and the work of the whole silicon PV community, and for the countless times he has helped me solve problems and adapt the program to my needs,
- Evan Franklin, Kean Fong, Andrew Blakers and all members of the ANU PV group for their hospitality during my stay,
- Elisabeth Schäffer for help on so many solar cell measurements over the years,
- Stephen Haag for the implementation of the LabView interface for the luminescence imaging setup that greatly improved the quality and speed of my experiments
- Mónica López Sáenz, Oliver Schreer and Christian Peppermüller from IRCAM GbmH for the fruitful collaboration in the development of the new lock-in thermography system,
- the other members of my group 'material and cell analysis' at Fraunhofer ISE, Florian Schindler, Friedemann Heinz, Jan Holtkamp, Wolfram Kwapil, Laura Mundt, Tim Niewelt, Jonas Schön, Matthias Breitwieser, Michael Knörlein, Sven Mägdefessel, Alireza Abdollahinia and Andreas Kleiber, for being such great colleagues and friends (Außerordentlichesgroupmeeting),
- the various colleagues helping me with proofreading of this document, namely Christian Reichel, Roman Keding, Martin Schubert, Marisa Selinger, Wilhelm Warta and Bernhard Michl,

- Brauerei Loscher GmbH for manufacturing a delicious mate-based caffeinated beverage,
- all people active in online Matlab and L^AT_EX forums that saved me countless hours of programming and debugging,
- Birgit Stadel and Stefanie Vieler for their great support in our departments secretariat,
- all the other colleagues of the SEC and PTQ departments that have made work at Fraunhofer ISE such an enjoyable experience,
- my parents Miguel Angel and Silvia and siblings Galia and Marcel for their love and support,
- and finally, the woman who from the beginning to the completion of this thesis went from being my girlfriend, to my fiancée to my beloved wife: Sarah Louise Lyons-Padilla.

In order to accelerate the development of photovoltaic energy conversion as a major source of renewable energy in the global energy mix, manufacturing solar cells with increasingly higher conversion efficiency is a powerful means of cost reduction. Interdigitated back contact (IBC) solar cells currently have the highest efficiency of all silicon solar cells on the laboratory and industrial scale. Great research efforts have been made to reduce the production costs and enable more widespread commercial application of this cell architecture.

Despite the great interest of companies and the research community in IBC cells and the recent success of spatially resolved characterization techniques, there was little knowledge about applying these characterization techniques on IBC cells. The complex device structure of IBC cells requires consideration of the three-dimensional current flow and carrier density distributions that these imaging techniques are based on.

This dissertation aims to close that knowledge gap by analyzing IBC cells through experiments and simulations using luminescence imaging, lock-in thermography and spectrally resolved light beam induced current mapping at all important solar cell operating conditions.

ISBN 978-3-8440-4242-9



9

783844

042429

SHAKER
VERLAG